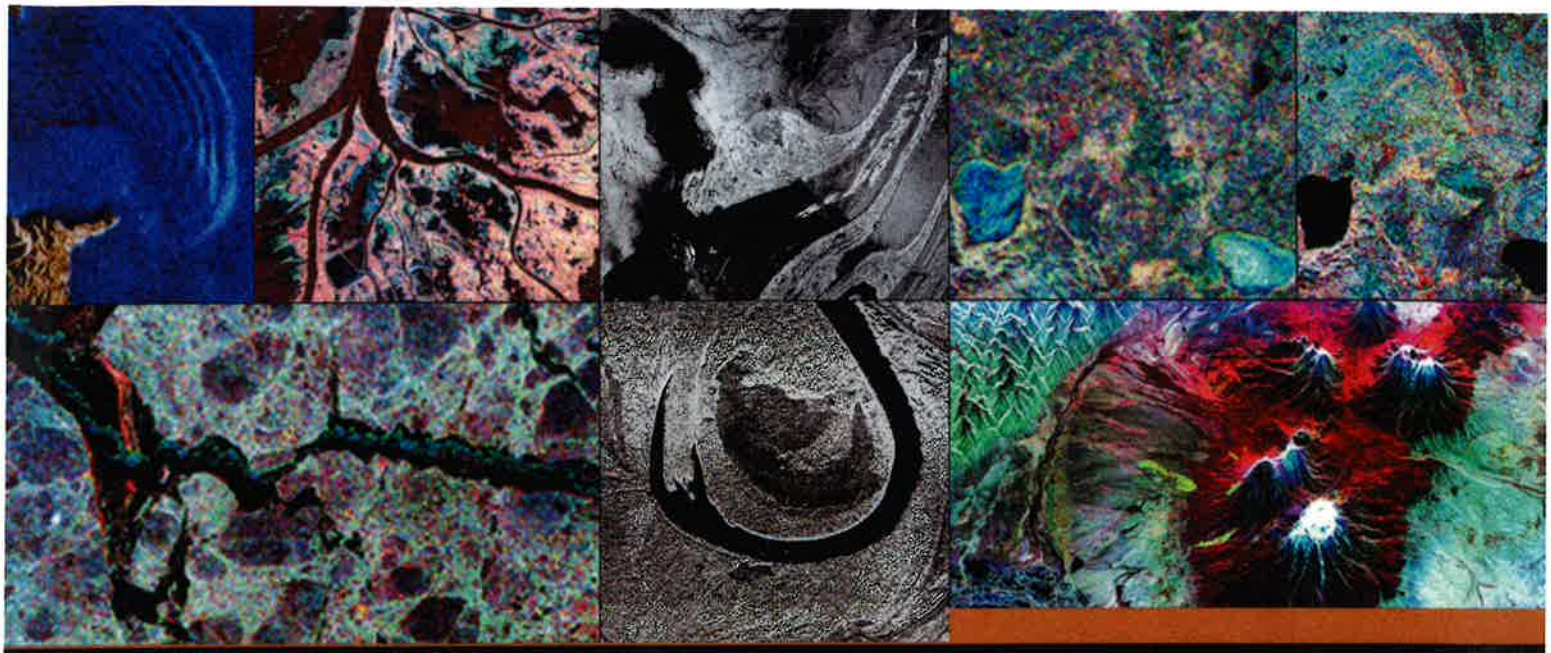

Principles & Applications of IMAGING RADAR

Manual of Remote Sensing Third Edition, Volume 2

Published in Cooperation with the American Society for Photogrammetry and Remote Sensing

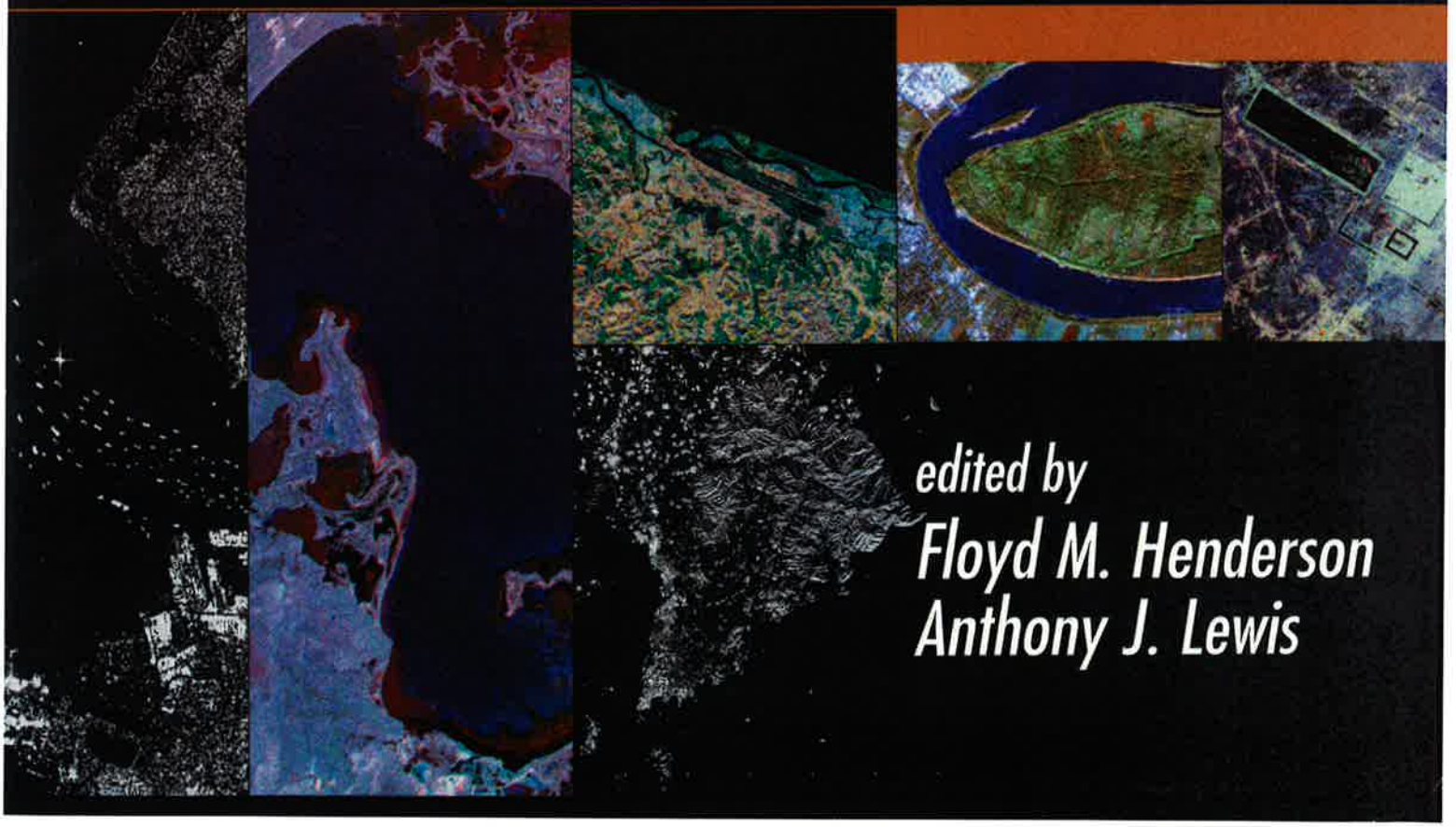

edited by
Floyd M. Henderson
Anthony J. Lewis

CHAPTER 4

Radargrammetry

Author: F.W. LEBERL

4-1 INTRODUCTION

Today we look back at almost a half-century of radargrammetry research, beginning with the work by Rinner (1948). As a result there exists a considerable amount of material about radar images, geometric models of radar sensors and applications to mapping tasks. The initial interest in remote sensing with radar images predates the introduction of the word "remote sensing."

For about two decades, the published body of radargrammetric work addressed the circularly scanning plan-position indicator or PPI-radar. The culmination of this interest was the monograph by Levine (1960), aptly coining in its title the word "radargrammetry" in analogy to "photogrammetry." To this day, one denotes with "radargrammetry" the extraction of geometric information about objects from radar images.

Side-looking (airborne) radar (SLR or SLAR), both with a physically long antenna (a so-called "real" aperture) or with an antenna whose length is obtained by signal processing (a so-called Synthetic Aperture Radar, SAR), became a focus of published studies after the first Symposium on Remote Sensing of Environment. LaPrade (1963) speculated on stereo-viewing and the stereo analysis using overlapping SLR-images. Rosenfield (1968) and Gracie *et al.* (1970) developed mathematical models for SLR and SAR sensors. Macchia (1957), Crandall (1969), Hockeborn (1971) and others reported on successful mapping projects with radar images, developing conventional and image maps of cloud-covered tropical areas.

The initial phase of radargrammetry development concluded with reports on equipment (Yoritomo, 1972; Graham, 1972, Greve and Cooney, 1974), mathematical analyses (DBA-Systems, 1974; Gracie *et al.*, 1970) and studies on mapping accuracies (Gracie and Sewell, 1972; Leberl, 1974 and others). Simultaneously there was a burst of commercial mapping activity along the world's tropical belt (Azevedo, 1971; Leberl, 1972 a,b; 1974; 1975d,e,f and others), producing often rather unsophisticated mapping products in the form of so-called "semi-controlled image mosaics." Radar film image strips were assembled into image mosaics by adjusting the strips to one another and by trying, in a crude process with wet paper, to place the images correctly over some control points. Obviously, the resulting accuracy was poor and the effects of topographic relief were entirely ignored.

This initial developmental phase of radargrammetry was followed by a series of studies which were inspired by NASA's satellite experiments SEASAT in 1978 (Teleki and Ramseier, 1978), Shuttle Imaging Radars A in 1981 (Elachi *et al.*, 1982a,b) and B in 1984 (Elachi *et al.*, 1986b). An early predecessor for these satellite radargrammetry studies was the lunar Apollo 17 mission with the Apollo Lunar Sounder Experiment (ALSE) imaging radar in 1972 (Phillips *et al.*, 1973; Leberl, 1975c; 1976a). A total of three orbital passes along the lunar equator resulted in two stereo image pairs covering nearly the entire lunar equatorial circumference. Extreme look angles from the nadir out to perhaps 15° off-nadir resulted in a combined altimeter/stereo measuring system. Angular disparities were very small, yet they produced useful stereo parallaxes. Mons Maraldi near one of the lunar landing sites was the target of stereoscopic topographic shape reconstruction (Figure 4-1).

These lunar radar images were available only in an analog form, whereas subsequent satellite images from SEASAT were ultimately created as a digital product. Radargrammetric work with SEASAT included geocoding by Curlander (1981a,b; 1982) and Curlander and Pang (1982), but no stereo work was reported, except for some review-type analysis by Leberl (1980) and Leberl *et al.* (1982).

SEASAT was followed by imaging radar experiments on Space Shuttle flights. With SIR-A it was possible to perform crossing orbit stereo (Kobrick *et al.*, 1986), but only from film images. SIR-B generated strictly digital data that led to a series of useful stereoscopic data sets with variable incident angle geometries (Leberl *et al.*, 1986a,b,c,d). Overlapping images taken with different look angles were orthorectified and co-registered. The resulting images were used to present color presentations showing individual images in red, green and blue. In fact, this encodes a so-called "incident angle signature" of various materials in color (Cimino *et al.*, 1986).

Digital radar image processing has led to several significant radargrammetric developments: a fully operational aircraft radar mapping system called STARMAP (see Section 4-13.2); an elaborate stereo radar analysis tool kit to process NASA's Magellan radar images of planet Venus; and numerous systems to "geocode" radar images, in particular European ERS-1 images (Schreier, 1993). The operational aircraft-based radargrammetric mapping system STARMAP is based on 1) a digital real-time imaging radar and 2) on aircraft position observations with the Global Positioning System (GPS), thereby avoiding any reliance on ground data and ground control points, with the exception of check points for differential GPS (Mercer *et al.*, 1986; 1989; Leberl *et al.*, 1987; Leberl and Mercer, 1987; Leberl, 1990).

NASA's Venus mapping project "Magellan" resulted in the most elaborate and consistent global radar image data, consisting

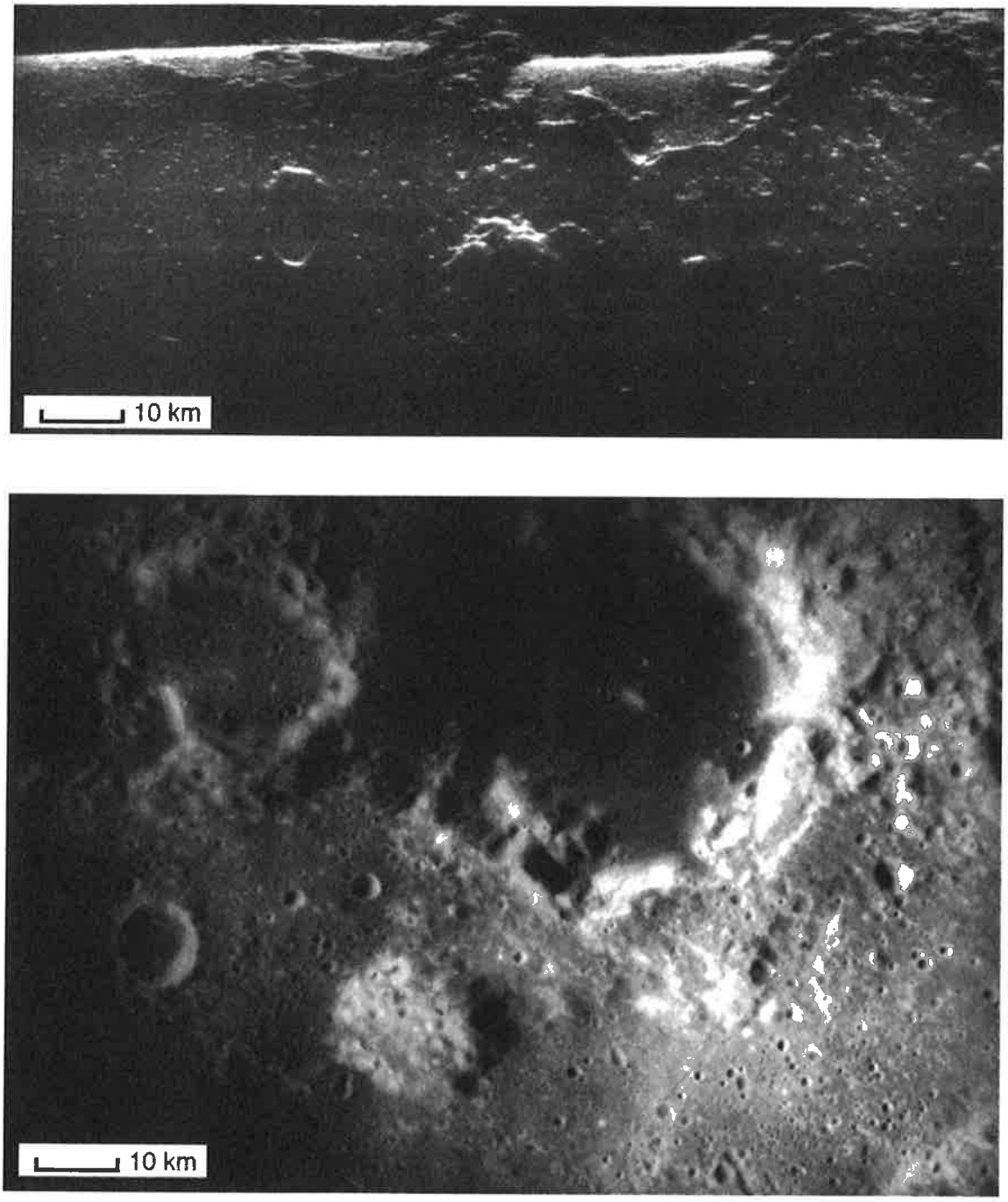

Figure 4-1. Apollo Lunar Sounder Experiment (ALSE) imagery over Mons Maraldi near the equator on the Moon (above). This radar image was taken at 2 m wavelength and was combined with a second image to form a stereo pair and to create a digital model of the mountain with about 1000 m elevation. Below: Optical camera image taken from the Apollo 17 command module (from Leberl, 1975c).

of about 400 Gigabytes of SAR images, covering the entire planet and developing a second and third coverage of large segments of the surface. This program lent itself to numerous stereo- and non-stereo mapping experiments (Leberl *et al.*, 1992a,b,d). An important element of the analysis was the reconstruction of relief from shading variations. For this purpose, several authors have contributed work on shape-from-shading (Wildey, 1986 a,b; Kirk, 1984, 1987; Thomas *et al.*, 1990) and applied it to Venus Magellan images (Kirk *et al.*, 1992; Leberl *et al.*, 1991b, 1992a,b,c). A Magellan stereo-radargrammetric software system has been designed and implemented for use by individual scientists at their desk side for processing small data sets (Leberl, 1993).

The ability to process overlapping images from opposite look angles has never been implemented. An initial study into this issue was performed by Fullerton *et al.* (1986), but considerably more work will be required to begin the use of image pairs from opposite look geometries. This issue has become particularly relevant for the Magellan data set, where an opposite look angle coverage exists, but cannot be used properly since matching of the two coverages has not been possible in accentuated terrain. Straight forward ortho-rectification of ascending and descending orbit ERS-1 images with a given digital elevation model typically results in mismatches of about ±4 pixels (±60 meters, as reported for example by Rott and Nagler, (1994)).

The most recent technology to become relevant for radargrammetric surface shape reconstruction is interferometry. While its use for terrain mapping goes back to the early 1970s (Graham, 1974) it had not become a serious option for operational terrain mapping until fully digital radars were available in combination with sensor positioning systems like GPS. While no operational system is being used today, its transition to operational use is imminent. A further discussion of interferometry is presented elsewhere in this text (see Chapter 6); its likely impact on radargrammetry is the topic of Section 4-12.

The push to develop interferometry derives from work at the Jet Propulsion Laboratory, where initial efforts were undertaken in the context of radar astronomy to employ digital radar signals for interferometric measurements. This culminated in demonstrations aboard an aircraft (Zebker and Goldstein, 1986).

The increased interest in this technology is largely supported by data from the European Remote Sensing satellites (ERS-1, ERS-2) with its synthetic aperture radar imaging system. These satellites have greatly stimulated radargrammetric work in Europe, as documented by the series of workshops with proceedings of the GeoSAR group (Proceedings of GeoSAR, 1987, 1989, 1991, 1994); and as described by a collection of papers compiled about ERS-1 geocoding (Schreier, 1993).

One may expect that the interest in radar image processing and radargrammetric issues will continue and even increase. At the time of this writing, Space Shuttle SIR-C has just shown spectacular multi-frequency images. SIR-C flew in combination with the German E-SAR in two flights in 1994; ESA's ERS-2 was launched (1995), ESA's ENVISAT is being prepared for launch in (1998) and Canada's RADARSAT was launched (1995). Russia's ALMAZ-2 and various airborne systems are on standby. The analysis of these data will increasingly become more sophisticated and employ images acquired 1) from different sensor positions to vary incident angles, 2) at different times to vary surface characteristics and to look for change, 3) with different imaging parameters such as frequency and polarizations to analyze sensitivity to certain characteristics of objects, 4) at arrangements for interferometric analysis. These analysis techniques will increase the importance of methods to manage the geometry of images and to unravel the ambiguity of backscatter effects from terrain shape and surface materials.

This chapter consists of 14 sections belonging to four parts: 1) Part A looks at a few images and considers some basic equations; 2) Part B discusses a radargrammetric tool kit with resection-in-space, simulation, image rectification or geocoding, radar image matching and matching of dissimilar images taken at different times; 3) Part C addresses the reconstruction of surface topography and matching of dissimilar radar images, taking a look at stereoscopy and other ways of extracting shape information from radar images such as Shape-from-Shading, and concluding with radar interferometry; and 4) Part D discusses NASA's Magellan mission to planet Venus, and Europe's ERS-project, and the Envisat-SAR follow-on effort.

The topic of "applications" is not specifically addressed, although information on applications is given. A very successful application with a focus on geometric processing of imaging radar concerns sea ice motion (see Section 4-13.1). This example of radargrammetric mapping is discussed in a cursory manner. Radar image mapping at a scale of 1:50,000 is also presented. Note that routine mapping with overlapping radar images is now a reality and promises to remain an offering of mapping technology; the move from the research laboratory into commercial application is, however, only a recent accomplishment. Radar stereopsis' role as a mapping tool is uncertain when considering the rapid advances made in radar interferometry, both from satellites with repeat orbits and a single antenna, or with dual-antenna single pass interferometry from aircraft, and possibly from space.

4-2 SAMPLE RESULTS OF RADARGRAMMETRY

Figure 4-2 is a pair of Intera Technology's Star-2 aircraft radar images from an operational 1:50,000 scale image mapping project. It illustrates the quality of stereo radar images that one will typically see in softcopy. Figure 4-2 presents pixels of 6 meters resolution, covering about 4 km x 4 km in parts (a), (b). The stereo impression shows that the (photo-equivalent) "base-to-height-ratio" is acceptable, *i.e.* the vertical dimensions are well accentuated. The peak of the mountain shown in parts (c), (d) is about 1000 m above the river valley. One also immediately becomes aware of the problem of radar stereo, namely the differences in illumination. In image 4-2(c), the shadow extends from the mountain top to some relatively short distance into the flat terrain, while in 4-2(d), it extends much further; there is not a stereo impression in the shadow area. The stereo impression and stereo measurement option exist only in areas that are free of shadows in both images.

The image pairs in Figure 4-2 present a same side geometry. That is the operational arrangement for radar stereo mapping. Figure 4-3 is a mapping result at a scale of 1:50,000. The height

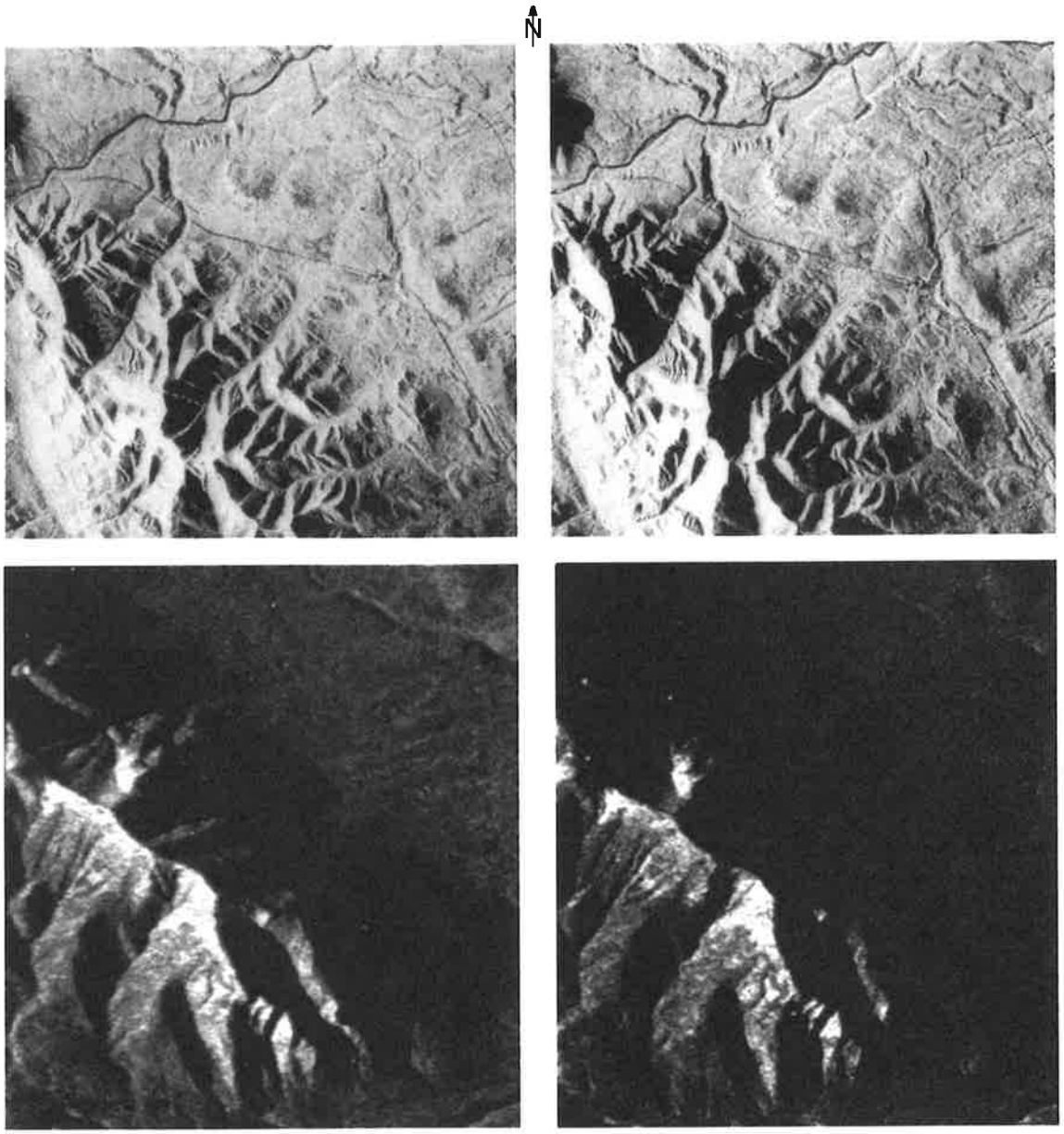

Figure 4-2. Image pair for same-side stereo radar, covering 4 km x 4 km (a,b) and 2.5 km x 2.5 km with 6 m pixels. X-band (3 cm wavelength), taken from about 9 km flying height. The areas are segments of the Brazeau-range in Alberta, Canada, with the STAR-2 synthetic aperture radar (courtesy Intera Technologies Ltd., Now INTERMAP).

accuracy supports a 100 meter contour interval. The 50 meter contours are interpolated in between those at 100 m. Note that the contour lines are being generated by digital elevation computations and are not directly plotted. Again, areas of shadows do not show height information; the contour lines are merely interpolated through the shadows by the computer.

This product is found to be useful for mineral and oil exploration. Typically the right to explore a certain area is obtained for a certain period of time. There may not be time for any conventional type of mapping. The radargrammetric process can reduce a result very quickly. One may process a 10,000 square km area within 4 weeks from receipt of raw images. Image maps are found to be satisfactory in supporting the exploration and field operations.

Figure 4-3 shows contour lines without editing by a cartographer; therefore, small geomorphological detail is in error. The digital elevation model (DEM) is obtained by regularly sampling a square grid and then adding terrain break lines. This input data set is used to interpolate contours and a dense square grid DEM with a resulting error of 20 to 40 meters in height. Figure 4-3 is representative of a 20 to 40 meter accuracy in height, which is not common in photogrammetric mapping. Therefore, a user may not have a good sense of what to expect from such a mapping prod-

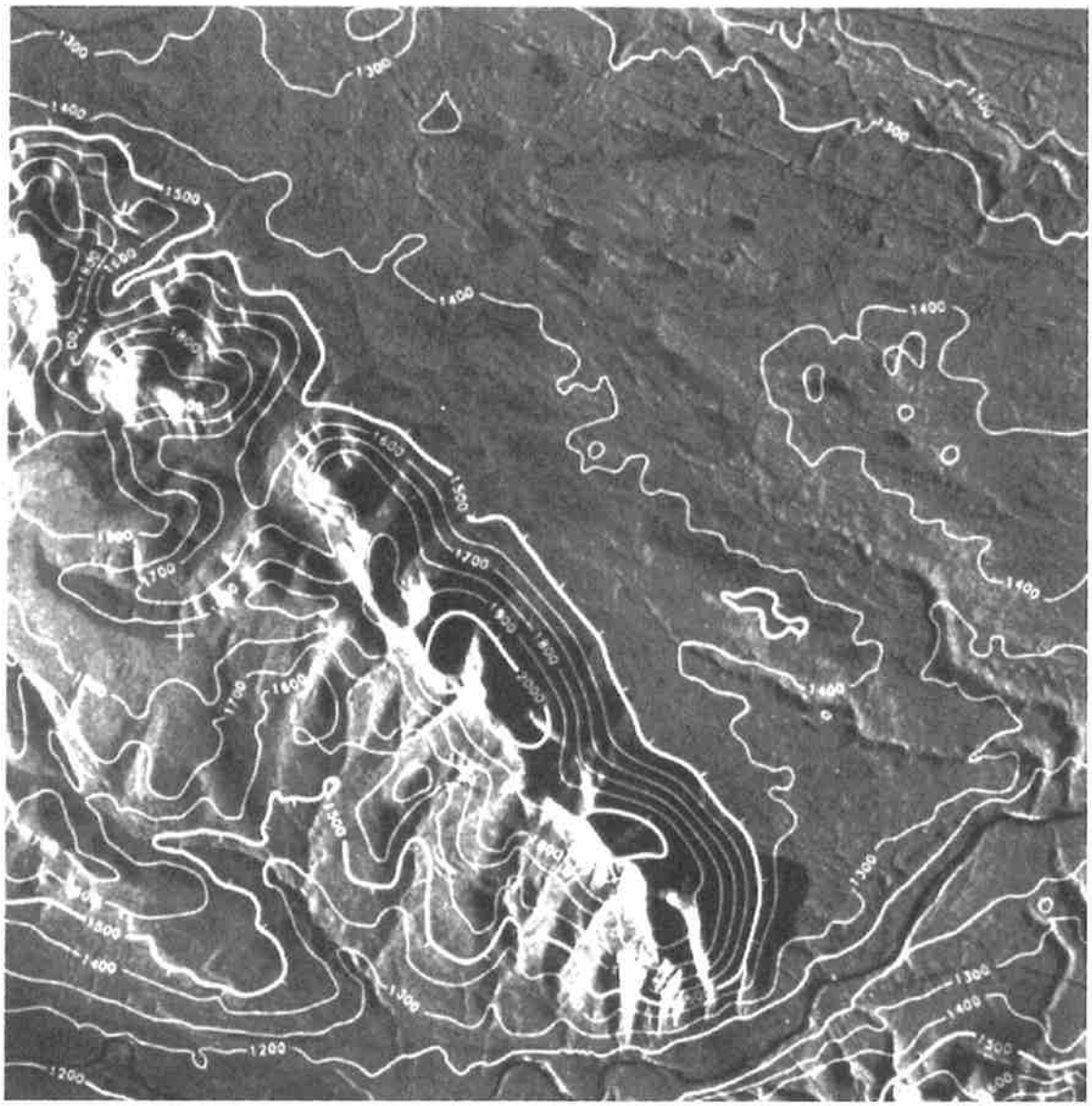

Figure 4-3. Segment of an image map produced from SAR images of the type shown in Figure 4-2. The geo-coded radar images are combined with terrain contour lines at 100 m intervals, and are typically presented at scale 1:50,000 (*i.e.*, with 8 pixels per mm). The deliverable paper map is accompanied by a digital file with an ortho-rectified radar image coverage and a digital elevation model (This sample was produced by Vexcel Corp., Boulder, Colorado, for Intera Technologies Ltd, Calgary, Canada).

uct, particularly when customary photogrammetric mapping is with accuracies of 1 point in 10,000 of the aircraft's flying height, ranging from ±5 cm to ±1.5 m.

In their DEM-format, the height data are also being utilized for geophysical/seismic modeling for exploration. The DEM can also support predictions of how formations continue underground.

Note that radargrammetric mapping is not based on any use of ground control points. Ground control would be very expensive in remote territories for which SLR/SAR images are useful. Therefore, the geometry depends completely on the global positioning system (GPS). An airplane carrying the radar sensor must be equipped with a differential GPS with one antenna on the airplane and one on the ground. Both are receiving at the same time. While the aircraft's position is measured as accurately as the GPS permits with a single on-board receiver, this would be insufficient for the measurement of radar stereo parallaxes. Therefore, the GPS observations on the airplane must be post-processed jointly with the observations at the ground-based receiver from the known location.

Earlier publications about this technology suffered from the lack of good GPS-satellite coverage, since, until recently, only a very narrow time window existed each day in tropical areas near the equator, in which one could track a sufficient number of at least 4 GPS satellites (Mercer *et al.*, 1989). Radar mapping is also

based on inertial navigation (INS) to control in real-time the imaging operation itself: this consists of steering the imaging antenna and adding the received radar echoes with compensation of small irregular aircraft motion (phase history processing of radar echoes). There are discrepancies between these INS-measurements and GPS-data. The inertial navigation data, however, have been used to generate the image in real time on board the aircraft. The inaccuracy of INS, with drifts of 3 to 4 kilometers over an hour, must be removed by GPS information. This, in turn, is collected at intervals of a second or so. Conversely the data gaps in-between GPS-observations are being filled in by INS-data.

Mapping with radar should include the capability to use the shadow areas to strengthen the height information that one would otherwise get from stereo alone. One can measure the height difference between the end points of a shadow and enforce this elevation difference in the DEM. Finally, one can further refine the DEM with shape-from-shading algorithms to improve geomorphological detail.

Operational radar mapping is organized by map sheets, covering perhaps an area of 50 km by 50 km at a time. Flight lines may cover several map-sheets, perhaps 150 km in length. This requires work with very large images, about 30,000 pixels in one direction (along-track) and 4,000 pixels across-track for each image. Operations use several images simultaneously. Interactive manipulation of multiple images with more than 100 megabytes in each still represents a challenge when configuring an operational end-to-end mapping system, even based on the most modern computing resources.

That this is a true statement has become evident also from the work done at NASA for its Magellan mission to map planet Venus (Leberl, 1993), and at the European Data Processing and Archiving Facilities (PAFs) for the images from the ERS-1-mission (Schreier, 1993). In both cases "mapping" excludes the routine and full use of overlapping imagery for 3-dimensional reconstruction of terrain relief. Instead, operational systems exist for routine "geocoding," *i.e.* the correction of images for systematic radar-perspectives, or for the terrain correction in cases where an external DEM is available. The term "operational" is not applicable to the correction of effects of terrain relief extracted from the radar images themselves by stereo or shape-from-shading.

4-3 PHENOMENA IN RADAR IMAGES

Radar images are examined next, with an eye on the geometric point of view. Figure 4-4 shows the Darien Province in Panama that was mapped in 1967 in a collaborative effort of several US companies, including Westinghouse and Raytheon, operating under contract to the US Army; it was the first systematic

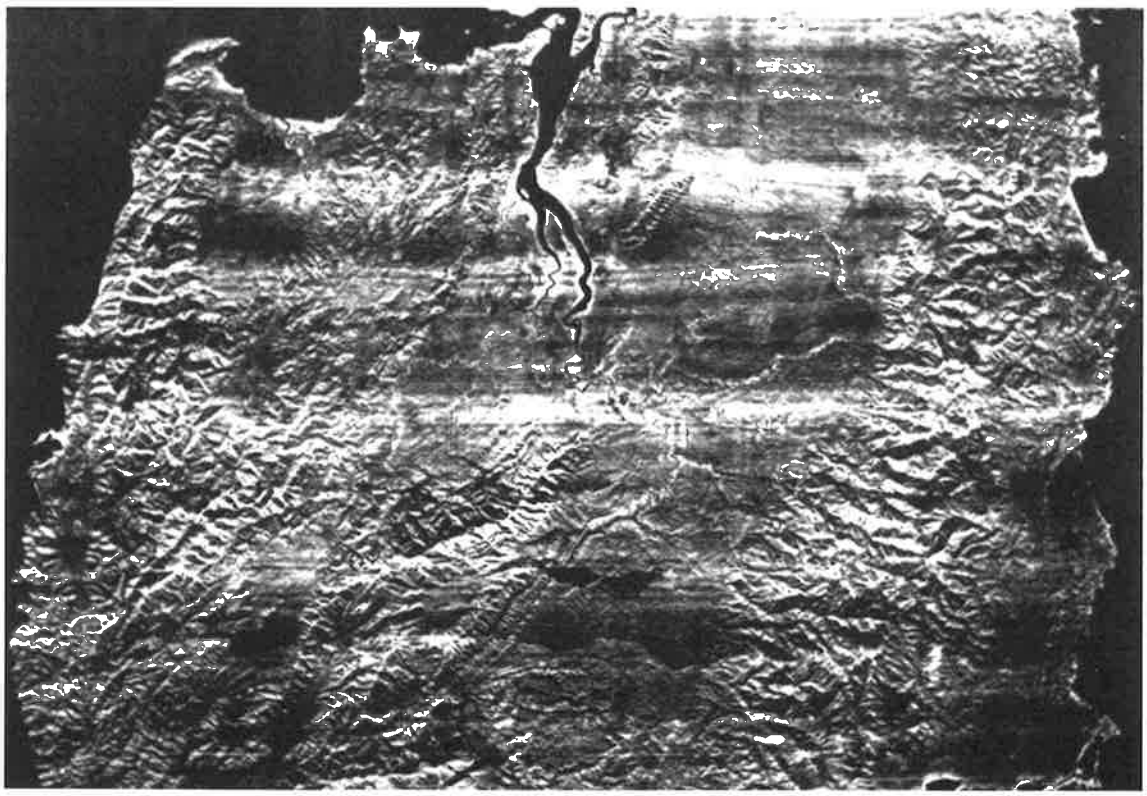

Figure 4-4. Historic radar image mosaic of the Darien Province of Panama, created in 1967 as part of project RAMP (Radar Mapping of Panama), using airborne real aperture radar imagery in the K_a-band (0.8 cm wavelength). For details see Crandall (1969).

mapping effort of a jungle area by radar. This area had not been mapped prior to 1967 (Crandall, 1969). The map displays contours based on a combination of techniques including altimetry and an early version of radar-interferometry (Graham, 1974). The use of interferometry was later abandoned. As already pointed out above, interferometry was subsequently revitalized in the digital domain and now holds much promise. Figure 4-5 may be the first contour maps ever produced from radar images.

Figure 4-6 serves as a reminder that in radar images sloping structures or structures extending in height from a reference plane manifest themselves in an unexpected manner. In this case the top of a moun-

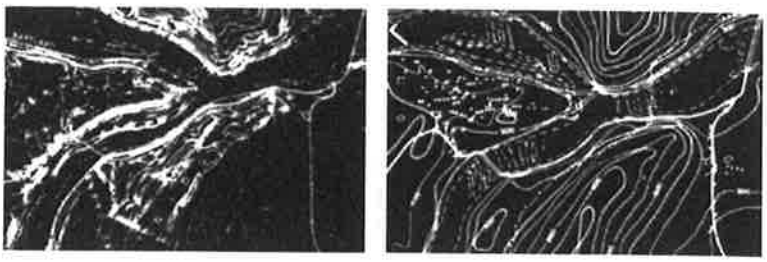

Figure 4-5. Segment of a contour map produced by conventional means (left) and from radar altimetry and radar interferometry as part of project RAMP for the Darien Province in Panama. This project was discussed by Hockeborn (1971). The interferometry work was described by Graham (1974).

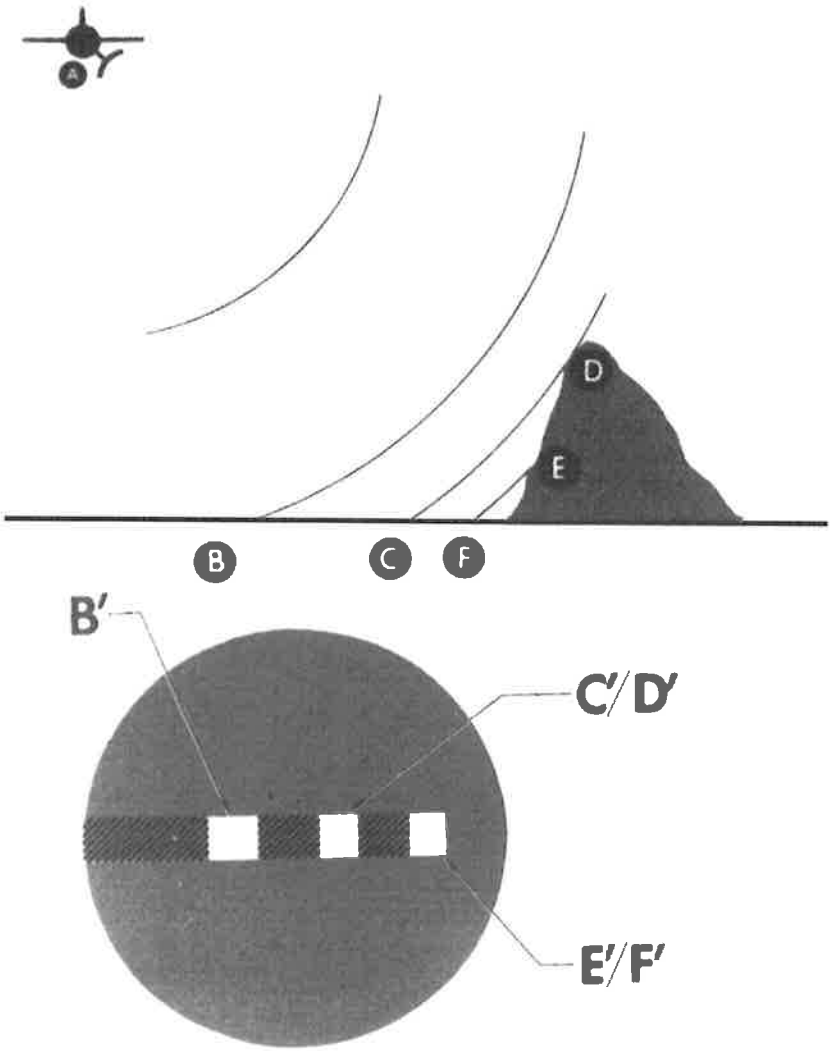

Figure 4-6. Radar images are the product of range measurements. As a result, one may image the top D of a mountain "laid-over" its base F. Note that each "projection line" is a circle with its center at the antenna. The sketch is in a plane perpendicular to the flight direction. (Graph courtesy Loral Defense Systems and G. LaPrade).

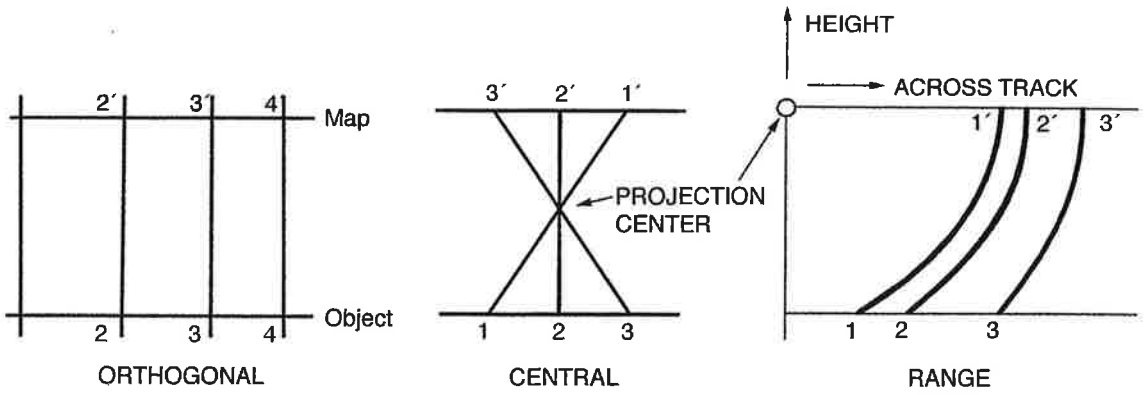

Figure 4-7. Projection lines in a radar imaging "perspective" are circles centered at the antenna, as seen at right. This compares with a central perspective projection (middle), or with an orthogonal projection (left), where projection lines are straight.

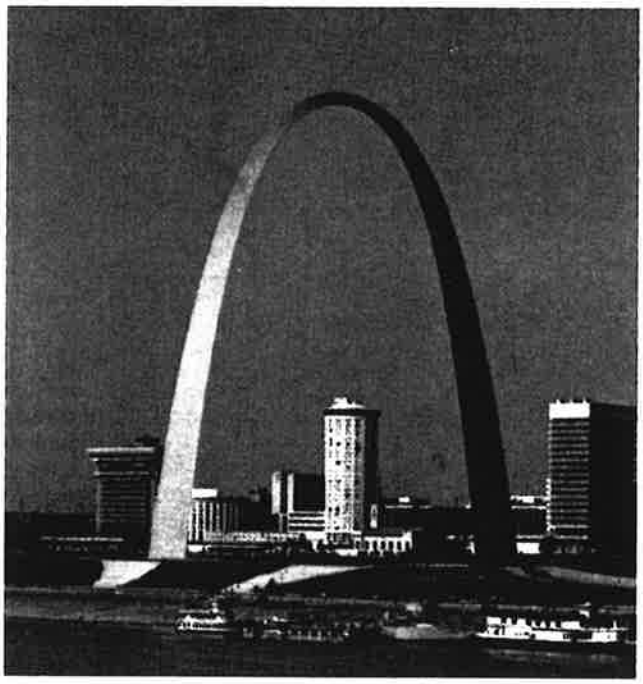

Figure 4-8. The Gateway Arch in St. Louis, as it extends 600 feet above the banks of the Mississippi, looking westward towards downtown St. Louis.

tain is imaged before its base so that a slope really "lays over." The topic of radar layover is discussed in more detail in Chapters 2 and 3.

The projection line connecting a ground point with an image point is a circle, unlike in a camera, where it is a straight line (Figure 4-7). If the ground is projected into an image plane, think of an image projection plane passing through the antenna. This may be a horizontal projection plane or also vertical, as will be seen later. Most geometric peculiarities of radar imagery result from having circular projection lines. Figure 4-7 illustrates that in the central perspective the lines connecting the object and image are all straight and pass through the projection center. In radar, the lines connecting objects and images are all circles and the circles are concentric with respect to the antenna location. In an orthogonal map projection, the object and image are connected by parallel straight lines perpendicular to the image plane.

An image presenting the full complexity of the radar imaging process shows the Gateway Arch in St. Louis (Figures 4-8 and 4-9). LaPrade (1975a) used this image in classes on radar image interpretation to challenge his students in interpreting the complex phenomena displayed in this view.

The image of the Gateway Arch consists of a complicated shape with small extruding elements. The shape is not only a result of the circular projection lines, but from mirror reflections (Figure 4-10). The lawn around the Gateway Arch is smooth, creating a mirror reflection. Secondly, there are also reflections off the walls of the Arch. This means that part of the structure will not be visible to the radar because it bounces energy away from the antenna. However, if the mirror reflection directs energy towards the ground, and the ground reflects back to the antenna, then we will see that part of the structure on the radar image. The radar combines direct reflections off the structure with indirect reflections via the lawn, and, there are parts of a so-called "no-show," *i.e.* a portion of the structure is not visible because it is reflecting away from the antenna. This so-called "no-show" phenomenon is often considered a major limitation of radar images for image interpretation and mapping. Dowman and Morris (1982) and Dowman and Gibson (1983) repeatedly complained that radar images miss many of the objects needed for general purpose maps. "No-shows" could be, however, a strong motivator for the use of multiple images taken from different vantage points to ensure that all relevant information is being covered by the sensor.

Figure 4-11 presents a set of sketches to explain radar images of cubes, pyramids and even spheres. Figure 4-12 is the image of a transmission tower at the side of a water body; Figure 4-13 explains the image. The beach reflects strongly towards the aircraft. The tower is laid over so that the tip of the tower falls towards the antenna and a mirror reflection of the tower exists. This mirror reflection via the water is not on top of

Figure 4-9. SAR image taken of the Gateway Arch with the GEMS-1000 radar system at X-band with ground resolution at 10 meters. Downtown St. Louis is at the bottom. The Mississippi and a few bridges are on the top of the image (courtesy G. LaPrade and formerly Goodyear Aerospace Corporation, now Loral Defense Systems).

the image of the water but on the land, since the "echo-time" or slant range to the mirror reflection is longer than that of the primary image.

In order to explain those images more completely, one needs to talk about specular and diffuse reflections as well as of dihedral and tri-hedral reflectors. A building surrounded by a smooth lawn will always produce dihedral reflections (Figures 4-14 and 4-15). The roof of a building may appear black because it acts as a mirror reflector. At the sides of a building, the radiation may hit the grass, the side of the building and bounce away never to reach the antenna. One may, therefore, see one side of buildings only. Typical are the L-shapes of buildings due to indirect reflections (Figure 4-15).

There are many gray tones in a radar image that must be explained. The gray tone may indicate, as in Figure 4-15, variations in moisture or in surface roughness. This ambiguity may not be resolved from a single image. The gray tone may result from mirror reflections as shown in Figure 4-16, an image of Sun City, Arizona. Circular streets have houses arranged in such a way that some have sides facing the antenna and others face away. In some cases there are mirror reflections off the sides of the houses.

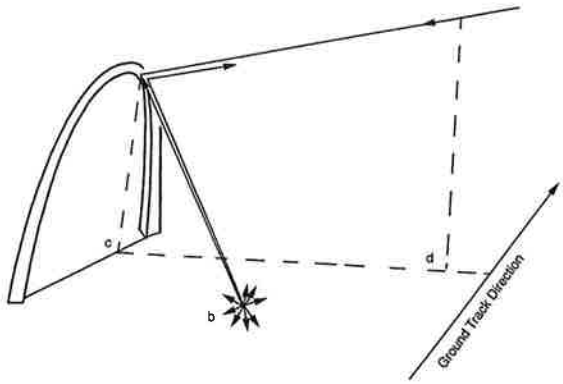

Figure 4-10. To explain the complex shape of the Arch in Figure 4-9, note the mirror reflections off the grassy area around the Gateway Arch, off the smooth surface of the Arch itself, and of combinations of reflections from the Arch onto the grass and back to the antenna (Courtesy G. LaPrade and Loral Defense Systems).

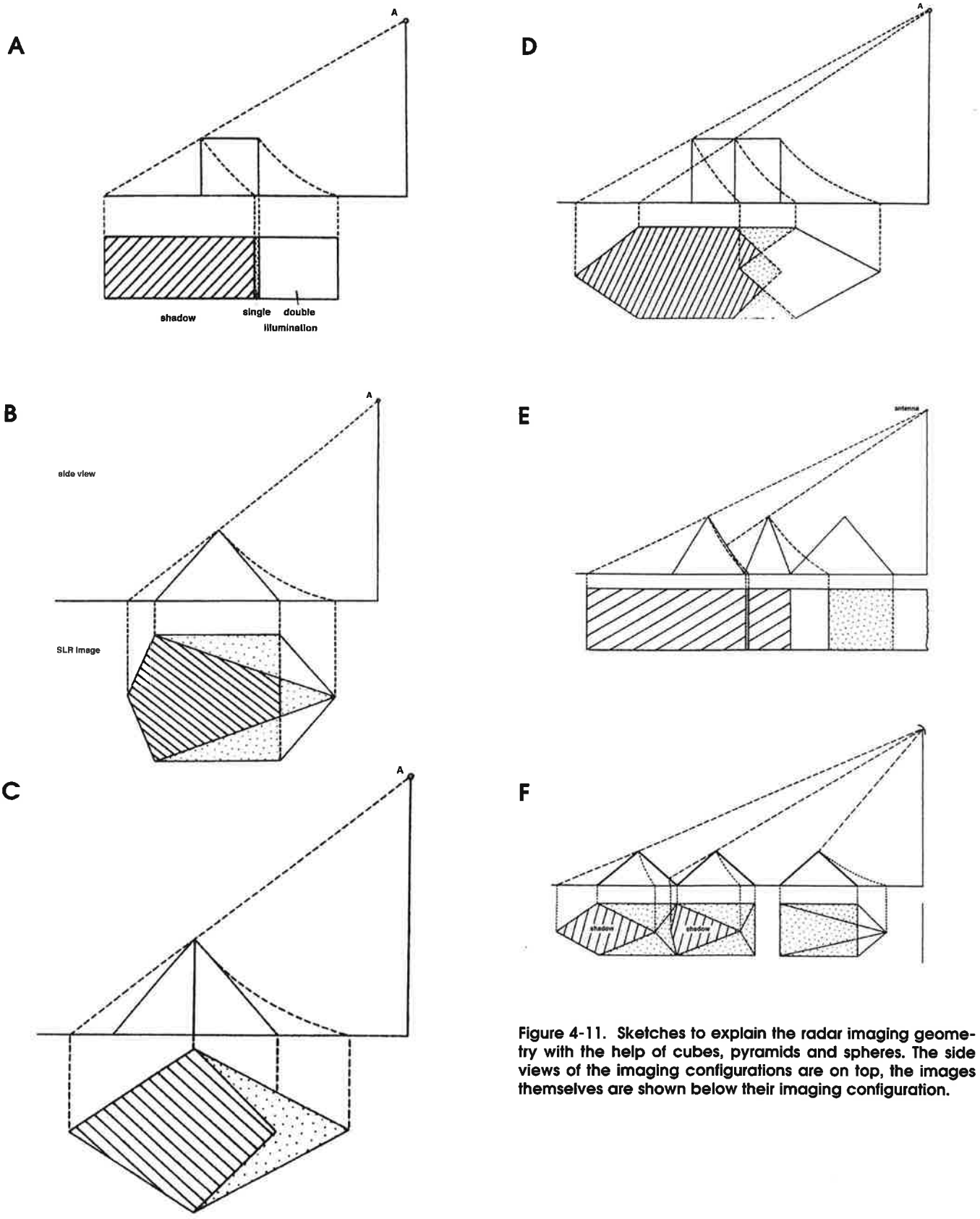

Figure 4-11. Sketches to explain the radar imaging geometry with the help of cubes, pyramids and spheres. The side views of the imaging configurations are on top, the images themselves are shown below their imaging configuration.

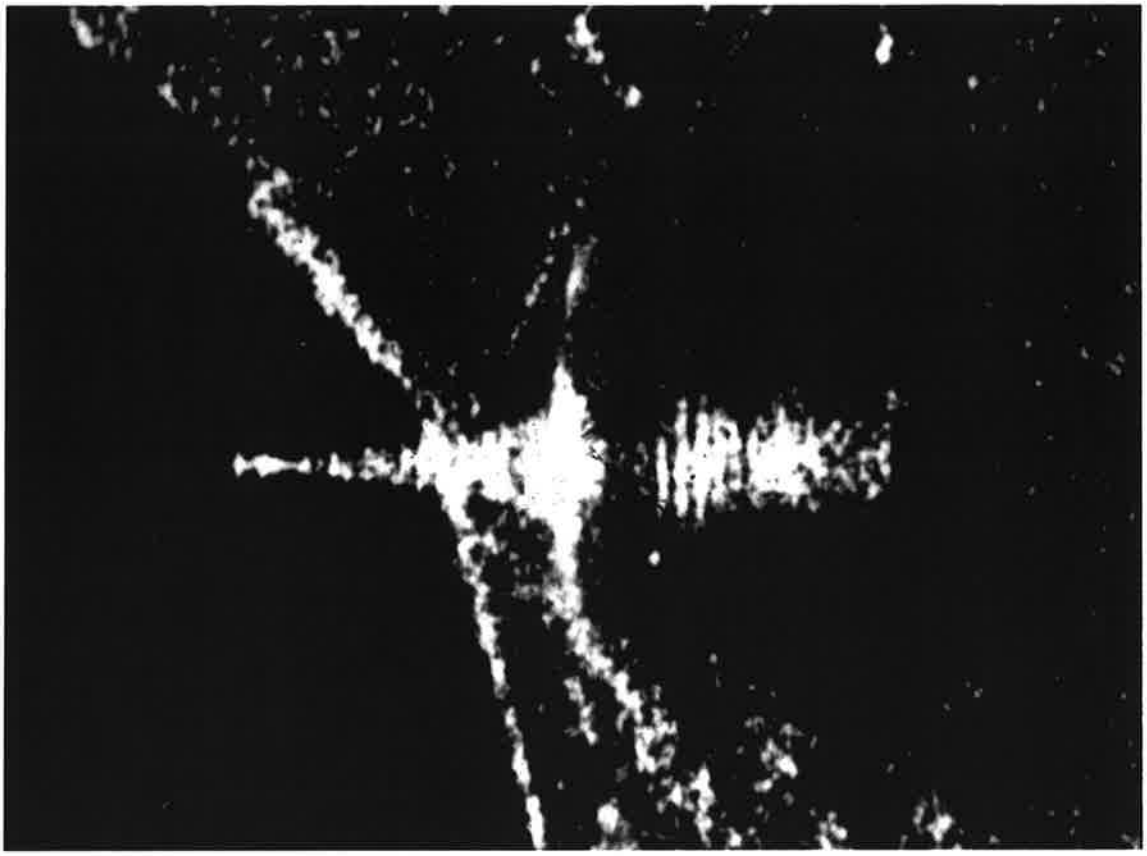

Figure 4-12. SAR-image of a transmission tower at the edge of a water body with a primary image and a mirror reflection (courtesy G. LaPrade and Loral Defense Systems).

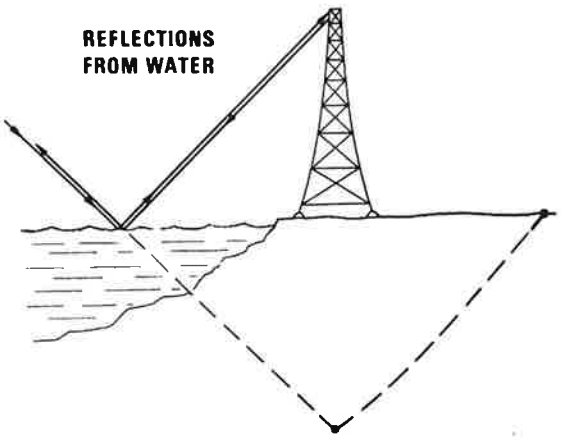

Figure 4-13. Sketch explaining the genesis of Figure 4-12. Note that the reflections of the water appear to create an image that coincides with the area behind the tower (courtesy G. LaPrade and Loral Defense Systems).

Figure 4-17 is an image that confuses the viewer into believing the image represents a perspective. In reality, however, it is a radar image from a system looking at the nadir and out to the side. Figure 4-18 explains the viewer's impression. In a slant range radar projection (the radar projection of Figure 4-17), points are projected along circles onto a projection plane which, for the sake of convenience, is shown in Figure 4-18 vertically rather than horizontally as in previous figures. What this produces then is the appearance of a cylindrical surface.

Figure 4-19 shows the same phenomenon as Figure 4-17 and 4-18, except this time from the Apollo 17 lunar sounder experiment (ALSE), which flew to the Moon in 1972. In that case, reflections were received and superimposed from both sides of the nadir. When one views this material in stereo (using a second orbit offset from the first one), one can separate the reflections from the left side of the spacecraft from those off to the right side. Stereo viewing helps to resolve the ambiguity of reflections from the left and right side of the orbit track. The stereo model produces a cylindrical surface (Figure 4-20). Figure 4-21 presents another ALSE image of a crater; it appears as if one could look through the ground through a glass surface to the other side of the crater wall. In layover situations one cannot separate which reflections are from which surface when viewing a single image. However, one can separate them visual-

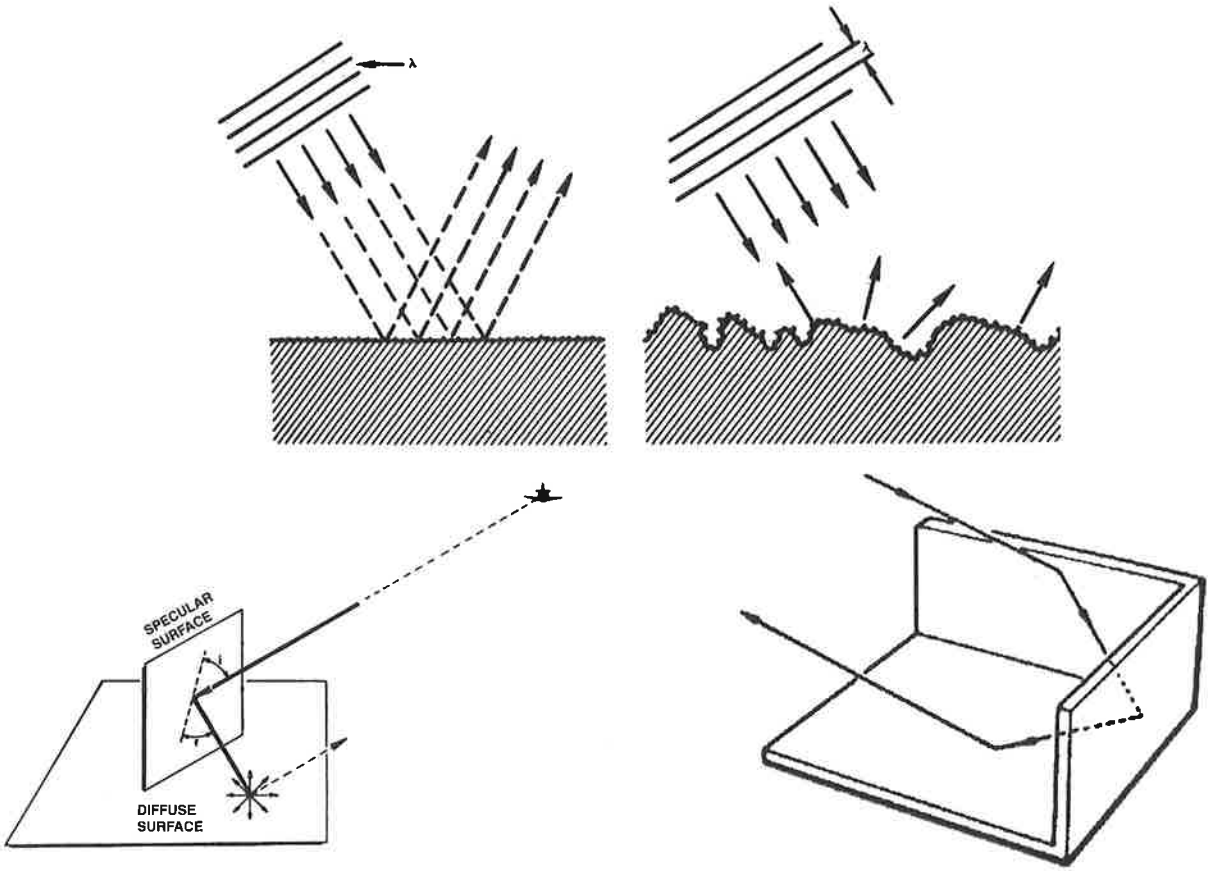

Figure 4-14. The concepts of mirror-like and diffuse reflections (see (a), (b)) and of di-hedral (d) and tri-hedral (d) reflections, typical with man-made objects (courtesy G. LaPrade and Loral Defense Systems). a - top left; b - top right; c -lower left; d - lower right

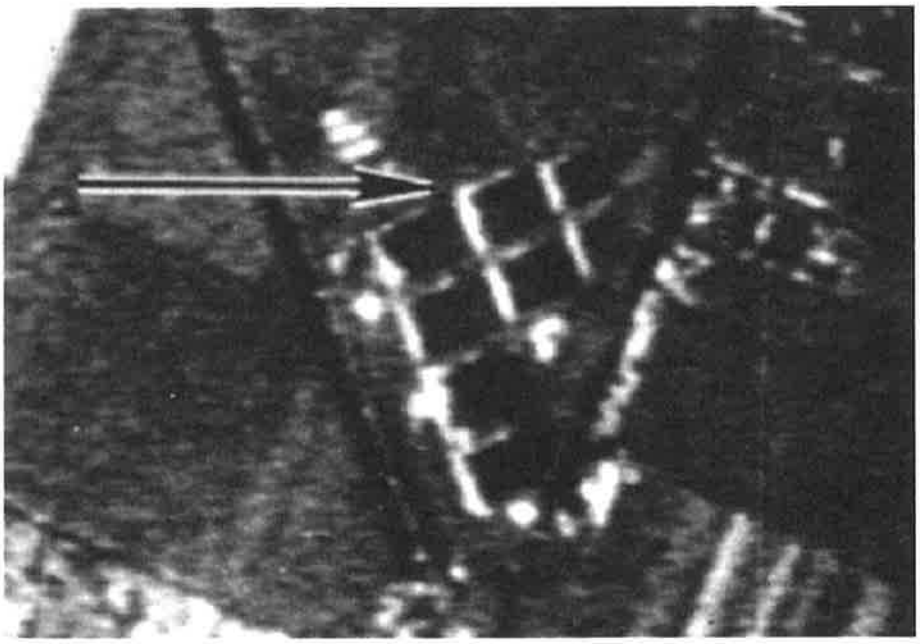

Figure 4-15. Radar images of flat-roofed houses shown in black since they reflect like mirrors, with typical L-shapes of the building's side-walls, and of open space (courtesy G. LaPrade and Loral Defense Systems).

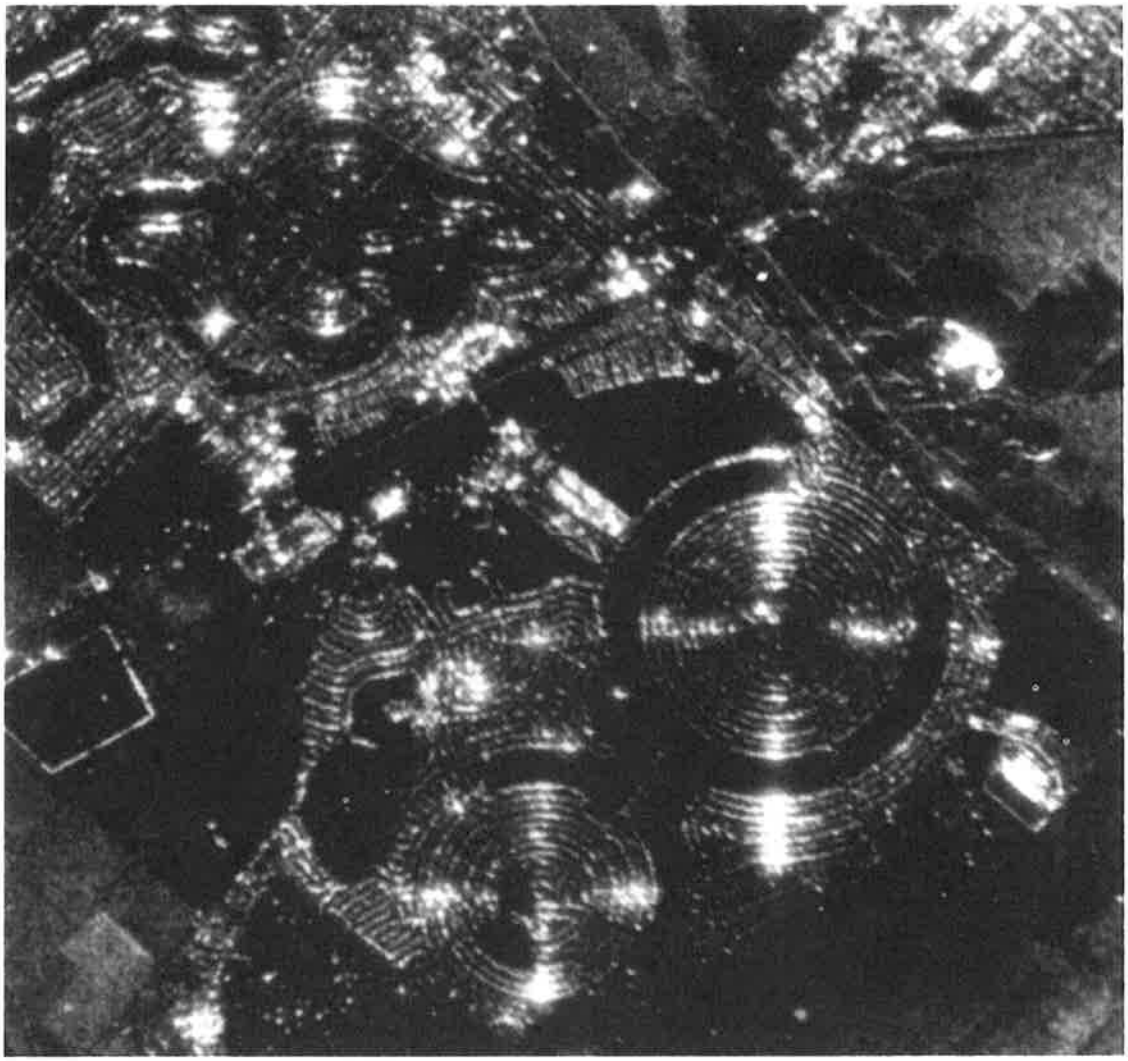

Figure 4-16. GEMS-1000 SAR image of Sun City, Arizona where streets are circular and di-hedral reflections from houses and grassy front lawns show up distinctly (courtesy G. LaPrade and Loral Defense Systems).

Figure 4-17. L-band (25 cm wavelength) SAR image of an island in the Atlantic, acquired by a NASA-JPL system. Slant range presentation covering about 10 km from the radar's nadir and sideways. Ground resolution about 10 m; flying height about 10 km (courtesy NASA-JPL).

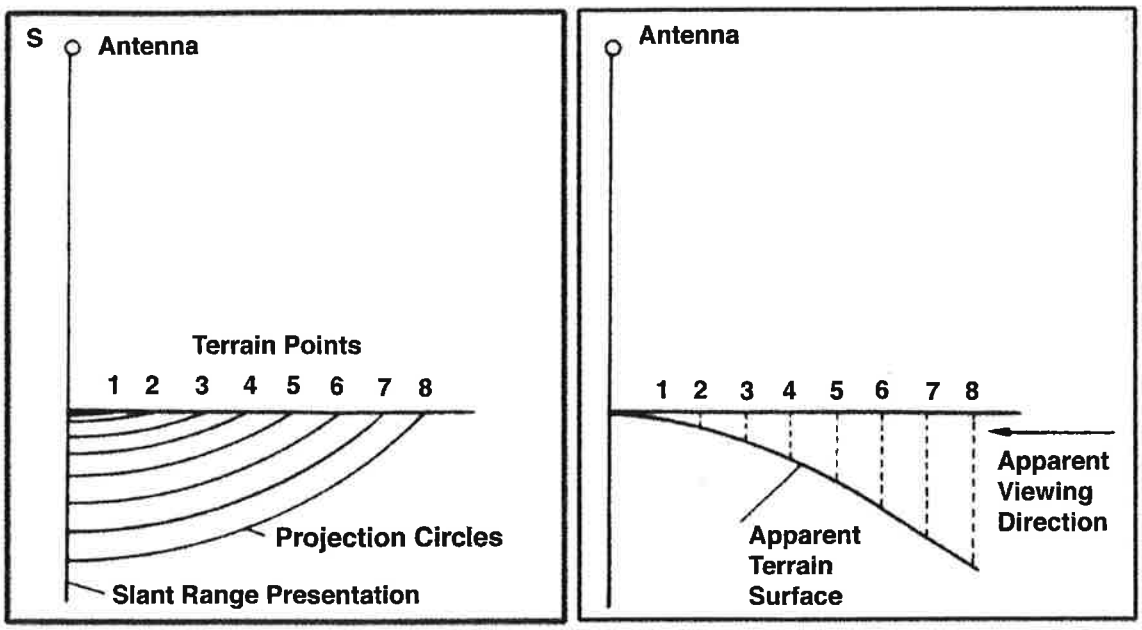

Figure 4-18. Sketch to explain the apparent "bird's eye perspective" of the radar image in Figure 4-17. The slant ranges represent a "circular projection" where the slant range is plotted linearly in the cross-track image direction. This corresponds to an intersection of each "projection circle" with a plane through the flight line. We illustrate this with a vertical plane. We note that points 1 through 8 are projected onto a slant plane as if these points had been on a cylinder and as if they had been projected by a parallel projection.

viewing a single image. However, one can separate them visually by stereopsis.

The need to fully understand the intricate imaging phenomena of radar has been illustrated in NASA's Magellan mission and in ERS-1 in Europe. Figure 4-22 presents an example of two images of an area 2° South of the equator of Venus, taken in Cycles 1 and 2 of the mission in 1990 and 1991. The fairly steep look angles of the imaging geometry compress some of the steep slopes by foreshortening into a narrow strip of pixels (Fig. 4-22a), and in the second coverage at an even steeper look angle, it is laid over (Fig. 4-22b). Consequently, a scientist looking for evidence of landslides on Venus may mistake the laid over imagery as a landslide, as actually happened during the heated "hunt" for interesting geological evidence as the Mission was unfolding in 1991.

A major advantage of radar images could be their sensitivity to look and azimuth angles. However, to date it is still not possible to reliably match images taken at different look angles and even less so at different azimuth angles. So-called opposite side image pairs are so different that any attempts at matching them have so far failed. Evidence of the difficulty of this matching task is obtained from Figure 4-23. These two ERS-1 images over alpine terrain in the Tyrolean mountains (Austria) are very different and illustrate that the information in the second image is either not the same as that in the first, or is encoded in a dramatically different manner.

4-4 SOME BASIC RADARGRAMMETRY EQUATIONS

The basic elements of modeling a radar sensor have been presented in the literature by various authors, involving Rinner (1948) and Levine (1960). Photogrammetric authors such as Rosenfield (1968), Gracie *et al.* (1970) and others have continued and refined this discussion. Here the basic ideas are presented in the form that this author has chosen in the past to describe the geometry of radar images (Leberl, 1972a,b; 1978a,b; 1979a,b; 1990).

4-4.1 PROJECTION EQUATIONS

The physical measurements which are obtained from radar images are slant distances from the antenna to an object point, denoted by r, and the time t at which that distance was measured. In addition, there may be measurements of the radar antenna's position and attitude, and some parameters of the sensing process such as the so-called "squint angle" τ. A general formulation relates object coordinates $(X,Y,Z) = \underline{p}$ to some sensor system with unit vectors $\underline{u},\underline{v},\underline{w}$ (see Figure 4-24).

One can write the following vector equation which represents three algebraic equations:

$$\underline{p} = \underline{s} + \underline{A} * \underline{p}^* \qquad (4.1a)$$

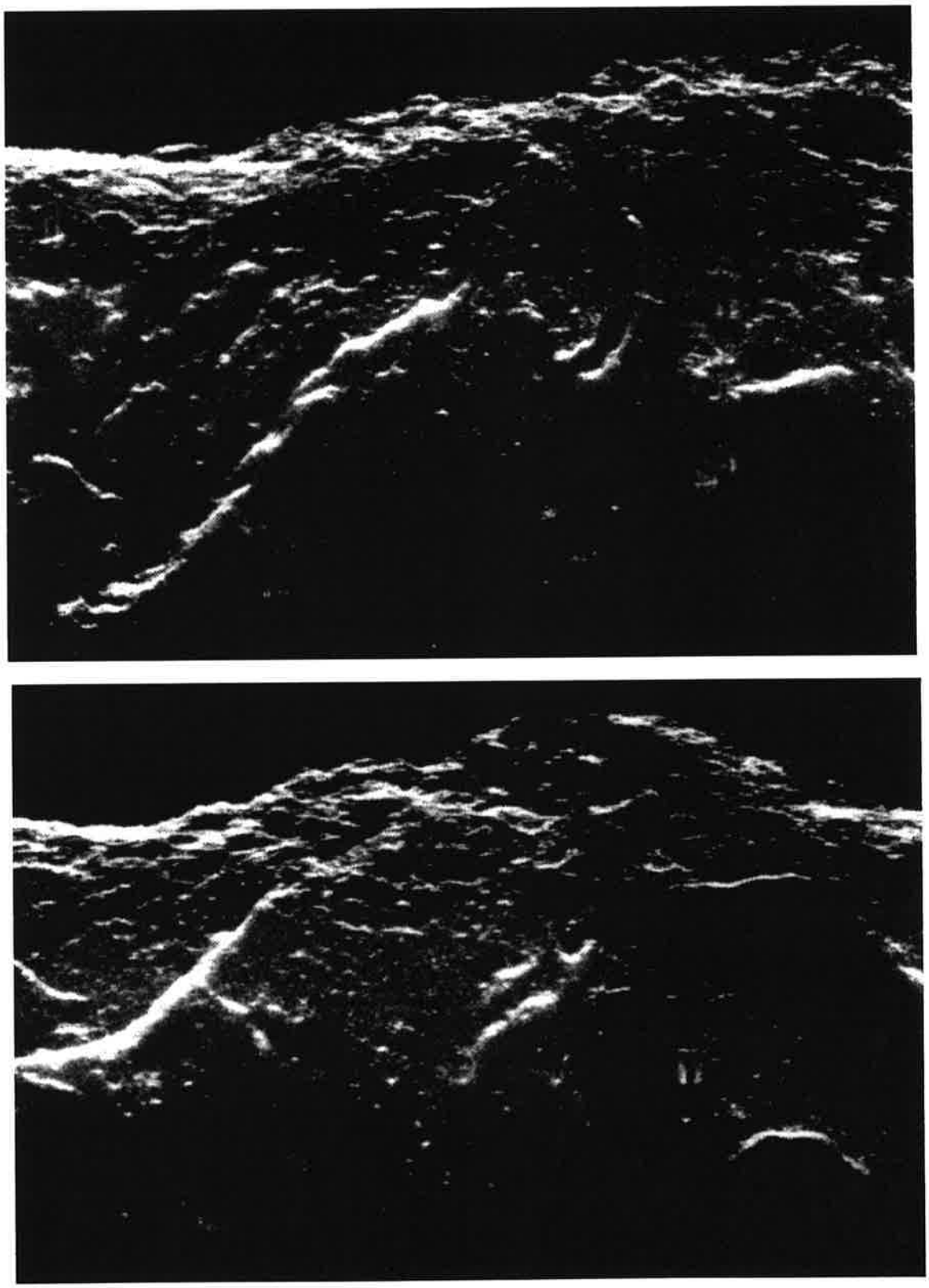

Figure 4-19. The Apollo Lunar Sounder Experiment (ALSE) in 1972 produced SAR images from Apollo 17 while it circled the Moon, using a radar imager from a lunar orbit at 116 km above the Moon at 2 m wavelength, pointing the antenna at the nadir and to one side. The images are presented with slant ranges. Partial reflections are displayed from the left side of the orbit, although the antenna received most echoes from the right side of the orbit.

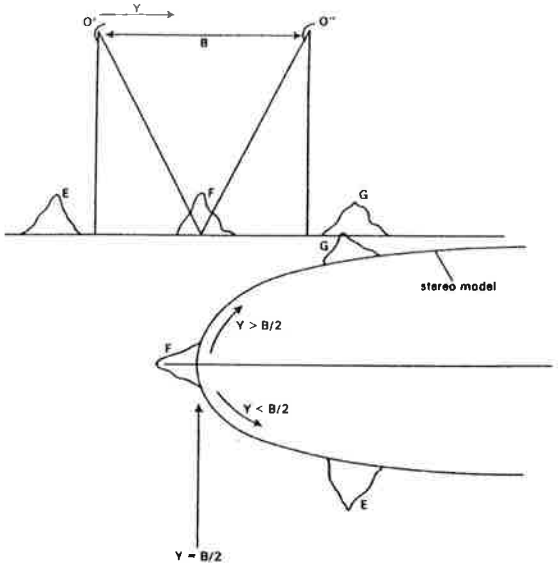

Figure 4-20. Sketch to explain the cylindrically shaped stereo model from two orbits O', O'' of the nadir-imaging ALSE-radar. The slant-range presentation distorts even a flat ground surface into a cylindrical shape. In ALSE this is very distinct since the radar pointed at the nadir and to the right. This is not common with other imaging radar systems, perhaps with some exceptions such as the NASA-JPL radar used to produce Figure 4-17.

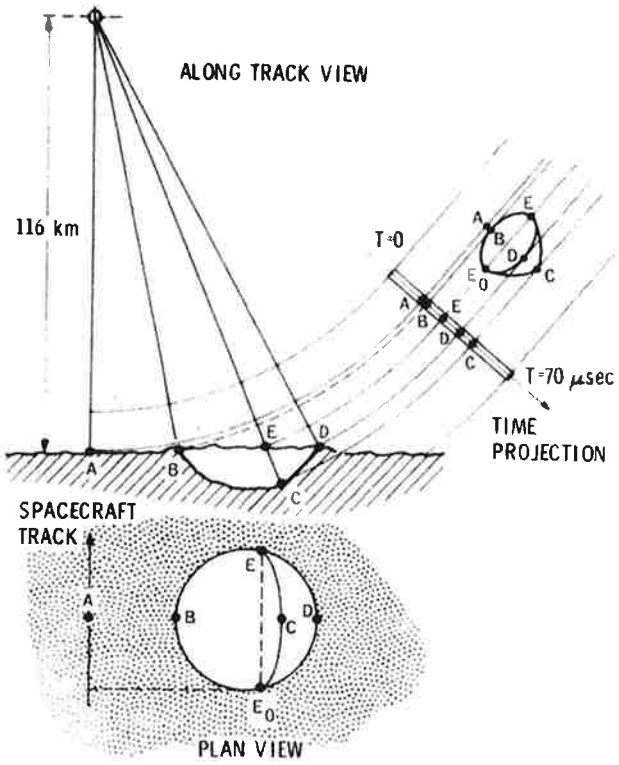

Figure 4-21a (above). Lay-over illustrated with a sketch illustrating the imaging geometry. (Courtesy C. Elachi, NASA-JPL).

with:

$$\underline{p}^* = u_p \cdot \underline{u} + v_p \cdot \underline{v} + w_p \cdot \underline{w}$$

$$u_p = r \cdot \sin\tau$$

$$v_p = r \cdot (\sin^2\theta - \sin^2\tau)^{1/2}$$

$$w_p = -r \cdot \cos\theta$$

where r is slant range, τ the squint angle, θ the "off-nadir-angle" of the object point within the sensor system, $\underline{u}$ the longitudinal axis of the radar antenna, $\underline{w}$ the vertical axis, and $\underline{v}$ completes the rectangular system. Vector $\underline{s} = (X_0, Y_0, Z_0)$ contains the sensor position coordinates; $\underline{A}$ is the rotation matrix between the X,Y,Z and u,v,w systems. It has elements a_{11}, a_{12}... a_{33}. One can rewrite the vector equation (4.1) as:

$$X = X_0 + a_{11} \cdot r \cdot \sin\tau + a_{12} \cdot (\sin\theta^2 - \sin^2\tau)^{1/2} \cdot r - a_{13} \cdot r \cdot \cos\theta$$

$$Y = Y_0 + a_{21} \cdot r \cdot \sin\tau + a_{22} \cdot (\sin\theta^2 - \sin^2\tau)^{1/2} \cdot r - a_{23} \cdot r \cdot \cos\theta$$

$$Z = Z_0 + a_{31} \cdot r \cdot \sin\tau + a_{32} \cdot (\sin\theta^2 - \sin^2\tau)^{1/2} \cdot r - a_{33} \cdot r \cdot \cos\theta$$

The inversion from sensor to object space of course produces:

$$\underline{p}^* = \underline{A}^T \cdot (\underline{p} - \underline{s}) \qquad (4.1\text{ b})$$

or

$$u = a_{11}(X - X_0) + a_{21}(Y - Y_0) + a_{31}(Z - Z_0)$$

$$v = a_{12}(X - X_0) + a_{22}(Y - Y_0) + a_{32}(Z - Z_0)$$

$$w = a_{13}(X - X_0) + a_{23}(Y - Y_0) + a_{33}(Z - Z_0)$$

This set of equations represents a "perspective equation" for imaging radar by relating an object point's $\underline{p}$ sensor coordinates to the equivalent world coordinates. This is analogous to common photogrammetric equations except that there are no image coordinates directly evident from the equations. Image coordinates are represented only indirectly. Assume that image coordinate x is proportional to time t, and that image coordinate y is proportional to slant range r. Then:

$$r = y \cdot f + d \qquad (4.2)$$

Figure 4-21b (above). An ALSE-SAR image of a lunar crater. Note how the slant ranges create a false bird's eye perspective. (Courtesy C. Elachi, NASA-JPL).

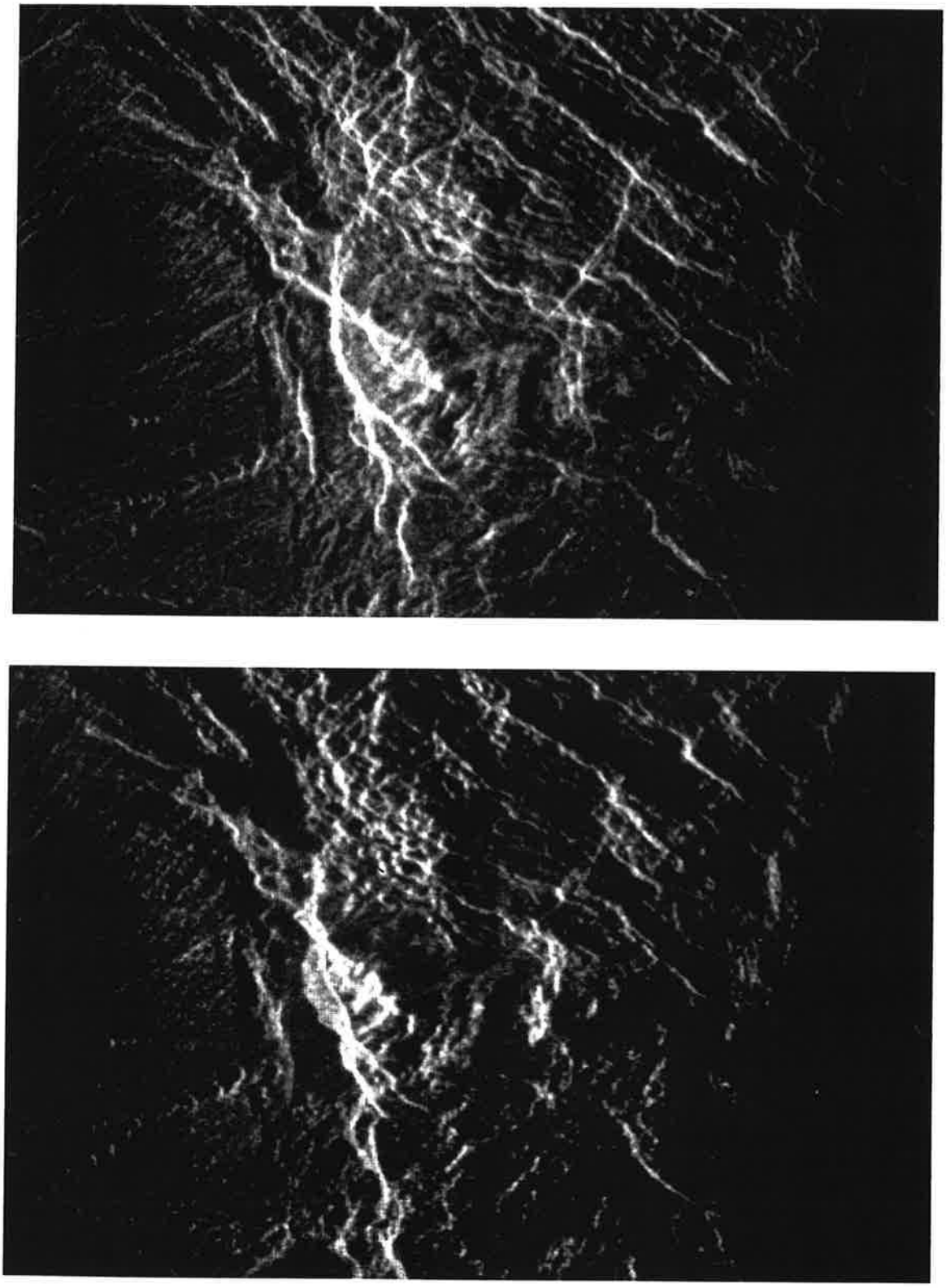

Figure 4-22. Example of two radar images from NASA's Magellan mission to planet Venus taken at different look angles of 43° and 22° off-nadir. As a result a steep slope appears in the shallower look angle foreshortened to a narrow strip of pixels, and in the steeper look angle geometry the same slope is laid over. An unsuspecting interpreter may conclude that the terrain has undergone a "land slide" between the time the first and second coverage was obtained (Leberl *et al.*, 1992d).

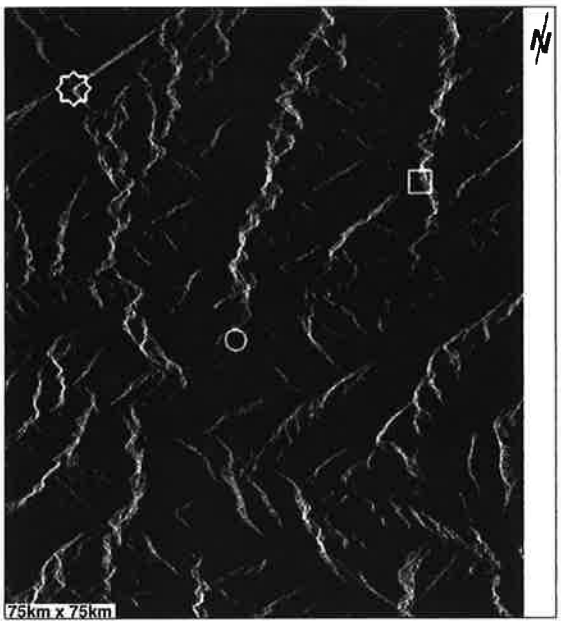

Figure 4-23a (above). ERS-1 radar images over the Tyrolean Oetz-Valley, taken from ascending and descending orbits, and therefore at opposite side look geometries. The dissimilarities between the two images seem to suggest that they each do not contain the same information but contain independent and fresh information. Pixel size is 12.5 m. Wavelength is 6 cm. To aid in orienting the viewer, there are 3 features marked in both images.

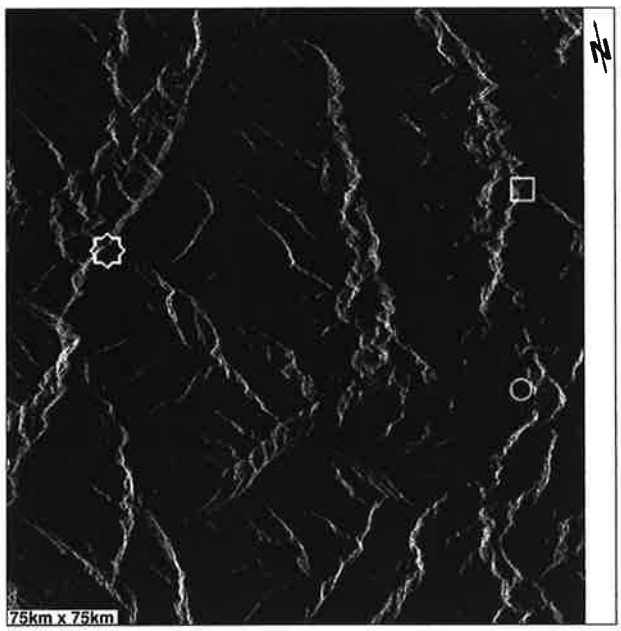

Figure 4-23b (above). ERS-1 radar images over the Tyrolean Oetz-Valley, taken from ascending and descending orbits, and therefore at opposite side look geometries. The dissimilarities between the two images seem to suggest that they each do not contain the same information but contain independent and fresh information. Pixel size is 12.5 m. Wavelength is 6 cm. To aid in orienting the viewer, there are 3 features marked in both images.

$$t = t_i + (t_{i+1} - t_i) \cdot (x_p - x_i)/(x_{i+1} - x_i)$$

where i is an index for a reference time t_i, and x_i is the along-track coordinate corresponding to clock time t_i; f and d are coefficients to convert y-coordinates into slant range r.

However, assume that an image point is measured in an arbitrary comparator coordinate system x_K, y_K. It is necessary to transform $x_K y_K$ into xy as follows:

$$x = (a_1 \cdot x_K + a_2\, y_K + a_0)$$

$$y = (-a_2\, x_K + a_1\, y_K + a_3)$$

where a_0, a_1, a_2, a_3 are the parameters of a linear conformal transformation.

The sensor position $\underline{s} = (X_0, Y_0, Z_0)$ results from the measure of imaging time, t. One works with t and r, but needs to compute them from image coordinates x, y. The conversion may be denoted by a process called "inner orientation," using classical photogrammetric terminology.

Just as in standard photogrammetric systems, equation (4.1) represents three equations for each image point. In a radar system where one knows all observable parameters one finds four unknowns to compute in order to position a point on the ground. These unknowns are X, Y, Z and angle θ. The slant range r is measured in the image. The squint angle τ is known as a parameter of the radar. The exterior orientation of the aircraft or satellite is known as a function of time t, so that one can develop the rotation matrix $\underline{A}$ at each instant t. Then it is necessary to eliminate the unknown θ, an analogy to the scale factor in photogrammetric equations (where the unknowns are X, Y, Z and scale). In photogrammetry there are also 3 equations for point $\underline{p}$; one typically divides the first equation (for X) by the third (for Z) thereby getting two equations with three unknowns X, Y, Z.

In radargrammetry, eliminating angle θ is slightly more involved. One builds from the three equations for X, Y and Z in equation (4.1a) or in equation (4.1b) two new ones by forming:

$$[u^2 + v^2 + w^2] = r^2 = [X - X_0]^2 + [Y - Y_0]^2 + [Z - Z_0]^2 \tag{4.3}$$

This is the equation of a sphere with center X_0, Y_0, Z_0 and radius r, thereby eliminating the rotation elements (antenna attitude), the look angle θ and the squint angle τ. One also forms

$$[u / (v^2 + w^2)] = \tan \tau \tag{4.4}$$

This is the equation of a cone with the vertex also at X_0, Y_0, Z_0 and a cone angle $180°\text{-}2\tau$. This is the co-called Doppler cone of SAR. The basic radargrammetric equations are thus those of a range sphere and a Doppler cone. Orientation matrix $\underline{A}$ of equation (4.1), and its elements a_{ij}, contain the "attitude" angles of the synthetic antenna of a SAR. This attitude is of course defined by

the velocity vector of the real antenna. In fact the synthetic antenna is formed by moving the real antenna through space. Its attitude is the direction of that motion.

The attitude is of no relevance in defining the range sphere (equation 4.3), and it defines the axis of the Doppler cone. How does the conventional rotation matrix $\underline{A}$ relate to the axis of the Doppler cone? Generally, the attitude of a 3-D coordinate system is represented by the rotation matrix $\underline{A}$. It has the customary form with 9 elements which represent the 3 angles of rotation around 3 coordinate axes *X, Y, Z*. These angles can be defined in many different ways, as is well documented in the photogrammetric literature. One particular implementation uses φ, ω and κ as a primary rotation around the *Y*-axis, a secondary around *X* and the tertiary around *Z*. The rotations are denoted as tilt (φ), roll (ω), and yaw (κ). This produces:

$$\underline{A} = \begin{vmatrix} a_{11} & a_{12} & a_{13} \\ a_{21} & a_{22} & a_{23} \\ a_{31} & a_{32} & a_{33} \end{vmatrix}$$

with $a_{11} = \cos\varphi \,.\, \cos\kappa$
$a_{12} = \sin\varphi \,.\, \cos\kappa \,.\, \sin\omega - \sin\kappa \,.\, \cos\omega$
$a_{13} = \sin\varphi \,.\, \cos\kappa \,.\, \cos w + \sin\kappa \,.\, \sin\omega$
$a_{21} = \cos\varphi \,.\, \sin\kappa$
$a_{22} = \sin\varphi \,.\, \sin\kappa \,.\, \sin\omega + \cos\kappa \,.\, \cos\omega$
$a_{23} = \sin\varphi \,.\, \sin\kappa \,.\, \cos\omega - \cos\kappa \,.\, \sin\omega$
$a_{31} = \sin\varphi$
$a_{32} = \cos\varphi - \sin\omega$
$a_{33} = \cos\varphi \,.\, \cos\omega$

Note from the elements of the rotation matrix $\underline{A}$ that in equations (4.3) and (4.4) there is no roll angle ω since all elements a_{ij} containing ω cancel out. The attitude of the sensor is only defined by two angles, namely yaw κ and pitch angle φ, but not by roll angle ω. Note also that the intersection of a co-located sphere and cone is a circle in space. This "projection circle" was discussed earlier in Figure 4-7 and is further illustrated in Figures 4-25a and 4-25b.

A special case exists when the squint angle τ is zero; that is an image with Doppler frequency zero; *i.e.,* imaging is in a plane perfectly perpendicular to the sensor's velocity vector. The cone simplifies (degenerates) into the equation of a plane.

As stated earlier, sensor "attitude" and rotation matrix $\underline{A}$ are defined by the antenna's yaw, pitch (and roll) angles. Space Shuttles or other satellites use synthetic antennas, thus with the antenna extending along the velocity vector; this means that the local antenna coordinate system $\underline{u}$, $\underline{v}$, $\underline{w}$ has its $\underline{u}$-axis along the velocity vector of the real antenna, and $\underline{w}$ points to the nadir. Yaw and pitch angles are therefore usefully defined. Again, since "roll" angle ω is of no relevance in equation (4.3) of a sphere or in equation (4.4) of a cone, the roll-motion of the antenna will not change the geometry of the radar image.

4-4.2 RELIEF DISPLACEMENT

The projection of the satellite's (or aircraft's) velocity vector onto some reference plane on the ground is called a "nadir line." If for an instant of time, *t*, the imaging plane (with squint $\tau = 0°$) and, inside that plane, a projection circle are defined, one can project a point along the projection circle into the object's reference plane. The distance between an object point's true projection and the orthogonal map projection into the reference plane is called "relief displacement."

In photogrammetry each imaged point *p* on a single photograph is the projection of the corresponding ground point *P* along a straight line from *p* through the projection center. The photograph does not identify where along the straight line the ground point *P* lies. In radargrammetry, a single image point defines a circle, but one does not know where the ground point is located on the circle. In photogrammetry, a photograph measures directions, but one does not know the range to each object. In radargrammetry, one knows the range but does not know the direction towards a point. Therefore one can say that a single photograph provides us with the geometry of a bundle of rays, all passing through the projection center (the lens), whereas a single radar image defines a set of concentric circles, all centered along the path of the antenna. Figure 4-26 shows the fundamental geometry of the relief displacement and quantifies its magnitude, *dp*, as a function of terrain elevation, *h*, above a reference plane, and as a function of look angle θ off-nadir. The approximate relationship is:

$$dp \cong h/\tan\theta \qquad (4.5)$$

Note that this equation applies to a so-called ground range geometry, something also denoted as "ground plane geometry." Range measurements are not directly displayed but are projected into a reference datum with the sensor at an assumed flying height *H* above the reference.

Equation (4.5) is based on the simplifying assumption that the spherical radar "wave-front" is a plane (rather than a sphere). This simplification is acceptable if terrain elevations are small and if imaging is at reasonably large look angles off-nadir, θ, of more than approximately 30°.

4-4.3 PROJECTING A RADAR IMAGE POINT ONTO A SPHERICAL PLANET

In order to compute ground point p that is observed in a radar image, one has to solve for three unknowns, *X, Y, Z*; but one only has two equations, one for a range sphere, one for a Doppler cone. Their intersection is the locus of *p*, a circle. To find *p* on the circle one needs a second circle, perhaps as part of a stereo process (see later). One can intersect the two circles and obtain a solution for *p*.

Of course, if one does not have a second image for stereo coverage, but knows the surface, for example the ocean, then one can establish a relationship between *X, Y,* and *Z*. In this special case one has a third equation, $Z = f(X,Y)$, and one can solve for the unknowns *X,Y*. A non-iterative solution exists to the problem of intersecting the range sphere, the Doppler cone and the Earth's sphere. This has been extensively discussed by Leberl (1979a, 1990). It is also the basis for Curlander's (1982) work.

4-4.4 MORE ABOUT ANTENNA ATTITUDE AND MOTION COMPENSATION

Antenna attitude affects synthetic aperture (SAR) differently from real aperture radar (SLAR). In a real aperture radar the antenna attitude determines the image geometry and defines the entries into the attitude matrix A. In a synthetic aperture radar the attitude of the real antenna has no effect on the image geometry. For example, in a real aperture, the yawing motion of the airplane or satellite may make the real antenna look forward. As a result the imaging surface is still a plane, but it is yawed. If the airplane's nose goes up, imaging is still in a plane, but a pitched one.

In a synthetic aperture radar one works with an integration of the real antenna's positions. The dense sequence of positions of the real antenna produces a fictitious line in space. It is the tangent to this line at each position which determines the synthetic antenna's attitude. So one will always image with respect to the antenna's velocity vector. An image created with respect to a Doppler frequency of zero will result from a plane perpendicular to the velocity vector. If the velocity vector changes direction, then of course the airplane must have moved irregularly too. But the example of a "yawing motion" will be caused by the velocity vector as the above-mentioned tangent; the attitude of the physi-

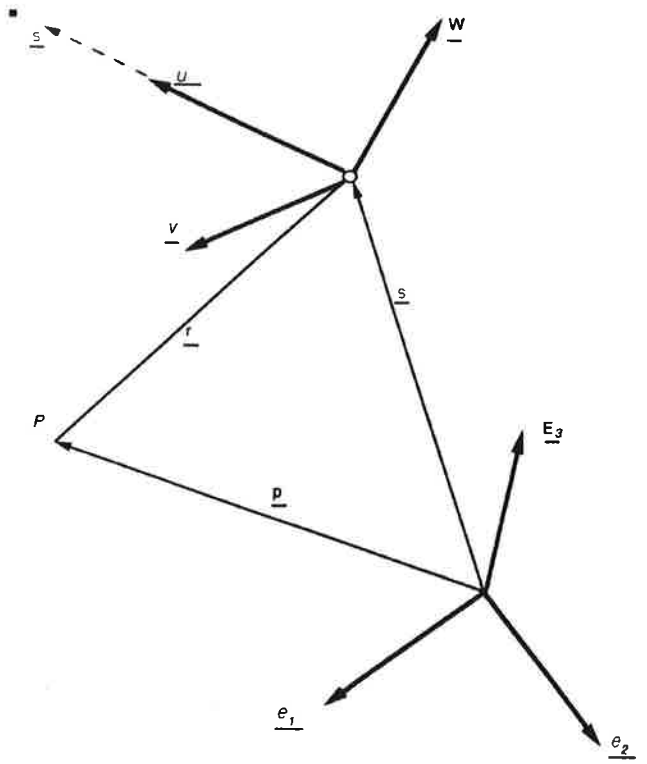

Figure 4-24. Coordinate systems of the object with *XYZ* and system attached to the sensor with unit vectors $\underline{u},\underline{v},\underline{w}$. The two systems are linked to another by the position vector $\underline{s}$ and rotation matrix $\underline{A}$.

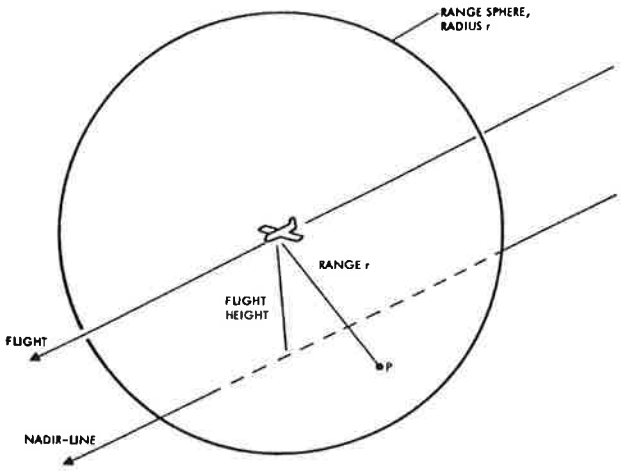

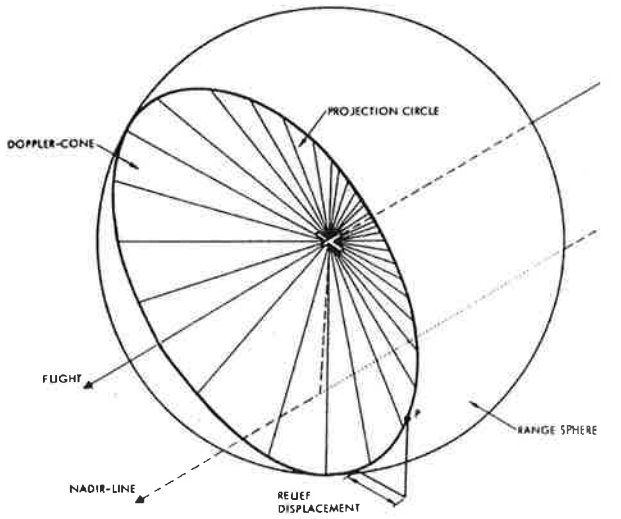

Figure 4-25a (top). Explaining the first locus of an object point, namely the "range sphere" with its center at the antenna. An imaged point is somewhere on the surface of the sphere, a distance *r* from the antenna.

Figure 4-25b (bottom). Sketch describing the second geometric locus for each radar image point, namely the "Doppler cone" obtained by the "squint angle." The actual object is at the intersection of sphere and cone, namely on a circle with the antenna at its center. The cone degenerates to a plane if the Doppler frequency used in the SAR is set at zero.

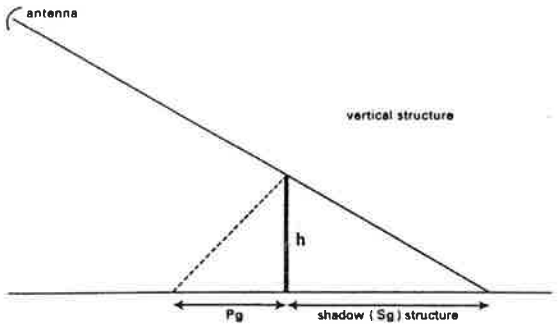

Figure 4-26. Definition of radar 'relief displacement' *Ps*, using a simplified radar wave front, replacing the circular wave front by its tangent (the "wave front" is shown as a dashed line). Also shown is a shadow cast by a vertical object.

cal antenna has become irrelevant to the geometry of the image. Should rapid changes in the attitude of the real antenna occur, then good SAR-systems will detect these and compensate them automatically. However, the purpose of such compensation is image quality, not image geometry.

Deviations of the real antenna's motion from a straight line (*i.e.* change of direction of the velocity vector during the time that the synthetic aperture is being generated) will degrade the resulting image. This is a serious issue for aircraft radar sensors. In order to obtain a new "perfect" antenna motion, a real-time closed-loop is used, based on an Inertial Navigation System (INS). During the two or three seconds that a synthetic aperture is being created, the accelerations are read off the INS, integrated into velocities and furthermore used to compensate for antenna motion (in aircraft radars this is the "Motion Compensation" or MOCOMP). The INS is used to electronically shift the phases that are coming back from the object so that one compensates for small variations of the antenna's position. This step is accurate enough for the length of a synthetic antenna.

While MOCOMP and velocity vectors are of great importance in aircraft radargrammetry, orbital systems are sufficiently stable over the length of a synthetic aperture so that refinements like MOCOMP are not relevant. In all cases, velocity vectors simply result as first derivatives, $\dot{\underline{s}}$, of the position vectors $\underline{s}$ themselves (note: $\underline{s} = (X_0, Y_0, Z_0)$. The velocity vector may be computed as

$$\dot{\underline{s}}_i \approx \frac{(\underline{s}_{i+1} - \underline{s}_i)}{(t_{i+1} - t_i)}$$

4-4.5 LINEARIZED RADARGRAMMETRY EQUATIONS

We start from the non linear equation (4.1b) and produce a linear form by means of a standard Taylor series' expansion. The result is shown without derivation in Figure 4-27. Figure 4-28 illustrates how an error $d\theta$ of the velocity vector's direction will cause an error in the image location, dx, in the along-track and in the cross-track, dy. The sensor position error dX_0 along track would simply translate into a position error in the image. The κ or yawing error of the synthetic antenna would translate into the image via a lever arm of length $Y = r \cdot \sin\theta$ in the cross track direction. It is intuitively easy to understand the effect of various errors. Figure 4-29 further illustrates how an imperfect imaging flight will distort a square grid on the ground.

4-4.6 RADARGRAMMETRIC RESECTION-IN-SPACE

One begins by measuring the location of several image points on a radar image. One has an approximate flight path to describe the flight position X_0, Y_0, Z_0 as a function of time t. One also knows the XYZ coordinates of some ground control points. Based on this information one can set up a system to improve the knowledge of the (approximate) flight path using the ground control points. The approach is analogous to that used in photogrammetry with perspective photographs. The result is denoted as "resection-in-space," just as it is called with photographs.

The process begins by computing where the ground points would fall in the image if the approximate flight data were true. The projected ground point, $p'=(x',y')$ is then compared to the actually measured image point, $p=(x,y)$. The differences in along track, $dx=x'-x$, and the cross track, $dy=y'-y$, enter into this computation as shown in Figure 4-27. Using a sufficient number of known dx, dy-values, one can compute an unknown error dX_0 of the sensor's along track coordinate X_0, cross track error dY_0, height error dZ_0, and also obtain errors of the attitude vector, $d\varphi$, $d\kappa$.

A radar flight is generated kinematically (by motion). Therefore, multiple errors occur, for example dX_0 for along track position X_0. One has a continuously variable error $dX_0(t)$ as a function of time, t. One can model this, for example, as a second order polynomial valid over a time span between t_1 and t_2:

$$dX_0(t) = a_0 + a_1 \cdot t + a_2 \cdot t^2, \quad (t_1 \le t \le t_2)$$

with coefficients a_0, a_1, a_2 and the independent variable, t, for time.

One substitutes a polynomial for each of the sensor errors, dX_0, dY_0, dZ_0, and so forth, in the linearized form shown in Figure 4-27. In this manner, one is setting up a system of 2 equations for each control point with "observations" dx, dy in the image to compute unknown coefficients of the polynomials.

For the example of a single radar image and second order polynomials to model the sensor errors (*i.e.* 3 coefficients per error function), how many ground control points are needed minimally to solve this system of equations so that the polynomial coefficients for the error of the along- and cross-track positions, the sensor height, and the direction angles of the velocity vector can be found? To derive the answer, one adds the number of unknowns:

(a) One has three sensor position elements, dX_0,dY_0,dZ_0 which result in 3 times 3 polynomial co-efficients that are unknown (*i.e.* a total of 9 coefficients).

(b) The attitude vector, the direction angles κ, φ, results from the velocity vector simply as first derivative of the

position. Since they are a function of the position, they do not add any new unknowns!

(c) One has a total of nine unknowns in this equation system.

(d) Each ground control point gives two equations. Therefore, one needs at least four and a half (or five) ground control points to solve this system of nine unknowns.

This consideration further simplifies for rectilinear segments of a flight. A long flight line could be modeled as a sequence of such straight line segments. In each segment one has 6 unknowns for the coefficients in the three position errors.

Several studies have been published to model the sensor errors by various methods, and to include polynomials (DBA-Systems, 1974), Fourier series (Dowideit, 1977a,b) and spline functions (Raggam, 1985). Such studies also always address the questions of where ground control points would best be located to compute the unknowns.

4-4.7 HOW TO PROJECT A GROUND CONTROL POINT INTO A RADAR IMAGE

A "resection in space" has the requirement to project each known ground point into the image. This seemingly trivial problem presents a challenge. There is no known sensor position $\underline{s} = (X_0, Y_0, Z_0)$ at the exact time t at which a specific ground point was imaged. Instead one has given a sequence of positions $\underline{s}_i$, that one may want to connect by straight line segments. Where along the flight path was a point P imaged, given the dynamic nature of the changing flight path and the multiple linear pieces describing the flight path?

If the flight path is modeled as a sequence of linear pieces, each beginning at time t_i and ending at t_{i+1}, then one defines in each ground point P a set of planes, each passing through that ground point, but oriented perpendicular to each of those linear pieces. These planes represent the imaging planes. One computes the intersection point of the linear flight path segment with that plane to identify the imaging position $\underline{s}$ for that point, assuming it to be on the current linear stretch of flight line. One finds whether the "intersection point" is within the range of definition $t_i \le t \le t_{i+1}$ for that linear piece. Figure 4-30 defines the solution for a set of linear pieces for the flight path. Upon completion of this search process one knows that one segment of the flight path for which the intersection with the imaging plane is within the definition interval. One has found the time t at which the ground point was imaged, and also its slant range r.

Generalizations to non-linear models of the flight path, and a replacement of the Doppler plane by a non-zero-Doppler cone are straight forward.

4-4.8 MORE ABOUT PROJECTING AN IMAGE POINT ONTO THE GROUND

This section expands upon the material in Section 4-4.3. A location in the SAR-image be given and one needs to know the

$$
\begin{aligned}
dy &= \sin\theta \cdot \left(-d\omega \cdot w_p - ds_y\right) - \cos\theta \cdot \left(d\omega \cdot v_p - ds_z\right) \\
&= d\omega \sin\theta \cdot r \cdot \cos\theta - \sin\theta \cdot ds_y \\
&\quad - \cos\theta \cdot d\omega \cdot r \cdot \sin\theta + \cos\theta \cdot ds_z \\
&= -\sin\theta \cdot ds_y + \cos\theta \cdot ds_z \\
dx &= -r \cdot \sin\theta \cdot d\kappa - r \cdot \cos\theta \cdot d\varphi - ds_x
\end{aligned}
$$

$$
\begin{aligned}
dx &= -ds_x - p_y \cdot d\kappa - H \cdot d\varphi \\
dy &= -\left(p_y / r\right) \cdot ds_y + \left(H/r\right) \cdot ds_z
\end{aligned}
$$

Figure 4-27. Linearized radar imaging equations relating errors of sensor position (ds_X, ds_Y, ds_Z) and sensor attitude ($d\varphi$, $d\kappa$) to errors of image locations, dx, dy. Note in the text we use a notation of $ds_X=dx_0$, $ds_Y=dy_0$, $ds_Z=dz_0$.

ground position that corresponds to this image point. One already knows from earlier discussions that one needs to take the circular radar projection ray and intersect it with the reference surface, be this a sphere, a geoid or a detailed digital elevation model (DEM) superimposed over the geoid. A direct (non-iterative) solution exists for an Earth sphere and begins by intersecting the range sphere with the local Earth sphere around the ground point of interest. The result of intersecting 2 spheres is a circle in space. This circle now needs to intersect the Doppler cone. This solution was implemented by Curlander (1982) for the rectification of SEASAT images and has then become a standard in geocoding of ERS-1 images (Schreier, 1993; in particular the chapter by Nuesch *et al.*).

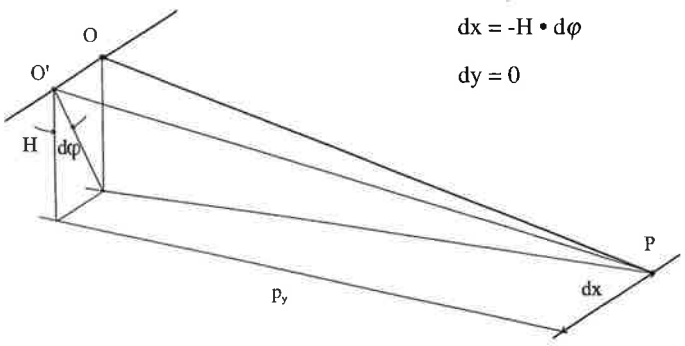

Figure 4-28. Sketch to explain the principle of the relationship between various errors of sensor position or attitude to errors of a point's image location. This example addresses the individual components $d\varphi$ in the equations of Figure 4-27 with the same notation.

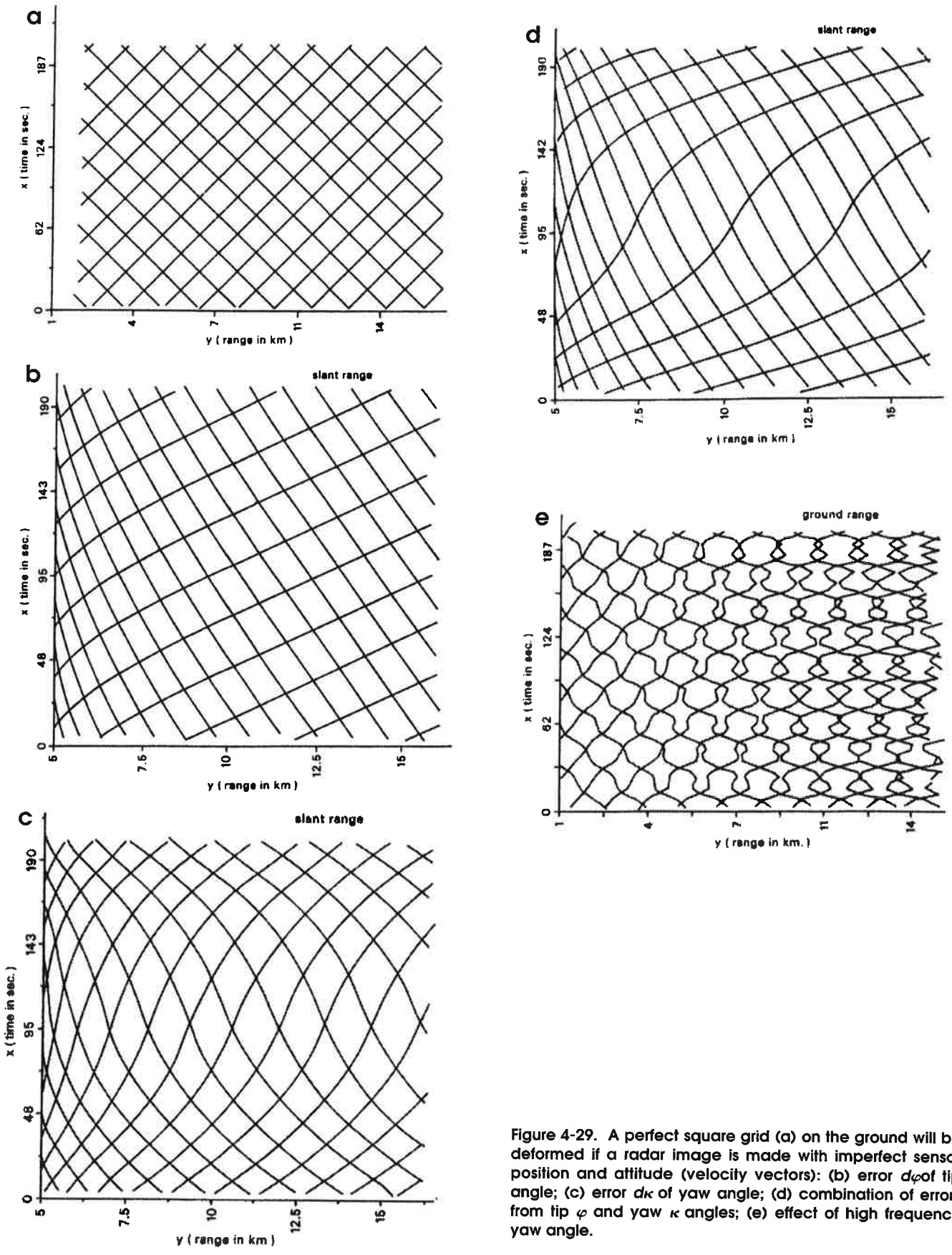

Figure 4-29. A perfect square grid (a) on the ground will be deformed if a radar image is made with imperfect sensor position and attitude (velocity vectors): (b) error $d\varphi$ of tip angle; (c) error $d\kappa$ of yaw angle; (d) combination of errors from tip φ and yaw κ angles; (e) effect of high frequency yaw angle.

A fairly complicated non-iterative solution also exists for an ellipsoid (see Leberl, 1978a). For bodies that are more complicated, iterative solutions need to be formulated.

Of particular interest is an approach that relates each image point to its corresponding *XYZ* ground location for the case where an elevation model $Z=f(X,Y)$ is known in the form of a DEM. This is the basis for so-called "terrain-corrected images" (Schreier, 1993). In photogrammetry, such images are also called "ortho-rectified." Creation of an ortho-image is a straight-forward resampling issue, provided the DEM-points and their corresponding image points exist, as is the case if the DEM were to be the result of a radar stereo procedure.

More generally, however, the DEM will already exist and a new radar image needs to be processed. This is the issue of this section. Of course one finds that all remote sensing scenarios – not just radar-related ones – are in need of algorithms for projecting a point onto the ground. Such algorithms vary due to different sensor models but are identical in intent. They are very similar to methods used with optical images. The generalized, radar-neutral image processing domain consists of three parts:

(a) Computing an "image set-up" by which image and ground coordinate systems get related to one another (determine the ephemeris, the radar sensor parameters, etc.);

(b) Obtaining for each image point (pixel) the corresponding object *XYZ*-coordinate triplet (actually solving for the *XYZ* coordinates when the ephemeris, sensor parameters and image positions *r, t* are known);

(c) Assigning a gray value to each pixel of the output image.

The set-up was always a difficult and important element to achieve geometric accuracy in the past. It required the computation of the sensor position and attitude (ephemeris) from the sensed images themselves, employing "ground truth" in the form of ground control points. Only where coarse approximations were acceptable was it sufficient to rely on some known sensor position and attitude and apply a process called "dead-reckoning." "Known" is either an aircraft's flight path that is rectilinear or a satellite orbit that has been predicted.

"Dead-reckoning" uses these predicted or approximate sensor platform data without further refinement by ground truth and applies the data to the computation of ground positions.

The European ERS mission is the first civilian satellite imaging project where the ephemeris is observed by means of laser tracking stations and communicated with sufficient accuracy in the range of ±1 meter so that ground control should no longer be needed. The relationship between image and object coordinate systems is being established by the satellite mission itself. However, the same does not hold true for some of the other current SAR projects such as the Space Shuttle's SIR-C flight, or RADARSAT. Therefore the traditional three-step process remains in place.

Step A – Image Set-Up: Typically this is accomplished by a resection-in-space, provided that ground control points exist and can be identified in the radar image.

In the absence of control points, or an inability to identify them in the image, "image simulation" has been successfully

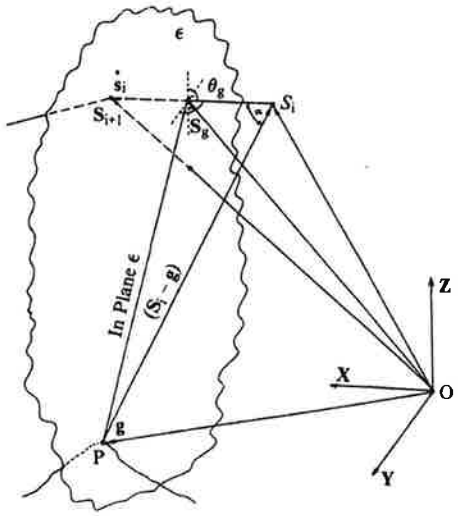

Figure 4-30. Projecting a ground point $p(X,Y,Z)$ into a radar image requires that the proper sensor position $s(t)$, as a function of time, be found from the recordings of the sensor flight path. sg is the sensor position from where point P was imaged. This is found by a search process through the pieces $(s_{i+1}-s_i)$ of the flight path.

employed in the past (Domik, 1985; Naraghi *et al.*, 1983; Curlander, 1986). There, the existing DEM and the predicted ephemeris serve to create an artificial SAR image. Image matching is used to relate the real to the artificial SAR image, thereby developing a large number of control points, or making such control points superfluous.

Step B – Computing Object Points: The search to associate with each image (r,t) a ground location (XYZ) must normally be iterative, unless the DEM represents a sphere or ellipsoid. A likely Z' is assumed and an $X'Y'$ is computed directly from equation (4.1a). However, at $X'Y'$, the DEM will typically not have the elevation Z', but Z''. Some new estimate Z''' needs to be assumed as a function of Z'- Z'', and with knowledge of the general shape of the DEM in the vicinity of X',Y'. While each geo-coding software system needs to have an implementation of this procedure it is generally not being discussed in the literature. An early paper on this problem is that by Greve and Cooney (1974).

If Step A was not solved by a resection-in-space but instead was the result of image simulation and image matching, then each image coordinate pair (r, t) is directly associated with a simulated r^*, t^* and in turn with the corresponding ground *XYZ* from the DEM. Therefore Step B needs merely to exploit the relationship between (r, t) and (XYZ) through a look-up table.

The previous discussion makes the assumption that the DEM is an externally provided data set. However, it may be the result of DEM-processing of radar images, be it by stereopsis, shape-from-shading or interferometry. In such cases the relationship between (r,t) and (XYZ) is also unambiguously established. For example, if the Z-value of a DEM has been computed for a given *XY* posting using two stereo-positions (r',t') and (r'',t''), then there is the explicit image-ground-relationship $r't' \rightarrow XY$ in place. Image set-up is a trivial process in this case.

4-5 REAL-TIME MATH MODEL FOR STEREO-PLOTTING

(a) Basic Principle

Photogrammetric "stereo-plotting" uses the analytical photogrammetric stereo-plotter or its successor, the digital softcopy stereo-workstation. The basic operation of "stereo-plotting" has a human operator control a computer input device to enter object *XYZ* positions into the machine. These positions serve to compute image points ($r't'$), ($r''t''$) in the overlap regions on which measuring marks are placed. These marks are observed together with the images by the operator who accepts the result, or uses the visual input to change the *XYZ* position. This is therefore a so-called "closed-loop" between machine and operator and repeats itself in real-time, *i.e.* about 60 times per second. Acceptance means that a satisfactory *XYZ* position gets recorded, together with the corresponding image coordinates.

It was stated earlier that routine real-time stereo-plotting follows a set-up process: an image stereo pair must first be set up so that it is then available for real-time plotting.

(b) Coordinate Systems

Photogrammetry defines three coordinate systems: 1) the object's, perhaps expressed as latitude, longitude and elevation above the geoid; 2) the stereo model's Cartesian *XYZ* and 3) the two images' two-dimensional systems. For a camera the transformations employ the camera's position and attitude which apply to an entire two-dimensional photograph.

With radar and other kinematically generated images one finds a somewhat more involved process because of a constantly changing flight path. Therefore a given sensor position only applies to an image line, not the two-dimensional extended area.

(c) Computing Image Points for a Chosen Object Position

Figure 4-31 sketches one radar-relevant implementation on an analytical plotter (Raggam, 1985). An operator moves to a point on the ground, so the hand will move in the Cartesian *XYZ*-system or in the spherical system with latitude, longitude, elevation. The measuring marks in the two images need to be placed onto those two image points (those two sets of image coordinates) which correspond to the chosen point on the ground. From the stereo-set-up one knows the parameters of the relationship between images and the ground. These are stored on-line.

As one moves the object point, the measuring marks in the images need to move also to image locations of the *XYZ* point (see also Section 4-4.7). An equation is solved by forcing the squint angle τ to be at its nominal value. As we move from one point to another one in *XYZ*-space, the sensor has to move along its flight path enough of a distance so that the nominal squint angle gets reestablished. This provides the sensor position X_0, Y_0, Z_0 and attitude angles κ, φ. This permits one to compute r,t and place the measuring mark over the desired corresponding image point. This real-time solution was originally implemented on a LEICA-KERN DSR analytical plotter (Raggam and Leberl, 1984). The flight path is non-linear, but is being approximated by straight line segments. The issue of how many segments can be used to model the flight path is a function of the stereo model set-up using ground control.

Similar models were independently developed 1) in Europe by Dowman and Morris (1982); 2) for US Defense applications on the photogrammetric stereo measuring device APPS-IV, on the analytical plotter AS-X-11 (Autometric, 1982), and on the photogrammetric stereo machines built by Intergraph using software developed at SAIC-Florida (Poehler *et al.*, 1993). All of these systems operate with film images. Softcopy images can be processed by software systems developed by Raggam and Leberl (1984) under the name "RSG," and by STARMAP, a system developed for INTERA (Canada) by Vexcel Corp. (Mercer *et al.*, 1989). Science Applications International Corp. (SAIC's) system is also being converted to operate on softcopy source material (Poehler *et al.*, 1993).

4-6 IMAGE SIMULATION

4-6.1 MATCHING RADAR IMAGE AND DEM

One may need to process radar images of mountainous areas. In that case it is often difficult to identify ground control points. Figure 4-32a is an example of an SAR-580 image that was obtained by the Canada Centre for Remote Sensing in the Austrian Alps. No ground control points exist that would be easily identifiable in that area. How does one orient oneself in an image like that?

In the absence of ground control points, image simulation helps relate the radar image to the ground. Figure 4-32b is a map-derived DEM. It is helpful for a first orientation to simulate an image with the nominal imaging parameters of the radar. One obtains an image with the same illumination geometry as the radar and can superimpose the radar image over the DEM area without ground control points (Domik, 1985; Domik *et al.*, 1984, 1987). This has routinely been used at NASA's Jet Propulsion Laboratory, initially to match digital SEASAT images with mountainous terrain. In such cases, distinct ground control points are typically not identifiable. Instead, one needs to employ just the high-contrast elements that result along ridges and drainage features in a radar image as correspondence features (Naraghi *et al.*, 1983, Curlander and Pang, 1982). Figure 4-32c presents the matched radar image and DEM. A second example with ERS-1 is illustrated in Figures 4-33 and 4-34.

The support obtained from simulations based on DEMs was used in the work by Domik (1985) and has become the standard for radar image processing in mountainous terrain. Such functions are therefore included in some radar image processing software packages, for example the commercial product "Easi-Pace" by the company PCI (Canada).

4-6.2 COMPARING IMAGES AND IMAGE PREDICTION

Some simulation work was used in SIR-B studies to obtain registration among images. An area of intense interest was in Argentina near the "crossover point" where all Shuttle-orbits intersected. This resulted in nine images, some of which were taken with ascending orbit, others with a descending orbit, producing coverages that look dramatically different from one another and present a limitation to one's ability to match the images (Cimino *et al.*, 1986).

The Shuttle SIR-B mission was the first to produce some quantity of generally available imagery with this variation in imaging geometries. Since then, ERS-1/2 and RADARSAT have augmented the stock of test data sets with some parameter variation. Several examples exist where areas are covered with two distinctly different incidence angles of 23° and 35° in the "roll-tilt" mode of the Shuttle.

Figure 4-35 presents SIR-B images of the same area that may look initially very dissimilar; these were part of a series of studies performed by Domik *et al.* (1988). Illumination direction varies by 90°. A town (Jose de S. Martin) can be recognized in one coverage because the buildings and streets are well illuminated and appear bright. The town is less visible in the second image. Such images motivated an effort to use one image as input and to predict how the other image would look. If the predicted and actual images were similar, then one could assume that prediction is a valid method to support a matching algorithm for opposite side radar images.

A geometric and a radiometric transformation to change from one aspect angle or illumination direction to a new one is needed in order to predict one image from the gray values of another. Image prediction presents both a radiometric and geometric challenge.

Domik *et al.* (1988) based their analysis on a DEM created from an aerial photography source (Figure 4-36). A mathematical model for the prediction of a descending orbit image from an ascending orbit image was defined and implemented by the authors. There were several methods studied and reported in the study. Figure 4-37 describes the one used successfully in this application. This Figure suggests that a relationship exists between the incident angle *"i"* of the radiation (which of course is a function of the slope of the ground and the imaging geometry), and the amount of energy that comes back to the antenna. This relationship can be exploited. The approach has an unknown coefficient "*a*" of the ground and the unknown incident angle *"i;"* these define the intensity received at the sensor. This approximate model was first put forward by radio astronomers, in particular Muhleman (1964) and Hagfors (1969), mostly to model microwave reflectivity of planetary surfaces at steep incident angles such as those under which planets would be imaged from Earth-based antennas.

Now if reflectivity "*a*" and the incident angle *"i"* were known the new image could be computed. One prediction technique demonstrated by Domik *et al.*, (1988) takes the input image to

- compute the surface property "*a*" from the known incident angle,

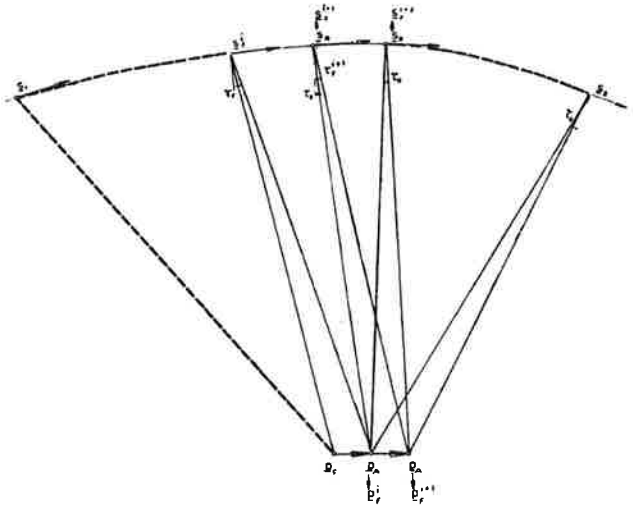

Figure 4-31. Real-time mathematical model updates the location of the stereo pair of image coordinates *r', t', r", t"* as a result of an operator action of moving the object location to *X, Y, Z* in the object coordinate system. In the solution by Raggam (1985) the measuring marks in the left and right images are moved until the squint angle *t* is again at its nominal value.

- then goes with that coefficient into the opposite-side geometry to compute the new incident angle from the DEM
- and computes a new backscatter value with the "known" surface property coefficient "a."

This is thus one of several possible techniques that are all similarly justifiable. They all raise the issue of being able to compare images, to compare the prediction with reality and to find an explanation for the differences among images and between image and prediction. If the terrain slope were known, if something further about backscatter curves of certain materials was known and if one had multiple observations of an object, then the multiple images could be used to draw conclusions about the materials on the ground.

Figure 4-38 shows a SIR-B input image from the ascending orbit, the prediction of the descending image and the actual image from the descending orbit. This study by Domik *et al.* (1988) stimulated ideas for the use of radar image simulation work based on DEMs. Simulation is of value because images can look very different from various orbits and aspect angles. Subtle, relevant differences need to be revealed by elimination of overpowering primary differences due to surface geometry. This elimination is accomplished if the two images are made similar through "image prediction" as described here.

As noted earlier a major radar image processing problem has so far remained unsolved, *i.e.* the problem of merging so-called opposite side radar images into a precision-registered data set. One is encouraged by the ongoing simulation and prediction work to see opposite side radar images matched with the help of DEMs and simulations.

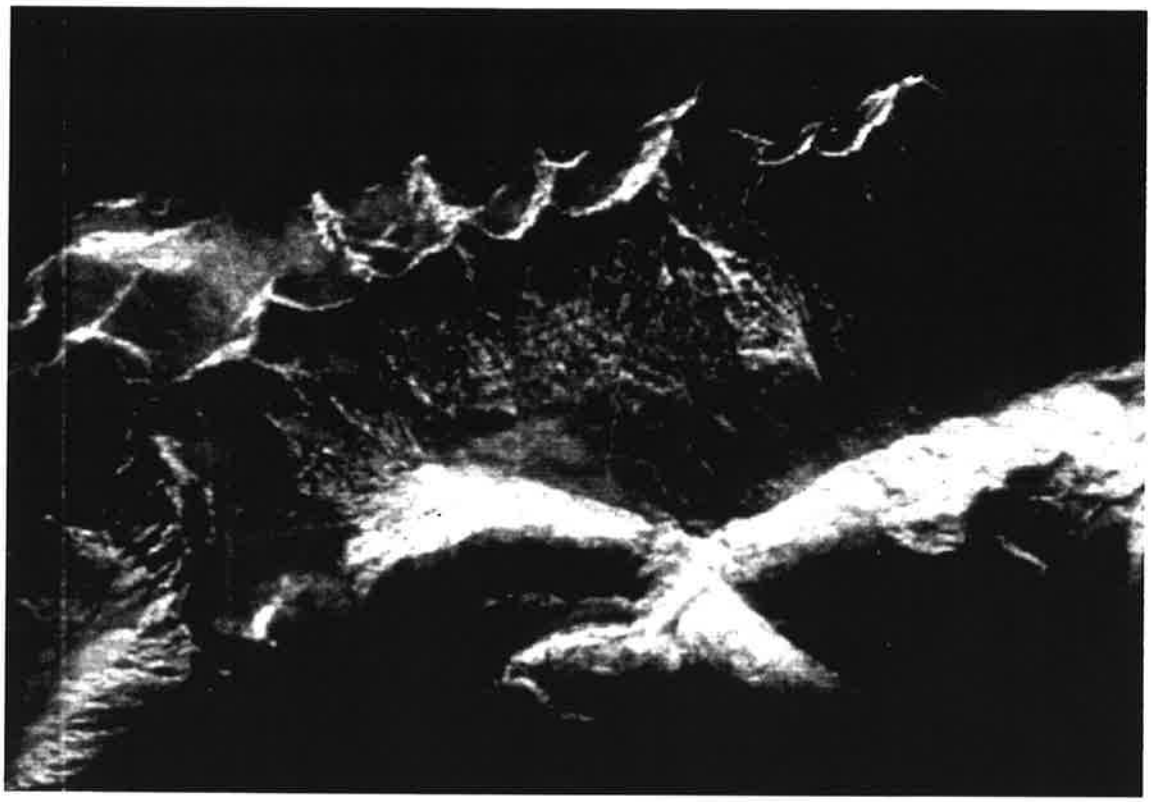

Figure 4-32a. Canadian SAR-580 image at X-band (3 cm wavelength) of an area in the Tyrolean Oetz-Valley, Austria, at 2 m pixel spacing.

Figure 4-32c. (Figure 4-32b appears on the next page) Geocoded (ortho-rectified) radar image to support the scientific analysis of radar signals in image Fig. 4-32a (Courtesy G. Domik).

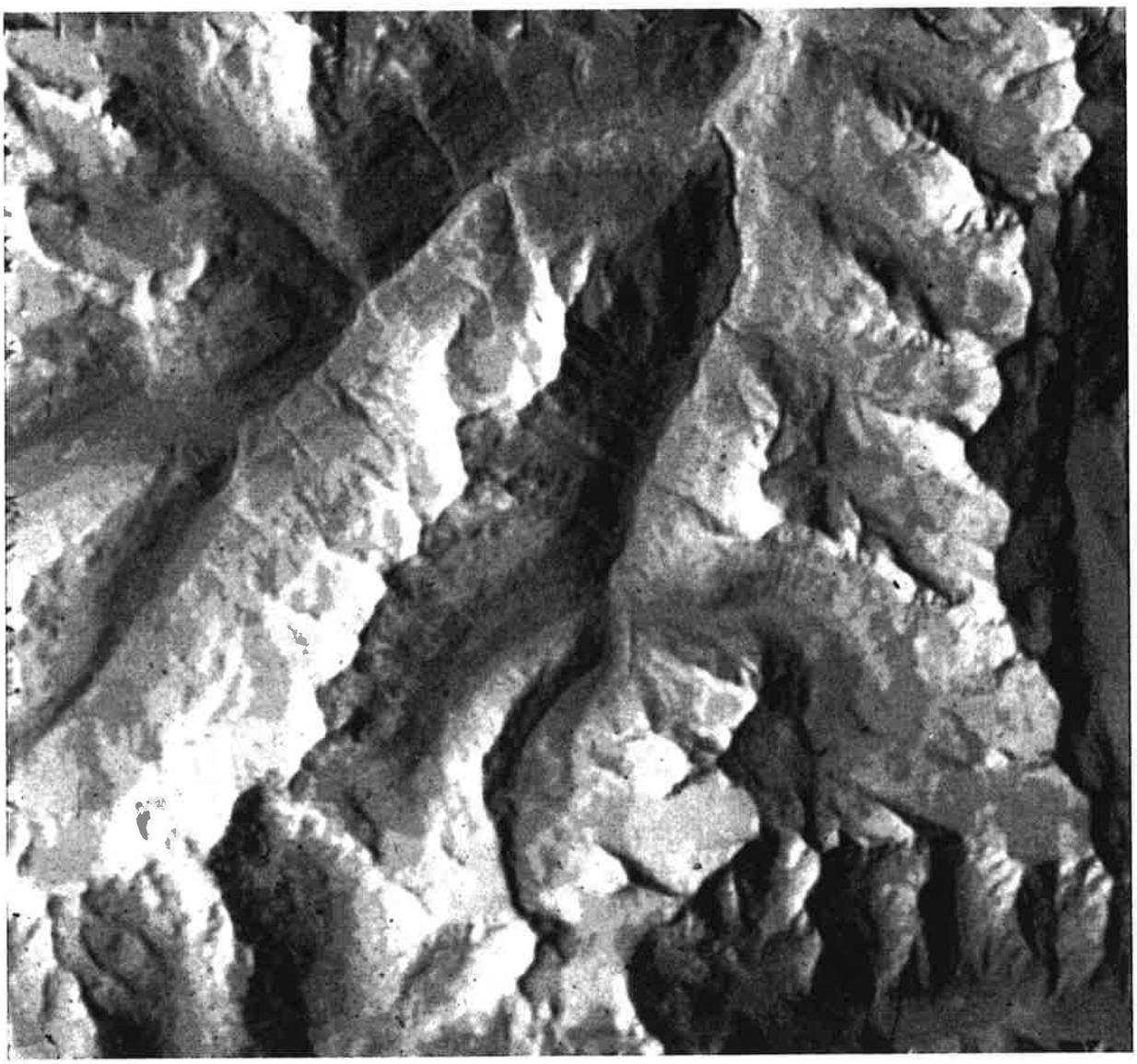

Figure 4-32b (above). Input DEM of an area that includes the portion covered in Figure 4-32a. DEM is derived from aerial stereo-photography.

4-6.3 SIMULATION FOR STEREO-STUDIES

Simulation has been used frequently to support stereo work, for example by Domik (1985), Kobrick *et al.* (1986) and Thomas *et al.* (1986). One illustration is the effort to predict how European ERS and Japanese ERS images could be combined. A SIR-B image from Mt. Shasta was the source for such an analysis by Thomas *et al.* (1989). Figure 4-39 shows one of the SIR-B Mt. Shasta coverages. Using the prediction technique mentioned above, this image served to predict a Japanese and European ERS image after rectification. Use was made of the differences in look angle. However, sensor wavelength was ignored. Predictions were assumed to be L-band images (as in SIR-B) when in fact, of course, the European Earth Remote Sensing satellite images are acquired in C-band.

4-6.4 DISCUSSION

(a) Concerns about Backscatter Models

One is often faced with critical comments that express concerns about an approximate backscatter model, *e.g.* Muhleman's (1964) when presenting radar image simulations and predictions. However, a simulation could use as complex a backscatter model as the user can define. Approximate backscatter models must be used as long as knowledge about the surface properties is not refined. One may argue that computation of a Muhleman parameter "*a*" from one single image with a known single incident angle is a more meaningful exercise than using no model at all. A generalization of the approach to two or more backscatter parameters, and therefore to more complex shapes of the

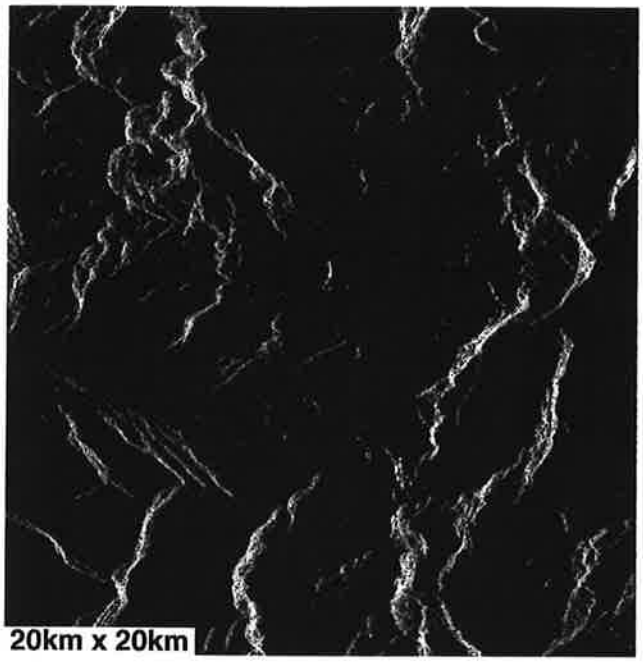

Figure 4-33a (above). Part (a) shows an European Space Agency ERS-1 radar image of the Ötz-Valley which was also shown on aircraft radar in Figure 4-32.

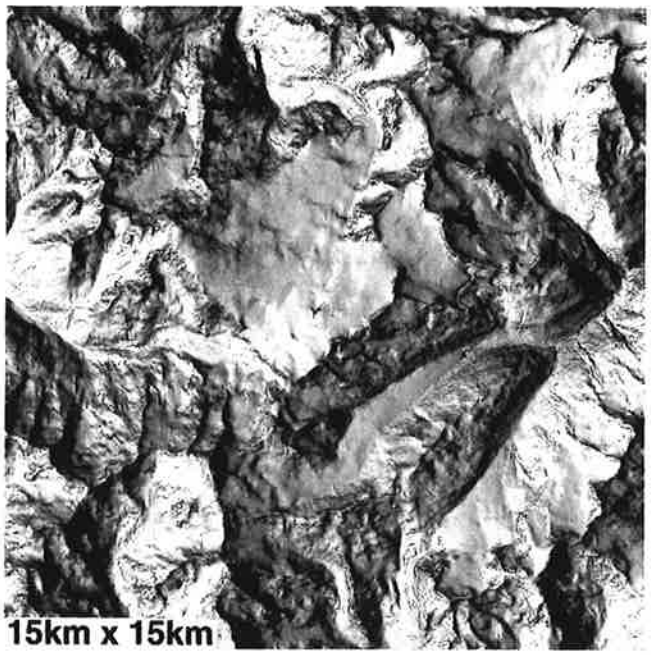

Figure 4-33b. A DEM of a larger area than that in Figure 4-32b, and at a reduced resolution.

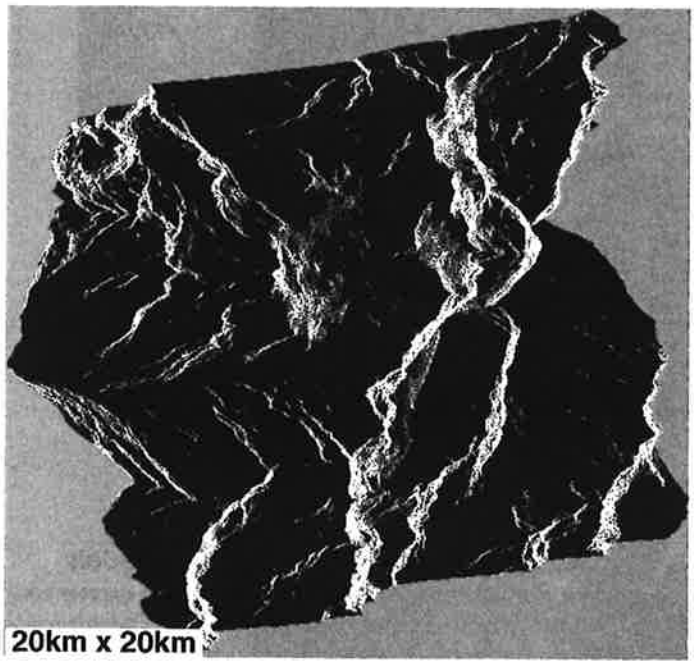

Figure 4-34a (above). Simulation of the ERS-1 image shown in Figure 4-33a using the DEM of Figure 4-33b and knowledge about the satellite orbit. Note the similarity between the real and simulated radar images. Attaching to each radar image pixel an elevation value permits one to create an orthorectified (geo-coded) image product (b). Comparing this with the illuminated DEM produces many homologue features which would not be identifiable from the original SAR image in Figure 4-33a.

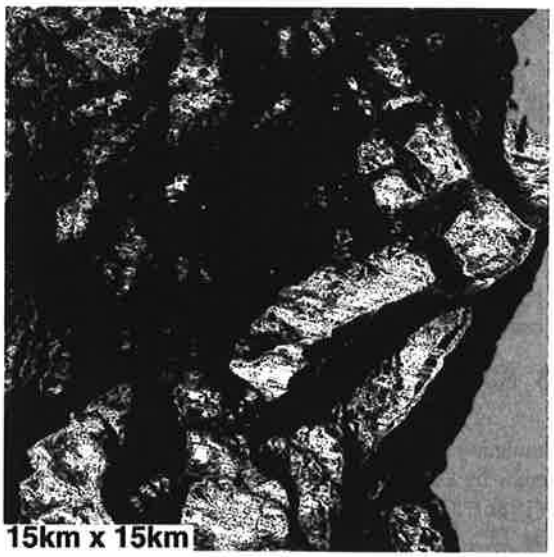

Figure 4-34b The change from the input image in Figure 4-34a to this ortho-rectified result is fairly dramatic. This is caused by the steep look angles of the ERS radar.

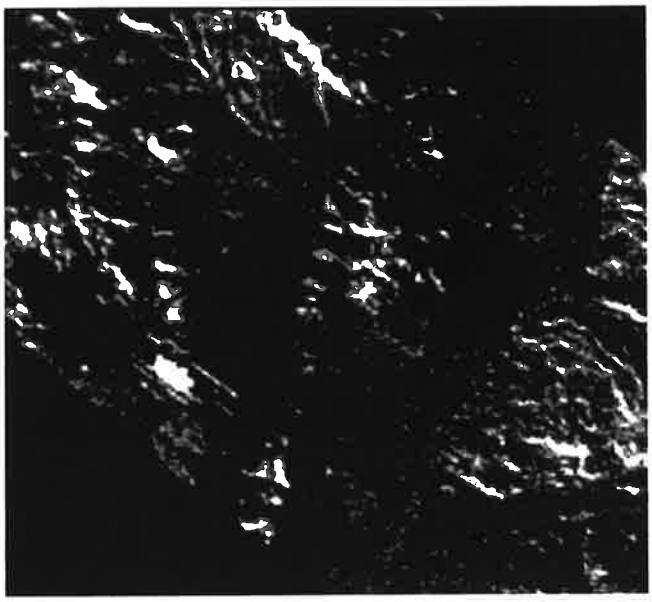

Figure 4-35a. One of the SIR-B radar images near the cross-over point in Argentina. The L-band image (25 cm wavelength) were taken from a decending orbit near a town called S. José de Martin (Courtesy G. Domik).

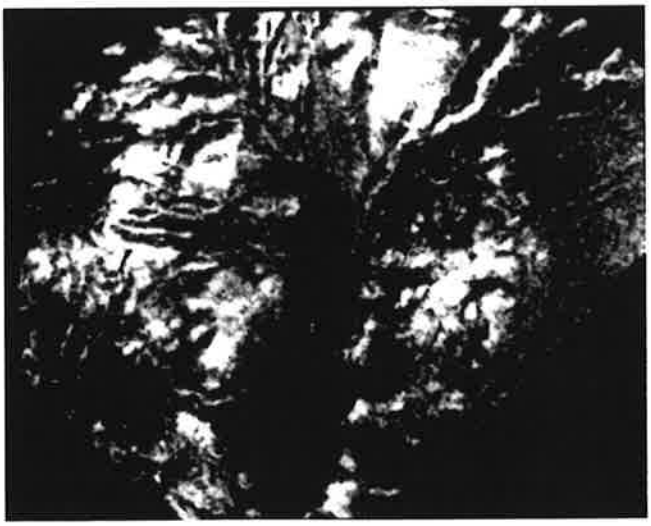

Figure 4-35c (above). Same as 4-35a, from descening orbit, but at a different look-angle off-nadir.

Figure 4-35b. Same as 4-35a, but from an ascending orbit.

backscatter curve, would be feasible if multiple images at different incident angles were available and could be co-registered. Co-registration can be accomplished if the terrain shape is known through stereo-matching or interferometry. Two gray values for an object point, at a known terrain slope, would define a two-parameter backscatter curve for that object point and therefore could lead to a promising classification scheme of surface materials.

(b) Simulation without Regard for Wavelength

Geometric radar image processing such as in stereopsis may be insensitive to specific wavelength bands. The stereo-work of Domik (1985) is an example of the usefulness of simulation for such geometric studies. Matching points between a DEM and a radar image represent a second class of problems that are largely neutral to wavelength.

(c) General Concerns with the Level of Sophistication in Radar Image Analysis

Most radar image analysis is "by eyeball" and directed at basic radar image pixel arrays. A dramatic example of this state of affairs is NASA's Magellan mission. The high-pressure period, from 1990 until 1993, of studying the incoming planetary coverage consisted nearly entirely of visual inspection of single images (see the *Magellan Special Issues of Science* (1991) and *Journal of Geophysical Research* (1992)).

Terrain shape or surface cover analyses from radar images have not yet evolved into very sophisticated methods; they often rely on single images. In this environment it would seem that work is needed to advance the state of the art of radar image analysis. As soon as surface radiometric properties become an issue it will become evident that successful radar image processing must cope with terrain elevations and slope data, and with the consideration of multiple radar observations at differing incident and aspect angles.

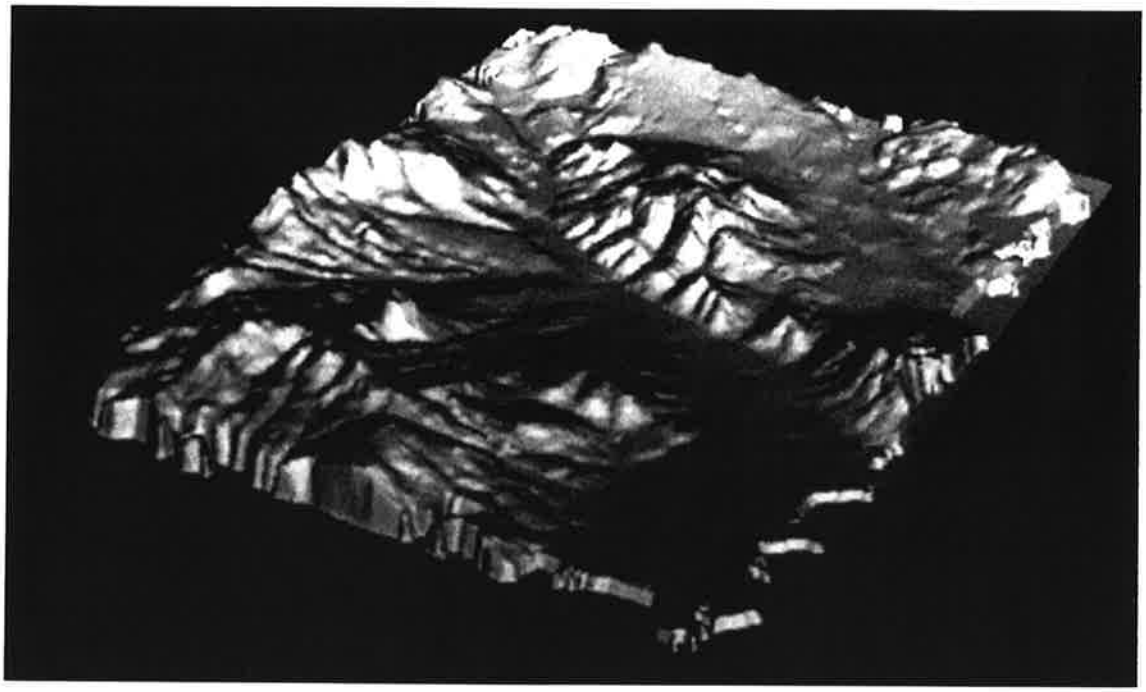

Figure 4-36. DEM from aerial stereo photography for the area covered by the images in Figure 4-35, covering 18 km x 14 km (Courtesy G. Domik).

4-7 RADAR IMAGE RECTIFICATION AND REGISTRATION

4-7.1 GEOMETRIC RECTIFICATION

What may appear today as simplistic rectification attempts were made in the 1950s. These were based on optical-mechanical devices to remove systematic image deformation due to slant plane geometry (Macchia, 1957). Such technologies are now obsolete due to the advent of digital image processing. Obsolescence applies also to work done on photogrammetric orthophoto machines (Leberl *et al.,* 1981), or special purpose solutions with specifically programmed CRT-image writers (Graham, 1972).

Another historical rectification tool was the elimination of flight path curvature from radar images after a block adjustment of radar images (Leberl *et al.,* 1976d). This was accomplished by a manual process in the "optical correlator" where the SAR image is produced (Peterson, 1976).

Clearly the geometric rectification problem must be solved if multi-images of the same area from different orbits are used, as in the case with four images received by SIR-B over some mountainous areas (Figure 4-40). Registration "as best as we can" results in ridges that are not superimposed. A color-coded presentation produces a chaotic mess of image detail; the images clearly do not match.

Images need to be "ortho-rectified" or "geo-coded" before an accurate image registration can be feasible, unless the image is of completely flat terrain. Figure 4-41 demonstrates the result of properly ortho-rectifying and co-registering multiple SIR-B satellite radar images. Individual rectification was done with the same DEM. The multiple co-registered images were used to classify the surface cover using standard classification techniques (Leberl *et al.,* 1986c; Cimino *et al.,* 1986). Rectification of these images was done with both a DEM from aerial photography, and one obtained from stereo-radar images themselves. Both techniques produced satisfactory rectification results.

The registered images were subject to "multi-spectral" classification. However, only one spectral band exists. What was variable was the angle of incidence. The classification therefore employed the object's so-called "incident angle signatures." The radargrammetric effort was in the precision registration, not in the classification. The error of the registration was within 1 to 2 pixels (Leberl *et al.,* 1986c).

Geometric rectification has been brought to a particularly high level of operation in Magellan and ERS-1. While no reports exist about the accuracies of the resulting Magellan products, such accuracies are well established in the European ERS-1 project. Schreier (1993) reports that about 1 to 2 pixel errors remain in routine products from that mission, as produced by the National Processing and Archiving Facilities (PAFs). These results are confirmed by Dowman *et al.* (1994).

4-7.2 RADIOMETRIC "RECTIFICATION" OR SLOPE-EFFECT-REDUCED-IMAGES

SIR-A data stimulated the initial efforts to create DEM-based simulations and to "subtract" the resulting images as the manifestation of the incident angle effect from a real SAR image

Ideally, one should have many overlapping radar images for analysis of one area. The example of detecting and mapping the areal extent of snow and ice in radar images can illustrate the great benefits of dealing with multiple images (Rott and Nagler, 1994). Radar images can be made at all times of day, any day or night of the year, although in many cases local weather will have some impact on the interpretability of certain features. If one had many observations at various angles of an area of interest, one could refine the theoretical rigor of the backscatter models that enter into, or result from the simulation, rectification or prediction studies. Backscatter curves can be very jagged if one deals with reflections from man-made objects such as vehicles. Those curves become smoother and thus parametrically manageable in natural terrain covered by forests, soil or grass.

(d) An Extra-Terrestrial Angle

In the analysis of images as they were obtained from NASA's Magellan mission to planet Venus, one needs to examine data taken from different look directions in three separate cycles of the mission. This presents a serious challenge to the analyst to match images and to understand brightness differences within images, or from image to image. At that point a radar image processing workstation with the capability of manipulating the geometry and radiometry of multiple images becomes very helpful. Simulation of such multiple incident angle radar images of known and well-understood terrestrial environments should be helpful in training the future analyst.

The issue of overlapping images from opposite sides of the terrain has been discussed at various points in this chapter. This issue alone already illuminates the great benefits available from image simulations of various radar imaging scenarios.

$$\sigma^* = \log_{10} \frac{a^3 \cdot \cos i^*}{(\sin i^* + a \cdot \cos i^*)^3}$$

$$a = \frac{\sin i}{\sqrt[3]{\frac{\cos i}{10^{\sigma}}} - \cos i}$$

Figure 4-37. Prediction model to create an output SAR image from an input image taken at a different geometry: "σ" is the parameter of the backscatter model, "i" is the incident angle and is a result of the look angle off-nadir, "θ", and the terrain slope.

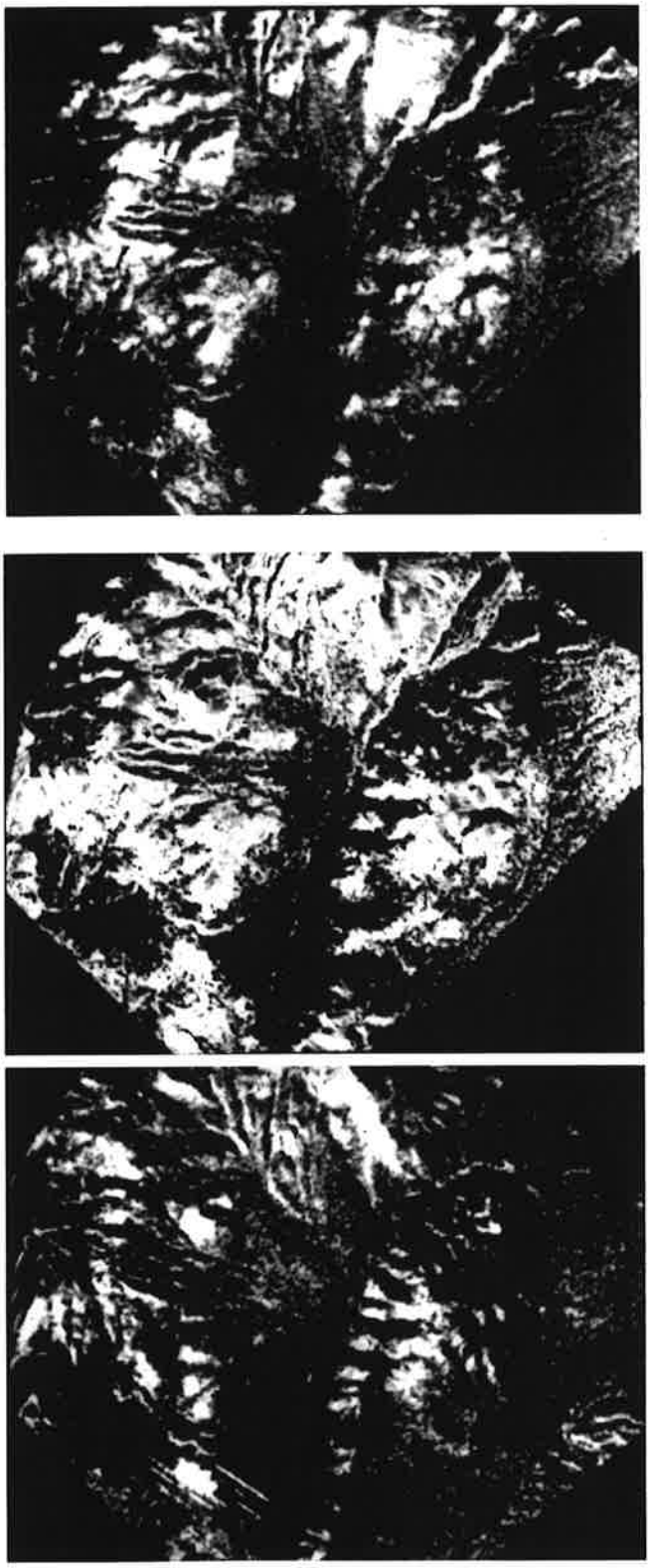

Figure 4-38a (top) 4-38b(center) and 4-38c (bottom). Images to illustrate the "prediction" concept. Input image (a), predicted output image (b), and actual output image (c) for comparison of the SIR-B cross-over point in Argentina. (Courtesy G. Domik).

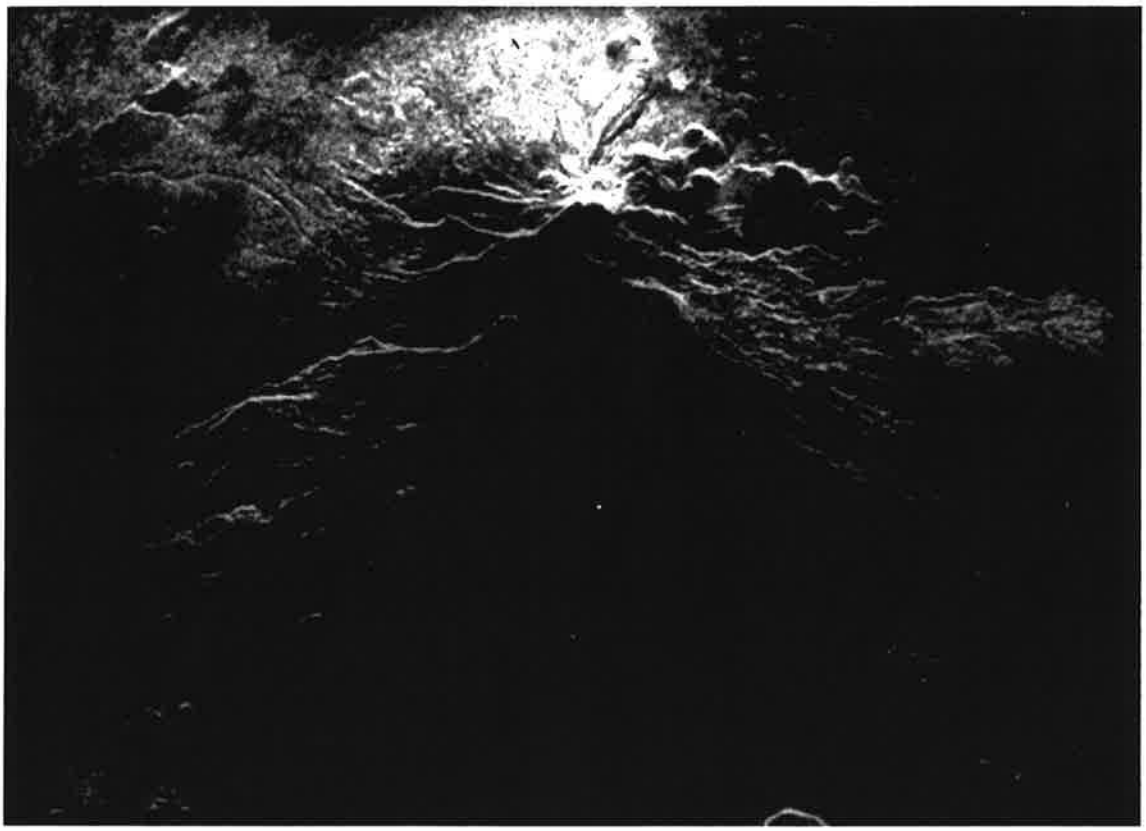

Figure 4-39a (above). Example of image prediction for stereo-analysis, above, SIR-B input image of Mt. Shasta from an incident angle of about 25°.

Figure 4-39b (below left) and c (below right). From figure 4-39a, the geometries of the (b) European E-ERS-1 and (c) Japanese J-ERS-1 radar satellites were used to predict how these images will look like. Look angle for J-ERS-1 is 45° and more, for E-ERS-1 is 20° and more. Shown are geocoded derivatives of ERS/JERS IMAGES.

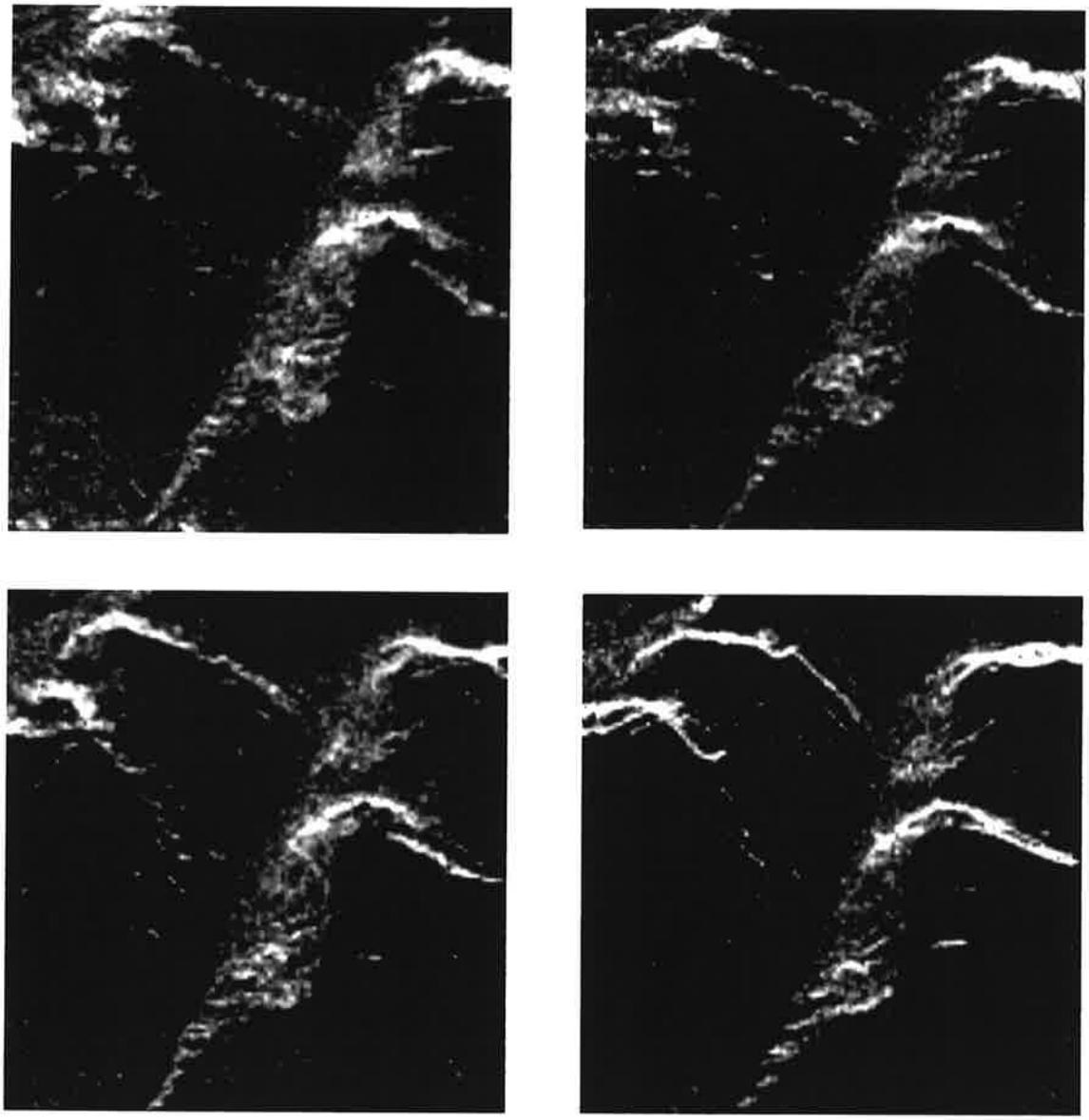

Figure 4-40. Four SIR-B L-band image segments of an area in Argentina show their geometric disparities (a to d, this page). Note the discrepancies along edges (e to h, next page) (Courtesy G. Domik).

(Domik *et al.*, 1984). The result led to the conclusion that the remaining image gray values describe two phenomena: 1) variations of ground cover; and 2) the effect of microrelief that is not present in the DEM. These small variations in the relief manifest a difference image which could be called a "radiometrically rectified" radar image. This is a radar image as if the ground were flat. A more appropriate name would be "slope-effect-reduced" image. Figures 4-42, 4-43 and 4-44 illustrate the concept.

4-7.3 MATCHING DISSIMILAR SAR IMAGES

Earlier sections emphasized differences in overlapping images due to topographic relief. However, topography is not the only reason why overlapping images may be different and dissimilar.

Figure 4-45 presents two SEASAT images of a flat area near New Orleans. While water bodies look like distinct objects in one image, they nearly disappear in the other image. In the images from two orbits over the same area a few features are found that are clearly the same, but many differences and great variability also exists even if the terrain is flat. Such differences may be caused by changes in the object, *e.g.* by wind changing the wave patterns on a lake, or wetness after a rain, or harvesting grain, etc. Such differences may also be caused by the sensitivity of the radar echo to the incident angle.

The need exists to compare time-sequential radar images automatically, particularly in light of high data rates such as the European ERS or ENVISAT satellites, from RADARSAT, Almaz, Shuttle SIR-C and satellites of the EOS era where the same area would be imaged many times over a period of 15 years.

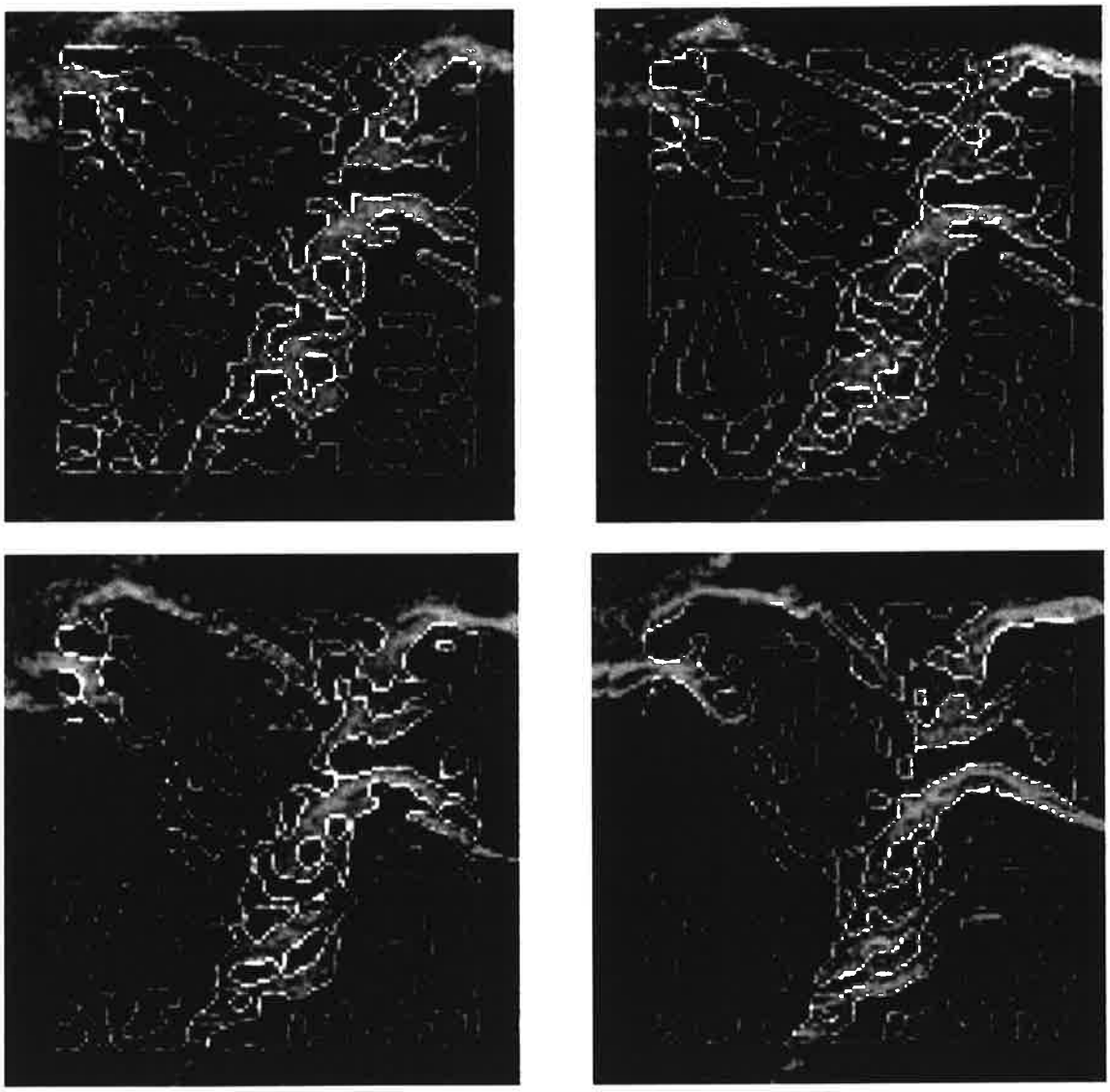

Figure 4-40. Four SIR-B L-band image segments of an area in Argentina show their geometric disparities (a to d, previous page). Note the discrepancies along edges (e to h, this page) (Courtesy G. Domik).

If one assumes that one had initially geo-coded (rectified) each image for the effect of topographic relief, one still has a problem of difference in appearance, even if the terrain were flat, and there may be effects of residual geocoding errors that prevent the images from being precisely co-registered.

A rectification technique that was found to work reasonably well uses a filter to extract linear features (McConnell *et al.,* 1989). The authors employed a so-called Marr-Hildreth operator using the zero crossings in a gradient image. This creates edges along the areas of consistent gray values. The operator forms edges in each point of inflection in the gray value "DEM." Consider "gray" to be "height," then an image is a DEM with heights varying between 0 and 255. The interesting feature of the operator is that the edges all form closed polygons, just like contour lines in terrain form closed polygons. At any point where the "relief" has a point of inflection in its slope the curvature changes its sign. Thus each edge has a positive and negative side.

Various ways exist to match two images based on Marr-Hildreth edges. Correlating two binary edge images is difficult, but there are techniques using "distance transforms" that fill in the areas within each polygon by values that increase as one goes away from the edge (Barrow *et al.,* 1977; 1978). Figure 4-46 presents the Marr-Hildreth edges for one of the images in Figure 4-45; Figure 4-47 shows the polygons filled, in one case with a distance transform, in the other simply with binary values. Since there is a positive and a negative side at each edge, the positive side of each edge can be filled. After accomplishing the same with the other image both are shifted against each other to obtain

Figure 4-41 (top). Three co-registered SIR-B images are combined and can be presented as a color-coded result in red-green-blue. The images are "draped" over the digital elevation model and a perspective visualization is computed (Courtesy M. Kobrick).

the maximum overlap of filled areas where the correspondence between the two images is particularly accentuated.

In order to illustrate the performance of this approach, one needs to obtain points of "maximum correlation" in individual image windows. Figure 4-48 presents the maximum correlation somewhere in the center. While this is the result for Marr-Hildreth edge images, the same result is not produced with a traditional image correlation method. Taking the raw radar gray values and trying to match the two sets produces many errors. Figure 4-49 is a case of a window with the maximum at the window edge when they should all be at the center; satellite images of flat terrain should not have large geometric disparities from one window to the next.

A major issue is quality control. A rejection/acceptance criterion is needed that defines where match points between two images are acceptable and where they are not. The typical result is then a regular grid from which unreliable matches are eliminated.

The problem is significant for images from different orbits, different times, different sensors or any combination thereof. There are two types of matching errors: those caused by dissimilarities (data-induced) and those inherent to a particular chosen matching process (method-induced). An example of the matching process is that of an accuracy analysis using various radar and optical images (Leberl *et al.*, 1994). A comparison was made between manual identification of match points in a photogrammetric plotter and automated matching in the pixel domain. Generally, errors between the two methods amount to ±1 to ±2 pixels rms. This is much larger than one may expect from optical

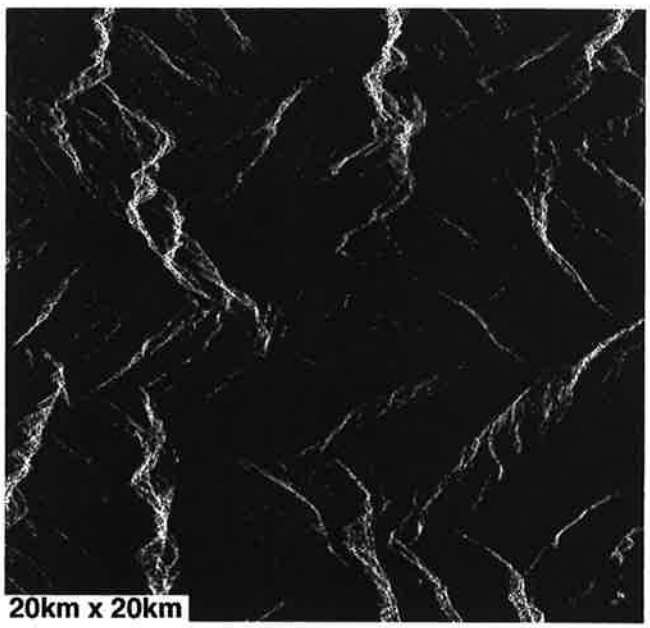

Figure 4-42. ERS-1 image of mountainous area in Tyrol, Austria, prior to radiometric manipulation. Area is 20 km x 20 km.

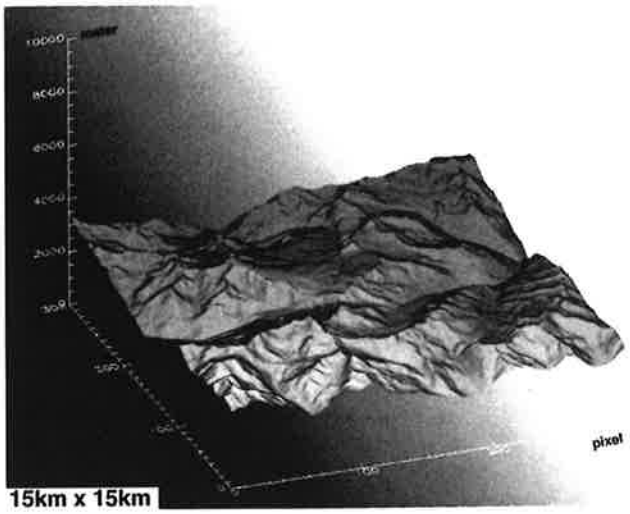

Figure 4-43. DEM of the area shown in Figure 4-42. Data from maps.

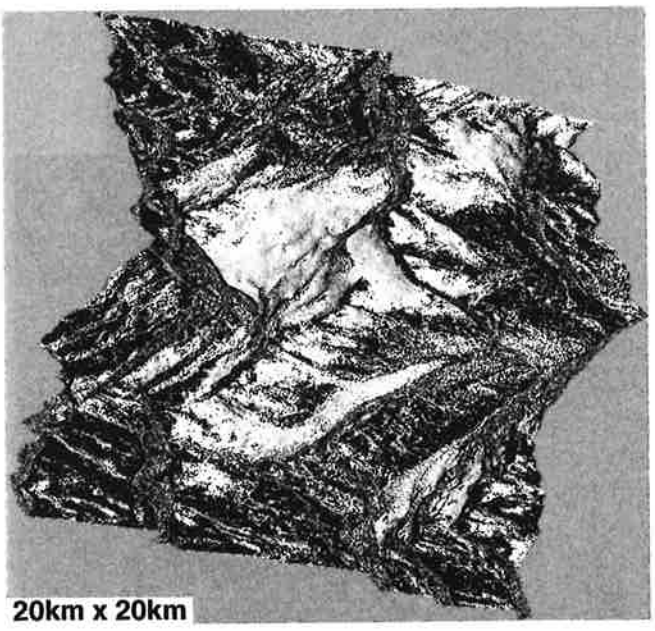

Figure 4-44. Slope-effect-reduced and geo-coded ERS-1 image produced from image in Figure 4-42, using the DEM of Figure 4-43. The image is obtained by "subtracting" the simulated image (based on the DEM) from the real image, and then by geocoding the difference image. The extreme incidence of radar layover leaves several areas in the radar image with improper correction. The difference image's gray values are "stretched."

images where subpixel mismatches can be expected. The much larger uncertainties of radar are presumably due to illumination differences in overlapping radar images, or to the effects of radar speckle noise that radar produces.

The most distinct dissimilarity between overlapping radar images results from an "opposite side" imaging geometry. As stated previously the problem of matching opposite side images has so far not been solved. No technique exists to routinely match opposite side images of accentuated terrain. Some matching has been accomplished when an externally produced DEM was employed to terrain-correct all component images; the opposite side images would then register to within a few pixels. Rott and Nagler (1994) report matching errors of ±4 pixels in high mountains with ERS-1 data. The reason for these remaining discrepancies may lie in the inaccuracies or lack of detail of the DEM, and in the errors of the sensor's position and attitude which are used to terrain-correct each image.

4-7.4 A SMART WAY TO LOOK FOR IMAGE DIFFERENCES

Figure 4-47(b) was an image of Marr-Hildreth edges with a distance-transform. Bright, of course, is the greater distance and dark is the zero distance from the edges. One now can take Marr-Hildreth edges from image number 2 and put them over the distance-transform of image number 1. At each pixel on the Marr-Hildreth edges of image number 1 a running sum is found of the distance values of the underlying image number 2. In each edge pixel, a running sum is entered that is computed over, say, 10 pixels forward and 10 pixels backward along the edge. If the distance values are large then this sum will assume a large value. If the edge in image number 2 were to fall nearly on top of an edge in image number 1, the sum of the distance values would be nearly zero because the distance values are all zero along edges in image number 1.

This may constitute a technique of automated image comparison and change detection. Wherever running sum values are very low, they represent similarity. Wherever those values are large, the images are different. "Similarity" is assessed by means of edges. Figure 4-50 illustrates this idea by an example.

In this manner an algorithm to support the search for identical features in dissimilar image pairs has been identified; and at the same time the algorithm can support a search for image differences.

4-8 RADAR STEREOPSIS

4-8.1 SAME SIDE STEREO

Obviously radar stereopsis depends on overlapping radar images which must be acquired with two different look geometries. Various ways of obtaining stereo radar images exist. An example was shown as Figure 4-2, presenting the so-called "same side geometry" conceptualized in Figures 4-51 and 4-52. In the example notice that the shadows are of different length in the two images. While there is only a single image in an area covered by a single shadow, or no image at all if the area is in

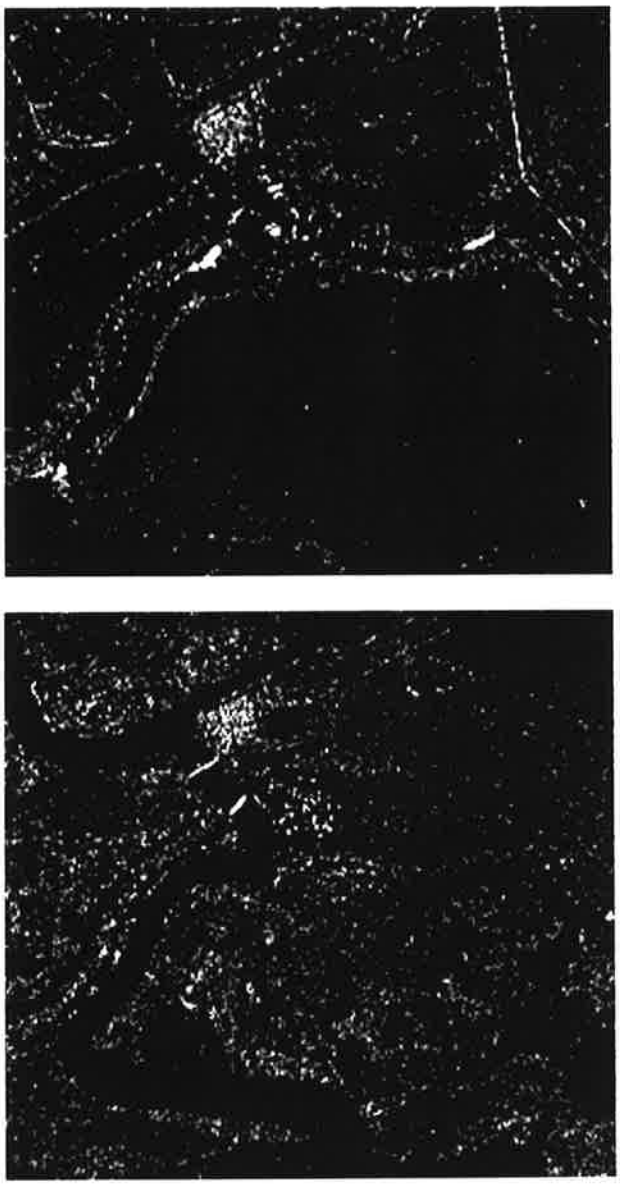

Figure 4-45. Two SEASAT SAR images at L-band, at 20° look angle off-nadir, but from an ascending and a descending orbit. Area is near New Orleans and highlights dissimilarities as a result of azimuth angle of the sensor path.

shadow in both images, the illuminated areas will be viewable stereoscopically. One needs to realize that a large stereo base does not automatically imply large stereo-relevant parallax differences. A look at the equivalent camera geometry reveals that the camera stereo base needed to define a specific parallax such as that obtainable from same side radar images can be very small. The conclusion may then be that the same side stereo radar geometry is one of poor geometric performance. However, as will be discussed later, this conclusion applies only in cases where the radar look angles are fairly large, *i.e.* in the range of 45° or more. Same side geometries offer the advantage of easy

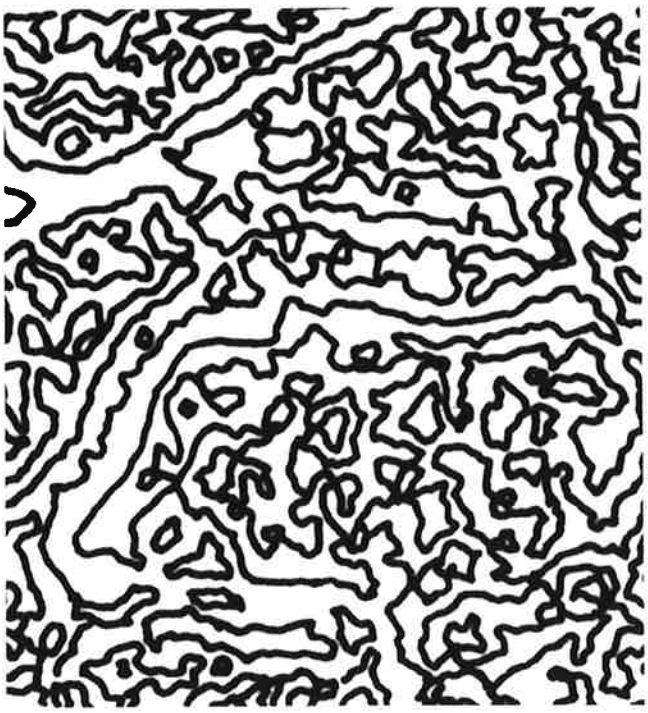

Figure 4-46. Marr-Hildreth edges computed from one of the images in Figure 4-45. Note that the edges represent continuous polygons.

stereo fusion since gray value dissimilarities are modest in the overlapping images (Figure 4-52).

Both look angle magnitude and look-angle difference are important factors in defining the geometry of a radar stereomodel. At shallow angles, a given look angle disparity may result in a poor equivalent base-to-height ratio; at steep angles, the equivalent base-to-height ratio is improved greatly, even at the same look angle difference (Figure 4-53).

The concept of a "base-to-height" ratio derives from photographic stereoscopy; it is a geometric concept which ignores the other important factor of stereopsis, *i.e.* the ability to find match points in overlapping images which depends on similarity of the two stereo images. A particular stereo imaging arrangement may produce a strong geometry in the form of a base-to-height ratio. With radar images the base-to-height-ratio may be in the high ranges of 3 or 4 and superior to what would be expected in photogrammetry with base-to-height ratios of 0.6 to 1.0. However, this model will not be useful if the thematic dissimilarities prevent matching the two images and the stereo-case cannot be viewed.

Typical stereo-viewability of radar images is successful when the equivalent base-to-height ratio is weak. Very steep look angles of 5° to 25°, such as in the Apollo 17 ALSE images on the Moon, with the Earth-orbiting satellite SEASAT, with the Venus-Magellan system and finally also with Europe's ERS radar, produce comparatively large parallax differences, or equivalent base-to-height ratios, even for very small look angle differences. Steep looks result in large differences in the relief displacement for

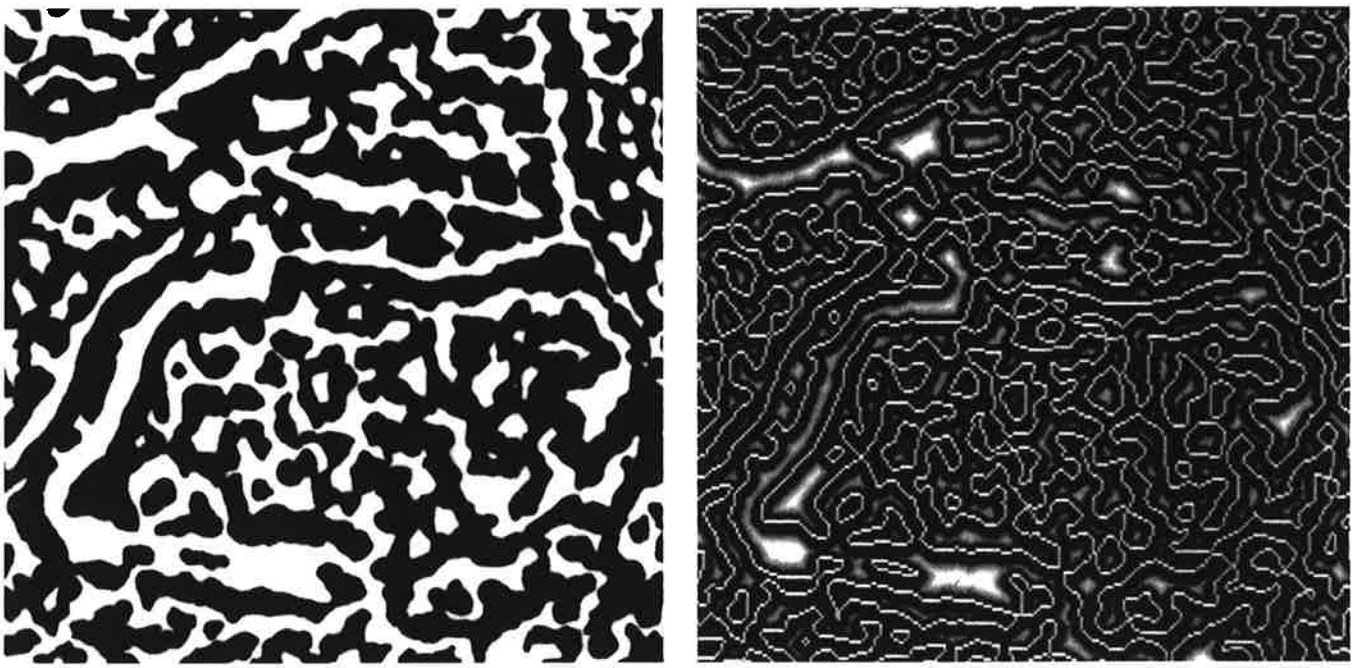

Figure 4-47. (a - left) Filled in polygons from Figure 4-46 represent a binary image. Two such binary images can be matched, thereby overcoming the gray value dissimilarities of the two images. (b - right) A "distance transform" of the Marr-Hildreth edges of Figure 4-46 can also be used for the same purpose. At each pixel is encoded the distance of that pixel from the nearest edge. Matching with a distance transform uses the "distance" found when superimposing the second image's edges over the first image's distance values. At a perfect match location the distances found along an edge are zero.

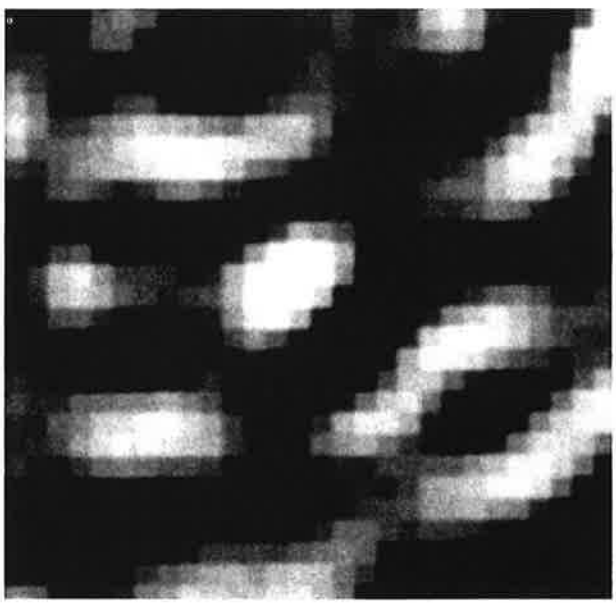

Figure 4-48. Sample image window in which maximum correlation is computed between the two input images; use is made of the Marr-Hildreth image and filled polygon. Note that correlation maximum is at window center.

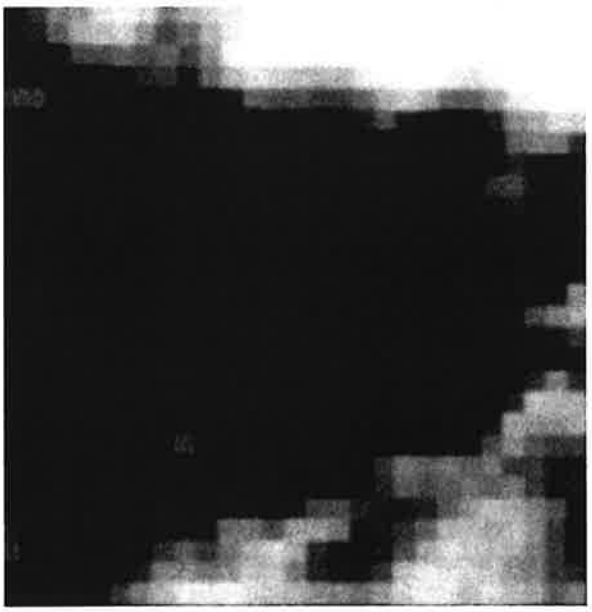

Figure 4-49. For comparison with Fig. 4-48, maximum cross correlation found from matching the raw image gray values instead of the edges only. Note that maximum correlation is not in window center, suggesting that matching is in error.

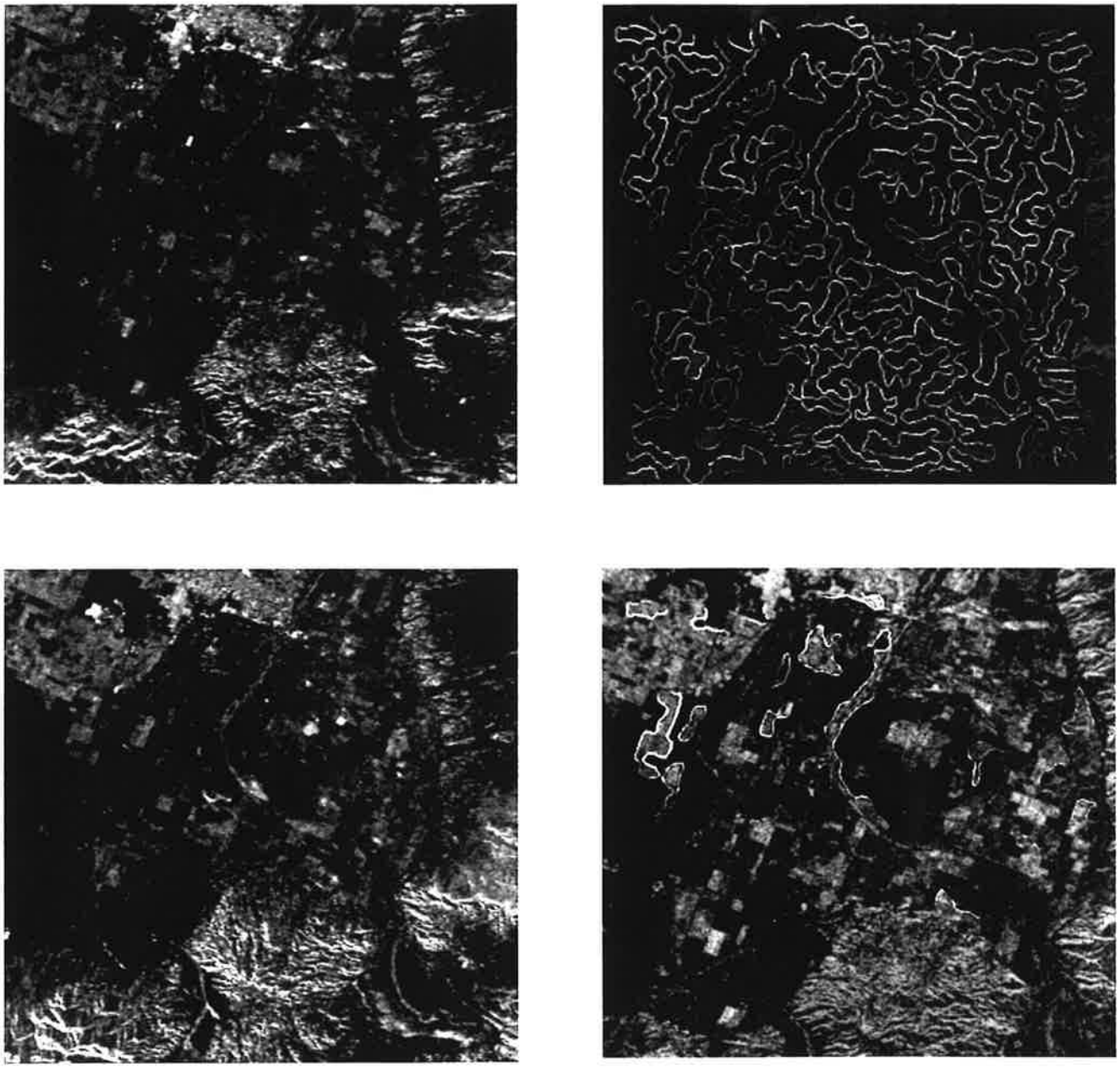

Figure 4-50. Illustrating a method of qualifying differences in two images: (a- top left), (b - lower left) are two dissimilar source images from SEASAT; (c - top right) Marr-Hildreth edge image; from this one creates a distance transform by computing the distance to the nearest edge point and coding the distance value in grey; (d - lower right) superimposing a second image with its own edges and assessing the difference between the two images by computing a "running sum" of distance values found along the edges in the second image. Values exceeding a threshold are considered to be "changes" and are highlighted.

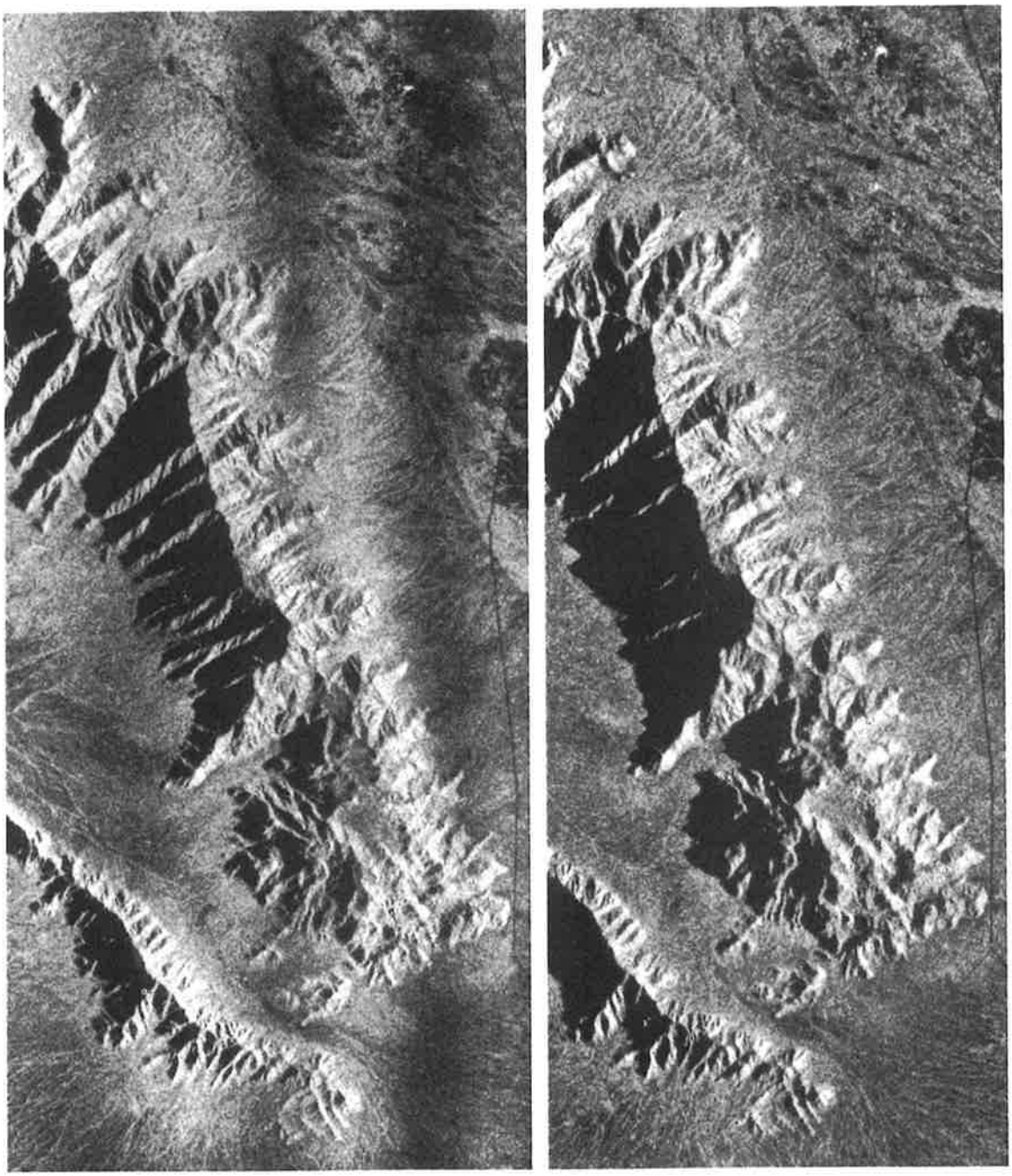

Figure 4-51. Example of a radar image pair for same-side stereo taken with the Goodyear GEMS SAR at 10 m resolution over an area of the Estrella Mts. near Phoenix, Arizona.

small differences in look angles. Since a steep look angle generates large relief displacements it is not surprising that the parallax differences will also be large. Steep look angles, however, reduce the geometric ground resolution. Therefore, while one may obtain an improved "base-to-height" ratio, one may also suffer from a much poorer geometric control compared to a shallower look angle.

4-8.2 OPPOSITE SIDE STEREO

Figure 4-54 presents an opposite side pair of radar images. Flat areas may be viewed stereoscopically; however, areas with topography cannot unfortunately be viewed stereoscopically. Figure 4-55 illustrates the equivalent position of photographic cameras and documents that a much longer base-to-height ratio would be feasible because the two relief displacements are not being subtracted from one another as in a same-side radar geometry; instead the relief displacements get added to a large parallax difference. However, normally one cannot match the stereo images unless the area is flat, which is not where stereoscopic analysis is useful. The limitations of opposite-side stereo-geometries may render them largely useless for stereopsis.

Attempts were made in the past to process opposite-side images by density mapping and digital image processing so that from one of the two images a new one is created that looks more similar to the other image (Graham, 1972; Fullerton *et al.*, 1986). One series of steps includes gray value reversal. This changes an image sufficiently to permit some limited stereopsis; however, the matching accuracy remains obstructed by one's inability to deal with the micro-relief which manifests itself differently in the two images. While global shapes such as mountains indeed present a vertical dimension to the observer, one is left with an inability to place the measuring mark accurately on the surface (Fullerton *et al.*, 1986). More refined gray-value reversal methods such as those proposed by Domik *et al.* (1988) have not yet been studied for an application to stereo viewing.

The inability to merge opposite-side radar images is not only unfortunate for the extraction of surface topography; it also impedes the joint analysis of multi-temporal satellite images taken from ascending and descending orbits. It furthermore obstructs the study of incident angle signatures and their use for surface classification. Multiple radar images taken with different look angles could otherwise reveal the characteristics of a terrain's backscatter properties as significantly different illumination geometries are being applied. Therefore it may be stated that the inability to accomplish precision matched opposite side radar images is one of the important radar image processing problems in need of a solution.

4-8.3 STEEP LOOK ANGLES

Figure 4-56 from the Apollo Lunar Sounder Experiment (ALSE, Phillips *et al.*, 1973) produces an excellent stereo impression under a stereoscope. This is surprising, given that the look angle difference is only about 3°. However, with look angles from 0° off-nadir to about 10° even a small height difference creates significant parallax differences.

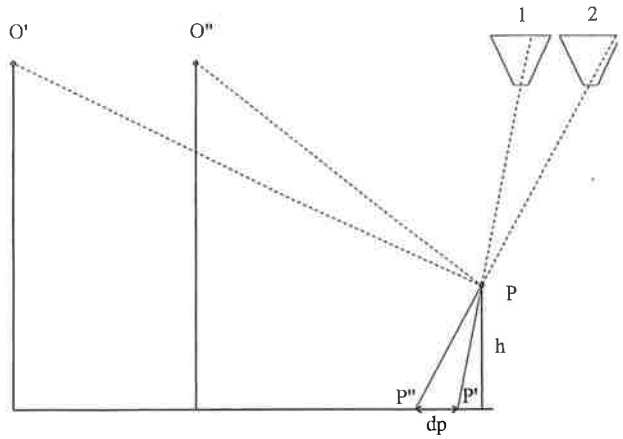

Figure 4-52. Configuration for a same side radar stereo arrangement with definition of the radar stereo-parallax, and equivalent photographic camera arrangement with a photographic stereo parallax. Note how the relief displacements are being subtracted from one another to form a parallax *dp*, whereas they would be summed up in a pair of camera images.

Another ALSE-example is Figure 4-57 where there is too much parallax for visually merging the overlapping images. The images are too different. While the look angle differences are still rather small, maybe only 6° or so, the difference is too great to view the result in stereo.

ALSE may have been the first radar imaging to show that steep look angles do produce very large stereo parallaxes even at rather minute look angle differences. This was verified in later satellite radar projects – which were not designed for good stereopsis – and good stereo-viewing was attained at small look angles in Magellan and ERS-1. These projects are the subject of two separate Sections 4-10 and 4-11.

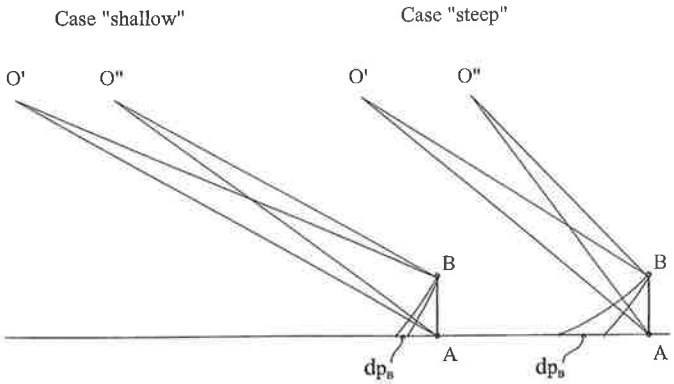

Figure 4-53 (below). Effect of look angle on radargrammetric stereo parallax: as the look angle reduces (or gets steeper) the greater will the parallax become, even if the look angle disparity remains constant.

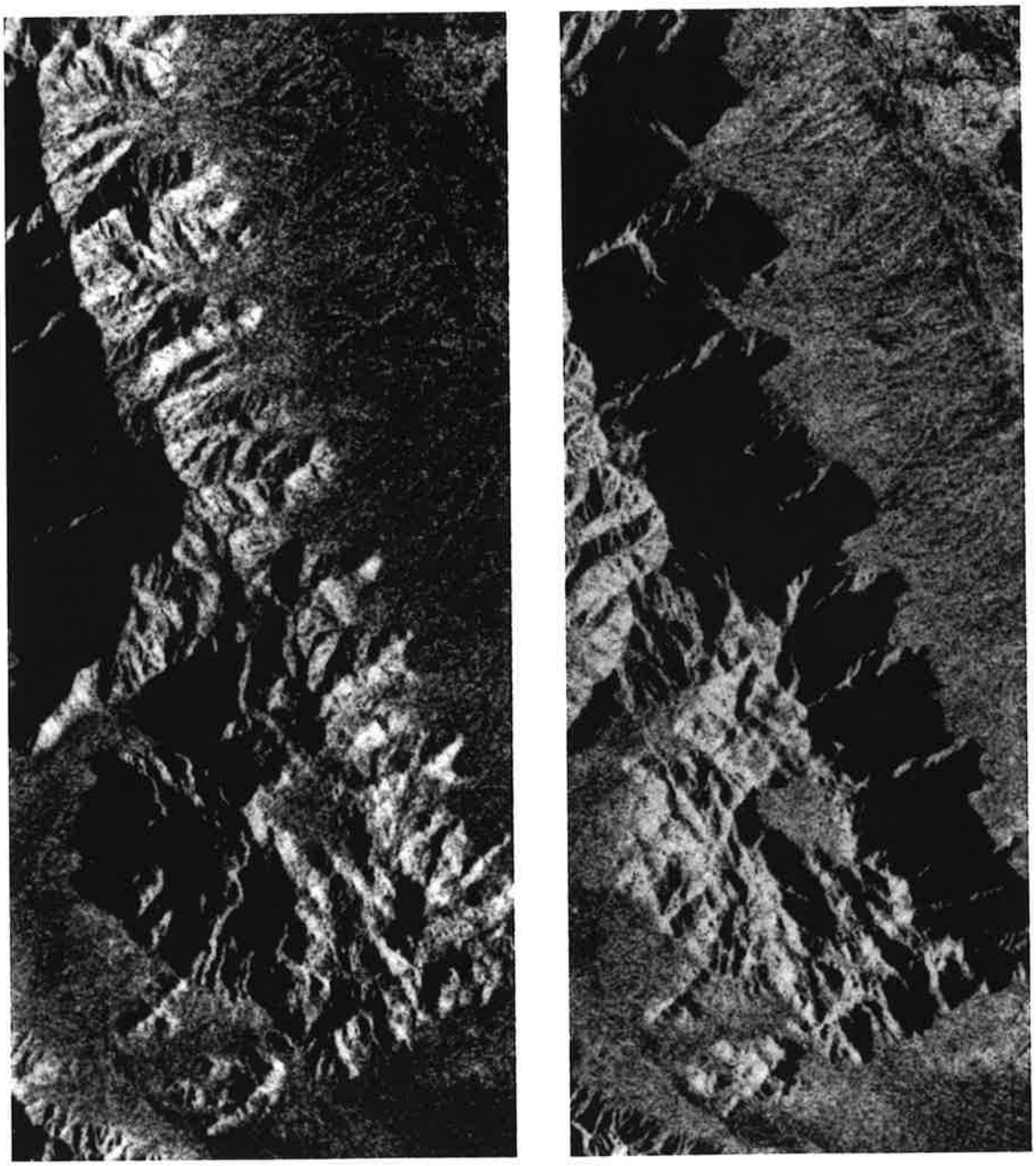

Figure 4-54. Example of opposite-side radar stereo imagery using the GEMS SAR over the Estrella Mts. in Arizona (compare Fig. 4-51).

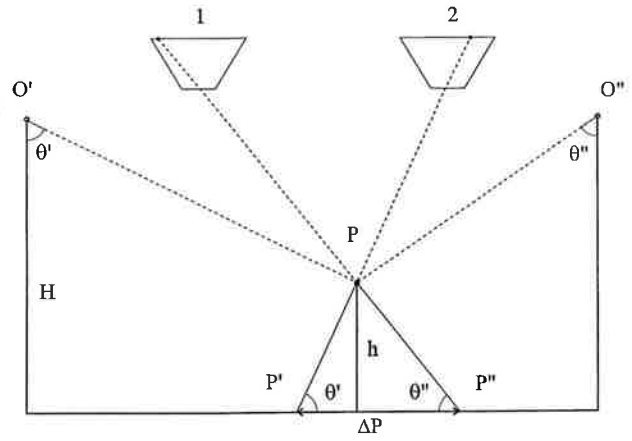

Figure 4-55 (above). Configuration for an opposite side radar stereo arrangement with definition of stereo parallax, and equivalent photographic camera arrangement. Note how relief displacements in the two images add up to a large parallax.

4-8.4 CROSSING ORBITS STEREO

One can also create stereopsis with radar images from crossing orbits. An example was produced by SIR-A (1981) over Kephalonia and Ithaka that has been thoroughly studied (Kobrick *et al.,* 1986). Figure 4-58 shows that shadows fall in different directions in the overlapping images, and that illumination directions are different. To view a stereo-model one has to set-up an image pair from cross-over orbits and remove the non-stereo parallaxes. Measurements of the elevation-induced stereo-parallax then need to be taken.

The opportunities from crossing orbit stereopsis are not apparent in the radargrammetric literature, except in reports by Domik (1985) and Kobrick *et al.* (1986). Domik (1985) demonstrated by image simulations based on digital elevation models, that orbit intersection angles within 40° or so will result in a valid visual stereo impression. Algorithmically, the rigorous stereo computation does not differ from that for other radar imaging geometries. Therefore stereo-mapping remains an issue of defining match-points in overlapping images.

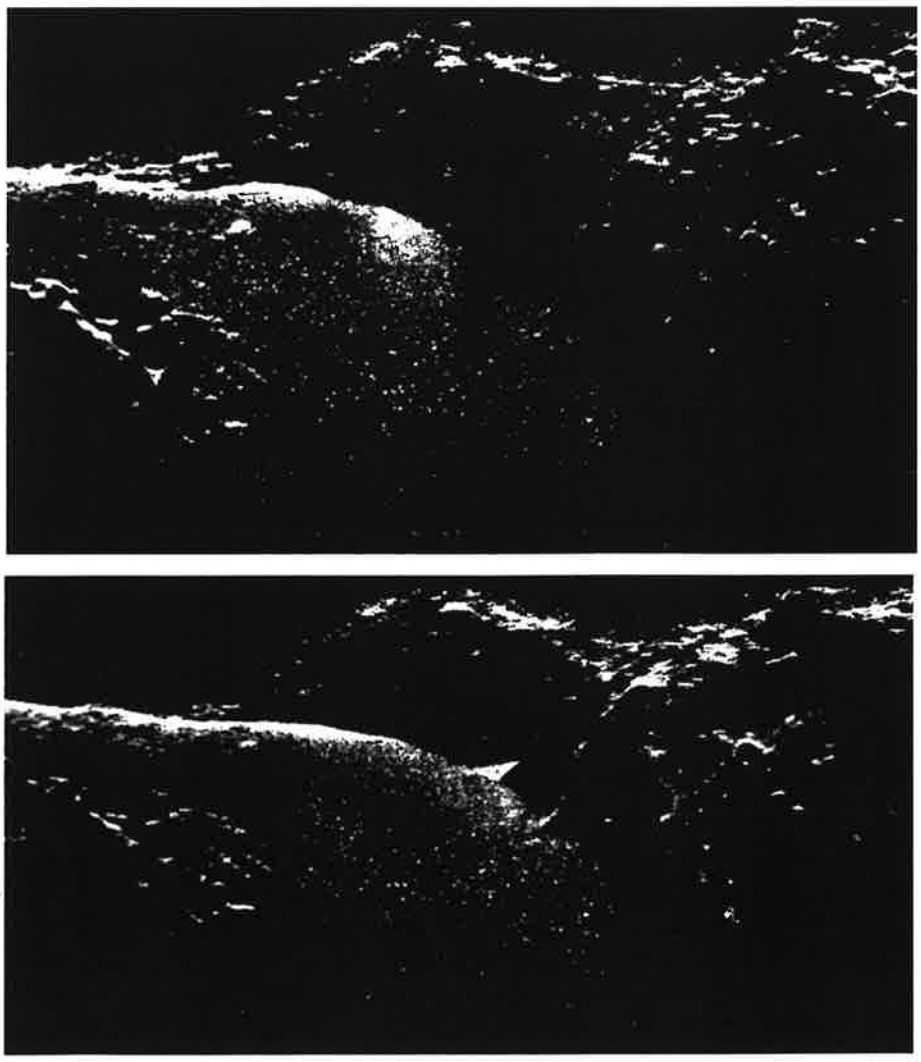

Figure 4-56 (left). Apennin Montes on the Moon, imaged from Apollo 17 by ALSE (1972) from an orbit at 116 km above the lunar surface. Intersection geometry is with about a 3° intersection angle. Area covered is 25 km wide. This can be viewed stereoscopically.

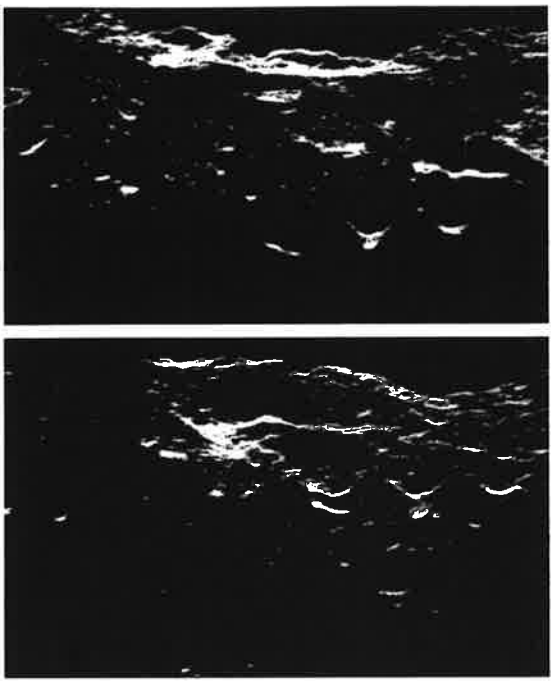

Figure 4-57 (above). Another lunar ALSE image pair, now with a larger intersection angle at twice that of Figure 4-56. This pair is not stereo viewable.

Each of two conjugate points in a stereo pair defines one circle in object space. At issue then is again the intersection point of these two circles. Whether opposite or same sides are examined, or crossing orbits are employed, there is a need to intersect two circles in space in a rigorous radargrammetric computation. Such computation models differ from simplified techniques which one may denote as "parallax models."

4-8.5 PARALLAX RADARGRAMMETRY

"Parallax photogrammetry" does not deal with 3-dimensional projection rays and a 3-D solution. Instead it deals with parallax differences which can be observed in the two overlapping image planes and it employs simplified geometric relationships to convert these parallax differences into elevation differences. For radar images this may be referred to as "parallax radargrammetry."

In this approximation each radar projection circle is replaced by a straight line to obtain rather simple equations that compute a point's elevation above a reference plane. Within a range of look angles, with small terrain elevation differences and at large flying heights, one may use simple parallax equations to compute height differences from observed stereo parallaxes much like in photogrammetry. LaPrade (1963) and Leonardo (1963) initially defined the underlying concepts, and Rydstrom (1968) developed some equations. These were further discussed by Leberl (1979a,b

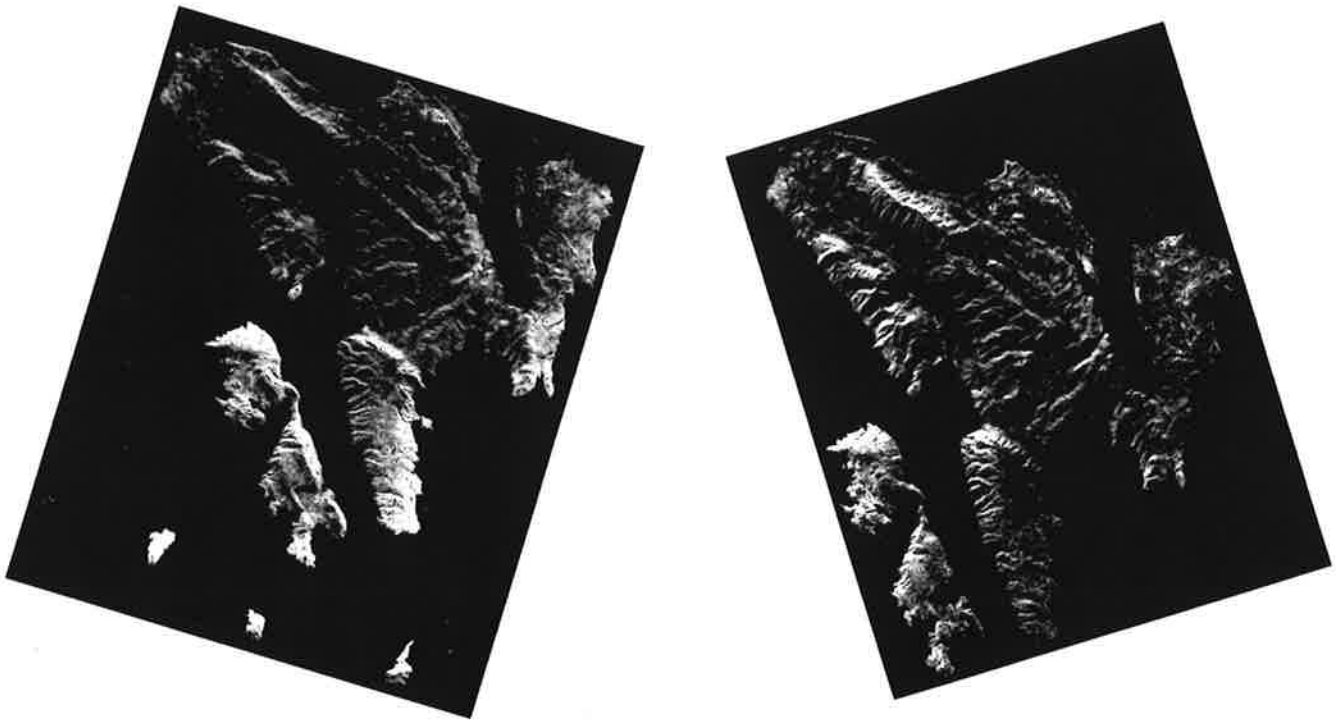

Figure 4-58 (a-left and b-right). Kephalonia and Ithaha, at a crossing angle of 34°, and look angles off nadir of about 50°, imaged from the Space Shuttle in the SIR-A experiment. To obtain a stereo impression, one must place the 2 images at the proper angle.

and 1990) and are summarized in Figure 4-59. The geometric relationships of these equations can be observed in Figure 4-60. Such equations convert the observed parallax differences between two pairs of image points into differences of terrain heights between the corresponding points on the terrain.

4-8.6 BASIC ERROR BOUNDS

Considerable literature exists on the potential accuracy of stereo radar measurements, beginning with Levine (1960), Rosenfield (1968), Gracie *et al.* (1970), Gracie and Sewell (1972), DBA-Systems (1974) and many others. An elaborate summary of the body of literature was presented by Leberl (1990) and identified three major sources of stereo-measurement errors. The basic limitation is the error of the measured radar slant range, σ_r. This causes the error of terrain height, σ_h to be:

$$\sigma_h^2 = \left\{ \frac{\left(\sin^2\theta' - \sin^2\theta''\right)}{\sin^2(\theta' - \theta'')} \right\} * \sigma_r^2 \qquad (4.6)$$

The error of slant range is presumably smaller than the slant range resolution. Figure 4-61 presents a sketch to explain Equation (4.6). Typical error budgets may be in the range of 2 to 5 times the error of slant range, or 1 to 2.5 times the slant range resolution if "resolution" is twice the "range error."

This first uncertainty of the surface definition due to range error is separate from the second uncertainty due to a mismatch of homologue image points, perhaps caused by illumination differences. Such a mismatch will create a false stereo parallax and therefore falsify the terrain elevation. A third category of uncertainty derives from errors of the sensor position and attitude. Clearly, if the antenna is displaced by a distance *dy* then a false stereo-parallax, *dp*, will be added to all points observed from that erroneous antenna position. This will cause a systematic elevation error *dh* in all those terrain points.

The algebraic expressions for the effects of a particular error of slant range, and of certain errors of the antenna's position and velocity vector, were presented by Leberl (1979 a,b; 1990) and are not repeated here. The underlying principle for this type of analysis is the change in the intersection of the two imaging circles (or their approximations by tangents) centered at the two sensor positions, as one of the positions changes differentially. Figure 4-62 sketches the concept, Figure 4-63 provides some simple algebraic relationships between an error of a terrain point and an error of sensor position.

The sensitivity of the stereo-reconstruction to an erroneous sensor position and velocity vector results in a stringent requirement to obtain accurate sensor positions. Aircraft locations are derived from GPS. Operational radar mapping requires this error to be kept to within a pixel. A somewhat more relaxed situation exists in satellite radar mapping due to the stability of satellite orbits. While this orbit also needs to be known rather accurately and to within a pixel, its error does not change rapidly. Instead, a satellite's position is predictable, and Earth-based laser tracking can keep such errors to less than ±1 meter. Unfortunately, laser

$$p_g' = h \cdot \cot\theta'$$
$$p_g'' = h \cdot \cot\theta''$$
$$dp = p_g'' \pm p_g' = dh\,(\cot\theta'' \pm \cot\theta')$$
$$dh = dp/(\cot\theta'' \pm \cot\theta')$$

Figure 4-59. Basic equations for "parallax radargrammetry," relating on observed parallax difference *dp* with an elevation difference *dh*.

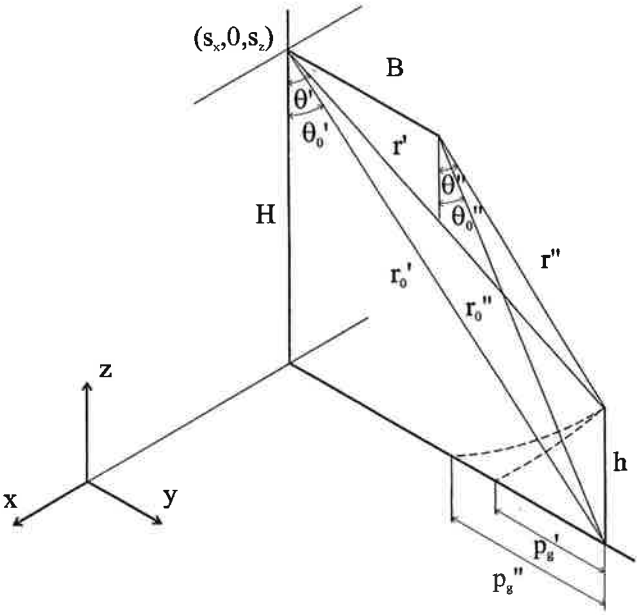

Figure 4-60. Geometric relationships for the equations in Figure 4-59. Note that the circular wavefront shown here is approximated by a tangent to arrive at Figure 4-59. This approximation is less valid as the look angle gets steeper.

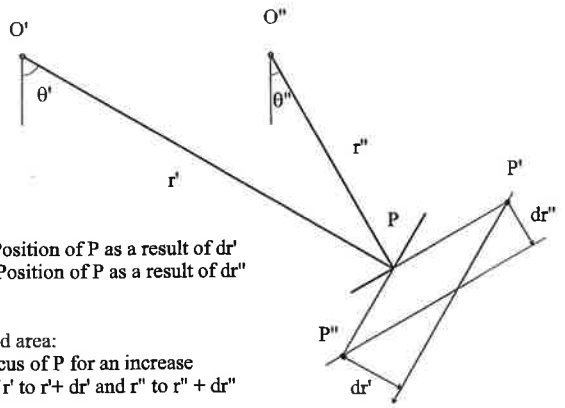

Figure 4-61. Graph to explain the terrain elevation uncertainty as a function of look angles and look angle disparity, caused by an error of slant range, in accordance with Equation (4.6).

tracking is not always used in satellite imaging missions. In those cases, the satellite's position and velocity vector must be refined with the help of ground control points.

4-8.7 VERTICAL EXAGGERATION

At times an image interpreter is interested in the ratio between dimensions in the *XY*-plane of a stereo model and in the vertical direction. This ratio is called the "vertical exaggeration." Terrain elevations commonly are rather small compared to the horizontal extensions of terrain. Therefore it is common to image terrain in such a manner that stereo-viewing will present the vertical dimension exaggerated 3 to 5 times over the horizontal dimensions (LaPrade *et al.,* 1980). A human observer will perceive elevation differences at a scale much greater than the scale of the *XY*-plane.

The concept is directly related to the "base-to-height ratio" and does not add new insights. As reviewed by Leberl (1990) a radar stereo model may well occur that has a larger exaggeration factor (base-to-height-ratio) than a traditional photographic stereo model. This will nearly always occur at very steep radar look angles. In ALSE on the Moon and at very small stereo intersection angles of only 6°, the vertical exaggeration was still found to be approximately 10 when common photographic values range between 3 to 5.

4-8.8 STEREO ACCURACY EXPERIENCES

As noted above the most elaborate body of work on radar stereo accuracies derives from the multiple image coverages obtained over a few sites during NASA's Space Shuttle SIR-B experiment. However, interest in assessing the feasibility of radar stereo mapping began earlier with the work sponsored by the US Army (Rosenfield, 1968; Gracie *et al.,* 1970; DBA-Systems, 1974; Hockeborn, 1971). This was followed by interest by the International Society for Photogrammetry and Remote Sensing and a Working Group with contributions from many authors including Dowideit (1977a,b), Derenyi (1975a,b), Leberl (1975c), Graham (1975b) and others, and directed by Konecny (1975).

The advantage of SIR-B over previous aircraft radar data was the range of look angles with which images had been obtained. SIR-B produced really the only data set so far that allows the study of large variations in the angles of stereo geometries. Other accuracy studies had to be based on singular stereo models, be that from aircraft radars or even recent European ERS images (Dowman *et al.,* 1994).

The SIR-B data set from Argentina, in particular, offers four images to form six different stereo models with various geometries (Leberl *et al.,* 1986c). Figure 4-64 presents the size of the terrain height errors from SIR-B data. The stereo images were set up with the help of ground control points since the satellite's ephemeris had not been tracked with lasers. Control points were taken from maps and aerial photography and were independently measured from SIR-B stereo radar. The rms differences in *X, Y* and height are presented for the various stereo cases in Argentina and along other segments of the SIR-B coverage. The actual results were found to be consistently poorer than what the theoretical best case could be just due to uncertainty in range errors.

Accuracy studies of practical relevance concern a commercial radargrammetric mapping service by Intera Technology Ltd. Calgary, Canada (addressed in Section 4-13). Using the 6-meter pixels from an aircraft flying at 8.5 km above sea level, stereo intersection geometries vary between 12° and 21°. The position of the sensor and the direction of the velocity vector are derived from GPS-observations. With this arrangement, Mercer et al.(1986a, 1989) reported absolute elevation mapping errors in the range of ±25 m.

Recent work on stereo mapping accuracies employs data from NASA's Magellan satellite and Europe's ERS. These are reported in separate Sections 4-10 and 4-11. Data from RADARSAT have been received and analyzed after this chapter was completed.

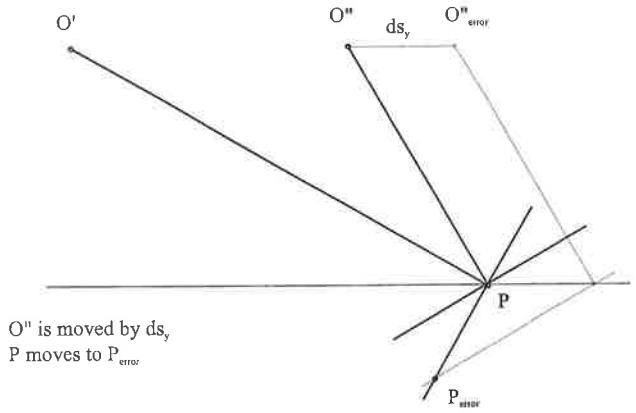

Figure 4-62. Sketch to explain a terrain elevation error caused by an error ds_y'' of the right radar position in a stereo configuration. Note that the correct position *P* will be falsified into P_{error}. Note also that in the text, ds_y'' is denoted as dY_0''.

$$dp_x = ds_x'/2 + ds_x''/2$$

$$dp_y = ds_y'/(1-\cot\theta'\cdot\tan\theta'') + ds_y''/(1+\cot\theta'\cdot\tan\theta'') + ds_z'/(\tan\theta''-\tan\theta') + ds_z''/(\tan\theta'-\tan\theta'')$$

$$dp_z = (ds_y'-ds_y'')/(\cot\theta''-\cot\theta') \; ds_z'/(1-\tan\theta'\cdot\cot\theta'') + ds_z''/(1-\cot\theta'\cdot\tan\theta'')$$

Figure 4-63. Some selected algebraic expressions explaining the effect of the three sensor position errors ds_X, ds_Y, ds_Z on the position of a terrain surface point P in a radar stereo model. Follow the idea in Figures 4-61 and 4-62 for a visualization of the error effects. Note that $ds_X=dX_0$, $ds_Y=dY_0$, $ds_Z=dZ_0$.

Area	Stereo Model Data Take	Look Angle Off-Nadir (°)	Intersection Angle (°)	Coordinate Errors (m) North	East	Height
Gordon la Graza	104/88	56/51	5	67	78	86
Argentina	88/72	51/43	8	78	70	110
	72/56	43/33	10	65	85	67
	104/72	56/43	13	77	73	65
	88/56	51/33	18	59	74	59
	104/156	56/33	23	62	49	62
Mt. Shasta,	37/55	57/51	6	106	106	125
California	55/87	51/28	23	44	75	53
	39/87	57/28	29	91	100	73
Illinois	49/97	28/-29	57	240	185	10
Jose de S.Martin	92/76	28/40	11	72	118	26
Argentina	56/72	30/41	11	76	155	42
Australia	68/86	33/?	?	46	49	25
	68/52	33/15	18	112	73	51
	54/52	51/15	36	88	83	74

Figure 4-64. Overview of SIR-B stereo accuracy results over Argentina and other areas. Note the look angles off-nadir and stereo intersection angles.

4-8.9 "BEST" STEREO RADAR INTERSECTION GEOMETRIES

The intersection geometry for radar stereopsis can be judged via visual inspection and a look at geometric accuracy. Current knowledge about visual stereo cues is based on image simulations by Domik (1985) and Thomas *et al.* (1986). These simulations lead one to conclude that look angles would be optimum in the range of 50° to 70° off-nadir and at an intersection angle of 25°. A similar conclusion was also obtained without simulations in an experimental comparison by LaPrade (1970, 1975b).

4-8.10 SQUINT-MODE SAR AND STEREO

A SAR imaging mode exists which offers some potential for stereo viewing and mapping, but which has not been studied, but for a sketchy hint at its potential (Bair and Carlson, 1974, 1975; Carlson, 1973; Kobrick *et al.,* 1986; Domik, 1985). This imaging mode is "squinting." Figure 4-65 is a simulation of a so-called "squint-mode" SAR image with a squint angle of 30°. "Squinting" is the mode in which a SAR illuminates the ground ahead (or behind) the position of the sensor, and obtains an image by having the signals processed with respect to a non-zero Doppler frequency. Squinting is a required element of every satellite SAR since it is used to compensate for the effect of the Earth's rotation. More generally, squinting is the tool used in SAR systems to have the real and synthetic antenna beam pointing in the same direction.

These squint angles could be helpful for terrain surface reconstruction and backscatter analysis when used in one of two procedures.

(a) Photometric Stereo

Assume that the object is imaged from one orbit. Figure 4-66a would be the result for a 45° squint in one image. If the squint-mode image were recorded in a straight forward manner, the result would be a "squished" image, like Figure 4-65b. It is trivial to remove the systematic sensor-induced (object-irrelevant) geometric distortion. Figure 4-66a shows the result of removing this systematic "squishing" effect due to squint. This rectified image is combined with a second non-squinted image in Figure 4-66a taken from the same azimuth as the first image. It turns out that the two images are geometrically identical to one another, pixel for pixel. The relief displacement is identical in the two images. Geometrically, the squinted image is identical to the unsquinted image taken from the same azimuth. What is different is the radiometry. The object has been illuminated from two different directions; therefore we could apply an analysis analogous

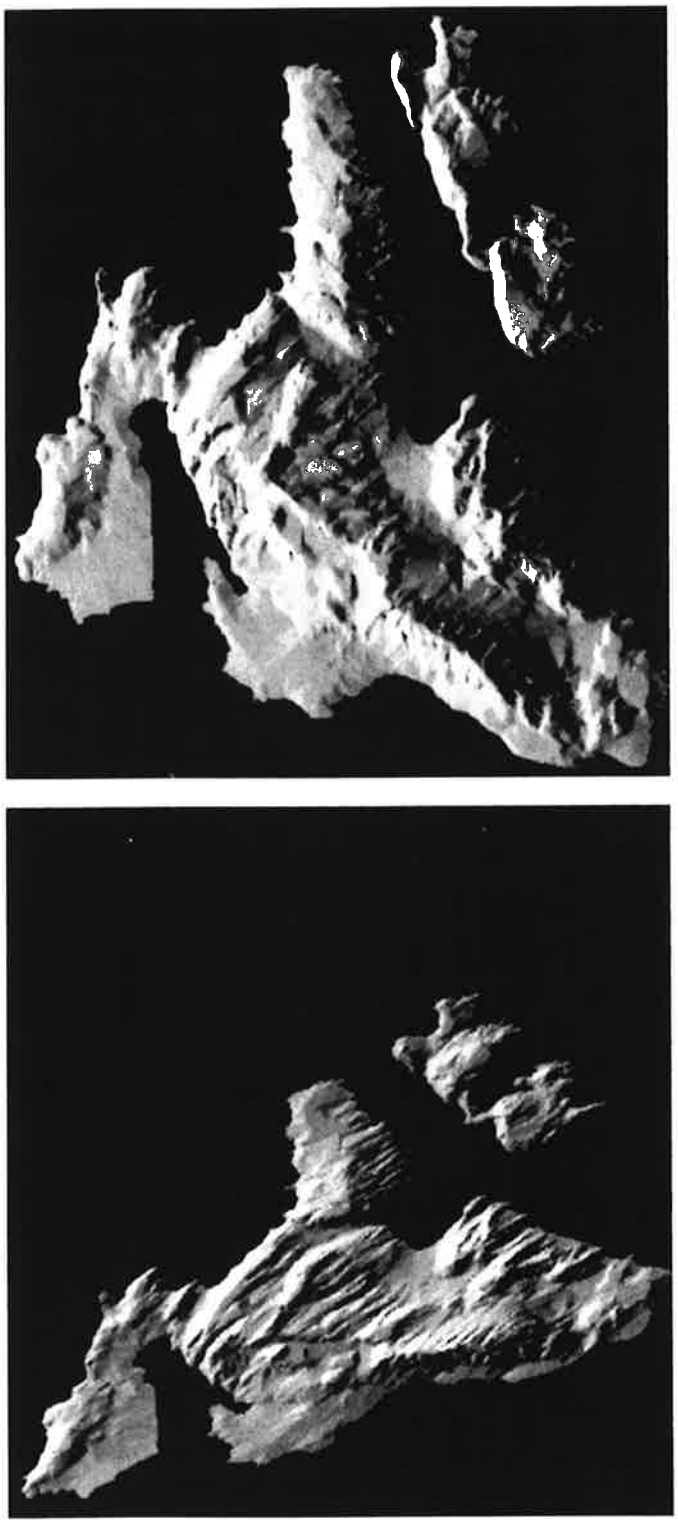

Figure 4-65. Simulated radar images with (a - top) zero squint angle, and (b - below) with squint angle at 30° (courtesy G. Domik).

to so-called "photometric stereo" (Horn, 1975, 1986). In this case illumination differences in two geometrically registered images and not the relief displacement is used for 3-D reconstruction.

(b) Squinting to Remove Illumination Differences from Overlapping Images

An inverse opportunity could also be developed with the help of squint mode imaging, *i.e.* the production of two images of differing geometry but identical illumination. Recall that stereo-radar suffers from the differences in illumination so that shadows fall differently and different areas are illuminated brightly. Using the squint mode one would have to fly one flight direction at a heading x and the other at x +45°. Actually these two images together would exhibit the exact same illumination geometry if one were using a squint angle t = 45°. However, the relief displacements would differ and could be exploited as a measure of terrain elevations without the notorious obstruction from illumination differences. Figures 4-66a and b are an example.

4-8.11 IMAGE MATCHING ACCURACY

Image matching accuracy is an important issue for image registration and stereo mapping. However, nearly the entire body of literature on the subject is based on optical imagery. Since stereo matching is a tedious operation it has long been considered a task to be automated. Numerous automation efforts have resulted, algorithms have been developed and experiences collected on automated stereo matching with optical imagery (see, for example, Förstner, 1992). It can be confidently stated that stereo matching with optical imagery is feasible by machine with errors in the range of ±0.3 pixels or better. Experienced stereo operators may match images consistently to within ±0.1 to ±0.2 pixels. The major limitation of automated matching of optical imagery are the so-called "gross errors" where matching may grossly fail, for example due to a lack of features on the object. Matching radar images has only recently become a topic of concern; it may suffer from radiometric differences, shadows, layovers and speckle effects.

(a) Matching Radar Images by Hand

At issue is the error of the radar parallax and the matching quality of two radar images. No impediment to matching radar images to a sub-pixel accuracy seems to exist in flat areas. One of a very few experiments has been reported by Mercer *et al.* (1986a). This was based on 5 human operators sitting at a conventional photogrammetric stereo plotter LEICA-KERN DSR-11 and observing a single pair of aircraft radar images. These test persons repeated measurements of stereo points around a flat section of terrain along the perimeter of a lake. The manual matching errors resulted in terrain height errors of ±3 pixels.

This type of terrain offers the promise of good results since no terrain slopes exist to produce the notorious effects of illumination differences. As soon as one goes to mountainous areas illumination differences produce confusion. It becomes increasingly difficult to maintain good accuracy in the parallax measurements. Unfortunately, it is within such areas that accurate results are most important.

There are no reports of tests assessing the true accuracy of image matching by hand. However, several reports provide a comparison between manual measurements taken by one operator at different times (Leberl *et al.,* 1994), and a comparison of this operator's results with those of an inexperienced stereo interpreter, as well as with a computer. Typically an experienced operator can repeat the matches of radar images to within ±0.6 pixels. An inexperienced person may differ from the matches of the experienced operator by as much as ±3 pixels rms (Leberl *et al.,* 1994).

(b) Matching Radar Images by Machine

Ramapryan *et al.* (1986) may have been the first to report on automatic radar image matching for stereo using SIR-B image pairs over Mt. Shasta (California). However the author's primary goal was not the accuracy of those matches; instead their interest was in parallel computing *i.e.* the use of a Massively Parallel Processing computer. Therefore the work produced only a few conclusions about the ability to automatically radar match images.

Only a limited effort was undertaken in the context of NASA's Magellan stereo experiment to obtain some range for the errors of machine matches (Leberl *et al.,* 1994). A series of image pairs from digitized aerial photography, SPOT, an aircraft radar sensor and Magellan were employed in a study matching an experienced human operator against a series of algorithms to find homologue points in overlapping images. Figure 4-67 presents a graphical summary of differences between the experienced operator (as the reference observation) and various customary matching algorithms. The study reported a root mean square difference between the human and the machine positions of match points in the range of ±2 pixels (Leberl *et al.,* 1994).

Note that the same study also considered SPOT images and digitized aerial photography. In those cases the differences were reduced to ±0.6 pixels.

4-9 RADAR SHAPE-FROM-SHADING

Shape-from-shading is an uncommon method of reconstructing the shape of an object using its illumination. It is related to "photometric stereo" where several photographs are taken with changing lighting. The method has its roots in the desire to detect the 3-D shape of industrial objects with diffusely reflecting surfaces using single images so that a robot can grab an object (Horn, 1970, 1986). In those applications one may assume that the reflective properties of the objects are well-known.

The application of this concept to radar images has not been studied widely, probably due to concerns that it may be an ill-posed problem. Figure 4-68 is a pair of airborne radar images. These were used in a shape-from-shading algorithm to define a terrain surface that is consistent with the imaging gray values (Thomas *et al.,* 1990). Skepticism is caused by the sensitivity of "shading" to reflective properties of a surface. They are usually unknown and introduce considerable ambiguity.

Several techniques exist for shape-from-shading. Originally it was used for planetary geology and denoted by "photoclinometry" (Rindfleisch, 1966; Wildey, 1975). Wildey (1986a,b) then applied it to radar images. The approach assumes heights along

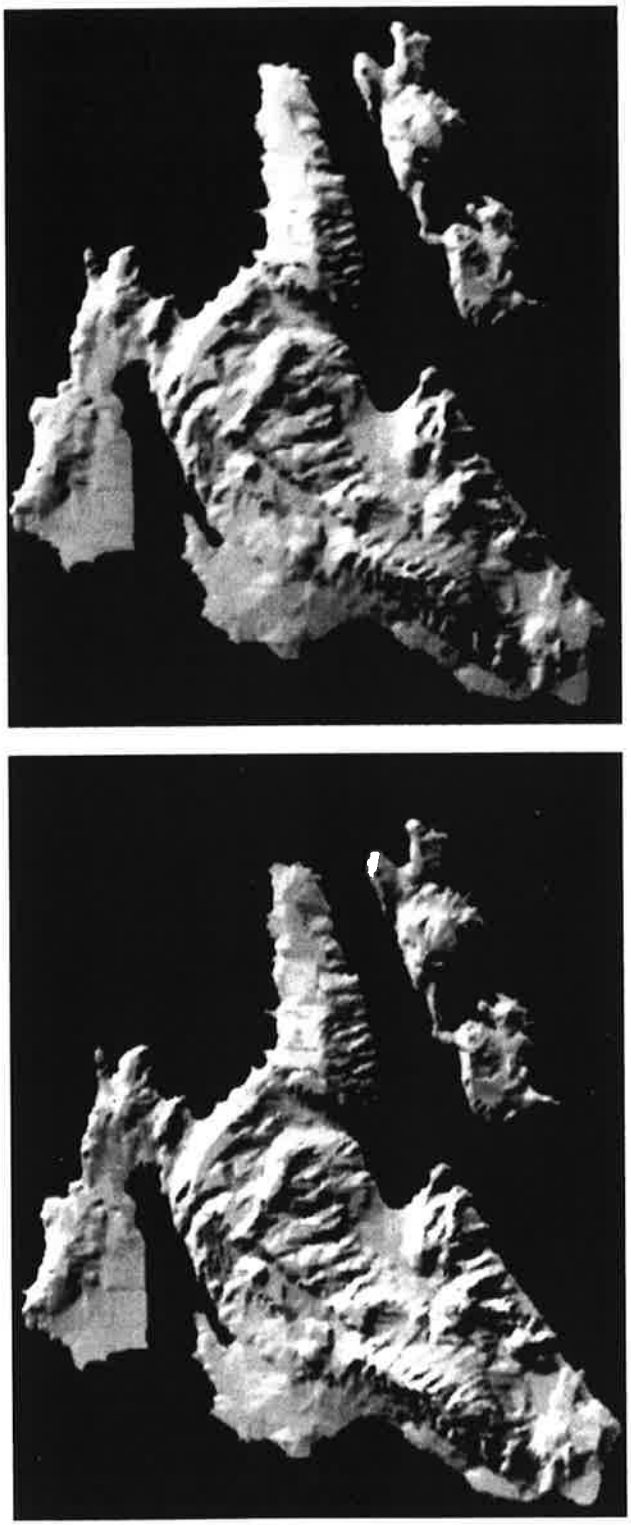

Figure 4-66. Comparing the squint-mode image with the undeformed (zero-Doppler) image. (a - top) Squint is 45° but rectified (from Figure 4.65(b)); (b - bottom) Zero-squint image at 45° rotated flight direction, to produce the same illumination as (a), but at a different geometry due to different azimuth. This image pair offers identical radiometry, but different geometry for stereo (courtesy G. Domik).

the edge of the imaged area and then sequentially assigns slopes to each image pixel at the inside of the area. By sequentially profiling and looking at all pixels of the image a DEM is built by converting slopes to elevation differences. This is based on enforcing continuity with previously obtained height values. Wildey's (1986a,b) demonstrations concerned a single image. Previous work on "photoclinometry" also was applied to measure the depth of planetary craters from single photographs.

Earlier work on planetary features also stimulated the method implemented by Kirk (1984, 1987). This was later applied to the image mosaics obtained from Magellan (Kirk *et al.*, 1992), and helped refine the low-frequency topography obtained from Magellan altimetry.

The most widely used shape-from-shading technique in industrial inspection has been discussed by Horn (1986). The same technique has been "ported" to radar images by Frankot and Chellappa (1987, 1989). In that case, an iterative approach compared actual with simulated gray values using the current DEM knowledge. Differences between the gray value extracted from the real image and the gray values predicted from a given DEM were used to improve the estimation of the terrain's heights and slopes. This method was further generalized by Thomas *et al.* (1990) to employ multiple radar images and to create Figure 4-69. Five to 25 iterations may be necessary to create such a shape-from-shading result. Zheng (1992) also combined stereopsis with shape-from-shading, employing SIR-B SAR images of Mt. Shasta.

It is important to limit the use of this technique with radar images of natural surfaces since one cannot make the assumption that the reflective properties of the terrain are known. Therefore recent proposals suggest the employment of shape-from-shading as a refinement for a DEM after other techniques have measured lower frequency relief (Frankot *et al.*, 1994). For example, one could introduce an existing DEM, or data from an altimeter could be introduced to create a "rough" DEM; then the radar images will refine that DEM through a shape-from-shading algorithm. Frankot and Chellappa (1989) demonstrated the use of this approach, and Thomas *et al.* (1990) expanded it to multiple images and to the use as a refinement of a stereo-derived DEM.

The mathematical tools for multiple image shape-from-shading are fairly complex and have been reported by Thomas *et al.* (1990a). Integration of slope values obtained from the image gray values must result in a continuous surface. The elevation postings of a stereo-derived DEM also need to be maintained to within a certain accuracy. However, an intuitive description of the method can be based on the idea that a radar image is simulated using the known elevation values of the DEM. If such values are not known then the terrain must be assumed to be flat in the first iteration. The simulated and real gray values will be identical if:

- the DEM had the correct slopes, and
- the radiometric properties of the terrain cover correspond to those seen in SAR images.

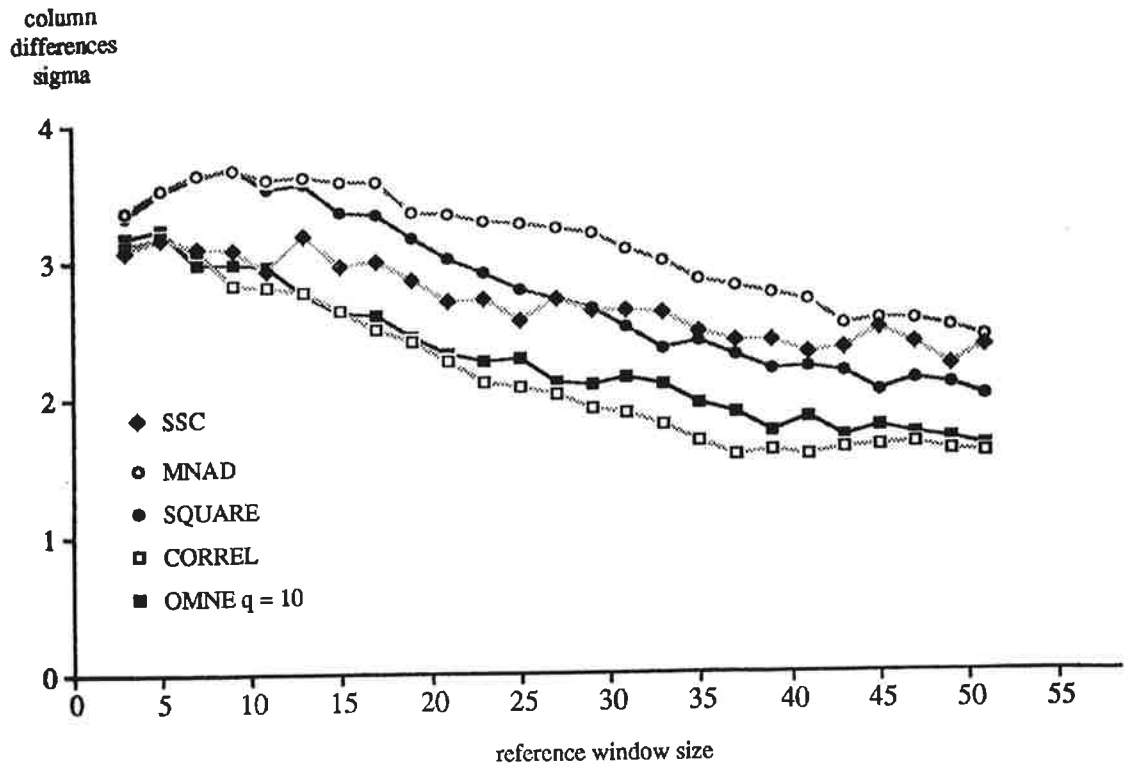

Figure 4-67. Diagram with r.m.s. differences in coordinates of match points found by hand versus found by machine (ordinate = pixels). The machine algorithms varied the size of the matching window from 5 to 50 pixels. The 5 curves each represent a different matching method, each compared to manual matching. The errors are at ±3.5 pixels with small match windows and reduce as the windows grow (for details see Leberl *et al.*, 1994).

Figure 4-68. Input radar image pair (a - top left), (b - above) and stereo derived DEM (c - left) to serve for shape-from-shading. Area covers 3 km x 3 km. STAR-1 SAR operated by Intera Technologies Inc., at 3 cm wavelength.

If these conditions are not satisfied, then one will note gray value differences *dg* between the one (or several) actual and one (or several) simulated gray values.

Values *dg* lead one to modify the slope estimates at each image pixel. Then the slope values need to be converted to height differences and to heights. To enforce continuity and integrability of the resulting surface one may merge the old and new slope values in the spectral domain. A refined DEM is obtained and a new iteration may begin.

Shape-from-shading has not evolved into an accepted tool for the automated analysis of radar images. Yet it is common practice for image interpreters to employ the topographic expression of terrain in radar images and to intuitively practice radarclinometric visual analyses. The major objection to shape-from-shading is the ambiguity from uncertain backscatter properties. This is reduced if use is made of multiple images at different incident angles. However, use of multiple images requires that they be co-registered. Yet co-registration is only feasible if terrain shape is already known.

Therefore successful shape-from-shading is closely linked to a solution of the problem of matching dissimilar radar images, for example those from ascending and descending orbits.

4-10 RADARGRAMMETRY FOR MAGELLAN

The prospect of sending a radar imaging sensor to map the entire surface of the planet Venus stimulated work in radargrammetry, beginning with the analysis of the lunar ALSE data from 1972. The Venus mission was conceptualized in 1969 (Friedman and Rose, 1973) and a satellite went into orbit around the planet in 1990. Previously, surface images were obtained from Earth using the radio-astronomy facilities in Arecibo and Goldstone (Goldstein, 1965). These images have a geometric resolution of 2 to 4 km. Surface images were also obtained from the Soviet Venera 15 and 16 satellites using orbital radar at a geometric resolution of about 1 to 2 km. Additional radar observations were made in NASA's Pioneer Venus mission in 1979 (Pettengill *et al.*, 1980a,b). NASA's Magellan project represents the culmination of

this series of exploration by achieving a near-complete coverage of the planet's surface at a pixel size of 75 m. Table 4-1 summarizes the mission's major parameters.

Magellan produced a large data base of images, consisting of about 5200 imaging orbits covering the planet's surface in three separate cycles. The radar images are complemented by radiometry and altimetry observations (*Science,* 1991; *Journal of Geophysical Research,* 1992). Each radar image swath consists of about 100 MB of image data with a swath width of 300 pixels and a swath length of up to 220,000 pixels, each pixel with a side length of 75 m. The data set provides numerous challenges: 1) to co-register multiple coverages; 2) to extract topographic relief; and 3) to manage a large image data repository. However, the data set has not reached much beyond the small community of planetary scientists. This is in stark contrast to the European remote sensing satellites ERS where a much larger exposure of the mission's data has occurred (see Section 4-11).

4-10.1 SHAPE MEASUREMENT FROM MAGELLAN IMAGES

Options for extracting 3-dimensional object shape from radar images generally include the following:

1) Stereopsis and stereo measurements on pixel arrays.
2) Shape-from-shading or clinometry as used in planetary science, for example on the Moon with images from the 1964 NASA-mission "Ranger."
3) Shadows as a measure of height differences between ground points.
4) Exploitation of the assumed symmetry of 3-dimensional objects such as volcanoes, craters etc.
5) Interferometry as used in radio astronomy incorporating two Earth antennas to look at a planet's surface, and as used with images taken with one antenna from two slightly different orbits.
6) A variant of photometric stereo with two (or more?) radar images at identical geometries, but with different illumination (see the discussion of squinted mode imaging).
7) Various combinations of methods are possibly useful as well. One such combination is stereopsis and shape-from-shading.

The nominal Magellan-mission was planned to create one coverage of the planet's surface with overlaps among images just occurring at higher latitudes, and at practically identical incident angles from an elliptical orbit. As the spacecraft survived one complete imaging cycle a second coverage was acquired with opposite side geometry (Cycle II) and finally a third Cycle resulted in a same-side coverage which combined with the nominal Cycle I data into a stereo-capable data set. Nearly all of the various shape-reconstruction methods listed above have been investigated and tried on Magellan radar images *(Science,* 1991; *Journal of Geophysical Research,* 1992).

4-10.2 STEREOPSIS FROM MAGELLAN IMAGES

The nominal Magellan-mission resulted in overlapping images with intersection angles in the range of 0.5° to 1.5° and at variable look angles of 15° to 45° off-nadir (Figure 4-70). Range resolution, at about 60 m, was also modest, so that stereoscopic height errors were unuseably large. For example, Magellan imagery of the Venus-equator produces a parallax-to-height conversion factor of 57 so that a one pixel parallax error would be magnified into 57 pixels of height error.

At the North-pole, Magellan produced crossing flight lines. The area with a useful intersection angle was only about 20 km x 20 km. However, in that area, the magnifying factor for parallax to height error was only reduced to about 13 (Leberl *et al.,* 1992c).

The extended mission's second image coverage in Cycle II was produced at a different incident angle, held nearly constant at about 25°, but from an opposite illumination direction (East-looking). To this day there has been no capability developed to combine the opposite side data from Cycle II with other Magellan images from Cycles I or III into a co-registered data set.

However, during a one-day experiment which interrupted the orderly data collection process of Cycle II, a same-side data set was created which, combined with the initial Cycle I, produced stereo viewable data. The analysis of this data set persuaded the Mission's management to dedicate a third data collection Cycle to a same-side stereo effort (Figures 4-70 and 4-71). The intersection angle disparities were in the range of 5° to 25°, resulting in elevation accuracies within ±2 or ±3 pixels or ±150 m to ±200 m (Leberl *et al.,* 1992a). The small intersection angles combined with very steep look angles of 7° to 12° that supported a good equivalent base-to-height ratio, vertical exaggeration and vertical accuracy.

The initial stereo technology employed for this data set was based on manual measurements of grid points and of terrain break lines in a fully digital softcopy environment. Mathematical modeling was identical to the processes employed in earlier satellite efforts such as SIR-B, but limited itself to simplified parallax-to-height conversion methods. A rigorous radargrammetric effort was not implemented in the belief that this presupposed a refined satellite ephemeris. Typically the nominal ephemeris available during the mission had errors in the range of ±1 km or more, with largest errors possibly as large as 15 km.

The decision to dedicate a full imaging cycle to the collection of stereo data resulted in an effort to augment the then-existing stereo-analysis capability by:

1) automated image matching;
2) refined mathematical modeling for rigorous radargrammetry and,
3) a refinement of the ephemeris data.

Some of this capability has been implemented in the form of a so-called Magellan Stereo Tool kit for use by Magellan scientists (Leberl, 1993b). Full utility of this capability will only be feasible after a precision ephemeris has been computed from the

Table 4-1
Essential Data about NASA's Magellan Mission to Map Planet Venus by Means of Imaging Radar*

Mission	**Date**
Date of Launch from Kennedy Space Center, Florida	4 May 1989
Date of Venus orbit insertion	10 August 1990
Beginning of systematic radar imaging	15 September 1990
Completion of initial coverage (all 360°, Cycle 1)	15 May 1991
Completion of second coverage (Cycle 2)	14 January 1992
Orbit inclination	85°
Spacecraft altitude above surface at periapsis	294 km
Spacecraft altitude above surface at apoapsis	8458 km
Radar Imaging:	
Width of radar image strip (and angular width of beam)	20 km (2.5°)
Length of radar image strip	17,000 km
Radar image pixel size	75 m x 75 m
Radar image range resolution	88 m (0.59 μsec)
Radar image azimuth resolution at 5 to 17 looks per pixel	120 m
Spacecraft altitude above surface at beginning of strip	2,225 km
Geographic latitude at beginning of each radar image	90° North
Look angle off-nadir at beginning of each radar image	11°
Geogrpahic latitude at periapsis	9.9° North
Maximum look angle off-nadir (at periapsis)	43°
Radar wavelength	12.6 cm
Angular width of image at antenna, at periapsis and 80° N	2° and 0.5°
Radar image overlaps at 80° North	18 km
Radar image stereo intersection angles at 80° North	0.1°
Altimetry:	
Footprint varies with S/C altitude from	10 x 12 km^2 to 20 x 29 km^2
Spacing of footprints along orbit	8 km, more at Pole
Error of altimetric elevations, exclusive of orbit errors	> 5 m
Passive Radiometry:	
Footprint varies with S/C altitude from	16 x 24 km^2 to 83 x 87 km^2
Sampling interval	5 km by Swath Width
Previous Imaging Data of the Surface of Planet Venus:	
Pioneer Venus	***1978-1981***
Radiometry at Resolution of	200 to 800 km
Altimetry with spacing measurements (along by across)	120 km x 150 km
Radar reflectivity measurements (radar imaging)	30 km pixels, 8 pixels/swath
Radar look angle off-nadir at periapsis	15° to 65°
Wavelength	17 cm
Venera 15 and 16:	***1983-1984***
Radar imaging with pixel size	0.8 km
Range resolution	1.5 km
Wavelength	8 cm
Radar look angle off-nadir	10°
Earth Based radar imaging (near 0° incident angle)	***Since 1964***
Wavelength	12.6 cm
Arecibo antenna, Puerto Rico	1-2 km
Goldstone (California) and other antennas	2-3 km

* From Leberl *et al.*, 1991b

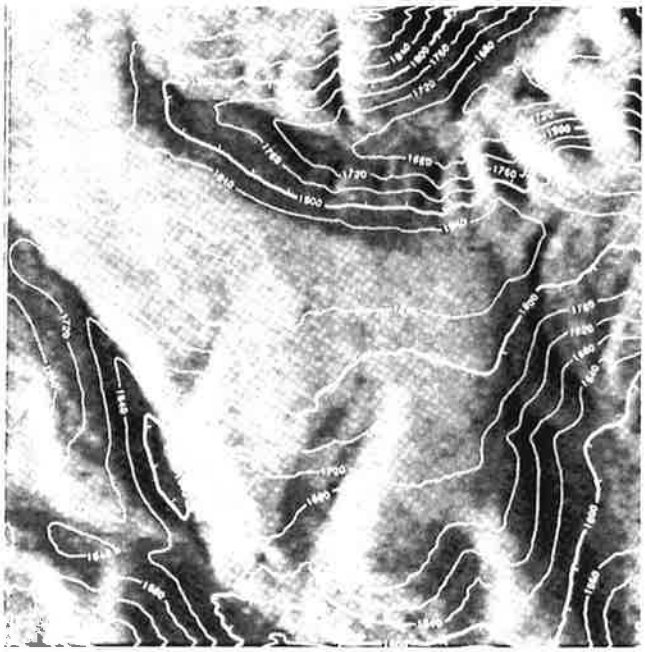

Figure 4-69. Surface shape, presented as an illuminated DEM, derived by stereo and by shape-from-shading from data in Figure 4-68, with superimposed contour lines. Note the "ringing" effects at the edge of the data set (see also Thomas *et al.*, 1991).

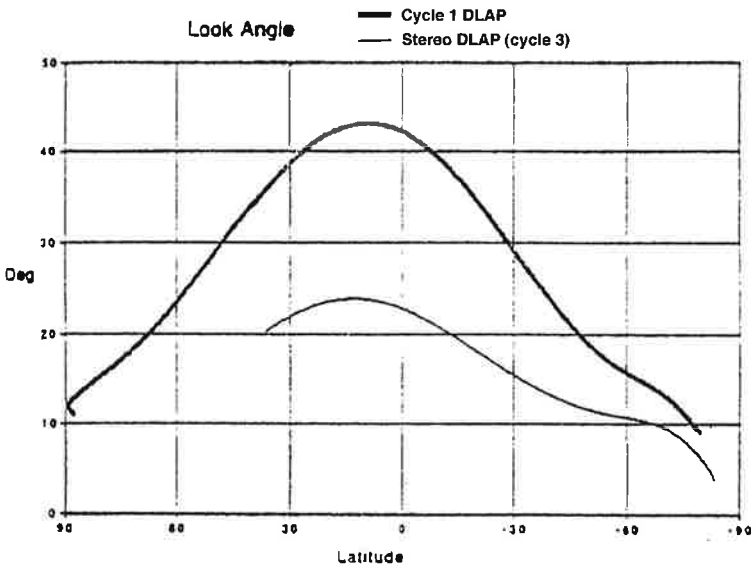

Figure 4-70. Imaging geometry for the initial Magellan coverage of planet Venus as a heavy line. The look angles off-nadir change along the orbit since the spacecraft is in an elliptical orbit, imaging steeply at 10° near the pole at 90° latitude from 2000 km altitude, and at shallower look angles near periapsis at 10° latitude (300 km altitude). At a northern latitude of 80° overlapping images would have intersection geometries with 0.5°. Then in Cycle III, a new Designed Look Angle Profile DLAP was used as shown as a thin line.

conventional satellite navigation data, but supplemented by landmarks on the planet's surface. Some evidence exists that the ephemeris accuracy will be improved from ±1 km to within ±30 m, as reported by Chodas (1993).

4-10.3 SHAPE-FROM-SHADING WITH MAGELLAN IMAGES

Shape-from-shading produces a slope and elevation estimate at every pixel. As was pointed out earlier the method produces good estimates of micro-relief, but is inaccurate in producing low frequency elevation data. The major limitation is ambiguity due to backscatter properties. In the absence of independent knowledge about backscatter, a generic model must be employed. Multiple image coverage can be helpful in minimizing the effect of this simplifying assumption. However, multiple images would have to be registered to within a pixel so that multiple gray values can be accessed at each pixel. To accomplish this registration the Shape-from-Shading process must be preceded by a stereoscopic analysis so that an estimate of low frequency terrain forms is obtained, and multiple images can be co-registered by means of stereopsis.

The initial Magellan imaging Cycle I produced only single images, or multiple images with entirely redundant coverage at nearly identical look angles. The only applicable shape-reconstruction method is therefore single image Shape-from-Shading (Figure 4-73). Ideally, the low-frequency information about elevation can be obtained by Magellan's radar altimetry. This was the process used in the 3D-shape-reconstructions published by Kirk *et al.* (1992).

Shape-from-Shading was also used to improve the terrain elevations obtained from stereoscopy (Figures 4-74, 4-75). In this case Shape-from-Shading serves as an interpolator in-between the DEM postings obtained from stereo (Frankot *et al.* 1994). It appears that the accuracy, in a relative sense, is of the order of the geometric ground resolution, *e.g.*, ±120 m for Magellan within small areas. Globally, the accuracy is that which derives from stereo-measurements or from altimetry.

4-10.3 SINGLE IMAGE "STEREO" OPPORTUNITIES

Interpretation of single images may employ a single radar image of a symmetric feature, conceptually "cut it in half" and deal with it as if the single symmetric feature resulted in two images taken from opposing view points. As a result one can now apply stereo-type geometric reasoning to reconstruct the third dimension from a single input image. This approach was proposed by Elachi (1990) and used in a study by Ford *et al.* (1993). An analysis of this idea with Magellan SAR images was also presented by Leberl *et al.* (1991b). Figure 4-76 describes the geometry and algebra to compute the terrain elevation. Applied to the image in Figure 4-77a it reveals that a crater's depth observed from altimetry is not 450 m, but instead is 1500 m (Figure 4-77c,d).

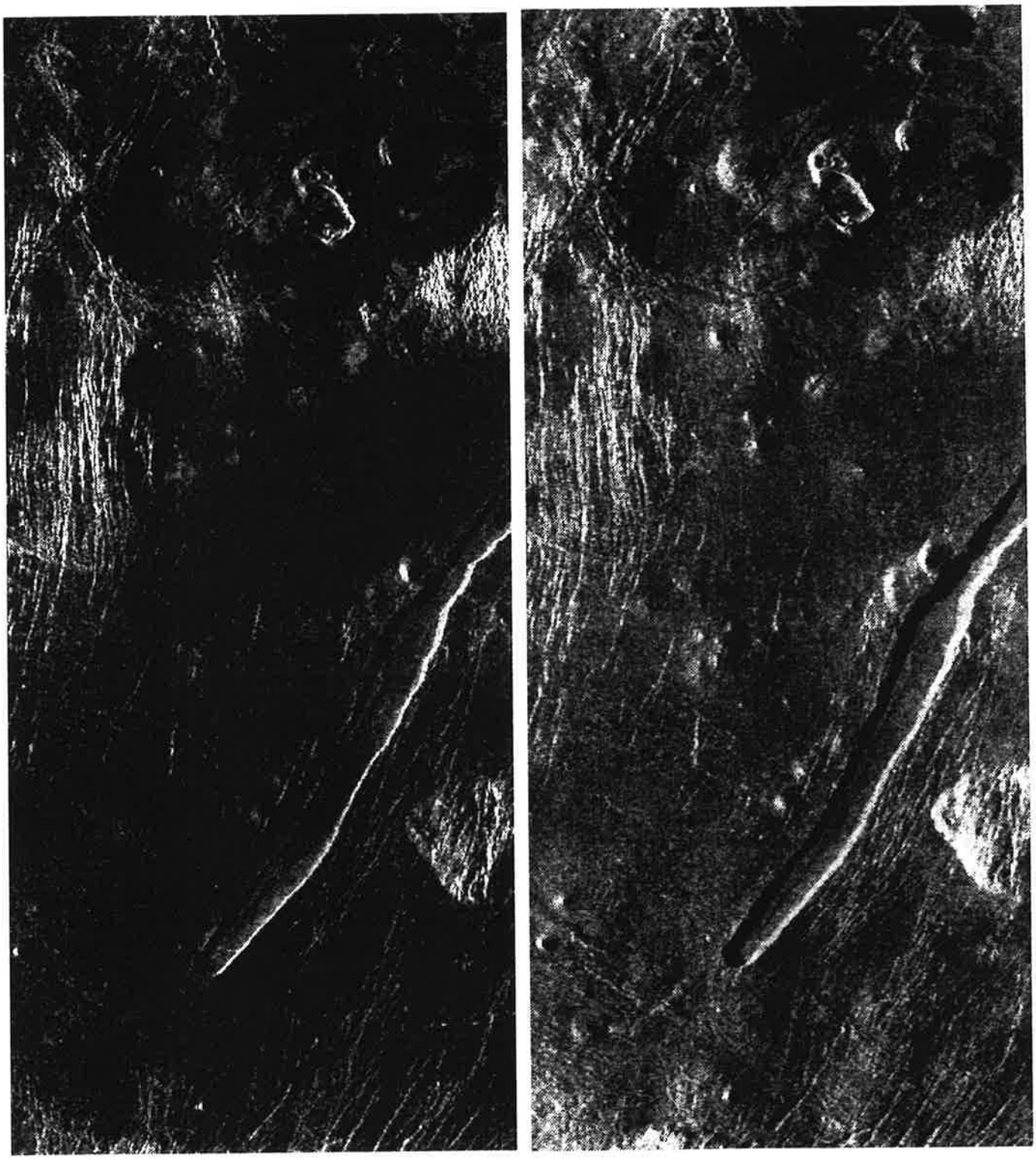

Figure 4-71. Magellan stereo image coverage of an area 59° degrees South. The area covered is 130 km x 50 km. Look angles are 15° and 11° off-nadir.

Figure 4-72. Perspective visualization of a DEM generated by stereo process from the images in Figure 4-71, and draping the images over the DEM.

4-10.4 MAGELLAN INTERFEROMETRY

Interferometry is based on measurements of the phase of reflected radiation at two antennas close enough together to receive coherent echoes. In the case of Magellan very little opportunity exists for interferometry, except where the orbits cross. This concept, "crossing orbit interferometry," has been discussed by Gabriel and Goldstein (1988). This requirement is met at the pole, and also in numerous other locations where images were taken in Cycles I, II and III at orbit crossings.

So far interferometric fringes have not been detected easily from Magellan radar images. Figure 4-78 is an example presented by Goldstein (1992) in an informal manner from an area around the North pole.

4-11 EUROPE'S ERS MISSION AND RADARGRAMMETRIC IMAGE PROCESSING

A dramatic increase in interest in geometric processing of radar images has been generated by the launch of the C-band radar on the European ERS-1 satellite in the summer of 1991 (Duchossois, 1986; ERS-1, 1992). National members of the European Space Agency have implemented near-operational facilities to produce geometrically corrected (geocoded) radar images. These Processing and Archiving Facilities (PAFs) are described in a collection of papers edited by Schreier (1993). Geometric processing is supported by an interest in correcting the image geometry not only for the range geometry of radar data, but also for terrain effects. These so-called terrain-corrected images result in residual errors of perhaps only ±1 pixel at 12.5 m per pixel (Dowman *et al.*, 1992).

ERS differs from previous radar sensing projects through the well-known satellite ephemeris which is tracked by means of Earth-based laser distance measurements. The orbit positions of the radar are known to within ±1 m. The only remaining image errors result from along-track timing problems and from residual errors of pixel dimensions (cross-track scale problem). These errors must be detected and removed via the use of ground control points in a calibration step (Raggam, 1994).

Co-registration of overlapping ERS-1 images to prepare for multi-temporal analyses has become a fairly straight forward image processing step (GeoSAR, 1994; ERS-1, 1992; 1994). Same side images are often taken with an orbit spacing of only 1 km. As a result the image geometry is identical and registration merely consists of a translation of one image with respect to another, with geometric disparities in the sub-pixel range.

ERS-1 has been employed to study stereopsis (Dowman *et al.*, 1994; Raggam, 1994; Kaufmann *et al.*, 1994). While overlapping images normally do not have significant look angle disparities, they are large enough to combine with the steep look angles

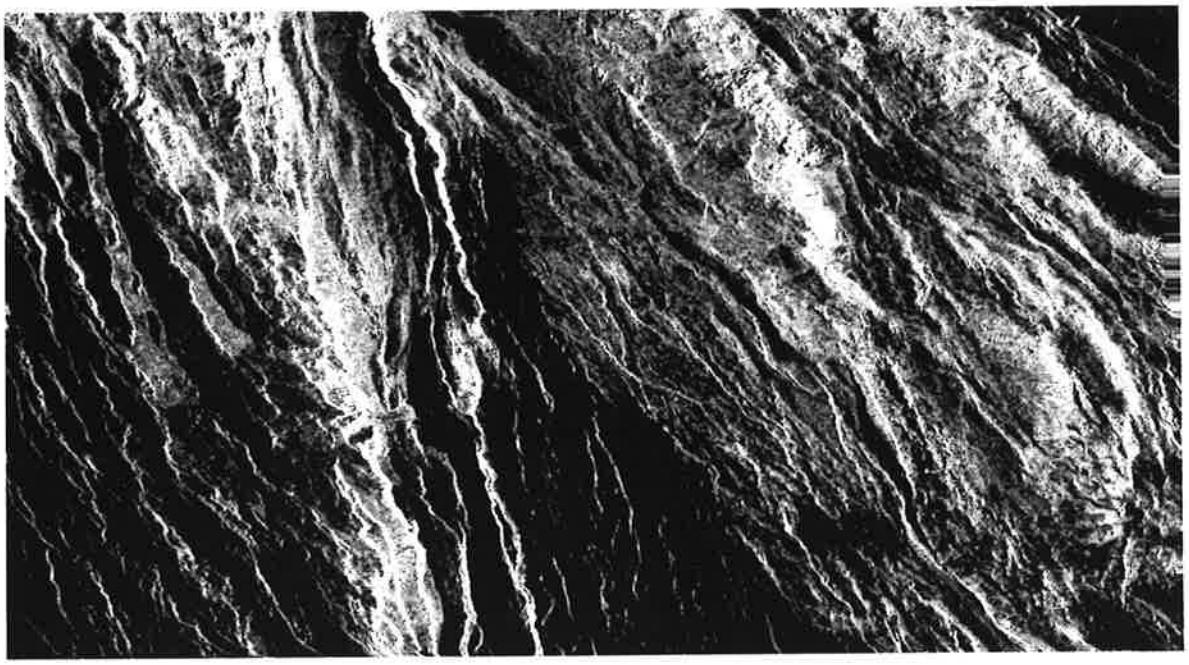

Figure 4-73a. Image from Magellan.

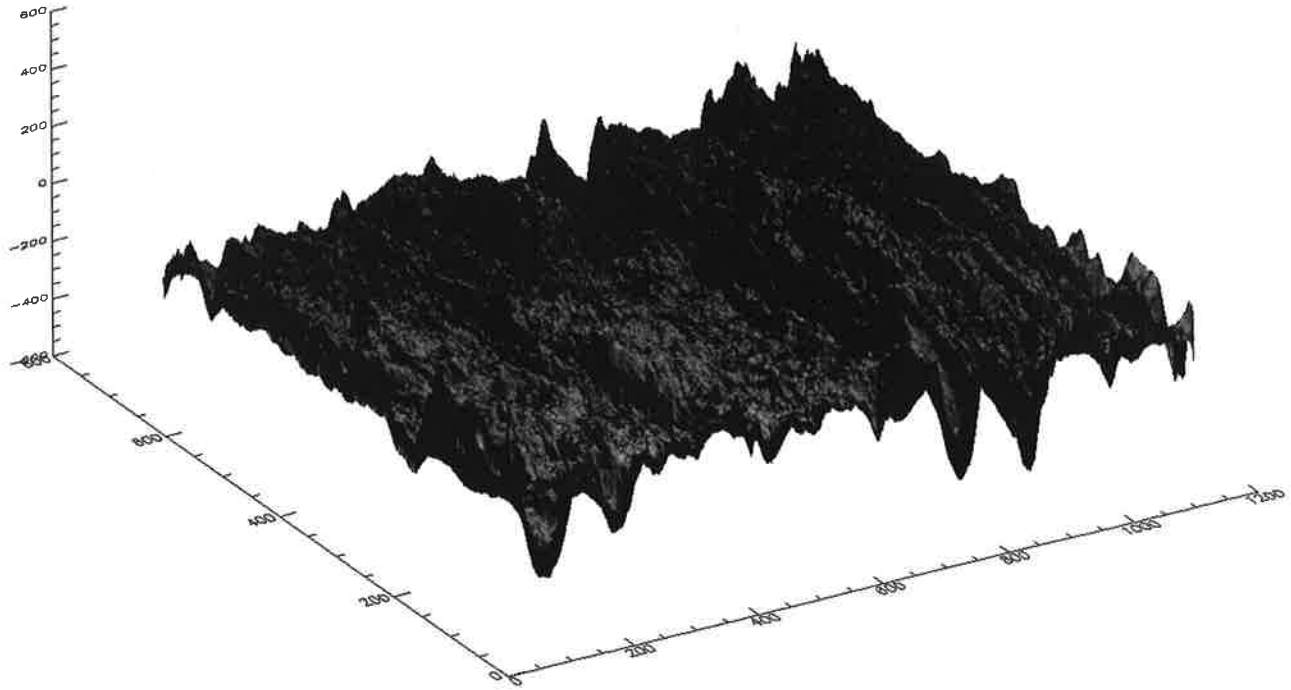

Figure 4-73b. Terrain shape estimated by shape from shading alone (from image 4-73a). The result provides great detail but is uncertain in the low frequencies of the elevation map. The coordinate axes show pixels (horizontal) and meters (vertical).

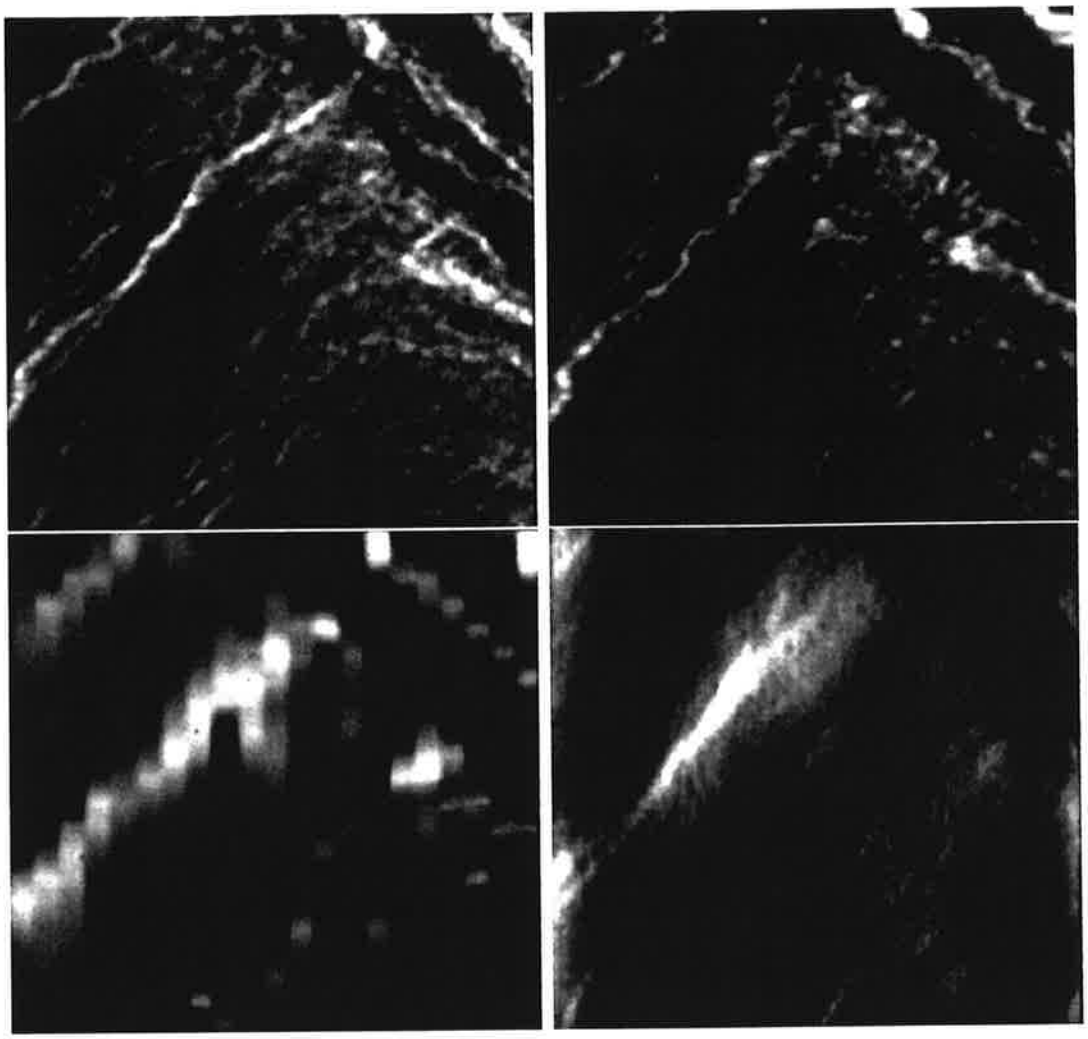

Figure 4-74. Image patches (a, top left), (b, top right) from two of Magellan's imaging cycles. (c, lower left) is the stereo result, (d, lower right) combines stereo and shape-from-shading.

at 25° off-nadir so that elevation accuracies in the range of ±60 m can be obtained. This represents a value of 5 times the slant range resolution of 12.5 meters.

During the initial phase of the mission, ERS-1 was partially tilted to produce radar images at different look angles. Consequently stereo image pairs can be found at certain locations with look angle disparities of 25°. These images have been analyzed by Raggam (1994) and by Dowman *et al.* (1994) and result in terrain elevation models with errors in the range of ±35 to ±50 meters.

A major new element of ERS-1 is the initial data set to support radar interferometric mapping. This is discussed in the next sub-section.

4-12 THE CURRENT MOVE TOWARDS RADAR INTERFEROMETRIC MAPPING

Initial proposals and experiments to employ the phase of radar signals for elevation mapping have been reported by Goldstein (1965) in the context of radar astronomy, and by Graham (1974) as an augmentation of airborne imaging radar. In both cases two antennas were carried on one platform, be it the Earth for planetary work, or an aircraft.

The advent of digital radar sensing has led to a refinement of interferometric technology with some exciting results reported with SEASAT image pairs by Goldstein *et al.* (1988), using aircraft (Zebker and Goldstein, 1986) and SIR-B radar images (Gabriel *et al.* 1988). Here the impact of this new capability on the application of radar images to geometry-related tasks is addressed.

Dual antenna, single platform interferometry lends itself well to an aircraft scenario, but less so to satellite arrangements. There,

Figure 4-75 (next page). Perspective view of the DEMs from Figure 4-74c, d, where a (upper image) is a DEM obtained from Magellan images using a stereo-process alone, and b (lower image) refines this result with the help of Shape-from-Shading.

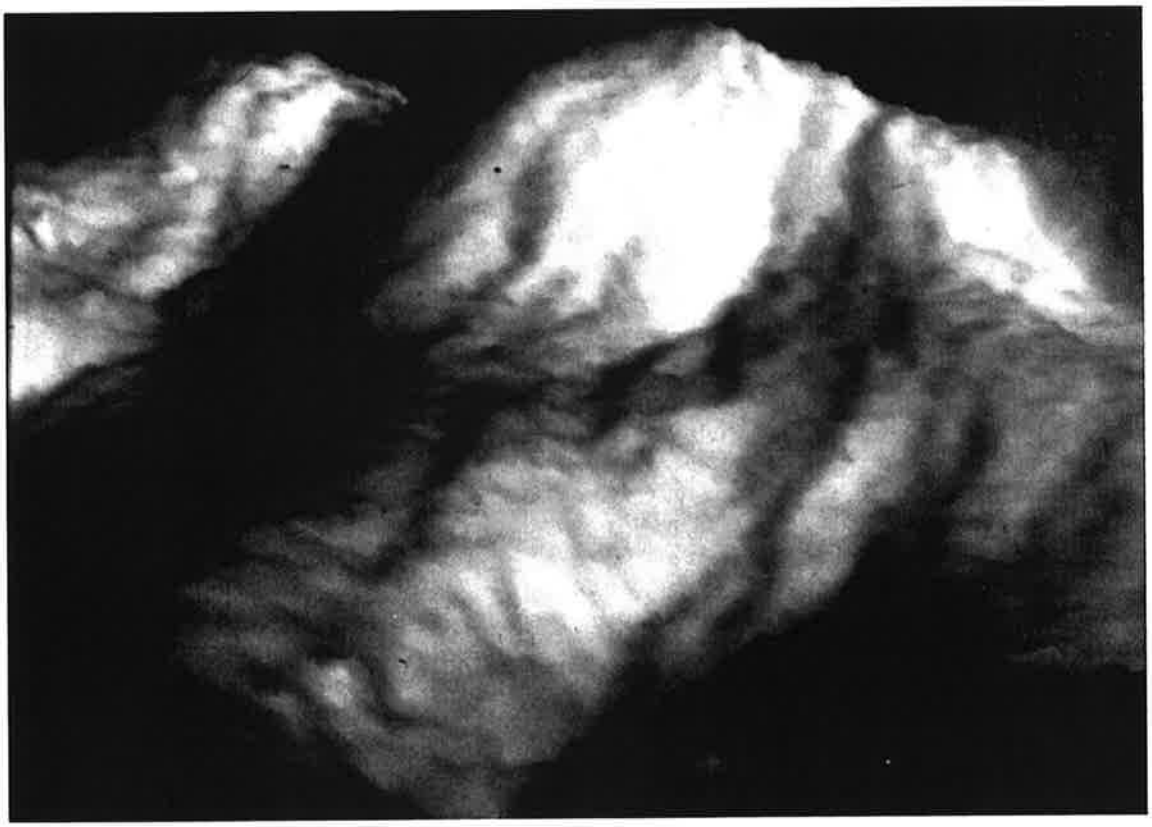

a single antenna would typically produce two interferometric passes in sequential orbits, or two satellites would need to operate in tandem.

It is abundantly clear that interferometry produces superior vertical resolution in the range of a fraction of a pixel, and an accuracy defined by the attitude of the interferometric base vector between the two antenna positions. Differential interferometry even goes further with vertical resolution to within the wavelength of the radar sensor, *i.e.* into centimeters. The only limitations are in the ability to resolve any ambiguity when converting the interferometric fringe patterns into elevation differences, and then into elevations themselves.

The major current advances in radar interferometry are due to ERS with its nearly identical orbits which were flown during the initial check-out of the system at the mission's beginning, and most recently with ERS-1 and ERS-2 "in tandem." Numerous studies and systems for interferometry were developed, for example by Prati *et al.* (1989); Prati and Rocca (1990, 1994); Massonnet (1993, 1994); Massonnet *et al.* (1993); Hartl and Thiel (1993); Hartl *et al.* (1994); and Werner *et al.* (1994).

These studies have shown that a worldwide DEM can be obtained from ERS-1 and a second satellite ERS-2 with errors of perhaps ±15 m, at a pixel size of 12.5 m, with an azimuth resolution of 6 meters and range resolution of 10.2 meters.

What can be hoped to come from this new capability? First radar images can be instantly and fully automatically ortho-rectified (terrain-corrected) with residual errors in the sub-pixel range. Secondly, such ortho-rectified images can be related to one another. Therefore the traditional limitation of radar images, namely the occurrence of so-called "no-shows" of significant and relevant object features, could be countered by obtaining multiple radar images from different aspect angles, and merging them into a "multi-incidence" and "multi-azimuth" data set. From this data set, a much more complete model of the object can be built than is available from a single image alone, or from multiple images taken with hardly any differences in incident angle or azimuth.

Interferometry will reduce the need for stereo-based terrain reconstruction; stereo may be applicable only if areas exist in the image where the typical interferometric "phase"-ambiguities cannot be resolved or where phase coherence is insufficient. In those cases the stereo-image pair may be considered as a supportive tool to fill in object shape where interferometry is obstructed.

It needs to be stressed, however, that dual orbit/single antenna interferometry must be expected to suffer from non-coherent signals over a large percentage of a coverage. Therefore one must either fill in such areas by a second interferometric data set or through the use of other techniques such as stereopsis.

In contrast, dual-antenna/single flight path operations promise a more complete interferometric coverage. This is the reason for developing aircraft-based systems at this time, and for testing such systems, as those at NASA's Jet Propulsion Laboratory, ERIM-Michigan, German Aerospace Corporation DASA, the European Union Joint Research Center JRC, Norden and the Canada Centre for Remote Sensing.

4-13 MAPPING APPLICATIONS: TWO EXAMPLES

Radargrammetric mapping applications have been addressed at various instances in this text. The range of applications includes some strictly 2-dimensional mapping issues such as looking for change over time, and 3-dimensional issues such as mapping remote regions in preparation for significant exploration activity. Two projects considered as representative operational radargrammetric applications are presented below. A shuttle-based global coveragge is expected from NASA's SRTM-mission.

4-13.1 SEA ICE MAPPING

Mapping the motion of sea ice requires that a geometric object parameter, namely the position of sea ice, be determined in time sequential radar images. A near-operational system to accomplish the task of routine mapping of sea ice motion has been put in place through an initiative of NASA (Kwok *et al.*, 1990). It has been in operation at the Alaska SAR Facility since the launch of ERS-1 and provides sea ice motion data on demand by specific users.

McConnell *et al.* (1989; 1990; 1991) describe the algorithms to find characteristic features or objects on sea ice which would manifest themselves in sequential images. A system to perform the task needs to accommodate in excess of 20 requests per day to determine the motion of sea ice, also characterize the ice and, should open water exist, extract an estimate of wind speed and direction from images of ocean wave patterns.

The source data for the Alaskan ice motion mapping system reside in the Archiving and Operations System (AOS) at NASA's Alaska SAR facility. These images are stored and meta data about the images are kept accessible. It is from a search through the meta data that one can determine which radar images may show the same ice and should therefore be further investigated for ice motion assessment.

Motion measurement consists of a comparison of detected ice features such as ice-water boundaries, ice ridges, open water ponds on top of the ice etc. As is discussed in detail by McConnell *et al.* (1990) and Kwok *et al.* (1990), the choice of features and of methods to describe them as well as the systematic search of the features for homologous details constitutes an intelligent use of various pattern recognition and image transformation tools.

Figure 4-79 is an example of an image pair in the Arctic. Figure 4-79c presents a motion map obtained from automatically tracking homologous features from one image into the next, and then interpolating a regular grid of motion vectors from the irregularly spaced feature-driven vectors. Figure 4-80 is a screen shot from an operational ERS-1 sea ice motion assessment.

Leberl *et al.* (1993) summarized the status of analyses from the ice motion mapping system in Alaska (see also Table 4-2). This revealed an extraordinarily successful operation with several thousand products generated from as many image pairs. Of the failed attempts to find ice motion, the most frequent reason was the absence of sea ice in the radar coverage.

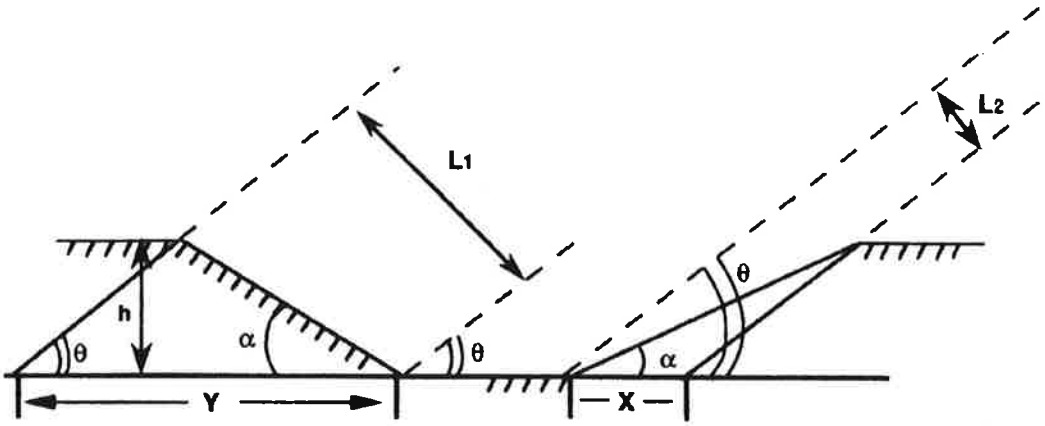

$$h = \frac{Y - X}{2} \tan \theta$$

Figure 4-76. Geometry and algebra for the single image 3-dimensional reconstruction of symmetrical features. Note how a profile through a symmetric volcano or crater could be used as if an opposite side stereo coverage were available (Courtesy C. Elachi).

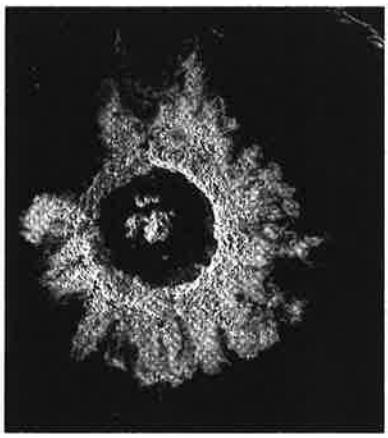

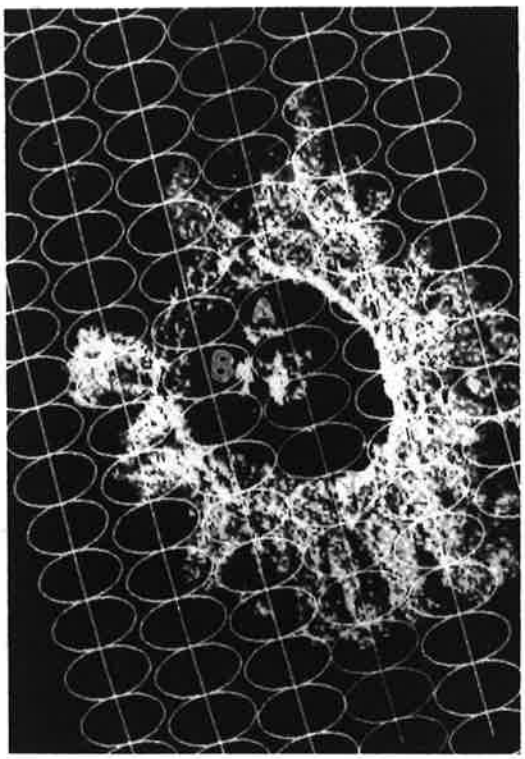

Figure 4-77a (above). Magellan image of the symmetric crater Danilova on Venus; 4-77b (right) sampling of the crater by altimetry showing its footprint. Figures 4-77c and 4-77d appear on the next page.

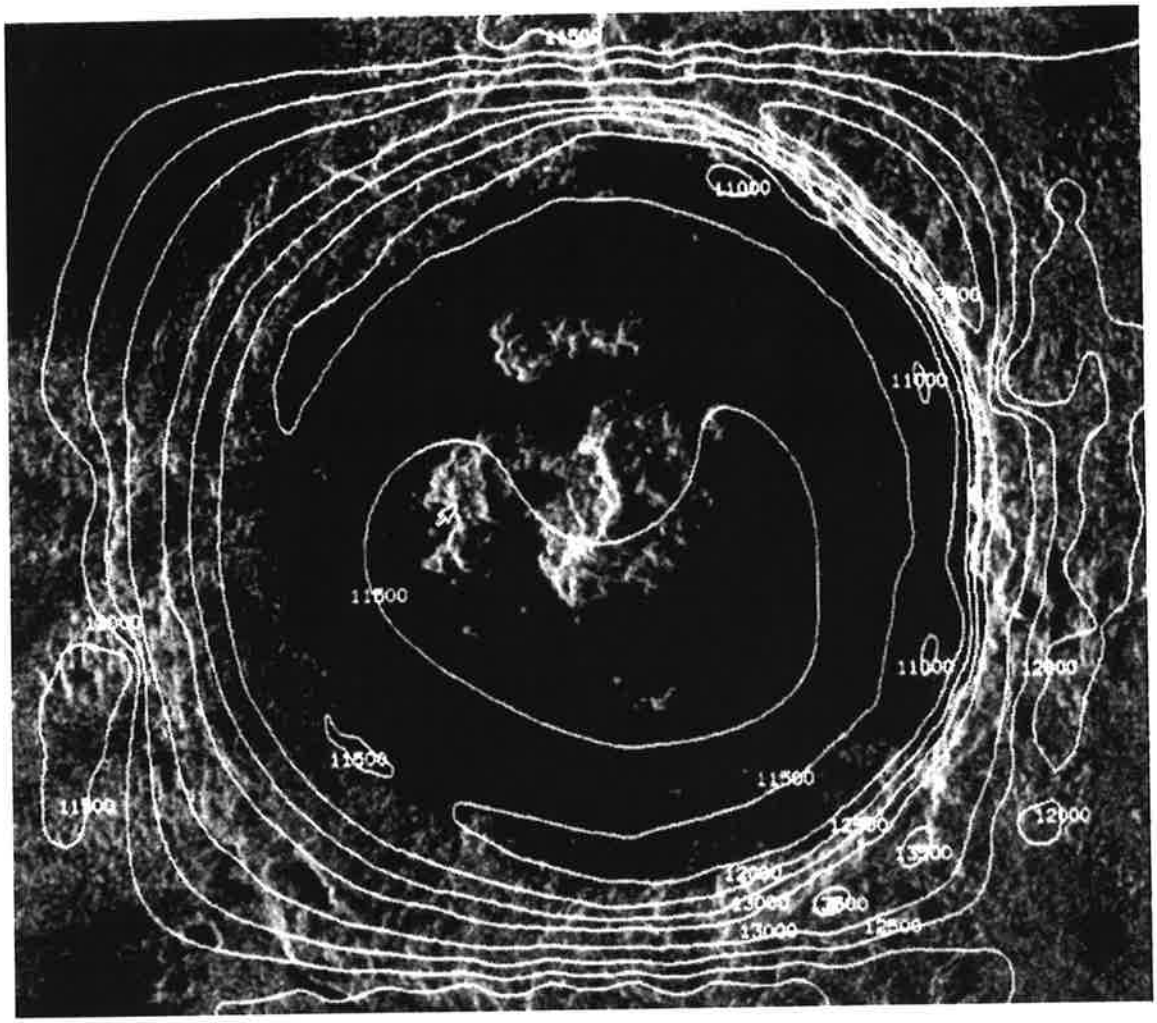

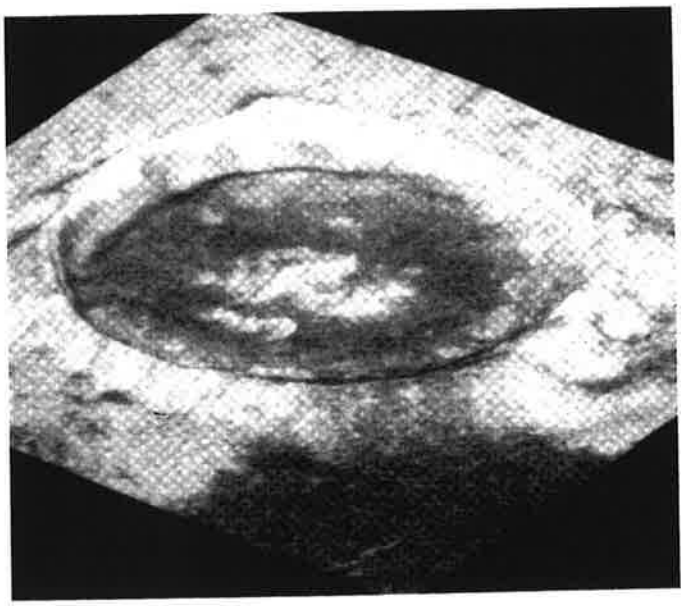

Figure 4-77c (above). Reconstruction from single image use of symmetry with contour lines; 4-77d (left) perspective rendering of crater Danilova.

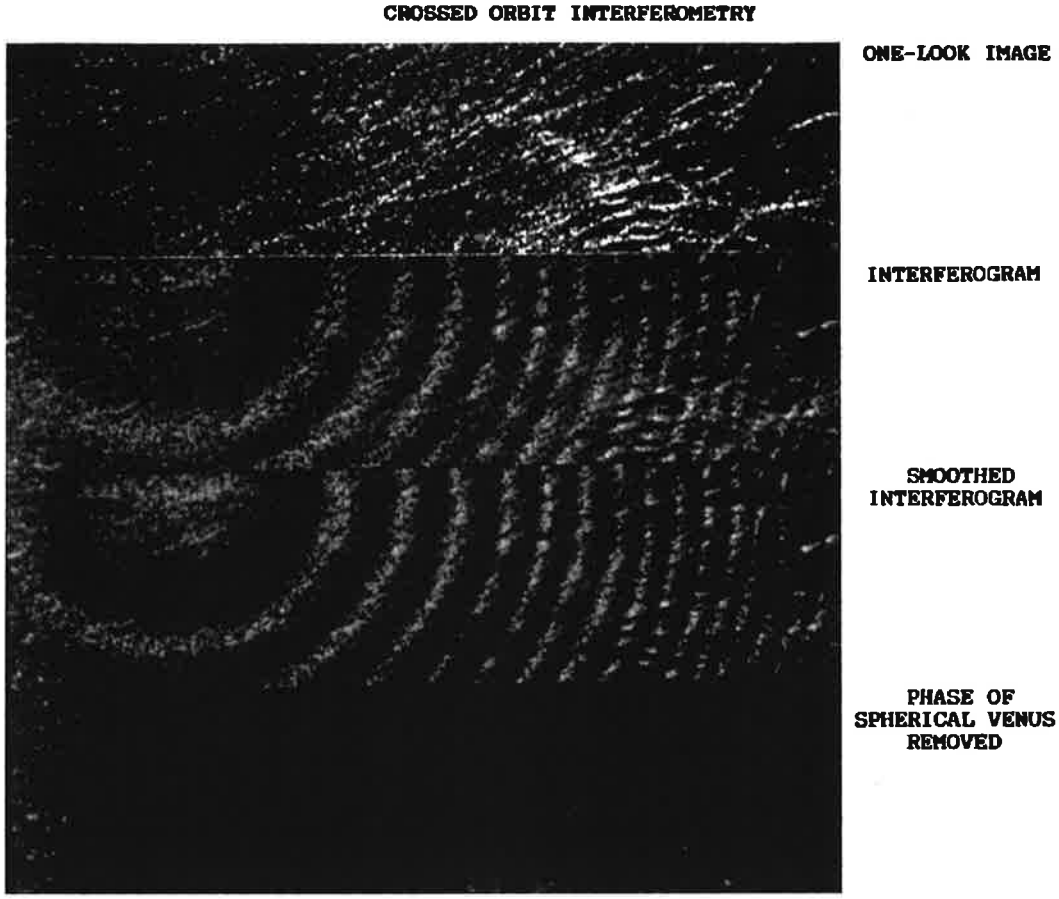

Figure 4-78. Interferometric fringes detected in Magellan images from the North Pole. Note that the fringes seem to be caused by the planet's spherical curvature (Courtesy R. Goldstein, personal communication).

4-13.2 COMMERCIAL TOPOGRAPHIC MAPPING WITH STEREO-RADAR

Radar images have long been produced commercially for reconnaissance type mapping in remote regions of the World. This started with the project to map the Darien province of Panama in 1967 (Crandall, 1969; Hockeborn, 1971; MacDonald, 1969). It continued with projects like Radam in Brazil (Azevedo, 1971, v. Roessel and deGodoy, 1974), Proradam in Colombia (Leberl, 1974) and projects in nearly all countries along the tropical belt. The perennial problem with the resulting map data was their unknown geometric accuracy, so that the presentation scale of the so-called "semi-controlled" image mosaics was chosen at 1:250,000.

The advent of the Global Positioning System (GPS) changed the technology to position an imaging sensor (Ackermann, 1988). This combined with methods to employ overlapping digital radar images for stereo-reconstruction of terrain elevations and subsequent terrain-correction of the input radar images. At pixel sizes of 6 meters, and at a presentation scale with 8 pixels per millimeter, a mapping scale of 1:50,000 became feasible. For this scale to become accepted one needed to improve the geometry of the map product to within ±0.5 mm at the presentation scale, or ±25 m on the ground.

This has been accomplished in the STARMAP-system of Intera Technologies Ltd. (Calgary, Canada) and is now available as a commercial mapping service. The methods used have been described by Leberl (1990). Images are acquired from parallel aircraft flight lines (Figure 4-81) and produce a block of overlapping images ready for individual stereo processing since individual flight lines are controlled by differential GPS. Each image pair is subject to a stereo mensuration process which results in a dense network of terrain surface points, given a stereo geometry shown in Figure 4-82.

An individual pair of images produces a patch of DEM. A map sheet is composed of several of these patches. Therefore, they need to be merged into a seamless topographic product. Individual flight lines may be rather long, 150 km. Map sheets at a scale of 1:50,000 cover only 25 km at the side, or sometimes 50 km. Data processing may initially disregard such map boundaries and operate with flight lines as the basic units. Only after completion of data processing is it possible to reformat the results into deliverable map sheets.

Figure 4-83a presents an early DEM obtained from 14 SAR flight lines, 7 of these looking West, another 7 looking East. The image lines are processed as a block of same side images. Only at

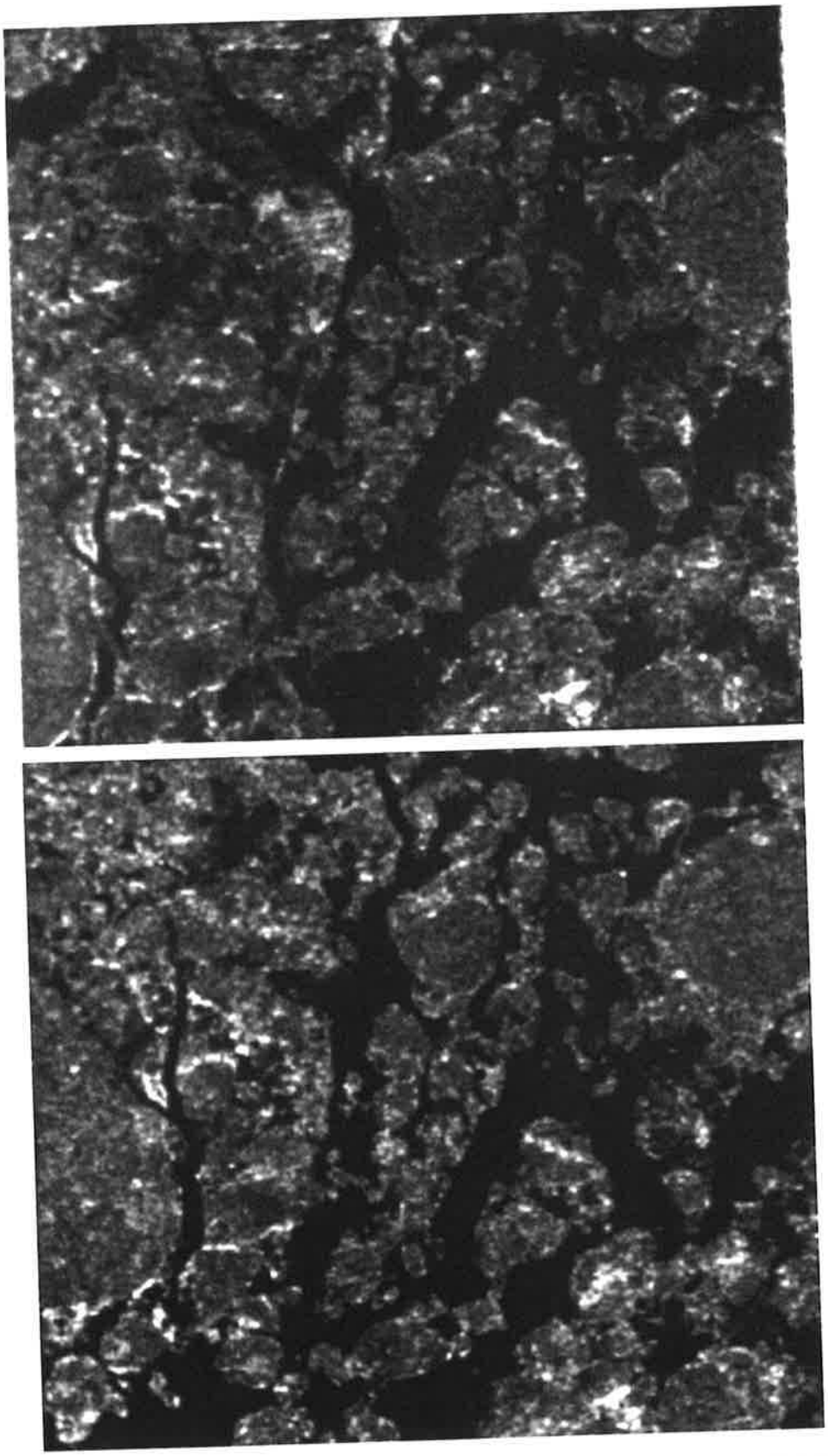

Figure 4-79a (top) and b (bottom). Pair of radar images in the Arctic taken by SEASAT (1978). Figure 4-79c appears on the following page.

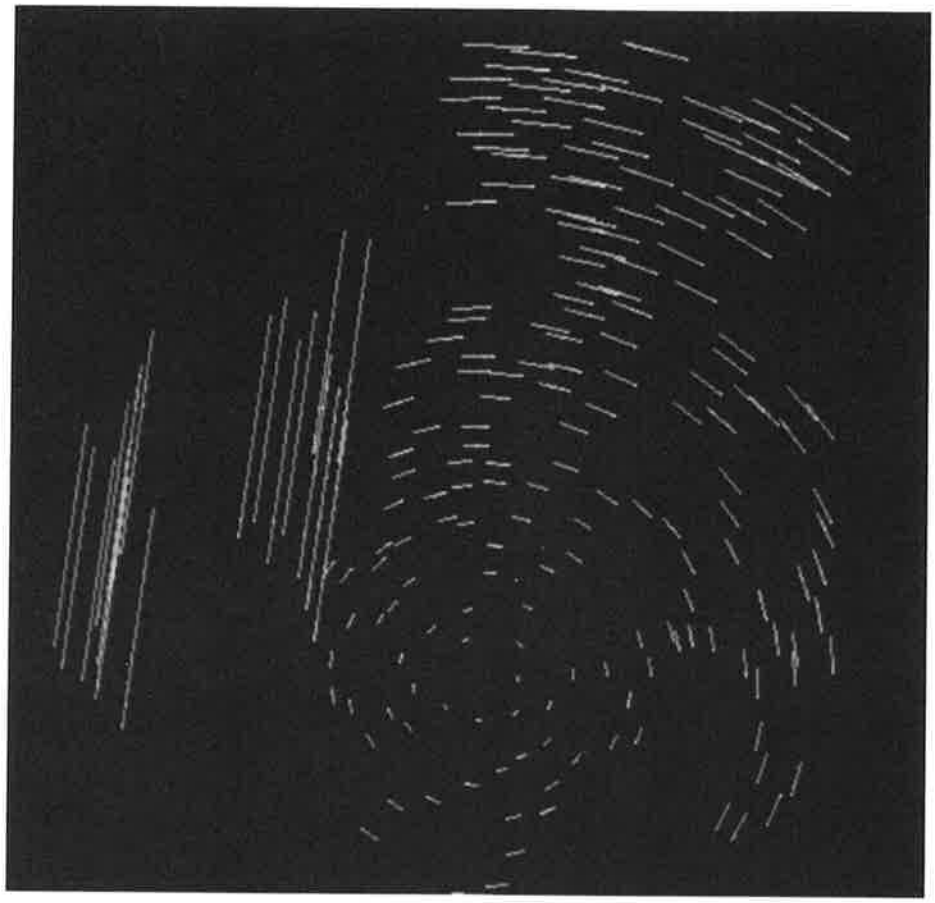

Fig 4-79c. Motion vectors automatically detected from images 4-79a and b (previous page).

Table 4-2
Summary of Accomplishments with ERS-1 Image Pairs for Ice Motion Mapping at the Alaska SAR Facility*

Operational since	1/1992
Number of ocean images in AOS	25,000
Memory used for images in AOS	~ 1,250 GB
Size of each image	100 x 100 km^2
Pixel sizes: Low Resolution	100 m
High Resolution	12.5 m
Time to process an image pair	20 minutes
Time to process for classification	5 minutes
Processing requests handles for motion	4,900
Processing requests handled for classification	3,800
Satisfactory results delivered for motion	3,500
Satisfactory results delivered for classification	3,500
2 major reasons for failure to deliver	No ice
(time of separation too great, *e.g.* 12 days)	

* (Status 1993, from Leberl *et al.*, 1993).

the end are the two coverages (one West-looking and the other East-looking) combined to fill any holes that may have been left from shadows in one coverage. Figure 4-83b presents a reference DEM produced from photogrammetric sources.

Extensive tests with radar images of well mapped areas have produced accuracy assessments reported in Table 4-3. These show that the desire to have a mapping product with accuracies in the ±0.5 mm range at presentation scale is being accomplished, considering that at scale 1:50,000 this represents ±25 m on the ground.

4-14 CONCLUSIONS AND OUTLOOK

Radar image processing is undergoing an exciting period in its development. A multitude of sensors exist or are on the drawing board. Massive amounts of data are being produced and are awaiting intelligent analysis. NASA's Magellan-Mission presents an example where unique and exciting radar mapping products need to be produced of the surface of Venus: More than 400 Gigabytes of image data are awaiting careful analysis which can benefit greatly from the use of radargrammetric methods.

The European ERS satellite program has spawned enormous interest in the research community to develop new techniques of

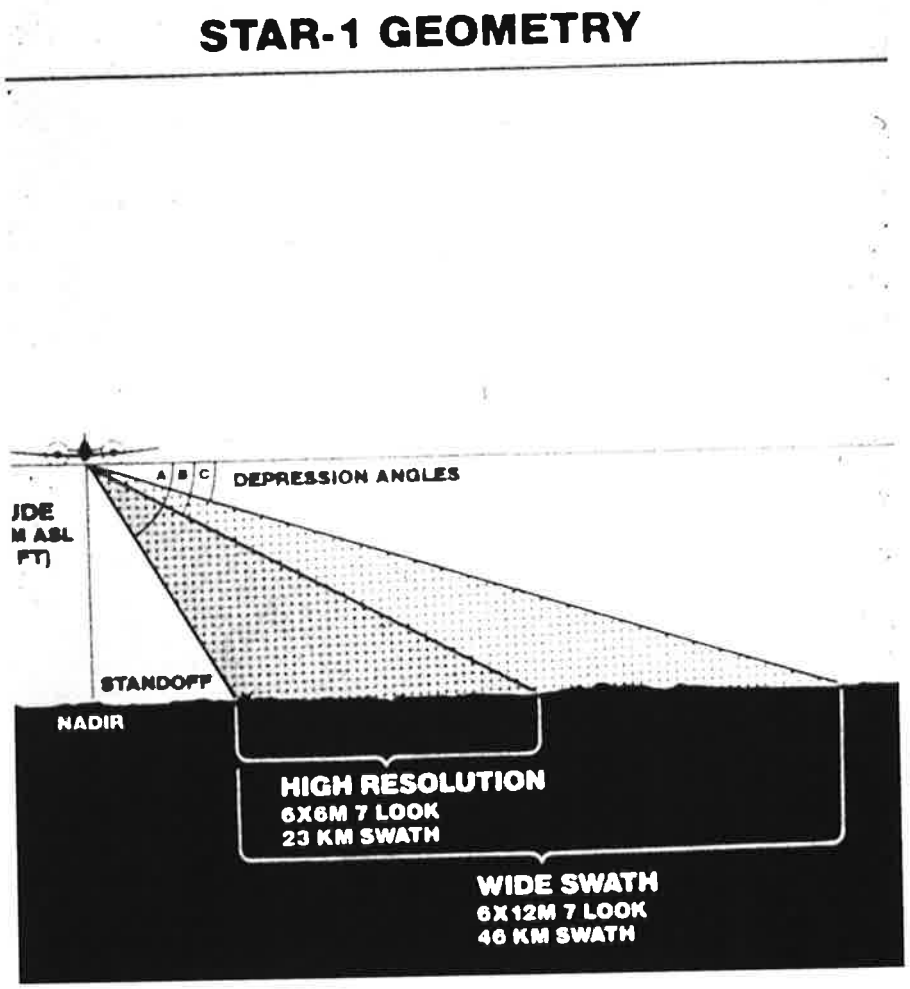

Figure 4-81. Flight configuration for commercial radar image mapping through STARMAP (Intera Technologies, Ltd., Calgary, Canada). Note the small stereo intersection angles and the idea of using lines 1+3, 2+4 etc. as stereo pairs.

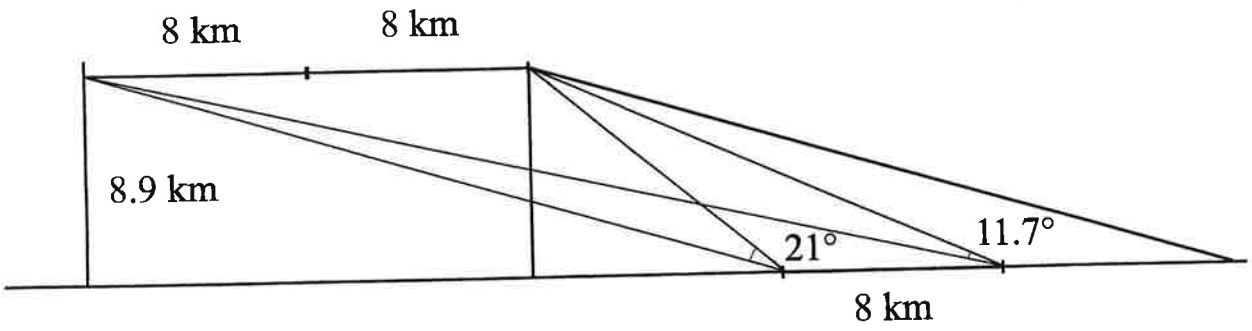

Figure 4-82. Individual stereo geometry from GPS-controlled radar image acquisition for STARMAP (Courtesy Intera Technologies, B. Mercer).

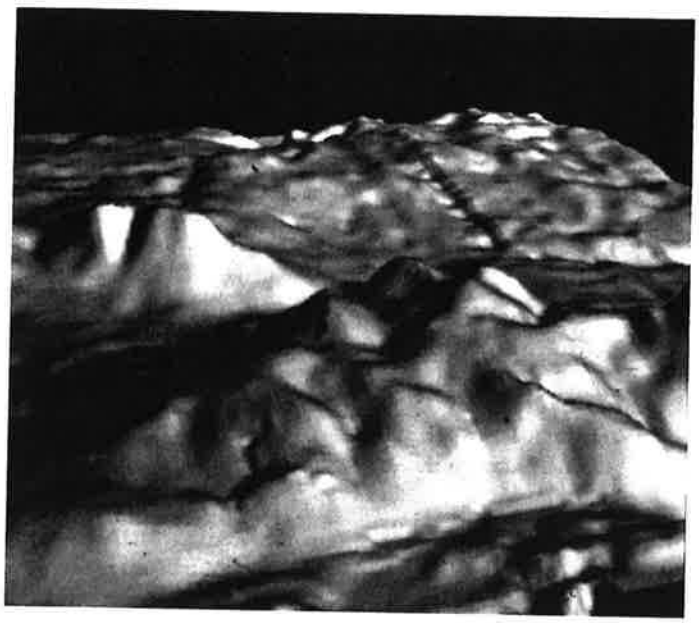

Table 4-3
Accuracies Achieved with the Commercial Stereo-radar Mapping System Starmap* using Test Flights over a Well-mapped area near Calgary**

Test	*Along Track (m)*	*Across Track (m)*	*Height (m)*
Theoretical Accuracy *(with 3 m range error)*	N/A	7.5	16
Brazeau Test *(with 1 control point per 10 km²)*	29	33	41
Brazeau Test *(with 1 control point per 6 km²)*	14	11	23
Brazeau Test *(With GPS, without ground control)* [Absolute Accuracy]	13	26	28

* Intera Technologies, Ltd., Calgary, Canada
**from Mercer *et al*, 1989

Figure 4-83a (above) and 4-83b (left). Figure 4-83a is a Digital Elevation Model (DEM) produced from commercial aircraft radar system Starmap. Input images: 7 West-looking and 7 East-looking. Elevation differences in the range of 1000 meters. Accuracies in accordance with results reported in Table 4-3 (see also Figure 4-3). For comparison: Figure 4-83b is a DEM produced from aerial photographs.

using multiple radar images, to geometrically process them, to register them, and to extract terrain shape from them. At the time of this writing a follow-on ERS-2 satellite is operational. Initially it has operated in tandem with the original ERS-1. The Space Shuttle has produced unique radar images in the SIR-C experiment. At the same time the Japanese, Russian, Canadian and US space agencies are involved in an unprecedented series of satellites and further Space Shuttle launches with imaging radars on-board.

Interferometry is not an entirely new, but certainly a newly applied remote sensing technology which solves geometric, and thus radargrammetric and image processing issues. Once its full impact is well understood and causes new sensing strategies to be more fully available, it may well generate a major shift in the role that is played by radar images in the current spectrum of imaging sensors.

These activities and interests clearly increase demands for radargrammetric capabilities and ensures that radar image processing faces significant challenges to match, compare, warp and correct images, to extract useful geometric data and geometry-induced radiometric information, and to support the intelligent application of radiometric data from multiple images.

4-15 REFERENCES*

Ackermann, F., 1988. Combined Adjustment of Airborne Navigation, Proceedings 16th Congress International Society Photogrammetry and Remote Sensing, Kyoto, Japan, Vol. 27, Part B8, pp. III-1 1 to III-23.

Ackermann, F., 1983. High Precision Digital Image Correlation, *Proceedings 39th Photogrammetric Week,* Institut für Photogrammetrie, Vol. 9, Stuttgart.

Akowetzky, W.I., 1968. On the Transformation of Radar Coordinates into the Geodetic System (in Russian), *Geodezia i Aerofotosyomka.*

Alexander, L., 1981. Computer Information Extraction from Radar Images, Ph.D. Thesis, Univ. of Pennsylvania, Philadelphia, 248 p.

Ali, A. E., 1982. Investigation of SEASAT-A Synthetic Aperture Radar (SAR) for Topographic Mapping Applications, Dissertation, Univ. of Glasgow.

Ambrose, W., 1967. A Radar Image Correlation Viewer, *Photogrammetric Engineering,* Vol. XXXIII.

Anon., 1975. Location Estimation and Guidance Using Radar Imagery, *IEEE Trans. Aerospace and Electronic Systems,* AES-11 , No. 6, pp. 1383.

Anuta, P., *et al.,* 1978. SAR-LANDSAT Image Registration Study-Final Report, LARS Contract Report 082478.

Anuta, P., M. Hixson and D. Swain, 1978b. *Multisensor Multidata Spatial Feature Matching, Correlation, Registering, Resampling and Information Extraction, Processing Techniques Development,* LARS, Purdue Univ., Lafayette, IN, Vol. 3, pp. C-1 to C-56.

Apolloni, B., A. Carrara and P.A. Murino, 1982. Uses of Elevation Models for Landform Analysis by SEASAT SAR Imagery, XXXII Cong. International Astronautical Fed., Italy, *Acta Astronautica,* Vol. 9, No. 6-7, pp. 365-74.

Aschbacher J. and J. Lichtenegger, 1990. Combined Analysis of Spaceborne SAR and Optical Data, In *GeoSAR* 1990.

Ausherman. D., 1987. Digital Versus Optical Techniques in Synthetic Aperture Radar (SAR) Data Processing, *Optical Engineering,* Vol. 19. No. 2.

Ausherman. D. *et al.,* 1984. Developments in Radar Imaging. *IEEE Trans. Aerospace and Electronic Systems,* Vol. AES-20, No. 4.

Autometric, 1982. Program Documentation for Analytical Mapping System Radar Model, prepared by Autometric, Inc. Falls Church, VA for USA Engineer Topographic Laboratory. Ft. Belvoir, VA, 36 p.

Azevedo, L. de, 1971. Radar in the Amazon, *Proceedings 7th International Symposium Remote Sensing of the Environment,* Ann Arbor, MI.

Bair, G.L. and G.E. Carlson, 1974. Performance Comparison of Techniques for Obtaining Stereo Radar Images, *IEEE Trans. Geoscience Electronics,* Vol. GE-1 1.

Bair, G.L. and G.E. Carlson, 1975. Height Measurement with Stereo Radar, *Photogrammetric Engineering and Remote Sensing,* XLI.

Baker, J. and E.M. Mikhail, 1975. Geometric Analysis and Restitution of Digital Multispectral Scanner Data Arrays, *LARS Information Note 05 28 75,* Purdue Univ., Lafayette, IN.

Barber. B., 1985. Theory of Digital Imaging from Orbital Synthetic.-Aperture Radar, *International Journal Remote Sensing,* Vol. 6. No. 7.

Barnea, D.I. and H. Silverman, 1972. A Class of Algorithms for Fast Image Registration, *IEEE Trans. Computer,* Vol. C-21, No. 2, pp. 179-186.

Barrow, H.G., *et al.,* 1977. Experiments in Map-Guided Photointerpretation, *Proceedings 5th International Joint on AI, IJCAI-77,* Cambridge, MA.

Barrow, H., *et al.,* 1978. Parametric Correspondence and Chamfer Matching – Two New Techniques for Image Matching, *Proceedings DARPA Image Understanding Workshop.*

Barsukov, V.L., *et al.,* 1986. The Geology and Geomorphology of the Venus Surface as Revealed by the Radar Images Obtained by Veneras 15 and 16, Proceedings 16th Lunar and Planetary Science Conference, Part 2, *Journal Geophyscal Research,* Vol. 91, No. B4, pp. D378 to D398.

**This also represents a bibliography with listings not referred to in the text.*

Bayer, T., R. Winter and G. Schreier, 1989. Investigation of Slope and Aspect Effects on Image Grey Values in Geocoded SAR Images, *Proceedings IGARSS '89,* pp. 454-457.

Beaubien, J., 1980. *Forestry Mapping Using SAR,* Intera Environmental Consultants Ltd., Report No. ASP 890-1 .

Berlin, L.G. and G.E. Carlson, 1974. Radar Mosaics, *The Professional Geographer,* Vol. XXIII, No. 1.

Bicknell, T. *et al.,* 1975. A Study to Determine the Feasibility of Using Radar Techniques for Public Land Surveying, Jet Propulsion Laboratory Report under contract to the Bureau of Land Management, Contract No. 5300-PH-995, Pasadena, CA.

Binnekade, P., H. van Kasteren and G. Heuk, 1985. Semi-Operational Identification of Agricultural Crops from Airborne SLAR Data, *Proceedings Machine Processing of Remotely Sensed Data,* pp. 241-247.

Blom, R.G. 1988. Effects of Variation in Look Angle and Wavelength in Radar Images of Volcanic and Aeolian Terrains, or Now You See It Now You Don't, *International Journal Remote Sensing,* Vol. 9, No. 5, pp. 945-965.

Blom, R.G. and C. Elachi, 1981. Spaceborne and Airborne Imaging Radar Observations of Sand Dunes, *Journal Geophysical Research,* Vol. 92.

Blom, R.G. and C. Elachi, 1987. Multifrequency and Multipolarization Radar Scatterometry of Sand Dunes and Comparison with Spaceborne and Airborne Radar Images, *Journal Geophysical Research,* Vol. 92, pp. 7877-7889.

Blom, R.G., C. Elachi and A.S. Sheehan, 1982a. Radar Scatterometry of Sand Dunes and Lava Flows, *Proceedings IGARSS '82,* Munich, pp. FA-5.1.1 to FA-5.1.5.

Blom, R.G., D. Evans and C. Elachi, 1982b. Results from OSTA-1: SIR-A Images of Volcanic Fields and Sand Dunes, *Proceedings IGARSS '82,* Munich, pp. FA-6.9.1 to FA-6.9.6.

Blom, R.G., L.R. Schenck and R.E. Alley, 1985. What Are the Best Radar Wavelengths, Incidence Angles and Polarizations for Geological Applications? A Statistical Approach, *Proceedings IGARSS '85,* Amherst, MA, pp. 659-664.

Blom, R.G., L.R. Schenck and R.E. Alley, 1987. What Are the Best Radar Wavelengths, Incidence Angles and Polarizations for Discrimination Among Lava Flows and Sedimentary Rocks? A Statistical Approach, *IEEE Trans. Antennas and Propagation,* Vol. AP-25, pp. 208-213.

Blom, R.G., P. Cooley and L.R. Schenck, 1986. On the Relationship Between Age of Lava Flows and Radar Backscatter, *Proceedings IGARSS '86,* Zurich, pp. 11 19-11 27.

Bloom, A.L. and E.J. Fielding, 1986. Tectonic Geomorphology of the Andes with SIR-A and SIR-B, Proceedings 2nd Spaceborne Imaging Radar Symposium, Jet Propulsion Laboratory, *JPL Publ. 86-26,* Pasadena, CA, pp. 5-10.

Bosman, E. *et al.,* 1971. Project Karaka-the Transformation of Points from Side Looking Radar Images into the Map System, Final Report, Part 1, Netherlands Interdepartmental Working Community for the Application and Research of Remote Sensing Techniques (NIWARS), Delft, The Netherlands.

Bosman, E.R., E. Clerici, D. Eckhart and K. Kubik (undated), Project BEBLOKA-the Transformation of Points from Ovelapping Images Obtained with Different Sensors into the Map System, Final Report, Netherlands Interdepartmental Working Community for the Application and Research of Remote Sensing Techniques (NIWARS), Delft, The Netherlands.

Brown, E., *et al.,* 1981. Application of SEASAT SAR Digitally Correlated Imagery for Sea Ice Dynamics, Invited Paper, 1981 AGU Meeting, Baltimore, USA.

Brown, R., B. Guindon, P. Teillet and D. Goodenough, 1984. Crop Type Determination from Multi-Temporal SAR Imagery, *Sensing,* pp. 638-691 .

Brown, W. and R. Fredericks, 1969. Range Doppler Imaging with Motion Through Resolution Cells, *IEEE Trans. Aerospace and Electronic Systems,* Vol. AES-1.

Bryan, M.L., 1982. Analysis of Two SEASAT Synthetic Aperture Radar Images of an Urban Scene, *Photogrammetric Engineering and Remote Sensing,* Vol. 48, No. 3, pp. 393-398.

Bryan, M.L. and J. Clark, 1984. Potentials for Change Detection Using SEASAT Synthetic Aperture Radar Data, *Remote Sensing of the Environment,* Vol. 16, No. 2, pp. 107-124.

Bryan, M.L., W. Stromberg and T. Farr, 1977. Computer Processing of SAR L-Band Imagery, *Photogrammetric Engineering and Remote Sensing,* Vol. 43, No. 10, pp. 1283-1294.

Buchroithner, M., G. Triebnig, G. Domik, W. Kropatsch, F. Leberl, G. Paar, J. Raggam, A. Rioza and D. Strobl, 1987. Radargrammetric Image Data Evaluation. DIBAG Report 30, Graz Research Centre, Dec. 1987, Final Report for ESA Contract No. 6.621/85/F/FL(SL), pp. 141.

Burns, B.A. and D.R. Lyzenga, 1984. Textural Analysis as a SAR Classification Tool, *Electromagnetics,* Vol. 4, No. 2-3, pp. 309-322.

Burns, J., A. Huertas and R. Nevatia, 1981. Object Detection in SAR Images, Univ. of Southern California Image Processing Institute, *USCIPI-Report 1050,* 14 p.

Camillerapp, J. and J. Quinqueton, 1977. Lines Extraction from Radar Images, NATO Advanced Study Institute, Series E: *Applied Science No. 20.,* Nordhoff, pp. 361-372.

Campbell, D.B., R.F. Jurgens, R.B. Dyce, F.S. Harris and G.H. Pettengill, 1970. Radar Interferometric Observations of Venus at 70 cm Wavelength, *Science,* Vol. 170, pp. 1090-1092.

Campbell, D. and B. Burns, 1980. Earth-Based Radar Imagery of Venus, *Journal Geophysical Research,* Vol. 85, No. A13, pp. 8271-8281.

Campbell, D., J. Head, J. Harman and A. Hine, 1983. Venus: Identification of Banded Terrain in the Mountains of Ishtar Terra, *Science,* Vol. 221, No. 4611, pp. 644-647.

Cappellini, V. *et al.,* 1984. Digital Comparison and Correlation Techniques of Remote Sensing Images with Differing Spatial Resolutions, *Proceedings Symposium on Integrative Approaches in Remote Sensing,* Guiledford, UK, pp. 23-29.

Carlson, G.E., 1973. An Improved Single-Flight Technique for Radar Stereo, *IEEE Trans. Geoscience Electronics,* Vol. GE-1 1, No. 4.

Carsey, F. and B. Holt, 1987. Beaufort-Chukchi Ice Margin Data from SEASAT: Ice Motion, *Journal Geophysical Research,* Vol. 92, No. C7, p. 7I63.

Casasent, D. and T. Barniv, 1978. Coherent Optical Processing for Multisensor Image Processing, *Proceedings SPIE,* Vol. 137, pp. 57-63.

Chodas P., S. Lewicki, S. Hensley and W. Masters, 1993. High-Precision Magellan Orbit Detremination for Stereo Image Processing, *Proceedings, AAS/AIAA Astrodynamics Specialists Conference,* AAS Publ. Office, P.O.Box 28130, S. Diego, Cal. 92198, pp 1-18.

Churchill, P., G. Hane and J. Trevett, 1984. An Evaluation of SAR-580 Multi-Frequency Radar Data over the Norfolk Test Site (GBG4), *Proceedings SAR-580 Investigator's Workshop,* ISPRS, Vol. 2, p. 6.

Cimino, J., *et al.,* 1986. Multiple Incidence Angle SIR-B Experiment over Argentina: Mapping of Forest Units, *IEEE Trans. Geosci. and Remote Sensing,* Vol. GE-24, pp. 498-509.

Clark, J., 1980. Training Site Statistics from LANDSAT and SEASAT Satellite Imagery Registered to a Common Map Base, *ASPRS Semi-Annual Convention, Niagara Falls,* pp. RS.1.F.1 to RS. 1.F.9.

Clark, J., 1981. Improved Land Use Classification from LAND-SAT and SEASAT Satellite Imagery to a Common Map Base, *Proceedings ASPRS Ann. Conv.,* pp. 591-599.

Clarke C., 1991. Geocoding and Stereoscopy of Synthetic Aperture Radar Images, PhD Thesis, University of London, Dept. of Photogrammetry.

Claveloux, B.A., 1960. Sketching Projector for Side Looking Radar Photography, *Photogrammetric Engineering,* Vol. XXVI.

Coll, E. and R. Pettigrew 1988. A High Fidelity, High Through-put System for Geocoding SAR Imagery, *Proceedings IGARSS '88,* pp. 687-690.

Colvocoresses, A., 1982. An Automated Mapping Satellite System, *Photogrammetric Engineering and Remote Sensing,* Vol. XLVIII, pp. 1585-1591.

Crandall, C.J., 1963. Advanced Radar Map Compilation Equipment, *Photogrammetric Engineering,* XXIX.

Crandall, C.J., 1969. Radar Mapping in Panama, *Photogrammetric Engineering,* Vol. XXXV.

Curlander, J.C., 1981a. *Geometric and Radiometric Distortion in Spaceborne SAR Imagery,* Invited Paper, NASA Workshop on Registration-Rectification for Terrestrial Applications, Jet Propulsion Laboratory, Pasadena, CA.

Curlander, J.C., 1981b. *Sensor to Target Range Determination,* Jet Propulsion Laboratory, JPL-Interoffice Memorandum 334.7-80-056, Pasadena, CA.

Curlander, J.C. and W.E. Brown, 1981. A Pixel Location Algorithm for Spaceborne SAR Imagery, *Proceedings IGARSS '81,* Vol. 2, pp. 843-850.

Curlander, J.C., 1982. Location of Spaceborne SAR Imagery, *IEEE Trans. Geoscience and Remote Sensing,* Vol. GE-20, No. 3, pp. 359-364.

Curlander, J.C. and S.N. Pang, 1982. Geometric Registration and Rectification of Spaceborne SAR Imagery, *Proceedings International Symposium Geoscience and Remote Sensing,* Germany, Vol. 2, No. FA-2, pp. 5.1-5.6.

Curlander, J., 1984. Utilization of Spaceborne SAR Data for Mapping, *IEEE Trans. Geoscience and Remote Sensing,* Vol. GE-22, pp. 106-1 12.

Curlander, J.C., *et al.,* 1985. Determination of Sea Ice Motion Using Digital SAR Images, *IEEE Journal Oceanic Engineering,* Vol. OE-10, No. 4, pp. 358.

Curlander, J.C., 1986. A Post-Processing System for Automated Generation of Geocoded SAR Imagery, *Proceedings 2nd Spaceborne Imaging Radar Symposium,* Jet Propulsion Laboratory, Pasadena, CA.

Curlander, J., 1987. A Post-Processing System for Automated Rectification and Registration of Spaceborne SAR Imagery, *International Journal of Remote Sensing,* Vol. 8, pp. 621.

Curlander, James, W. Kober and F. Leberl, 1989. SAR Image-Terrain Database Registration. *Proceed. IGARSS '89,* IEEE, Vol. 4, p. 2487.

Curlander, James and W. Kober, 1990. Innovative Algorithms for SAR-to-Optical Image Registration, *Proceedings IGARSS 1990,* College Park, MD, May, pp 329-331.

Daily, M., 1979. Geologic Interpretation from Composited Radar and LANDSAT Imagery, *Photogrammetric Engineering and Remote Sensing,* pp. 1109-1116.

Daily, M. *et al.,* 1978. Application of Multispectral Radar and LANDSAT Imagery for Geologic Mapping in Death Valley, *JPL Publ. 78-19,* p. 47, Pasadena, CA.

Dalke, G. and R. McCoy, 1968. Regional Slopes with Non-Stereo Radar, *Photogrammetric Engineering,* Vol. XXIV.

DBA-Systems, 1974. *Research Studies and Investigations for Radar Control Extensions,* DBA-Systems, Inc., Defense Documentation Center Report No. 530784L, Melbourne, FL.

De Barros Aguire, J. *et al.,* 1978 Un Novo Produto de INPE; Imagen do Satellite LANDSAT Produzida Para Utilizacao Conjunta Com Imagens de Radar, *Proceedings Symposium Boras. de Sensoriamento Remoto,* pp. 935-954.

Denos M. I., 1991. An automated approach to stereo matching SEASAT imagery, *Proceedings of British Machine Vision Conference 1991,* Glasgow, UK, Springer-Verlag, 335-339.

Dellwig, I.F., 1980. A New Look at Togo through the Eyes of a SLAR, in Radar Geology, an Assessment, Jet Propulsion Laboratory, *JPL-Publ. 80-61,* Pasadena, CA.

Derenyi, E.E., 1975a Topographic Accuracy of Side Looking Radar Imagery, *Bildmessung und Luft-bildwesen,* Vol. 43, No. 1, pp. 17-22.

Derenyi, E.E., 1975b. Terrain Heights from SLAR Imagery, Pres. Paper, *41st Annual Conv. American Society Photogrammetry,* Washington, DC.

Derenyi, E.E., 1972. Geometric Consideration in Remote Sensing, *Proceedings 1st Canadian Symposium on Remote Sensing,* Ottawa.

Derenyi, E.E., 1974. SLAR Geometric Test, *Photogrammetric Engineering,* Vol. XL.

Derenyi, E.E., 1974. Metric Evaluation of Radar and Infrared Imageries, *Proceedings 2nd Canadian Symposium on Remote Sensing,* Univ. of Guelph, Guelph, Ontario.

Derenyi, E.E., 1980. SAR-580 Mapping Evaluation-Final Report, Sursat Project Exper. No. 74, 11 p.

Derenyi, E.E. and L. Szabo, 1980a. Cartographic Accuracy of SAR Imagery, *Proceedings 6th Canadian Symposium on Remote Sensing,* pp. 287.

Derenyi, E.E. and L. Szabo, 1980b. Planimetric Transformation of Synthetic Aperture Radar Imagery, *14th Con. International Society Photogrammetry,* Hamburg, 7 p.

Derenyi, E. and L. Szabo, 1981. Cartographic Aspects of Dual-Frequency Dual-Polarization SAR Imagery, *Proceedings 7th Canadian Symposium on Remote Sensing,* pp. 450-453.

Derenyi, E.E. and A. Stuart, 1984. Height Determination from Spaceborne Radar Imagery, *Proceedings ASPRS Ann. Conv.,* pp. 243-252.

Derenyi, E. E. and A. Stuart, 1985. Geometric Aspects of Spaceborne Stereo Imaging Radar, *Archives of ISPRS, Comm. VII, 15th Congress at Rio de Janeiro,* pp. 153-162.

Derin, H., H. Elliot, R. Soucy and J. Kuang, 1985. Segmentation of SAR Imagery using GIBBS Distribution Models, *Proceedings Machine Processing of Remotely Sensed Data,* pp. 282-291.

DiCarlo, C., *et al.,* 1968. All Weather Mapping, pres. paper, International Congress of Surveyors (FIG), London.

DiCarlo, C., *et al.,* 1971. DoD Data Processing Equipment for Radar Imagery, pres. paper. International Congress of Surveyors, Wiesbaden.

DiCenzo. A., 1981. Synthetic Aperture and Digital Processing: An Introduction, Jet Propulsion Laboratory, *JPL Publ. 80-90,* Pasadena. CA.

Domik, G., M. Kobrick and F. Leberl, 1984. Radar Image Simulation and its Application in Image Analysis, *International Archives of Photogrammetry and Remote Sensing,* Vol. 25, No. 3a, pp. 99-108.

Domik, G., F. Leberl and J. Cimino, 1986. Multiple Incidence Angle SIR-B Experiment over Argentina-Generation of Secondary Image Products, *IEEE Trans. Geoscience and Remote Sensing,* Vol. GE-24, pp. 492-497.

Domik, G., F. Leberl, E. Kienegger and J. Raggam, 1985. Study on the Use and Characteristics of SAR for Geological Application, Radargrammetric Aspects, ESA Study Contract 5443/83/D/IM, sc), ESOC Darmstadt), Graz Research Center, Austria, 50 p.

Domik, G., F. Leberl and J. Raggam, 1983. Evaluation of Radargrammetric Stereo, DIBAG Report 11, Graz Research Center, Austria, 127 p.

Domik, G., J. Raggam and F. Leberl, 1984. Rectification of Radar Images Using Stereo-Derived Height Models and Simulation, *International Archives of Photogrammetry and Remote Sensing,* Vol. 25, No. 3A, pp. 109-116.

Domik, G., 1984. Evaluation of Radar Stereo Viewability by Means of a Simulation Technique, *IGARSS '84,* Paris, ESA-SP-215, pp. 643-646.

Domik, G., M. Kobrick and F. Leberl, 1984. Radarbildanalyse mit digitalen Hoehenmodellen, *Bildmessung und Luftbildwesen,* Vol. 52, No. 5, pp. 249-263.

Domik, G., 1985. *Verfahrensentwicklungen zur Analyse von digitalen Seitsicht-Radarbildern gebirgigen Geländes mittels digitaler Höhenmodelle und Bildsimulation,* Dissertation, Techn. Univ. Graz, Austria.

Domik, G. and F. Leberl, 1986. Using Secondary Image Products to Aid in Understanding and Interpretation of Radar Imagery, *Proceedings IGARSS '86,* Zurich, pp. 467-468.

Domik, G. and F. Leberl, 1987. Image Based SAR Product Simulation for Analysis, *Proceedings Amer. Society Photogrammetry and Remote Sensing, 53rd Ann. Conv.,* Baltimore, MD, pp. 355-364.

Domik, G., F. Leberl and J. Cimino, 1988. Dependence of Image Grey Values on Topography in SIR-B Images, *International Journal Remote Sensing,* Vol. 9, pp. 1013-1022.

Dowideit, G., 1975. A Simulation System for Theoretical Analysis of Radar Restitution and a Test by Adjustment, *Proceedings Symposium Comm. III, International Society Photogrammetry,* Stuttgart, in Deutsche Geodätische Kommission, Reihe B, Heft No. 214.

Dowideit, G., 1977a. Eine Blockausgleichung fuer Aufzeichnungen des Seitwärts-Radar, (SLAR) *Bildmessung und Luftbildwesen,* Vol. 45, No. 1, pp. 17-23.

Dowideit, G., 1977b. Eine Blockausgleichung für Abbildungen des Seitwärtsschauenden Radar (SLAR), Wissensch. *Arbeiten der Lehrstühle für Geodäsie, Photogrammetrie und Ingenieurvermessung,* No. 75, Techn. Univ. Hannover, FRG, 185 p.

Dowman, I.J. and R. Gibson,, 1983. An Evaluation of SAR 580 Synthetic Aperture Radar for Map Revision and Monitoring, Report for Ordnance Survey and Dept. of Environment, 21p.

Dowman, I.J. and A.H. Morris, 1982. The Use of Synthetic Aperture Radar for Mapping, *Photogrammetric Record,* Vol. 10, No. 60, pp. 687-696.

Dowman I., C. Clark and M. Denos, 1992. Three-Dimensional Data from SAR Images, *International Archives of Photogrammetry and Remote Sensing*, Vol. 24 (B4) pp. 425-427.

Dowman I., J. Laycock and J. Whalley, 1993. Geocoding in the UK. In Schreier G (ed.) *SAR Geocoding: Data and Systems,* Wichmann-Verlag, Karlsruhe, 435 p.

Dowman I., 1994. The OEEPE Test of Geocoding ERS-1 SAR Data: Background and Status, GeoSAR.

Dowman I., 1994. The OEEPE GeoSAR Test of Geocoding ERS-1 SAR Data: First Results, *ESA SP-361*, pp 643-646.

Dowman I., C. Pu-Hai, O. Clochez and G. Soundercock, 1994. Heighting from Stereoscopic ERS-1 Data, *ESA SP-361,* pp 609-614

Duchossois, G., 1986. Overview and Status Program of the ERS-1 Programme, *Proceedings IGARSS '86,* Zurich, ESA-Sp254, Vol. I, pp. 155-159.

Dunbar, M., 1975. Interpretation of SLAR Imagery of Sea Ice, *Journal Glaciology*, Vol. 15, pp. 193-213.

Durand, J.M., 1987. Theoretical Feasibility of SAR Interferometry, *Proceedings IGARSS '87,* Ann Arbor, MI.

Egbert, E., 1969. Calculation of Ground Street Lengths and Area from Radar Measurements, in Simonnett, D.S. (ed.), The Utility of Radar and Other Remote Sensors in Thematic Land Use Mapping from Spacecraft, *Annual Report, US Geological Survey, Interagency Report-NASA 140.*

Elachi, C., D. Evans and P. Rebillard, 1982. *Comparative Analysis of Co-Registered SIR-A, SEASAT and LANDSAT Images, IGARSS,* Munich, Vol. 2.

Elachi. C. *et al.,* 1982a. Spaceborne Synthetic-Aperture Imaging Radars: Applications, Techniques and Technology. *Proceedings IEEE,* Vol. 27. No. 10.

Elachi, C. *et al.,* 1982b. Shuttle Imaging Radar Experiment, *Science,* Vol. 218, pp. 996-1004.

Elachi, C., 1986a. *Spaceborne Radar Remote Sensing: Applications and Techniques,* IEEE Press, New York, 254 p.

Elachi, C., *et al.,* 1986b. Overview of the Shuttle Imaging Radar-B Preliminary Scientific Results, *Science,* Vol. 232, pp. 151 1-1516.

Elachi C., 1990. *Informal Memorandum to the Magellan Investigation Group,* Jet Propulsion Laboratory, Pasadena, Cal. See also Ford J., J. Plaut *et al.,* 1993. Chapter 7, p. 85

EOS, 1988. SAR- Earth Observing System Reports, Vol. IIf, Instrument Panel Report, NASA, Washington, DC, 233 p.

ERS-1, 1992. *Proceedings of the First ERS-1 Symposium, Space at the Service of Our Environment,* ESA-SP 359, 2 Volumes, 930 Pages.

ERS-1, 1994. *Proceedings of the Second ERS-1 Symposium, Space at the Service of Our Environment,* ESA-SP 361. 2 Volumes, 1360 p.

ESA, 1984. *Study of Land Feature Extraction for SAR Images,* ESA, (ESRIN), (Contract No. 5855/84/GPI, SC).

Esten, R.D., 1953. Radar Relief Displacement and Radar Parallax, *USAERDL-Report No. 1294,* Ft. Belvoir, VA.

Evans, D. and R. Blom, 1982. Potential of Multisensor Data and Strategies for Data Acquisition and Analysis, *JPL Publ. 82-93*, pp. 2.5-2.18.

Evans, D. and B. Stromberg, 1983. Development of Texture Signatures in Radar Images, *Proceedings IGARSS '83,* San Francisco, Vol. 1, pp. 6. 1-6.6

Evans, D., 1982. Analysis of a Multisensor Image Data Set of South Rafael Swell, Utah, *Proceedings ISPRS Comm. VII,* Toulouse, Vol. 1, pp. 255-259.

Eyton, J., R. Li and F. Ulaby, 1979. *Combined Radar and LANDSAT Multi-Imaged Crop Classification,* Univ. of Kansas, P/SL Tech. Rep. 360-10.

Filey, M., D. Rothrock, 1985. Extracting Sea-Ice Data from Satellite SAR Imagery, *Proceedings International Geoscience and Remote Sensing Symposium,* pp. 432-437.

Fiore, C., 1967. Side Looking Radar Restitution, *Photogrammetric Engineering,* Vol. XXXIII.

Fisher, T.A. and N. Minielly, 1985. Processing of Multi-Sensor Remotely Sensed Data to a Standard Geocoded Format, *Proceedings Machine Processing of Remotely Sensed Data,* Purdue Univ., pp. 183-188.

Fleming, E.A., 1980. Determination of the Geometric Accuracy of SEASAT-SAR Imagery Products, Sursat Project: Land Applications of SAR Cartography, Exper. 72, 15 p.

Fleming, E.A., 1982. Cartography Experiments, Sursat Project, Final Report, Vol. 2, 14 p.

Förstner, W., 1992. Image Matching. Chapter 16 in R. Haralick, L. Shapiro (eds.) *Computer and Robot Vision,* Addison-Wesley.

Ford, J.P., J.B. Cimino, C. Elachi, 1983. Space Shuttle Columbia Views the World with Imaging Radar: The SIR-A Experiment, Jet Propulsion Laboratory, *JPL Publ. 82-95,* Pasadena, CA, 179 p.

Ford J.P. and J.J. Plaut *et al.,* 1993. Guide to Magellan Image Interpretation. NASA *JPL Publ. 93-24,* 148 p.

Foster, J.L. and D.K. Hall, 1981. Multisensor Analysis of Hydrologic Feature with Emphasis on the SEASAT SAR, *Photogrammetric Engineering and Remote Sensing* Vol. 47, No. 5, pp. 655-664.

Frankot, R.T., 1983. SAR Image Registration by Multi-Resolution Correlation, *Proceedings SPIE,* Vol. 432, pp. 195-203.

Frankot, R. and R. Chellappa, 1987. Application of a Shape-from-Shading Technique to Synthetic Aperture Radar, *Proceedings IGARSS '87,* Ann Arbor, MI.

Frankot, R. and R. Chellappa, 1989. A Method for Enforcing Integrability in Shape from Shading Algorithms, in B. Horn, M. Brooks (eds.), *Shape from Shading,* MIT Press, Cambridge.

Frankot R., S. Hensley and S. Shafer, 1994. Noise Resistant Estimation Techniques for SAR Image Registration and tereo Matching, *Proceedings IEEE Geoscience Remote Sensing Symposium,* Pasadena, CA, pp 1151-153.

Friedman L. and J. Rose, 1973. Venus Orbital Imaging Radar Study (VOIR), NASA *JPL Report 760-89,* Pasadena, CA.

Froidevaux, C.M., 1980. Radar, an Optimum Remote Sensing Tool for Detailed Plate Tectonic Analysis and its Application to Hydrocarbon Exploration (an Example in Irian Jaya, Indonesia), in Radar Geology, an Assessment, Jet Propulsion Laboratory, *JPL-Publ. 80-61,* Pasadena, CA.

Frost, V. S. *et al.,* 1982. The Application of SAR Imagery to Stereo Viewing and Mapping, *Topics in Radar Image Analysis,* Univ. of Kansas, Rem. Sen. Lab., Ch. 8, pp. 179-212.

Frost, V. S., K. Shanmugam and J. Holtzman, 1982. Edge Detection for SAR and Other Noisy Images, *IGARSS,* Vol. 2., No. FA-2, Munich.

Frost, V.S. and L.S. Yurovsky, 1985. Maximum Likelihood Classification of Synthetic Aperture Radar Imagery, Comp. Vision, *Graphics & Image Proceedings,* Vol. 32, No. 3.

Frost, V.S., *et al.,* 1982. A Model for Radar Images and Its Application to Adaptive Digital Filtering of Multiplicative Noise, *IEEE Trans. Pattern Analysis Machine Intelligence,* Vol. PAMI-4, No. 2.

Fullerton, K., F. Leberl and R. Marque, 1986. Opposite-Side SAR Image Processing for Stereo Viewing, *Photogrammetric Engineering and Remote Sensing,* Vol. LII, No. 9, pp. 1487-1498.

Gabriel, A.K. and R.M. Goldstein, 1988. Crossed Orbit Interferometry: Theory and Experimental Results SIR-B, *International Journal Remote Sensing,* Vol. 9, No. 5.

Gabriel A. K., Goldstein R. M. and Zebker H. A., 1989. Mapping Small Elevation Changes Overlarge Areas: Differential Radar Interferometry, *Journal of Geophysical Research,* Vol. 94, No. B7, 10 July 1989, pp. 9183-9191.

Gardner, J.V. and L.F. Dellwig, 1980. Map Revision Using SLAR Imagery, *14th Congress International Society for Photogrammetry,* Hamburg.

Garinet, J.Y. and R. Jeansoulin, 1984. Evaluation of Topographic Profiles and Geometric Rectification on a SEASAT SAR Image, *Proceedings International Symposium on Remote Sensing of Environment,* Paris, Vol. 3, pp. 1333-1341.

Geier, F., 1971. *Beiträge zur Geometrie des Radarbildes,* Dissertation, Techn. Univ. Graz, Austria.

Geier, F., 1972. *Fundamentals for Orientation for Radar PPI Images with Approximated Horizontal Distances,* Pres. Paper, 12th Congress, International Society Photogrammetry, Ottawa., Canada

GEOSAR, 1987. Synthetic Aperture Radar Image Rectification Techniques, *Proceedings of the 1st Int'l GEOSAR-Workshop,* Loipersdorf, Austria.Published by Joanneum Research, Graz Austria.

GEOSAR, 1989. Geocoded and Value-Added Products. *Proceedings of the 2nd Int'l GEOSAR-Workshop,* Loipersdorf, Austria. Published by Joanneum Research, Graz Austria.

GEOSAR, 1991. Geocoded Products: Intercomparisons and Applications, *Proceedings of the 3rd Int'l GEOSAR-Workshop,* Farnham Castle, UK. Published by Earth Observation Sciences Limited, Brankhome Chambers, Branksomewood Road, Fleet, Hants, UK.

GEOSAR, 1994. Quality and Standards of High Level SAR Data. *Proceedings of the 4th Int'l GEOSAR-Workshop,* Loipersdorf, Austria, May 1993, Published by Earth Observation Sciences Limited, Brankhome Chambers, Branksomewood Road, Fleet, Hants, UK, ISBN 0-951-7722-52.

Gerbrands, J., 1984. Multiple Input Segmentation Algorithms for SLAR Imagery, *ESA-SP 227,* pp. 35-39.

Gerbrands J. and E. Backer, 1983. Segmentation of Multi-temporal SLAR Images, *Proceedings SPIE,* Vol. 397, pp. 173-179.

Giess, S.C., 1985. Aspects of SAR (Synthetic Aperture Radar) Image Segmentation, RSRE, Memorandum Report, 26 p.

Glushkov, W.M., *et al.,* 1972. Toros-Side Looking Radar System and its Application for Sea Ice Condition Study and for Geologic Explorations, Pres. Paper, 12th Congress, International Society Photogrammetry, Ottawa.

Goldstein, R.M. and W.F. Gillmore, 1963. Radar Observations of Mars, *Science,* Vol. 41, pp. 1171-1172.

Goldstein, R.M., 1965. Preliminary Venus Radar Results, *Radio Science,* Vol. 69D, pp. 1090-1092.

Goldstein, R.M., H. Zebker and C. Werner, 1988. Satellite Radar Interferometry: Two-Dimensional Phase Unwrapping, *Radio Science,* Vol. 23, No. 4.

Goldstein, R.M., 1967. Radar Studies of Venus, in *Moon and Planets,* E. Dolfus, ed., North-Holland, Amsterdam.

Goldstein, R.M. and H.C. Rumsey, 1970. A Random Snapshot of Venus, *Science,* Vol. 169, pp. 974-977,

Goldstein, R.M., R.R. Green and H.C. Rumsey, 1976. Venus Radar Images, *Journal Geophysical Research,* Vol. 81, No. 26, pp. 4807-4814.

Goldstein, R.M., 1992. Interferometry on Venus, Personal Communication, Jet Propulsion Laboratory, Pasadena, CA, USA.

Goodenough, D.G., B. Guindon and P.M. Teillet, 1979. Correction of Synthetic Aperture Radar and Mul-tispectral Scanner Data Sets, *Proceedings 13th International Symposium on Remote Sensing of Environment,* Ann Arbor, MI, pp. 259-270.

Goodenough, D.G., 1980. Quantitative Analysis of SAR for Detecting Forest Infestations of Insects, Final Report of the Airborne SAR Project, Intern. Environmental Consultants Ltd, Report No. ASP 80-1.

Goodenough, D. *et al.,* 1980. Integration and Comparison of SAR and MSS Data for Potato Crop Area Estimation, *Proceedings 6th Conference Symposium on Remote Sensing.*

Goodyear, 1972. Flight Test Report All-Weather Topographic Mapping System An/ASQ-142, Contract No. F 33657-70-0769, Goodyear Aerospace Corp., Litchfield Park, AZ.

Goodyear, 1974. Preliminary Imagery Data Analysis Goodyear Electronic Mapping System (GEMS), Goodyear Aerospace Corp., Report GIB-9342, Code 99696, Litchfield Park, AZ.

Gorbunov, Yu.,and S. Losev, 1974. Side-Looking Radar Imagery Assembly Topics for Studying Ice Drift, *Trans. Libtiki Autaktiki,* Nauch. Issued. Inst., Vol. 316, pp. 153-162.

Gracie, G., *et al.,* 1970. Stereo Radar Analysis, US Engineer Topograhic Laboratory, Report No. FTR-1339-1, Ft. Belvoir, VA.

Gracie, G. and E.D. Sewell, 1972. The Metric Quality of Stereo Radar, *Proceedings Techn. Program, Electro-Optical Systems Design Conference,* NY.

Graf, C., 1988. Verwendung geodätischer Abbildungen bei der Geocodierung von Satellitenbildern, *Remote Sensing Series,* Vol. 13, Remote Sensing Laboratories, University of Zurich.

Graham, L.C., 1970. Cartographic Applications of Synthetic Aperture Radar, *Proceedings American Society Photogrammetry, 37th Annual Meeting;* and Goodyear Aerospace Corp., Report GERA-1626.

Graham, L.C., 1972. An Improved Orthographic Radar Restitutor, pres. paper 12th Congress ISPS, Ottawa; Report GERA-1831, Goodyear Aerospace Corp., Litchfield Park, AZ.

Graham, L.C., 1974. Synthetic Interferometer Radar for Topographic Mapping, *Proceedings IEEE,* 62 (6).

Graham, L.C., 1975a. Geometric Problems in Side-Looking Radar Imaging, *Proceedings Symposium Comm. III, International Society Photogrammetry* Stuttgart, in Deutsche Geodaetische Kommission, Reihe B, Heft No. 214.

Graham, L.C., 1975b. Stereoscopic Synthetic Array Application in Earth Resources Monitoring, Report GERA-2076, Goodyear Aerospace Corp., Litchfield Park, AZ.

Graham, L.C., 1975c. Flight Planning for Stereo Radar Mapping, *Proceedings American. Society of Photogrammetry, 4lst Annual Conv.,* Washington, DC.

Graham, L.C., 1976a. *Exploitation of SAR Imagery,* SPIE, Vol. 79, pp. 107-116.

Graham, L.C., 1976b. *Earth Resources Radar Stereo Considerations,* Goodyear Aerospace Corp., AEEM-550, Litchfield Park, AZ, 13 p.

Greve, C. and W. Cooney, 1974. The Digital Rectification of Side Looking Radar, *Proceedings American. Society of Photogrammetry, 40th Annual Conv.,* Washington, DC.

Guertin, F. and E. Shaw, 1981. Definition and Potential of Geocoded Satellite Imagery Products, *Canadian Symposium Remote Sensing,* Winnipeg, obtainable from Canadian Centre for Remote Sensing, Ottawa.

Guindon, B., J.W.E. Harris, P.M. Teillet, D.G. Goodenough and J.F. Meunier, 1980. Integration of MSS and SAR Data for Forested Regions in Mountainous Terrain, *Proceedings 14th International Symposium Remote Sensing of Environment,* San Jose, Costa Rica, pp. 1673-1690.

Guindon, B. *et al.,* 1980. Relief Effects and the Use of Terrain Models in SAR Image Processing, *Proceedings 3rd SEASAT-SAR Workshop,* Frascati, Italy.

Guindon, B., D. Goodenough and P. Teillet, 1982. The Role of DTMs in the Remote Sensing of Forests, *Proceedings 8th Canadian Symposium on Remote Sensing,* Vol. 8, No. 1, pp. 4-16.

Guindon, B. and D.G. Goodenough, 1982. Spectral-Spatial Analysis of X and L Band SAR Imagery of Arctic Sea Ice, *Proceedings Comm. 2, International Society Photogrammetry and Remote Sensing,* Ontario, pp. 506-520.

Guindon, B., 1985. Automated Control Point Acquisition in Radar Optical Image Registration, *Canadian Journal Remote Sensing,* Vol. 1 1, No. l, pp. 103-112.

Guindon, B. and H. Maruyama, 1986. Automated Matching of Real and Simulated SAR Imagery as a Tool for Ground Control Point Acquisition, *Canadian Journal of Remote Sensing,* Vol. 12, pp. 149-158.

Guindon B., 1988. Multi-temporal Scene Analysis: A Tool to Aid in the Identificaiton of Cartographically Significant Edge Features on Satellite Imagery, *Canadian Journal of Remote Sensing,* Vol. 14, No. 1, May .

Guy, M. *et al.,* 1982. Apport des Images Composites SEASAT-LANDSAT pour l'Interpretation Thèmatique, *Proceedings*

Int. Society Photogrammetry and Remote Sensing Comm. VII, International Symposium, Toulouse, Vol. 1, pp. 215-230.

Guy, M., C. Lallemand, G. Legendre, A. Marie and J. Riom, 1982. Composite SEASAT-LANDSAT Digital Images for Thematic Mapping, *International Society of Photogrammetry and Remote Sensing Comm. VII,* International Symposium, Toulouse, Vol. 1, pp. 215-230.

Haack, B., 1979. Multi-Sensor Data Analysis of Urban Environments, *Photogrammetric Engineering and Remote Sensing,* pp. 1471-1477.

Hagfors, T., 1969. Backscattering from an Undulating Surface with Applications to Radar Returns from the Moon, *Journal Geophysical Research,* pp. 3779-3784.

Hall, D. and J. Ornsby, 1983. Use of SEASAT-SAR and LANDSAT-MSS Subsystem Data for Alaskan Glaciology Studies, *Journal Geophysical Research,* Vol. 88. No. C31 pp. 1597-1607.

Hall. G.T. and D. Rothrock, 1981. Sea Ice Displacement from SEASAT SAR, *Journal Geophysical Research,* Vol. 86, pp. 1 1078-1 1082.

Harmon, J.K., D. Campbell, J. Bindschadler, J. Head and I. Shapiro, 1986. Radar Altimetry of Mercury: A Preliminary Analysis, *Journal Geophysical Research,* Vol. 91, No. B1, pp. 385-401.

Hartl P. and K.H. Thiel, 1993. Bestimmung von Topographischen Feinstrukturen mit Interferometrischem ERS-1 SAR, *Z. für Photogrammetrie und Fernerkundung,* Vol 3, pp. 108-114.

Hartl P., K.H. Thiel and X. Wu, 1994. Information Extraction from ERS-1 SAR Data by Means of INSAR and DSAR in Antarctic Research, *ESA SP 361,* pp 697-701.

Hazen, R.S., 1985. Co-Registered Remote Sensing Imagery for Reconnaissance Engineering Geologic Mapping, *Bull. Assn. of Engineering Geologists,* Vol. 22, No. 1, pp. 3-7.

Henninger, D. and J. Carney, 1983. SIR-A Data as a Complement to LANDSAT MSS Data, *IGARSS'83,* San Francisco, Vol. 2, pp. 7.12-7.16.

Hevenor, R.A., 1985. Third Order Co-Occurence Texture Analysis Applied to Samples of High Resolution SAR Imagery, US Army ETL Report, ETL-0396, 32 p.

Hiller, E.R., (ed.) T.F. Wiener and E.L. Hall, 1979. Map-Matching Technique for Synthetic Aperture Radar Images, *Proceedings Society of Photo-Optical Instrumentation Engineers,* Vol. 186, pp. 115-122.

Hinse, M. *et al.,* 1988. Radiometric Correction of C-Band Imagery for Topographic Effects in Regions of Moderate Relief, *IEEE Trans. Geoscience and Remote Sensing,* Vol. GE-26.

Hirose, T.J. Cihlar and A. Mack, 1984. Discrimination of Agricultural Crops in Canada with SAR plus VIR Data: Initial Results, *Proceedings 8th Canadian Symposium on Remote Sensing,* pp. 387-403.

Hirsch, T. and J. van Kuilenburg, 1976. Preliminary Tests of the EMI-SLAR Mapping Quality, Netherlands Interdepartmental Working-Community for the Application and Research of Remote Sensing (*NIWARS. Internal Report No. 39,* Delft, The Netherlands.

Hockeborn, H.A., 1971. Extraction of Positional Information from Side Looking Radar, *Bildmessung und Luftbildwesen,* Vol. 39, No. 1.

Hoekman, D., 1984. Texture Analysis of SLAR Images as an Aid in Automized Classification of Forested Areas, EAS-SP227, pp. 99-109.

Hoffmann, P., 1958. Photogrammetric Applications of Radar Scope Photographs, *Photogrammetric Engineering,* Vol. XXIV.

Hohenberg, F., 1950. Zur Geometrie des Funkmessbildes, Austrian Academy of Sciences, *Math.-Naturwissenschaftliche Klasse,* Vienna, 2-3.

Holtzman, J.C. *et al.,* 1977. Radar Image Simulation: Validation of the Point Scattering Method, Report ETL-0017, 1, USA Engineer Topographic Laboratory, Ft. Belvoir, VA.

Holtzman, J.C., V.S. Frost, J.L. Abbott and V.H. Kaupp, 1978) Radar Image Simulation, *IEEE Trans. Geoscience Electronics,* Vol. GE-16, No. 4, pp. 296-303.

Hoogeboom, P., 1984a. Preprocessing of Side-Looking Airborne Radar Data, *International Journal Remote Sensing,* Vol. 4, No. 3. pp. 631-637.

Hoogeboom, P., 1984b. Optimization of Agricultural Crop Identification in SLAR Images: Hierarchic Classification and Texture Analysis, *ESA-SP 227,* pp. 41-48.

Hoogeboom, P., P. Binnenkade and L. Veugen, 1984. An Algorithm for Radiometric and Geometric Correction of Digital SLAR Data, *IEEE Trans. Geoscience and Remote Sensing,* Vol. GE-22, No. 6, pp. 750-776.

Horn, B., 1970. Shape-from-Shading: A Method for Obtaining the Shape of a Smooth Opaque Object from One View, MIT Artificial Intelligence Laboratory, Publ. AI-TR-232.

Horn, B., 1975. Obtaining Shape-from-Shading Information, in *Psychology of Computer Vision,* P. Winston, ed., McGraw-Hill, New York.

Horn, B., *et al.,* 1978. Using Synthetic Images to Register Real Images with Surface Models, *CACM,* Vol. 21.

Horn, B., 1986. *Robot Vision,* MIT Press, Cambridge, MA.

Howard, P.D., 1985. Radargrammetry: The Link Between Radar Imagery and Geographic Information Systems, *Proceedings Conference Advanced Technology for Monitoring and Processing Global Environmental Data,* Remote Sensing Society, pp. 319-329.

Hsu, A., S. Bruzzi and J. Lichtenegger, 1984. Evaluation of CV580 SAR Images for Mapping Applications, *Proceedings 50th Annual Meeting ASP-ACSM,* Washington, DC, pp. 699-711.

Hug, J.F. *et al.,* 1984. An Approach for the Geometric Rectification of Radar Imagery, *Proceedings Thematic Conference International Symposium on Remote Sensing of Environment,* Colorado Springs, CO, Vol. 2, pp. 929-938.

Hug, J.F., V. Kaupp, W. Waite and H. MacDonald, 1986. Interferometer Applications for the Rectification of Radar Images, *Proceedings IGARSS '86,* Zurich, pp. 473-477.

Innes, R.B., 1964. Principles of SLAR Measurement of the Third Coordinate of Target Position, Report of Project Michigan, No. 2900-474-T.

Jackson, P.L., 1983. Reflection and Identification Studies Applied to Terrain Imaging Radar, US Army ETL Report, ETL-0331, 75 p.

Jensen, H., 1972. Mapping with Coherent-Radiation Focused Synthetic Aperture Side Looking Radar, in *Operational Remote Sensing: An Interactive Seminar to Evaluate Current Capabilities,* American Society Photogrammetry, Falls Church, VA.

Jensen, H., 1975. Deformations of SLAR Imagery-Results from Actual Surveys, *Proceedings Symposium Comm. III, Int. Society Photogrammetry,* Stuttgart, in Deutsche Geodaetische Kommission, Reihe B. Heft No. 214.

Jonah, M.V. and C. DiCarlo, 1970. DoD Data Processing Equipment for Radar Imagery, *Proceedings, American Society of Photogrammetry Annual Convention,* pp. 207-232.

Journal of Geophysical Research, 1992. Magellan at Venus, Volume 97, Nr. E8 and E10, August and October. pp 13063-16382.

Kashef, B.G. and A.A. Sawchuck, 1983. A Survey of New Techniques for Image Registration and Mapping, *Proceedings Society of Photo-Optical Instrumentation Engineers,* Vol. 432, Applications of Digital Image Processing VI, pp 222-239

Kasischke, E.S., G.A. Meadows and P.L. Jackson, 1984. Use of Synthetic Aperture Radar Imagery to Detect Hazards to Navigation, ERIM-169200-2-F, Contract N00014-83-C-2223, 253 p.

Kaufmann V., W. Mattner, J. Raggam, A. Almer and J. Schnell, 1994. Stereo-Radargrammetric Evaluation of ERS-1 SAR Images: A Case Study in Southern Italy. ESA SP 361, pp 1211-1216.

Kaupp, V.H., H.C. MacDonald and W.P. Waite, 1983. The Impact of Terrain Models and Computer Analysis on Future Shuttle SAR Missions, *ASP-ACSM, Fall Conv., Salt Lake City,* pp. 226-235.

Kaupp, V.H., H.C. MacDonald, W.P. Waite, J.A. Stiles and F.S. Frost, 1982. Analysis of Geologic Terrain Models for Determination of Optimum SAR Sensor Configuration and Optimum Information Extraction for Exploration of Global Non-Renewable Resources, Pilot Study: Arkansas Remote Sensing Laboratory, Part 1, Part 2 and Part 3, in Cooperation with Univ. of Kansas, Center for Research.

Kaupp, V., *et al.,* 1986. SAR Simulation, *Proceedings IGARSS '86,* Zurich.

Kaupp, V., H. MacDonald and W. Waite, 1981. Image Radar: Analysis of Propagation Distortions, Arkansas Remote Sensing Laboratory Technical Report, ARSL TR 81-1, Univ. Arkansas, Fayetteville.

Kaupp, V., L. Bridges, M. Pisaruk, H. MacDonald and W. Waite, 1983. Simulation of Spaceborne Stereo Radar Imagery-Experimental Results, *IEEE Trans. Geoscience and Remote Sensing,* Vol. GE-21, No. 3, pp. 400-405.

Kaupp, V., W. Waite and H. MacDonald, 1982. Incidence Angle Considerations for Spacecraft Imaging Radar, *IEEE Trans. Geoscience and Remote Sensing,* Vol. GE-20, No. 3, pp. 384-390.

Kavanagh, P., I. Wong, B. Guindon and G. Princz, 1989. Canada's Fast Operational ERS-1 SAR Precision Processing and Geocoding System, *Proceedings IGARSS '89,* pp. 1795-1798.

Khizhnichenko, V.I., 1984. Mathematical Model of Earth's Surface Imaging by Spaceborne Synthetic Aperture Radar, *Soviet Journal Remote Sensing.*

Kiremidjian, G.K., 1980. Image-to-Map Registration, *Proceedings Society Photo-Opt. Instrum. Engineering,* Vol. 238, pp. 184-192.

Kiremidjian, G.K., 1981. Registration of a Synthetic Aperture Radar, (SAR) Reconnaissance Image with a Map Reference Data Base, *Proceedings Society of Photo-Optical Instrumentation Engineers,* Vol. 281, Washington, DC, pp. 110-115.

Kiremidjian, 1981. Radar Image to Map Registration, *Optical Engineering,* Vol. 20, pp. 899-906.

Kirk, R.L., 1984. A Finite-Element Approach to Two-Dimensional Photoclimometry, (abstract), *Bull. Amer. Astron. Society,* Vol. 16, p. 709.

Kirk, R.L., 1987. A Fast Finite-Element Algorithm for Two-Dimensional Photoclimometry, Part III, Ph.D. Thesis, California Institute of Technology, pp. 165-258.

Kirk R., L. Soderblom and E. Lee, 1992. Enhanced Visualization for Interpretation of Magellan Radar Data: Supplement to the Magellan Special Issue, *Journal Geophysical Research,* Vol. 97, No. 10, pp 16371-16380.

Kober, C.L., *et al.,* 1950. Determination of a Target Height from Radar PPI-Photographs, Air Force Techn. Report No. 6500, Wright Air Development Center, Wright Patterson AFB, OH.

Kobrick, M., F. Leberl and J. Raggam, 1986. Radar Stereo Mapping with Crossing Flight Lines, *Canadian Journal Remote Sensing,* Vol. 12, No. 2, pp. 132-148.

Konecny, G. and E.E. Derenyi, 1966. Geometric Consideration for Mapping from Scan Imagery, *Proceedings 4th Symposium Remote Sensing of the Environment,* Ann Arbor, MI.

Konecny, G., 1970. Metric Problems in Remote Sensing, *International Inst. for Aerial Surveying and Earth Sciences (ITC), Series A,* No. 50, Delft, The Netherlands.

Konecny, G., 1971. Orientierungsfragen bei Streifenbildern und Aufnahmen der Infrarotabtastung, *Bildmessung und Luftbildwesen,* Vol. 41, No. 1.

Konecny, G., 1972a. Geometrical Aspects of Remote Sensing, *Archives International Society Photogrammetry, 12th Congress,* invited paper, Ottawa.

Konecny, G., 1972b. Geometrische Probleme der Fernerkundung, *Bildmessung und Luftbildwesen,* Vol. 42, No. 2.

Konecny, G., 1975. Approach and Status of Geometric Restitution for Remote Sensing Imagery, *Proceedings Symposium Comm. III, International Society Photogrammetry,* Stuttgart, in Deutsche Geodaetische Kommission, Reihe B, Heft No. 214.

Konecny, G., P. Lohmann and W. Schuhr, 1984. Practical Results of Geometric SAR-580 Image Evaluation, *Proceedings SAR-580, Investigators Workshop,* ISPRA, Italy, Vol. L, No. 2, pp. 187-193.

Konecny, G., W. Schuhr and J. Wu, 1982. Untersuchungen über die Interpretierbarkeit von Bildern unterschiedlicher Sensoren und Plattformen fuer die kleinmasstäbige Kartierung, *Bildmessung und Luftbildwesen,* Vol. 50, No. 6, pp. 187-200.

Koopmans, B., 1974. Drainage Analysis on Radar Images, *ITC-Journal* 1973-2, Enschede, The Netherlands.

Koopmans, B., 1974. Should Stereo SLAR Imagery Be Preferred to Single Strip Imagery for Thematic Mapping?, *ITC Journal* Vol. 2, No. 3, Enschede, The Netherlands.

Korneev, I.N., 1978. Analytical Method for Photogrammetric Processing of a Single Radar Photograph, *Geodezia i Aerofotosjomka,* Vol. 2, pp. 115-124.

Kosman D., A. Roth and G. Schreier, 1992. Operational Geocoding of ERS-1 SAR Imagery, *Int'l Archives of Photogrammetry and Remote Sensing,* Washington, D.C.

Kosman D., A. Roth, G. Schreier and R. Winter, 1992. ERS-1 Radarmaps of Germany and the Antarctic Pensinsula, *ESA-ISY-2,* pp 321-326.

Kosman D., R. Winter and M. Wiggenhagen 1993. Mosaicking for the Radarmap Germany, *GEOSAR'93.*

Kratky, V., 1979. SEASAT Orbit Effects on Imaging Geometry of Synthetic Aperture Radar, *Proceedings of the 3rd GDTA Symposium,* Toulouse, France.

Kropatsch, W., F. Leberl, G. Paar, J. Raggam, A. Rioza and D. Strobl, 1988. Radargrammetric Image Data Evaluation, *DIBAG Report 30,* Graz Research Center, Austria, Final Report for ESA Contract No. 6.121/85/F/FL(SC), M. Buchroithner, G. Triebnig (eds.), 141 p.

Kwok, R., J. Curlander and S. Pang, 1987. Rectification of Terrain Induced Distortions in Radar Imagery, *Photogrammetric Engineering and Remote Sensing,* Vol. 53, pp. 507-513.

Kwok, R. and J. Curlander, 1987. Automated Rectification and Geocoding of SAR Imagery, *Proceedings IGARSS '87,* Ann Arbor, MI.

Kwok R., J.C. Curlander and R. McConnell, S. Pang, 1990. An Ice Motion Tracking Ssystem at the Alaska SAR Facility, *IEEE Journal of Oceanic Engineering,* Vol. 15, Nr. 1, pp 44-45

Lannelongue, N., T. Charpentier and R. Serriere, 1980. Realisation d'une Mosaique Radar, *Bulletin of the Society Francaise de Photogrammetrie et de Télédétection,* No. 3-4, pp. 41-48.

LaPrade, G.L., 1963. An Analytical and Experimental Study of Stereo for Radar, *Photogrammetric Engineering,* Vol. XXIX.

LaPrade, G.L., 1969. Elevations from Radar Imagery, *Photogrammetric Engineering,* Vol. XXXV.

LaPrade, G.L., 1970. Subjective Considerations for Stereo Radar, Goodyear Aerospace Corp., *Rep. GIB-9169;* also in *Photogrammetric Engineering,* Vol. XXXVI.

LaPrade, G., 1972. Stereoscopy-A More General Theory, *Photogrammetric Engineering,* Vol. XXXVIII, pp. 1177-1187.

LaPrade, G., 1973a. Stereoscopy-Will Facts or Dogma Prevail? *Photogrammetric Engineering,* Vol. XXXIX, pp. 1271-1275.

LaPrade, G., 1973b. A More General Theory of Stereoscopy, Goodyear Aerospace Corp., *GIB-9268, Rev. A,* Litchfield Park, AZ, 58 p.

LaPrade, G.L., 1975a. Radar Signature of Inverted Catenary with Equilateral Triangular Cross Section (St. Louis Gateway Arch), *Arizona Electronics Engineering Memo. No. 525,* Goodyear Aerospace Corp., Litchfield Park, AZ.

LaPrade, G., 1975b. Stereoscopy, Goodyear Aerospace Corp., *GERA-2120, Code 99696,* Litchfield Park, AZ, 57 p.

LaPrade, G.L., 1975c. *Addendum to GIB-9f69, Subjective Considerations for Stereo Radar,* Loral Defense Systems (formerly Goodyear Aerospace Corp.). Litchfield Park, AZ.

LaPrade, G.L., *et al.,* 1980. Stereoscopy, in *Manual of Photogrammetry, 4th Ed.,* Amer. Society Photogrammetry, Falls Church, VA.

Lawton, D., T. Glicksman, G.D. Conner and R.J. Drazovich, 1985. Linear Feature Extraction from Radar Imagery, *Final Report ETL-0405,* 149 p.

Leberl, F., 1970. Metric Properties of Imagery Produced by Side Looking Airborne Radar and Infrared Line Scan Systems, Publications of the International Institute for Aerial Survey and Earth Sciences *(ITC), Series A, No. 50,* Delft, The Netherlands.

Leberl, F., 1971. Vorschläge zur instrumentellen Entzerrung von Abbildungen mit Seitwärts Radar (SLAR) und Infrarotabtastsystemen, *Bildmessung und Luftbildwesen,* Vol. 39.

Leberl, F., 1971. Remote Sensing-Neue Methoden zur Wahrnehmung auf Abstand, Österr. Zeitschrift fuer Vermessungswesen, No. 6.

Leberl, F., 1972a. On Model Formation with Remote Sensing Imagery, Oesterr. Z. fuer Vermessungswesen und *Photogrammetrie,* No. 2, pp. 43-61.

Leberl, F., 1972b. Evaluation of Single Strips of Side Looking Radar Imagery, *Archives International Society Photogrammetry, 12th Congress,* Invited Paper, Ottawa.

Leberl, F., 1972c. Radargrammetria para los interpretes de imagenes, *Centro Interamericano de Fotointerpretacion (CIAF),* Bogota, Colombia.

Leberl, F., 1974. Evaluation of SLAR Image Quality and Geometry for Proradam, *ITC Journal,* Vol. 2, No. 4, Enschede, The Netherlands.

Leberl, F., 1975a. The Geometry of and Plotting from, Single Strips of Side Looking Airborne Radar Imagery, International Institute for Aerial Survey and Earth Sciences, *ITC Technical Report, No. l,* Enschede, The Netherlands.

Leberl, F., 1975b. Photogrammetric Interpolation, *Photogrammetric Engineering,* Vol. XLI.

Leberl, F., 1975c. Lunar Radargrammetry with ALSE-VHF Imagery, *Proceedings American Society Photogrammetry, Fall Techn. Meeting,* Phoenix, AZ.

Leberl, F., 1975d. Radargrammetry for Image Interpretation, *ITC Technical Report, No. 2,* 136 p.

Leberl, F., 1975e. Radargrammetric Point Determination PRORADAM, *Bildmessung und Luftbildwesen,* Vol. 43, No. 1, pp. 11-17.

Leberl, F., 1975f. Sequential and Simultaneous SLAR Block Adjustment, *Photogrammetria,* Vol. 31, pp. 35-51; also in *Proceedings American Society Photogrammetry, 41st Ann. Conv.,* Washington, DC, pp. 528-538.

Leberl, F.,1976a. Mapping of Lunar Surface from Side-Looking Orbital Radar Imagery, *The Moon,* Vol. 15, pp. 329-342.

Leberl, F., 1976b. Imaging Radar Applications to Mapping and Charting, *Photogrammetria,* Vol. 3, pp. 75-100.

Leberl, F., T. Farr, L. Bryan and C. Elachi, 1976c. Study of Arctic Sea Ice Drift from L-Band Side Looking Radar Imagery, *Proceedings American Society Photogrammetry, 42nd Annual Conv.,* Washington, DC.

Leberl, F., J. Jensen and J. Kaplan, 1976d. Side-Looking Radar Mosaicking Experiment, *Photogrammetric Engineering and Remote Sensing,* Vol. XLII.

Leberl, F. and C. Elachi, 1977a. Mapping with Satellite Side-Looking Radar, Proceedings *2nd GDTA Symposium,* St. Mande, France, pp. 451-465.

Leberl, F., 1977b. Radar Mapping Applications Using Single Images, Stereo Pairs and Image Blocks: Methods and Applications, *Revista Brasileira de Cartographia,* No. 20, pp. 16-26.

Leberl, F., 1978a. *Satellitenradargrammetrie, Deutsche Geodätische Kommission,* Series C, Vol. 239, Munich, 156 p.

Leberl, F., 1978b. Current Status and Perspectives of Active Microwave Imaging for Geoscience Application, *ITC Journal,* 1978-1.

Leberl, F. and H. Fuchs, 1978c. Photogrammetric Differential Rectification of Radar Images, Pres. Paper, Symposium International Society Photogrammetry, Comm. III, Moscow; also in *Mitteilungen der geodaetischen Institute,* No. 33, Techn. Univ. Graz, Austria.

Leberl. F., M.L. Bryan, C. Elachi, T. Farr and W. Campbell, 1979. Mapping of Sea-Ice and Measurements of its Drifts Using Aircraft Synthetic Aperture Radar Images, *Journal Geophysical Research,* Vol. 84, No. C40, pp. 1827-1935.

Leberl, F., 1979a. Accuracy Aspects of Stereo-Side-Looking Radar, Jet Propulsion Laboratory, *JPL Publ. 79-17,* Pasadena, CA.

Leberl, F., 1979b. Accuracy Analysis of Stereo Side-Looking Radar, *Photogrammetric Engineering and Remote Sensing,* Vol. 45, pp. 1083-1096.

Leberl, F. and E. Clerici, 1980. Current Status of Metric Reduction of Active Sensor Data, *Archives International Society Photogrammetry,* Vol. 23, No. B.3, pp. 435-450.

Leberl, F., 1980. Preliminary Radargrammetric Assessment of SEASAT-SAR Images, *Mitteilungen der geodaetischen Institute, No. 33,* Techn. Univ. Graz, Austria, pp. 59-80.

Leberl, F., 1981. The Venus Orbital Imaging Radar (VOIR) Mission, *Proceedings Alpbach Summer School,* ESA SP-164.

Leberl, F., H. Fuchs and J. Ford, 1981. A Radar Image Time Series, *International Journal of Remote Sensing,* Vol. 2, No. 2.

Leberl, F., 1982a. Radargrammetr.y and Merging of Multi-Sensor Data, *Proceedings International Society Photogrammetry and Remote Sensing, Comm. ll, Ottawa, International Archives of Photogrammetry,* Vol. 24-II, pp. 536-545.

Leberl, F., 1982b. The Applicability of Satellite Remote Sensing to Small and Medium Scale Mapping, ESA Symposium on

Satellite Remote Sensing for Developing Countries, *ESA SP175,* pp. 81-85.

Leberl, F., J. Raggam and M. Kobrick, 1982. Stereo Side-Looking Radar Experiments, *Proceedings IGARSS '82,* Munich, Vol. II, pp. TA-5/2.1 to 5/2.7; also in *Proceedings ISPRS Comm. III Symposium,* Techn. Univ., Helsinski, pp. 597-611.

Leberl, F., 1983. Photogrammetric Aspects of Remote Sensing with Imaging Radar, *Remote Sensing Reviews,* Vol. 1, No. 1, pp. 71-158.

Leberl, F., J. Raggam, C. Elachi and W. Campbell, 1983. Sea Ice Motion Measurements from SEASAT SAR Images. *Journal Geophysical Research,* Vol. 88, No. C3, pp. 1915-1928.

Leberl, F., G. Domik and J. Raggam, 1984. Rectification of Radar Images Using Stereo-Derived Height Models and Simulation, *Archives International Society Photogrammetry and Remote Sensing,* Vol. XXV, No. A3 pp. 109-111.

Leberl, F., J. Raggam and M. Kobrick, 1985. On Stereo Viewing of SAR Images, *IEEE Trans. Geoscience and Remote Sensing,* Vol. GE-23, No. 2, pp. 110-117.

Leberl, F., G. Domik and M. Kobrick, 1985. Mapping with Aircraft and Satellite Radar Images, *Photogrammetric Record,* Vol. 11. No. 66, pp. 647-666.

Leberl, F., G. Domik, J. Raggam, J. Cimino and M. Kobrick, 1986a. Radargrammetric Experiments with Space Shuttle SIR-B Imagery, *Proceedings ISPRS-Commission II, Baltimore, Archives of ISPRS,* Vol. 26, pp. 333-344.

Leberl F., G. Domik, J. Raggam, J. Cimino and M. Kobrick, 1986b. Space Shuttle Radargrammetry Results, *Proceedings Ann. Conv. of ASPRS/ACSM,* Vol. 5, pp. 198-201.

Leberl, F., G. Domik, J. Raggam, J.B. Cimino and M. Kobrick, 1986c. Multiple Incidence Angle SIR-B Experiment over Argentina: Stereo-Radargrammetric Analysis, *IEEE Trans. Geoscience and Remote Sensing,* Vol. GE-24. No. 4, pp. 482-491.

Leberl, F., G. Domik, J. Raggam. J.B. Cimino and M. Kobrick, 1986d. Radar Stereo-Mapping Techniques and Application to SIR-B lmages of Mt. Shasta, *IEEE Trans. Geoscience and Remote Sensing,* Vol. GE-24, pp. 473-481.

Leberl, F., G. Domik and B. Mercer, 1987. Methods and Accuracy of Operational Digital Image Mapping with Aircraft SAR, *Proceedings Ann. Conv. American Society Photogrammetry and Remote Sensing,* Vol. 4, pp. 148-158.

Leberl, F. and B. Mercer, 1987. Chasing the Clouds Away, *Computer Graphics World,* April 1987, pp. 50-52.

Leberl, F., 1987. Some Mapping Applications for SAR Imagery. In Remote Sensing: Towards Operational Cartographic Application, *1st W. Nordberg Symposium,* Graz Research Centre, M. F. Buchroithner, R. Kostka (eds.), pp. 109-114.

Leberl, F., W. Mayr, G. Domik and M. Kobrick, 1988. SIR-B Stereo Radargrammetry of Australia, *Intl. Journal Remote Sensing,* Vol. 9, pp. 997-1011.

Leberl, F. and M. Karspeck, 1988. Stereo SAR from Film and Softcopy Imagery--System CRAVEX, *Proceed. Intl. Workshop on Analytical Instrumentation,* Phoenix, AZ, 2-6 November 1987.

Leberl, F., G. Domik, B. Mercer and R. Ingster, 1988. Stereo-Mapping with Radar Imagery, *Proceed. Intl. Workshop on Analytical Instrumentation,* Phoenix, Arizona, 2-6 November 1987.

Leberl, F., 1990. *Radargrammetric Image Processing,* Artech House, Norwood, MA, 700 pages.

Leberl, F., M. Millot, R. Wilson, M. Karspeck, B. Mercer and S. Thornton, 1991a. Radargrammetric Image Processing with a Softcopy Stereo Workstation. Proceedings, *8th Thematic Conference on Geologic Remote Sensing,* Denver, CO, April 29 - May 2, pp. 639-647.

Leberl, F., K. Maurice, J. Thomas and W. Kober, 1991b. Radargrammetric Measurements from the Initial Magellan Coverage of Planet Venus, *Photogrammetric Engineering and Remote Sensing,* Vol. 57, No. 12, pp. 1561-1570.

Leberl, F.W., K.E. Maurice and J.K. Thomas, 1992a. Radargrammetric Analysis With Magellan Data of Planet Venus. Proceedings 58th Annual Convention, *American Society of Photogrammetry and Remote Sensing Conference,* Albuquerque, NM, pp. 253-263.

Leberl, F. W. and K. Maurice, 1992b. Stereo-Mapping of Planet Venus From Magellan SAR Images: A Status Report, *Archives of the 17th ISPRS Congress,* Washington, DC, Vol. XXIX, Part B2, pp. 795-800.

Leberl, F., K. Maurice, J. Thomas, C. Leff and S. Wall, 1992c. Images and Topographic Relief at the North Pole of Venus. *Journal of Geophysical Research,* 13667-13674.

Leberl, F.W., J.K. Thomas and K.E. Maurice, 1992d. Initial Results From the Magellan Stereo-Experiment, *Journal Geophysical Research,* 13675-13687.

Leberl, F.W., R. Kwok and T. Baltzer, 1993. Sea Ice Mapping With ERS-1 Images, *Proceedings of the 25th International Symposium on Remote Sensing and Global Environmental Change,* 4-8 April, Volume I, pp. 595-603.

Leberl, F.W., 1993a. How To Extract Venus Topographic Information From Magellan Radar Images, *SPIE Proceedings* Vol. 1943.

Leberl, F.W., 1993b. Development of a Stereo Analysis and Visualization Tool Kit for Planetary Radar Images, *International Workshop on Image Analysis and Synthesis, Graz,* Published by R. Oldenbourg, Wien, pp. 45-56.

Leberl, F.W., 1993c. An Experiment to Match Radar Images., *Proceedings of the 4th GeoSAR Workshop,* Publ. by EOS Ltd., England.

Leberl, F.W., K. Maurice, J. Thomas and M. Millot, 1994. Automated Radar Image Matching Experiment, *ISPRS Journal of*

Photogrammetry and Remote Sensing, Vol. 49, No. 3, pp.19-33.

Leonardo, E., 1963. Comparison of Imaging Geometry for Radar and Photographs, *Photogrammetric Engineering,* Vol. XXXXIX.

Leonardo, E., 1964. Capabilities and Limitations of Remote Sensors, *Photogrammetric Engineering,* Vol. XXX.

Leonardo, E., 1969. An Application of Photogrammetry to Radar Research, *Photogrammetric Engineering,* Vol. XXV.

Levine, D., 1963. Principles of Stereoscopic Instrumentation for PPI-Photographs, *Photogrammetric Engineering,* Vol. XXX.

Levine, D., 1960. *Radargrammetry,* McGraw-Hill, NY.

Levine, D., 1965. Automatic Production of Contour Maps from Radar Interferometric Data, pres. paper, Fall Tech. Meeting, American Society Photogrammetry, Dayton, OH.

Lewis, A.J. and H.C. MacDonald, 1970. Interpretive and Mosaicking Problems of SLAR Imagery, *Remote Sensing of the Environment,* Vol. 1, No. 4.

Li, F. and R. Goldstein, 1990. Studies of Multi-Baseline Spaceborne Interferometric Synthetic Aperture Radars, *IEEE Trans. on Geoscience and Remote Sensing,* Vol. 28, No. 1, pp 88-97.

Loelkes, G.L., 1965. Radar Mapping Imagery-its Enhancements and Extraction for Map Construction, pres. paper, Fall Tech. Meeting, American Society Photogrammetry, Dayton, OH.

Loshchilov, U.S. and U.A. Voyevodin, 1972. Determining Elements of Drift of the Ice Cover and Movement of the Ice-Edge by the Air of the TOROS Aircraft Lateral Scan Radar Station, Problemi Artiki, *Antartiki,* No. 40, pp. 23-30.

Luchininov, V.S., 1976. Contactless Radar Mapping of Warm Valley Glaciers-Transformation of Radar Coordinates, Trans. from Russian in Soviet Physics, *Technical Physics,* Vol. 20, No. 4.

Luo, B., C.C. Yang, S.K. Chang and M.C.K. Yang, 1984. Detecting Potential Ship Objects from Satellite Pictures, *IEEE Comp. Society Workshop on Visual Languages,* Japan, pp. 6-13.

Macchia, R.P., 1957. Radar Presentation Restitutor, *Photogrammetric Engineering,* Vol. XXIII.

MacDonald, H. and W. Waite, 1971. Optimum Radar Depression Angles for Geological Analysis, *Modern Geology,* Vol. 2, pp. 179-193.

MacDonald H., 1969. Geologic Evaluation of Radar Imagery from Eastern Panama and Northwestern Colombia. Ph.D. Dissertation, University of Kansas, 120 p.

Mader, G. and W. McCandless, 1981. *Space Based Topographic Mapping Experiment Using SEASAT-SAR and LANDSAT-3-RBV Imagery,* Phoenix Corporation, McLean, Virginia, 36 p.

Maeda, K. and H. Sato, 1988. Data Processing and Calibration of SAR Data in Japan, *Proceedings 16th Congress International Society Photogrammetry and Remote Sensing,* Kyoto, Japan, Vol. 27, Part B11, pp. I-232 to I-241.

Manual of Photogrammetry, 1966. Photogrammetric and Radargrammetric Techniques, Vol. II, 3rd Ed., Published by the American Society for Photogrammetry and Remote Sensing, Falls Church, VA.

Marconi, 1984. SAR Simulation Concept and Tools, Final Report. Marconi Research Centre (UK), Report MTR 84/34, 109 p.

Marque, R. and H. Maurice, 1978. Combined SAR/LANDSAT Imagery, Manuscript, Goodyear Aerospace Corp., Litchfield Park, AZ, 8 p.

Martin-Kaye, P.H.A., *et al.,* 1980. Fracture Trace Expression and Analysis in Radar Imagery of Rain Forest Terrain (Peru), in Radar Geology, an Assessment, Jet Propulsion Laboratory, *JPL Publ. 80-61,* Pasadena, CA.

Massonet D. and M. Rossi *et al.,* 1993. The Displacement Field of the Landers Earthquake Mapped by Radar Interferometry. *Nature,* Vol. 364.

Massonnet D., 1993. Geoscientific Applications at CNES. Chapter 18 in G. Schreier (ed.) *SAR Geocoding: Data and Systems.* Wichmann-Verlag, Karlsruhe, Germany, pp. 397-415.

Massonnet D., 1994. Validation of ERS-1 Interferometry at CNES. *ESA SP-361,* pp 703-709.

Masursky, H., E. Eliason, P.G. Ford, G.E. McGill, G.H. Pettengill, G.G.Schaber and G. Schubert, 1980. Pioneer Venus Radar Results: Geology from Images and Altimetry, *Journal Geophysical Research,* Vol. 85, No. A13, pp. 8232-8260.

Matthews, R.E., ed., 1975. Active Microwave Workshop Report, *NASA Special Report SP-376,* Washington, DC.

Maurer, H., J.I. Oberholtzer and P. Anuta., 1979. Synthetic Aperture Radar/LANDSAT MSS Image Registration, *NASA Ref. Publ. No. 1039,* 235 p.

McCandless, W., 1982. Multiple-Sensor Processing-the Importance of its Influence on System Design, *Proceedings International Society Photogrammetry and Remote Sensing Comm. II Symposium,* Ottawa, pp. 553-560.

McConnell, R., W. Kober, F. Leberl, R. Kwok and J. Curlander, 1989. Automated Tracking of Arctic Ice Floes in Multitemporal SAR Imagery. *Proceed. IGARSS '89,* Vol. 2, pp. 1112-1114.

McConnell R., F. Leberl and W. Kober, 1990. Tracking of Ice Floes in SAR Images. Chapter 19 in *Radargrammetric Image Processing,* Artech House, Norwood, MA, pp. 499-525.

McConnell R., P. Kwok, J. Curlander, S. Pang and W. Kober, 1991. PSI-S Correlation and Dynamic Time Warping: Two

Methods for Tracking Ice Floes in SAR Images. *IEEE Trans. Geoscience Remote Sensing.* Vol. 29, pp 1004-1014.

Megier, J., W. Mehl and R. Ruppelt, 1984a. Methodological Studies of Rural Land Use Classification of SAR and Multi-Sensor Imagery, *Proceedings SAR 580 Investigators Workshop,* ISPRA, Italy, Vol. 2.

Megier, J., W. Mehl and R. Ruppelt, 1984b. Per-Field Classification and Application to SPOT Simulations, SAR and Combined SAR-MSS Data, *Proceedings 18th Symposium Remote Sensing of the Environment,* Vol. 2, pp. 1011-1018.

Meier, E., 1989. Geometrische Korrektur von Bildern orbitgestuetzter SAR Systeme, *Remote Sensing Series, Vol. 15,* Remote Sensing Laboratories, University of Zurich.

Meier, E., C. Graf and D. Nuesch, 1989. Generation of Geocoded Spaceborne SAR Image Products, *Proceedings IGARSS '89,* pp. 2473-2477.

Mercer, J.B., R.T. Lowry, F. Leberl and G. Domik, 1986a. Digital Terrain Mapping with STAR-1 SAR Data, *Proceedings IGARSS '86,* Zurich, pp. 645-650.

Mercer, J.B., G. McAvoy, E. Leavitt and R. Lowry, 1986b. Advanced Radar Systems for Support of Arctic Marine Operations, *Proceedings International Polar Transportation Conf.,* Vancouver, BC.

Mercer, B., P. Button, H. Millot, M. Karspeck and F. Leberl, 1989. Topographic Mapping from GPS-Supplemented Airborne Radar, Pres. Paper, *IGARSS '89,* Vancouver.

Mercer, B., P. Button, M. Millot, F. Leberl and K. Soofi, 1991. Starmap Processing of SAR Imagery for Petroleum Exploration in Irian Jaya, *Proceed. 8th Thematic Conf. on Geologic Remote Sensing,* Denver, CO, 29 April-2 May, pp. 101-103.

Merifield, P., R. Hazen and D. Evans, 1984. Discrimination of Desert Surficial Materials for Engineering/Environmental Geology Applications Utilizing Co-Registered LANDSAT-MSS and SEASAT SAR Data, *Proceedings 3rd Thematic Conference Intl. Symposium on Remote Sensing of the Environment,* Fort Collins, CO, Vol. 2, pp. 487-696.

Moore, R.K., 1964. Heights from Simultaneous Radar and Infrared. *Photogrammetric Engineering,* Vol. XXXV.

Moreira, H.F., 1973. Project RADAM-Remote Sensing Application to Environment Analysis of Amazon Region, *2nd Ann. Remote Sensing of Earth Resources Conference,* Univ. of Tennessee Space Inst., Tullahoma, TN.

Muhleman, O.D., 1964. Radar Scattering from Venus and the Moon, *Astronomical Journal,* Vol. 69, pp. 34-41.

Murai, S. and H. Maeda, 1981. Image Registration of LANDSAT MSS Data and SEASAT SAR Data, *Proceedings Asian Conference on Remote Sensing,* pp. F-1.1 to F-1.13.

Murphrey, S.W., 1978. *SAR-LANDSAT Image Registration Study-Final Report,* IBM Corp., Gaithersburg, MD, 164 p.

Naraghi, M., W. Stromberg and M. Daily, 1983. Geometric Rectification of Radar Imagery Using a Digital Elevation Model, *Photogrammetric Engineering and Remote Sensing,* Vol. XLIX, pp. 195-200.

Naraghi, M. and W. Stromberg, 1982. Radar Image Registration and Rectification, Proceedings SPIE, Vol. 359, *Applications of Digital Image Proceedings IV,* San Diego, pp. 186-192.

Nichols, A., J. Wilhelm, T. Gaffield, R. Inkster and S. Leung, 1986. A SAR for Real-Time Ice Reconnaissance, *IEEE Trans. Geoscience and Remote Sensing,* Vol. GE-24.

Nuesch, D.R., 1982. Augmentation of LANDSAT MSS Data by SEASAT SAR Imagery for Agricultural Inventories, *Techn. Univ. Zurich, Remote Sensing Series,* Vol. 7, NASA IT-E2-04233, 114 p.

Oddy, C.J. and A.J. Rye, 1983. Segmentation of SAR Images Using a Local Similarity Rule, *Pattern Recognition Letters* (Netherlands), Vol. 1, No. 5-6, pp. 443-.

Parashar, S. and G.J. Wessels, 1989. Synthetic Aperture Radar Data Simulation Software Package at CCRS, *Proceedings IGARSS '89,* pp. 1729-1732.

Perlant, F., 1993. *Terrain Geocoding and SAR Interferometry,* (See GeoSAR, 1994)

Peterson, R.K., 1976. Radar Correlator Geometric Control, Report GIB 9397, Goodyear Aerospace Corp., Litchfield Park, AZ; Pres. Paper, *13th Cong. International Society Photogrammetry,* Helsinki, Finland.

Petrie, G., A. Hsu and A.E. Ali, 1984. Geometric Accuracy Testing of SAR-580 and SEASAT-SAR Imagery, *Proceedings SAR-580,* Investigators Workshop, ISPRA, Italy, Vol. L, No. 1, pp. 71-101.

Pettengill, G.A., C.C. Counselman, L.P. Rainville and I.I. Shapiro, 1969. Radar Measurements of Martian Topography, *Astron. J.* Vol. 74, pp. 461-482.

Pettengill, G., 1978. Physical Properties of the Planets and Satellites from Radar Observations, in *Annual Review of Astronomy and Astrophysics,* Vol. 16, pp. 265-292.

Pettengill, G.H., E. Eliason, P.G. Ford, G.B. Loriot, H. Masursky and G.E. McGill, 1980a. Pioneer Venus Radar Results: Altimetry and Surface Properties, *Journal Geophysical Research,* Vol. 85, No. A13, pp. 8261-8270.

Pettengill, G.H., D.B. Campbell and H. Masursky, 1980b) The Surface of Venus, *Scientific American,* Vol. 243, No. 2, pp. 54-65.

Pfeiffer, F. and F. Quiel, 1985. Geometric Registration and Land Use Classification of SAR-580 and Airborne Multi-Spectral Scanner Data, *Proceedings SAR-580* Investigators Workshop, ISPRA, Italy, Vol. 2.

Phillips, R.J., *et al.,* 1973. Apollo Lunar Sounder Experiment, Apollo 17 Preliminary Science Report, *NASA Special Publ. SP-330,* Washington, DC.

Ploessing, M.. W. Kropatsch and D. Strobl., 1989. Sherlock Supports the Geocoding of SAR Images, *Proceedings IGARSS '89,* pp. 856-859.

Poehler P., *et al.,* 1993. Digital Workstation for Vensu Topographic Mapping. *SPIE Proceedings* Vol. 1943, pp. 45-56.

Prati, C., F. Rocca and A. Monti-Guarnieri, 1989. Effects of Speckle and Additive Noise on the Altimetric Resolution of Interferometric SAR (ISAR) Surveys, *Proceedings IGARSS '89,* Ann Arbor, MI.

Prati C. and F. Rocca, 1990. Limits to the Resolution of Elevation Maps from Stereo SAR Images, *International Journal Remote Sensing,* Vol. 11, No. 12, 1990, pp. 2215-2235.

Prati C., F. Rocca and A. Monti Guarnieri, 1992. SAR Interferometry experiments with ERS-1, Presentation at the First ERS-1 Workshop, Canne, France, 4-6 November

Prati C. and F. Rocca, 1994. Use of the Spectral Shift in SAR Interferometry. *ESA SP-361,* pp. 691-696.

Protherse, W.M., *et al.,* 1950. The Geometry of the Radarscope, Mapping and Charting Laboratory, Technical Paper No. 107, Ohio State Univ., Columbus, OH.

Quegan, S., 1984. Measurement of Geometric Distortion in Airborne SAR Images, *Proceedings IGARSS '84,* ESA-SP215, pp. 595-599.

Quegan, S., N. Veck, A. Wright, D. Cruse and J. Skingley, 1985. The Development of Automatic Methods for Handling SAR Images Over Land, *ESA SP-223,* pp. 23-29.

Radar Geology, 1980. *Radar Geology, an Assessment, JPL Publ. 80-61,* Jet Propulsion Laboratory, Pasadena, CA.

Raggam, J., 1985. Untersuchungen und Entwicklungen zur Stereoradargrammetrie, Dissertation, Techn. Univ., Graz, Austria, 152 p.

Raggam, J. and F. Leberl, 1984. SMART-A Program for Radar Stereo Mapping on the Kern DSR-1, *Proceedings 50th Ann. Conv., American Society Photogrammetry,* pp. 765-773.

Raggam, J., D. Strobl and G. Triebnig, 1986. The Rectification of SAR Image Data Using a Digital Elevation Model and Image Simulation Techniques, Technical Note No. 17, Graz Research Center, Graz, Austria.

Raggam J., 1994. Investigation of the Stereoscopic Potential of ERS-1 SAR Data. *Proceedings of the 4th GeoSAR Workshop,* Loipersdorf, Austria (see GEOSAR, 1994).

Raggam J., A. Almer and D. Strobl, 1992. Multisensor Mapping Using SAR in Conjunction with Optical Data, *Proceedings of the Int'l Congress of the ISPRS,* Washington, USA.

Ramachandran, S., 1984. *Terrain Elevation Data Compaction for Radar Simulation,* Goodyear Aerospace, OH, 5 p.

Ramapryan, H.K., C.W. Murray, J.P. Strong and H.W. Blodget, 1984. *Automatic Elevation Mapping and Registration, in SIR-B Science Investigations Plan, JPL Publ. 84-3,* Jet Propulsion Laboratory, Pasadena, CA, pp. 4.1 18-4. 120.

Ramapryan, H.K., J.P. Strong, Y. Hung and C.W. Murray, Jr., 1986. Automated Matching of Pairs of SIR-B Images for Elevation Mapping, *IEEE Trans. Geoscience and Remote Sensing,* Vol. GE-24, pp. 462-472.

Raney, R.K. and G.J. Wessels, 1988. Spatial Considerations in SAR Speckle Simulation, *IEEE Trans. Geoscience and Remote Sensing,* Vol. GE-26, No. 5.

Rauste, Y., 1988. DEM-Based Image Processing Methods for SAR Images, *Proceedings International Society Photogrammetry and Remote Sensing,* Kyoto, Japan.

Rauste, Y., 1986. Rectification of Spaceborne SAR Images Using Polynomial Rectification and a Digital Elevation Model, *Photogrammetric Journal Finland,* Vol. 1 1, pp. 53-67.

Raytheon Co., 1973. Digital Rectification of Sidelooking Radar (DRESLAR. Final Report, Raytheon Co., Autometric Operation, Project for US Army Engineer Topographic Laboratories, Report No. ETL-CR-73-18, Ft. Belvoir, VA.

Rebillard, P. and D. Evans, 1983. Analysis of Co-Registered LANDSAT, SEASAT and SIR-A Images of Varied Terrain Types, *Geophysical Research Letters,* Vol. 10, No. 4, pp. 277-280.

Rebillard, P. and J. Ballais, 1984. Surficial Deposits of Two Algerian Playas as Seen on SIR-A, SEASAT andLANDSAT Co-Registered Data, *Zeitschrift fuer Geomorphologie,* Vol. 28, No. 4, pp. 483-498.

Rebillard, P., C. Elachi, M. Naraghi, J. Soha and W. Stromberg, 1982. SEASAT/SIR-A Digital Registration over Algeria, *International Society Photogrammetry and Remote Sensing Comm. VII,* International Symposium, Toulouse, pp. 271-276.

Rebillard, P., P. Pascaud and D. Sarrat, 1984. Merging LAND-SAT and Spaceborne Data over Tunisia, in *Advances in Space Research,* Vol. 4, No. 1 1, pp. 133-138.

Reynolds, D. and E. Smith, 1979. Detailed Analysis of Composited Digital Radar and Satellite Data. *American Meteorological Society Bull.,* Vol. 60, No. 9, pp. 1024-1037

Rindfleisch, T., 1966. Photogrammetric Method for Lunar Topography, *Photogrammetric Engineering,* Vol. XXXII, No. 2.

Rinner, K., 1948. Die Geometrie des Funkbildes, Austrian Academy of Sciences, Math. Naturwiss. Klasse, also in Handbuch der Vermessungskunde, Vol. VI, Jordan-Eggert-Kneissl, eds., *Metzler'sche Verlagsbuchhandlung,* Stuttgart, FRG.

Rocca, F. and C. Prati, 1992. Innovative applications of satellite SAR surveys, *Satellite Symposium No.2,* ISY Conference, Munich, March 1992, ESA ISY-2, 193-197.

Roessel, J. van and R. de Godoy, 1974. SLAR Mosaics for Project RADAM, *Photogrammetric Engineering,* Vol. XL.

Rogers, D. and T. Heimburger, 1981. SAR Coordinate Processing System, *Proceedings SPIE,* Vol. 278, pp. 124-131.

Rogers, A.E. and R.P. Ingalls, 1969. Venus: Mapping the Surface Reflectivity by Radar Interferometry, *Science,* Vol. 165, pp. 797-799.

Rosenfield, G.B., 1968. Stereo Radar Techniques, *Photogrammetric Engineering,* Vol. XXXIV, pp. 586-594.

Roth, A., H. Craubner and T. Bayer, 1989. Prototype SAR Geocoding Algorithms for ERS-1 and SIR-C/X-SAR Images, *Proceedings IGARSS '89,* pp. 604-607.

Rothrock, D.A. and A.S. Thorndike, 1984. *Sea Ice Movements from Synthetic Aperture Radar, Final Report,* Univ. of Washington, Seattle, 84 p.

Rott, H. and Th. Nagler, 1993. Snow and Ice Investigations by ERS-1 SAR - First Results, *Proceedings First ERS-1 Symposium – Space at the Service of our Environment,* Cannes, France, 4-6 November; ESA SP-359, pp 577-582.

Rott, H., K. Sturm and H. Miller, 1993. Signatures of Antarctic Firn by Means of ERS-1 AMI and by Field Measurements, *Proceedings First ERS-1 Symposium – Space at the Service of our Environment,* Cannes, France, 4-6 BNov., ESA SP-359.

Rott H. and T. Nagler, 1994. *Capabilities of ERS-1 SAR for Snow and Glacier Monitoring in Alpine Areas. ESA SP-361,* pp 965-970.

Roueche, D. and J. Brumfield, 1981. An Evaluation of LANDSAT MSS and Merged LANDSAT-MSS/SEASAT-SAR Classified Data Sets for Land Cover/Category Analysis, CSC Tech Memo 81-6238.

Rumsey, H.C., G.A. Morris, R.R. Green and R.M. Goldstein, 1974. A Radar Brightness and Altitude Image of a Portion of Venus, *Icarus,* Vol. 23, pp. 1-7.

Rydstrom, H.C., 1968. *Radargrammetric Applications of the Right Angle Solution Nomogram, Report GIB-9124,* Goodyear Aerospace Corp., Litchfield Park, AZ.

Sasse V., 1989. Correlation of SAR Data with Optical Data and with Simulated Data, *Proceedings 2nd International Workshop on Image Rectification Techniques for Spaceborne Synthetic Aperture Radar,* Loipersdorf, Austria, January (see GEOSAR, 1989).

Sasse V., 1989. Korrelation von SAR Daten mit optischen Daten und mit simulierten Daten. Z. *Photogrammetrie und Fernerkundung.* Vol. 57, pp 211-221.

Schanda, E., 1985. A Radargrammetry Experiment in a Mountain Region, *International Journal Remote Sensing,* Vol. 6, No. 7, pp. 1 113-1124.

Science, 1991. *Magellan at Venus.* Special Papers in Volume 252, Nr. 5003, pp. 247-312.

Scheps, B., 1960. To Measure is to Know-Geometric Fidelity and Interpretation in Radar Mapping, *Photogrammetric Engineering,* Vol. XXVI.

Schertler, R., *et al.,* 1975. Great Lakes All-Weather Ice Deformation, *Proceedings 10th International Symposium Remote Sensing of Environment,* Ann Arbor, MI.

Schreier G., D. Kosmann and A. Roth, 1990. Design Aspects of a System for Geocoding Satellite SAR Images, *ISPRS Journal of Photogrammetry and Remote Sensing,* 45, 1-16.

Schreier G. (ed), 1993. SAR Geocoding: Data and Systems. With 18 papers. Wichmann Verlag, Karlsruhe, Germany, 435 pages.

Schreiter, J.B., 1950. Strip Projection for Radar Charting, *Mapping and Charting Laboratory, Techn. Paper No. 130,* Ohio State Univ., Columbus, OH.

Shakine, A. and T. Le Toan, 1978. A Study of Digitized Radar Images, *Proceedings International Symposium of Remote Sensing of Environment,* Ann Arbor, MI.

Shanmugam, K. *et al.,* 1981. Textural Features for Radar Image Analysis, *IEEE Trans. Geoscience and Remote Sensing,* Vol. GE-19, No. 3, pp. 153-156.

Shaw, E. and E. Langham, 1989. RADARSAT: Canada's Microwave Satellite, *Proceedings IGARSS '89,* pp. 197-199.

Shuchman, R.A. *et al.,* 1979. SAR Geometric Distortions and an Optical Correction Algorithm, *SAR Ocean Wave Algorithm Dev. Prog.* pp. 21-57.

Smith H.P., 1948. *Mapping by Radar – the Procedures and Possibilities of a New and Revolutionary Method of Mapping and Charting,* US Air Force, Randolph Field, TX.

Sowter A. *et al.,* 1990. *An Error Budget for ERS-1 SAR Imagery,* GEC-Marconi Research Centre, MTR 90/02.

Stilwell, J.E.,1963. Radar Network Adjustment, *Photogrammetric Engineering,* Vol. XXI.

Super, A.D. *et al.,* 1975. Remote Sensing Applied to the International Ice Patrol, *Proceedings 10th Symposium Remote Sensing of the Environment,* Ann Arbor, MI.

Sutton J. and D. Mudry, 1983. Iceberg Distributions in the Labrador Sea from SLAR Imagery 1978 to 1980, *Proceedings Conference on Port and Ocean Engineering under Arctic Conditions (POAC),* Helsinki, Vol. 3, pp. 214-221.

Teleki, P. and R. Ramseier, 1978. The SEASAT-A Synthetic Aperture Radar Experiment, *Proceedings International Symposium Comm. VII, International Society Photogrammetry,* Univ. of Freiburg, pp. 92-1 14.

Thomann, G., 1969. Distance Computation on Radar Film, in Simonnett. D.G. (ed.), The Utility of Radar and Other Remote Sensors in Thematic Land Use Mapping from Spacecraft, *Annual Report, NASA*-140.

Thomas. J., V. Kaupp, W. Waite and H. MacDonald, 1987. Considerations for Optimum Radar Stereo, *Proceedings IGARSS '87.* Ann Arbor, MI, pp. 1531-1536.

Thomas, J., R. Mullen, F. Leberl, W. Kober and J. Cimino, 1988. Concepts for Processing and Analyzing of Multiple SAR and LANDSAT Images. *SPIE - Proceed. Conference on Remote Sensing,* Orlando, FL, April 1988, pp. 1741-1747.

Thomas, J., W. Kober and F. Leberl, 1989. Multiple Image SAR Shape-from-Shading, *Proceedings IGARSS '89,* pp. 592-596.

Thomas, J.K., *et al.,* 1989. *Automated Stereo Correlation,* Contract Report Prepared for Mitsubishi International Corporation. Vexcel Corp., Boulder, CO (USA).

Thomas, J., V. Kaupp, W. Waite and H. MacDonald, 1986. Computer Derived Height from SIR-B Stereo Radar Images, *Proceedings IGARSS '86,* Zurich. Vol. 1, pp. 639-643.

Thomas J.K., W. Kober and F. Leberl, 1990. Radarclinometry – Shape from Shading, Chapter 15 of F. Leberl: *Radargrammetric Image Processing,* Artech House, Norwood, MA.

Thomas, J., W. Kober and F. Leberl, 1991. Multiple Image SAR Shape-from-Shading, *Photogrammetric Engineering and Remote Sensing,* Vol. 57, No. 1, pp. 51-59.

Thompson, T.W. *et al.,* 1972. Progress Report on 25 cm Radar Observations of the 1976 AIDJEX Studies, Arctic Ice Dynamics Joint Experiment (AIDJEX) *Bulletin No. 12,* Univ. of Washington, Seattle.

Thorndyke, A.S. and D. Rothrock, 1983. in Wells, G., *et al.,* Science Program for an Imaging Radar Receiving Station in Alaska, *Report of the Science Working Group, NASA-JPL,* Pasadena, CA.

Tiernan, M. *et al.,* 1976. Lunar Cartography with the Apollo 17 Radar Imagery, *The Moon,* Vol. 15, No. 1-2.

Tilley, D.G., 1984. Amplitude Distributions for SEASAT SAR and Skylab Data with Statistics for Classification and Correlation, *Electromagnetics,* Vol. 4, No. 2-3, pp. 297-308.

Togliatti, G. and A. Moriondo, 1984. Metric Evaluation of SAR-580 Optical Images for Cartographic Purposes, in *ESA-SP 214,* pp. 251-255.

Toll, D.L., 1985. Analysis of Digital LANDSAT MSS and SEASAT SAR Data for Use in Discriminating Land Cover at the Urban Fringe of Denver, Colorado, *International Journal Remote Sensing,* Vol. 6, No. 7, pp. 1209-1229.

Triebnig, G., ed., 1987. Synthetic Aperture Radar Image Rectification Techniques, *Proceedings GeoSAR International Workshop, Loipersdorf, Austria,* published as DIBAG-Report 29, Graz Research Center, Graz, Austria, 108 p.

Ulaby, F., R. Li and K. Shanmugam, 1984. Classification Using Airborne Radar and LANDSAT Data, *Univ. of Kansas Remote Sensing Lab, Report 360-313.*

Ulbricht, A., 1979. Tentative Image Processing With SEASAT Image Correlated onto LANDSAT Scene, *ESA-SP 154,* pp. 19-23.

United States Coast Guard, 1972. Analysis of SLAR Imagery of Arctic and Lake Ice, Rep. DOT-CG-0l-800-A, US Dept. of Transportation, Office of Research and Development, Washington, DC.

Vesecki, J., *et al.,* 1988. Observation of Sea-Ice Dynamics Using Synthetic Aperture Radar Images: Automated Analysis, *IEEE Trans. Geoscience and Remote Sensing,* Vol. GE-26, pp. 38-47.

Waite, W. and H. MacDonald, 1970. Snowfield Mapping with K-Band Radar, *Remote Sensing of Environment,* Vol. 143-150.

Waterman, S., D. Clark and D. Stevenson, 1984. Conceptual Design for an Ice Data Integration and Analysis System, *Proceedings 9th Conference Symposium on Remote Sensing,* pp. 25-38.

Welch R., T. Jordan and J. Luvall, 1990. Geocoding and Stereo Display of Tropical Forest Multisensor Datasets, *Photogrammetric Engineering and Remote Sensing,* Vol. 56, pp 1389-1392.

Werner C.,U. Wegmueller, D. Small and P. Rosen, 1994. Applications of Interferometrically Derived Terrain Slopes: Normalization of SAR Backscatter and the Interferometric Correlation Coefficients, *ESA SP-361,* pp. 723-726.

Wildey, R.L., 1975. Generalized Photoclimometry for Mariner 9, *Icarus,* Vol. 25, pp. 613-626.

Wildey, R.L., 1986a. Radarclinometry for the Venus Radar Mapper, *Photogrammetric Engineering and Remote Sensing,* Vol. LII, No. 1, pp. 41-50.

Wildey, R.L., 1986b. Radarclinometry, *Earth, Moon and Planets,* Vol. 36, pp. 217-247.

Wildey R., 1984. Topography from Single Radar Images. *Science,* Vol. 200, pp. 153-156.

Wise, P. and J. Trinder, 1987. Assessment of SIR-B for Topographic Mapping, *Photogrammetric Engineering and Remote Sensing,* Vol. 53, pp. 1539-1544.

Wohlers, M.R., S. Hsiao, J. Mendelsohn and G. Gardner, 1980. Computer Simulation of Synthetic Aperture Radar Images of Three Dimensional Objects, *IEEE Trans. Aerospace and Electronic Systems,* Vol. AES-16, No. 3, pp. 258-271.

Wong. R. and R. Orth, 1980. Registration of SEASAT/LANDSAT Composite to UTM Coordinates, *Proceedings 6th Conference Symposium on Remote Sensing.*

Wong, R., 1979. Radar to Optical Scene Matching, *Proceedings SPIE,* Vol. 186.

Wong, R., 1980. Intensity Signal Processing of Images for Optical to Radar Scene Matching, *IEEE Trans. on Acoustics, Speech and Signal Processing,* Vol. ASSP-28, No. 2, pp. 280-283.

Wu, S., 1982. Multisensor Data Analysis and its Application to Monitoring of Cropland, Forest, Strip Mines and Cultural Targets, *Proceedings 8th Conference on Machine Processing of Remote Sensing Data,* pp. 313-320.

Wu, S. and F. Schafer, 1980. Side Looking Radar Using Analytical Plotters, *Archives ISPRS, 14th Congress,* Vol. 23, Part B-11, pp. 174-179.

Wu, S., 1980. An Improvement in Land Cover Classification Achieved by Merging Microwave Data with LANDSAT MSS Data, *Proceedings American Society Photogrammetry Conv.,* pp. 293-309.

Yamane, K., S. Maeda and M. Matsuo, 1984. A Construction Method of Terrain Height Map with Stereo Radar, *Trans. Inst. Electron. Comm. Engineering,* Japan, Vol. J67B, No. 10, pp. 1064-1071.

Yao, S. and J. Gilbert, 1983. Registration of a Synthetic Aperture Radar Image and Thematic Mapper Imagery for Remote Sensing Applications, *IGARSS '83,* San Francisco, Vol. 1, Pt WP-4, pp. 1.1

Yorimoto, K., 1965. All Weather Mapping, *Proceedings of the Fall Technical Meeting,* American Society Photogrammetry, Dayton, OH.

Yorimoto, K., 1972. Methods and Instruments for the Restitution of Radar Pictures, *Archives International Society Photogrammetry, 12th Congress,* invited paper, Ottawa.

Zebker, H. and R.M. Goldstein, 1986. Topographic Mapping from Interferometric Synthetic Aperture Radar Observations, *Journal Geophysical Research,* Vol. 91, No. B5, pp. 4993-4999.

Zheng Q., 1992. Robust Algorithms for Estimation of Illuminant and Shape from Shading. Ph.D. Dissertation, University of S. California, Dept. Electrical Engineering, Los Angeles, 283 p.

Zhurkin, I.G. and N. Korneyev, 1974. Relationship Between the Coordinate of Terrain Points and the Coordinates of Image Points in Side-Looking Radar Systems with an Antenna Along the Fuselage, *Geodesy, Mapping, Photogrammetry,* Vol. 16, No. 3, pp. 140-146.

Zobrist, A.L., R.J. Blackwell and W.D. Stromberg, 1979. Integration of LANDSAT, SEASAT and Other Geo-Data Sources, *Proceedings 13th International Symposium on Remote Sensing of Environment,* Ann Arbor, MI, Vol. 1, pp. 271-289.